Omar Rafae Mahmood Al Omar

Modeling and simulation of complete liquid-vapor phase change process inside porous media

Cuvillier Verlag Göttingen
Internationaler wissenschaftlicher Fachverlag

Modeling and Simulation of Complete Liquid – Vapor Phase Change Process inside Porous Media

Modeling and Simulation of Complete Liquid–Vapor Phase Change Process inside Porous Media

To the Faculty of Mechanical, Process and Energy Engineering
of the Technische Universität Bergakademie Freiberg

approved

THESIS

to attain the academic degree of
Doktor-Ingenieur
(Dr.-Ing.)

Submitted

by **M.Sc. Omar Rafae Mahmood Al Omar**
Born on the 07. September 1979 in Mosul-Iraq

Reviewers:
Prof. Dr.-Ing. Dimosthenis Trimis (KIT, Karlsruhe)
Prof. Dr. Subhashis Ray (TU Freiberg)
Prof. Dr.-Ing. Christian Hasse (TU Freiberg)

Date of the award: 16th September 2016

Bibliographical information held by the German National Library

The German National Library has listed this book in the Deutsche Nationalbibliografie (German national bibliography); detailed bibliographic information is available online at http://dnb.d-nb.de.

1st edition - Göttingen: Cuvillier, 2016

Nonnenstieg 8, 37075 Göttingen, Germany
Telephone: +49 (0)551-54724-0
Telefax: +49 (0)551-54724-21
www.cuvillier.de

1st edition, 2016
This publication is printed on acid-free paper.

ISBN 978-3-7369-9370-9
eISBN 978-3-7369-8370-0

To my family
and friends

ACKNOWLEDGEMENTS

I am really thankful for the time which I spent here, at the Institute of Thermal Engineering and Thermodynamics, of the Technische Universität Bergakademie Freiberg, until I could bring this thesis to the end. I want at least to mention and to thank some people who were involved in their own different ways.

First, I would like to express my sincere gratitude to my advisor, Prof. Dr.-Ing. Dimosthenis Trimis for giving me the chance to get DAAD scholarship and for his continuously supports me with guidance and advice during my DAAD scholarship until the completion of the dissertation. I would also like to thank him for his generous support and encouragement to attend the FDTT conference. His vast experience taught me a lot. Furthermore, I would also like to thank him for support me to get a scholarship from Collaborative Research Centre (SFB 920). Additionally, I would like to express my sincere appreciation to Prof. Dr. Subhashis Ray for his guidance, support during my research on this thesis. His ideas, discussions, wonderful advice play a very important role in accomplishing this work. I learned a lot from him in both technical and non-technical discussions. Learning Computational Fluid Dynamics under him was a rich experience for me. The credit to my strength in Fluid Mechanics and in Numerical programming goes to him. I would also like to thank him for support me with guidance during both my DAAD and SFB 920 scholarships.

I would also like to gratefully acknowledge the financial support from the German Academic Exchange Service (DAAD) and the Ministry of Higher Education and Scientific Researcher of Iraq for their scholarship grant to me. Moreover, I would also like to gratefully the financial support from the German Research Foundation (DFG) for supporting the investigation in the sub-project B02 that is part of the Collaborative Research Center CR920.

Moreover, I want to thank Dr. Miguel Mendes, who greatly supported me with his knowledge and experience in the FORTRAN language, and for his valuable comments and discussions. His timely clarifications have helped me to smoothly progress in my work. Furthermore, I thank all the team at the Chair of Gas and Heat Technology - IWTT for the hospitality and nice work environment. I need to mention some of them, not only due to our excellent working collaboration, but also because their support and friendship have a particular meaning for me. My special thanks go to my unforgettable colleagues Alexandra Loukou in the Combustion group as well as Eric Werzner, Cornelius Demuth and Li,Ye in the Numeric's group is not only for sharing the office with me but also for their encouragement, supports, interests and providing their help so willingly every time "daily life trouble" occurred and made the past couple of years more delightful as well as for the countless working hours in the same office, where we also got the chance to exchange our views on research and other aspects of life. It is not possible to get more friendship than they provided to me. I would also like to thank our Technical Assistants – IT, without their support, this work would certainly not have been possible.

Beside my advisors and colleagues, I would like to express my deep gratitude to my wife and children for their patience and for helping me to keep a valuable balance in my life between past and present. Their love gave me the strength and incentive to overcome challenges. Finally, I do not find words to thank my parents and describe what they have done for me. They have been a continuous source of encouragement and moral support at all phases of my life and they always wanted to see me at the top.

Omar Al Omar

Freiberg, September 2016

ABSTRACT

This work deals with modeling and numerical simulation of the complete liquid–vapor phase change process inside porous media, based on the Two-Phase Mixture Model (TPMM) along with the assumption of Local Thermal Equilibrium (LTE) and Non-Equilibrium (LTNE) conditions. In particular, it demonstrates the necessity and usefulness of a newly proposed smoothing algorithm for handling the sharp discontinuities in the effective diffusion coefficient in order to avoid the occurrence of non-physical “jump” in the predicted temperature distribution during numerical simulation of the complete phase change process within porous media. For the purpose of demonstration, one- and two-dimensional phase change problems inside a porous evaporator operated in the Darcy flow regime have been considered, both under steady-state and transient conditions. The Finite Volume Method (FVM) has been used on both staggered and non-staggered grid layouts in order to solve the governing conservation equations for both the fluid and solid phases. A thorough parametric study indicates that the adoption of the proposed smoothing algorithm does not alter the true or expected solution. All tested cases, covering applicable ranges of parametric variations, could be physically interpreted. The methodology is, therefore, recommended for future simulations of complete phase change processes within porous media.

In the present work, after critically analyzing the drawbacks of the existing enthalpy formulation based on TPMM, a modified formulation has been developed that can easily accommodate substantial density variations in the single phase regions. The results obtained from the modified enthalpy formulation have been compared with that predicted by the conventional volumetric enthalpy formulation and excellent agreements have been observed for all tested cases. Additionally, the modified enthalpy formulation requires significantly less computation time and therefore, is strongly recommended for the simulation of the complete phase change process inside porous media. On the other hand, a comparison between results obtained using LTE and LTNE models indicates that wherever applicable, particularly for lower inlet Reynolds number and higher heat input, the latter should be used. Different models for the partitioning of wall heat flux using the LTNE model have negligible influence on the overall predictions, except in the vicinity of the wall. The results also show that LTE model fails to produce realistic predictions for multi-dimensional problems, particularly when the superheated vapor phase is formed inside the evaporator. On the other hand, the conduction heat transfer through the solid phase and the internal heat exchange between the solid and the fluid phases across the interface separating the superheated vapor and the two-phase regions provide two additionally required mechanisms for realistic predictions of the LTNE model. The LTNE model is more appropriate and necessary for the accurate estimation of the wall heat flux, and hence strongly recommended for the simulation of the complete phase change process inside porous media. In addition, the results also show that the LTNE model as well as the smoothing algorithm are successful in dealing with the rapid change in the modeled effective heat capacity ratio and effective diffusion coefficient for transient simulations of the complete phase change process. Staggered and non-staggered grid layouts have been implemented, showing identical results in orthogonal geometries.

The last part of this study involved coupling the anisotropy in both mechanical and thermal porous media properties along with the LTNE model in order to investigate the complete phase change process in channel flow. The computed results show that the anisotropy of permeability and thermal conductivity of the solid phase have significant effect on the complete phase change process. This study also includes numerical simulations of the complete phase change process inside a divergent porous evaporator. Effects of various parameters on the temperature distribution have been carefully investigated, which clearly indicate that operating conditions and the geometry of the diffuser strongly influence the outlet conditions of steam, whereas porous medium properties have only a minor impact.

CONTENTS

LIST OF FIGURES

LIST OF TABLES

NOMENCLATURE

Some symbols, which are introduced briefly through the derivations and, otherwise are not referred to in the text, are locally defined in the appropriate locations and are not listed here. The SI units are used throughout.

a	coefficient of the discretized equation
a_s	Specific surface of the porous medium, $1/\mathrm{m}$
a_{l2}, a_{v2}	Second order coefficients for liquid and vapor densities, respectively
A_c	Cross-sectional area of the pipe per unit radian $= R^2/2$, m^2
$\mathbf{b}$	Body force vector per unit mass, $\mathrm{m/s^2}$
$\tilde{\mathbf{b}}$	Normalized body force vector per unit mass $= \mathbf{b}/g$
C_p	Specific heat, $\mathrm{J/kgK}$
d_p	Characteristic pore size of porous matrix, m
D	Capillary diffusion coefficient, $\mathrm{m^2/s}$
D_h	Hydraulic diameter $= 2L_{ref}$, m
ev	Total evaporated volume fraction
f	Hindrance function
Fr	Froude number $= u_{in}/u_g = u_{in}/\sqrt{g\,L_{ref}} = Re_{in}/Re_g$
F_m	Mass flow rate, $\mathrm{kg/sec}$
$\mathbf{g}$	Acceleration due to gravitational vector, $\mathrm{m/s^2}$
h	Specific enthalpy, $\mathrm{J/kg}$
h_{co}	Convective heat transfer coefficient at the outer surface of the pipe, $\mathrm{W/m^2K}$
h_{fg}	Latent heat of vaporization $= h_{v,sat} - h_{l,sat}$, $\mathrm{J/kg}$
$h_{s\alpha}$	Convective heat transfer coefficient in the pores, $\mathrm{W/m^2K}$
H	Modified volumetric enthalpy $= \rho\left(h - 2h_{v,sat}\right)$, $\mathrm{J/m^3}$
$\mathbf{j}$	Diffusive mass flux vector, $\mathrm{kg/m^2s}$
J	Capillary pressure function
k_{rl}, k_{rv}	Relative permeabilities for liquid and vapor, respectively
k	Thermal conductivity, $\mathrm{W/mK}$
k_R	Thermal conductivity ratio $= k_{sy}/k_{sx}$
K	Permeability of porous matrix, $\mathrm{m^2}$
K_R	Permeability ratio $= K_y/K_x$
l	Length of individual segments, m
L	Length of the porous either channel or pipe, m
m	Mass flow rate, $\mathrm{kg/sec}$
m_ϕ, m_s	Exponents for smoothing Γ_H or Γ_h in single and two-phase regions, respectively
n	Exponent of saturation in the expression for relative permeabilities
N_{CV}	Number of employed control volumes
Nu_o	Nusselt number based on liquid properties $= h_{co}\left(2L_{ref}\right)/k_l$
p	Effective pressure, Pa

p_c	Capillary pressure, Pa
P	Perimeter of the pipe per unit radian $= R$, m
Pe	Peclet number $= u_{in} L_{ref} / \alpha = RePr$
Pr	Prandtl number $= \mu C_p / k$
$\dot{q}''$	Heat flux, $\mathrm{W/m^2}$
Q^*	Normalized heat flux $= \dot{q}'' L_{ref} / \mu h_{fg}$
$\dot{q}'''_{sf}$	Heat exchange term between fluid and solid phases, $\mathrm{W/m^3}$
$\dot{q}'''$	Heat generation, $\mathrm{W/m^3}$
R	Pipe radius, m
Re	Reynolds number $= u_{in} L_{ref} / \nu$
Re_g	Gravitational Reynolds number $= u_g L_{ref} / \nu_l$
Re_p	Reynolds number based on pore diameter and local phase properties
Re_K	Fluid Reynolds number based on the length scale of the permeability
s	Liquid saturation
s_l, s_v	Cut-off liquid saturations for Γ_H or Γ_h in liquid and vapor phases, respectively
S_{H^*}	Discretized source term for energy equations of the fluid phase
S_s	Discretized source term for energy equation of the solid phase
S_{P^*}	Discretized source term for pressure equation
t	Time, sec
T	Temperature, K
T_w	Wall temperature, K
$\mathbf{u}$	Velocity component vector, m/s
$\mathbf{u}_g$	Gravitational velocity vector $\sqrt{\mathbf{g} L_{ref}}$, m/s
V	Volume, $\mathrm{m^3}$
W	Height of the duct, m
$\mathbf{n}$, $\mathbf{s}$, $\mathbf{d}$	Locally orthogonal coordinates system
x, y, r	Axial, transverse and radial Coordinates, respectively, m

Greek Symbols

α	Thermal diffusivity $= k/\rho C_p$, $\mathrm{m^2/s}$
β	Isobaric expansion coefficient, $\mathrm{K^{-1}}$
δx, δy	Nodal distances in the axial and radial directions, respectively, m
ΔT	Temperature difference for relaxation of Γ_H or Γ_h in the single-phase regions, K
Δx, Δy	Width of the control volume in axial and radial directions, respectively, m
$\Delta \rho$	Difference in densities $= (\rho_l - \rho_v)$, $\mathrm{kg/m^3}$
ϕ	Normalized temperature for relaxation of Γ_H or Γ_h
γ	Advection correction coefficient
Γ_H and Γ_h	Diffusion coefficient for modified volumetric enthalpy and enthalpy, respectively, $\mathrm{m^2/s}$ and $\mathrm{kg/m\,s}$
$\Gamma_{h,\phi}$, $\Gamma_{h,s}$	Asymptotes for smoothing Γ_H or Γ_h in single and two-phase regions, respectively
ε	Porosity
λ	Relative mobility

μ	Dynamic viscosity, $\mathrm{kg/ms}$
ν	Kinematic viscosity, $\mathrm{m^2/s}$
ρ	Density, $\mathrm{kg/m^3}$
σ	Surface tension coefficient, $\mathrm{N/m}$
$\tilde{\sigma}$	Normalized surface tension coefficient $=\rho_l \sigma L_{ref} / \mu_l^2$
Ω	Effective heat capacitance ratio
θ	Degree of angle
φ	Any quantity
ψ	Factor, used to modify Γ_H or Γ_h at saturated condition ($s=0$ and $s=1$)

Subscripts

e,w,s,n	Pertaining to cell faces at e,w,s and n, respectively
eff	Effective
$E,W,S,$ N,P	Pertaining to nodes at E,W,S,N and P, respectively
f	Fluid
i, e, h	Inlet, exit and heated, respectively
o, D	outlet of the pipe and Divergent section, respectively
in	Inlet properties
k	Kinetic
l	Liquid
max	Maximum value
min	Minimum value
CV	Control volume
ref	Reference case
s	Solid
sat	Saturation
r, x, y	Pertaining to radial, axial and transverse directions, respectively
v	Vapor
w	Wall

Superscripts

$*$	Dimensionless
n	New value
$\circ$	Old value for transient problem and reference value for both steady and transient problems

Acronyms

CDS	Central Differencing Scheme
CFD	Computational Fluid Dynamics
FVM	Finite Volume Method
LHS	Left hand side
LTE	Local Thermal Equilibrium
LTNE	Local Thermal Non-Equilibrium
RHS	Right hand side
SFM	Separate Flow Model
SPM	Separate Phase Model
TPMM	Two-Phase Mixture Model
UDS	Upwind Differencing Scheme

CHAPTER 1. INTRODUCTION

The range of scientific and industrial applications of fluid flow and heat transfer associated with either complete or incomplete liquid-vapor phase change process inside porous media is extremely broad and hence in many engineering disciplines, one has almost no difficulty in finding a process, associated with phase change. The vastness of this realm can only be partially explored through a brief discussion of the related recent and ongoing research on the phase change process inside porous media. Therefore, this chapter provides an introduction to the research subject, together with a thorough literature review on the history and development of the related research. Moreover, the chapter outlines the main purpose and the scope of the investigation, presented in this thesis.

1.1. Research Topic, Relevance and Motivation

Phase change problems within porous media arise in a substantial number of scientific and engineering applications for the past four decades. This interest stems from the complicated and interesting phenomena associated with energy transport within the solid matrix. Furthermore, the attractiveness of porous media lies in the contemporary and wide applications available today, which have led to numerous investigations in this area. Examples include safety and post-accident analysis of nuclear reactors [1 – 6], disposal of high-level nuclear wastes [7, 8], packed-bed reactors [9], enhancement of condensation [10, 11], thermal (latent) energy storage [12], porous heat pipes [13, 14], drying equipment [15], heat and moisture transfer in insulation materials [16], oil reservoir engineering [17 – 20], and geothermal systems [21 – 23]. Moreover, a number of complex interacting transport phenomena may take place in non-isothermal multiphase systems. Most often, multiphase flows inside porous media are driven by a complex interaction of gravitational, capillary and viscous forces [24, 25].

A typical example, where complete phase change inside porous media takes place is the humidification of air. In order to humidify dry air to the desired relative humidity, super-heated steam is often added at a measured quantity with a known degree of super-heat. The typical requirement for steam flow rate for such applications is generally quite low. For this purpose, if sub-cooled liquid water is heated inside a pipe by electric heaters, boiling takes place only close to the pipe wall and hence a layer of vapor film is formed over them. Since the thermal conductivity of steam at saturation condition $(100^{o}\mathrm{C})$ is considerably lower than that of the liquid water, this vapor layer acts as the insulation to the heat flow. Therefore, the liquid flowing through the core region continues to remain sub-cooled and an inhomogeneous mixture is obtained at the pipe outlet. In order to obtain a homogeneous mixture at the pipe outlet, a mixing chamber may be used, although it could be extremely difficult to accurately control the degree of super-heat in such a process. A technological alternative, therefore, could be to realize the complete phase change process inside a duct filled with a porous medium. The higher thermal conductivity of the solid matrix of the porous medium facilitates heat transfer from the duct periphery to the core such that the fluid is more or less uniformly heated. The degree of super-heat, however, depends on several parameters, such as, applied heat flux, mass flow rate, inlet temperature, properties of porous media, etc. Therefore, in order to have a better understanding and hence precise control over the phase change process, accurate predictions are required. However, difficulties in numerical simulations occur mainly due to the strongly nonlinear nature of governing equations and constitutive relations. Moreover, as will be shortly apparent in chapter 2, discontinuities in the modeled thermo-physical properties at phase change boundaries also pose a major challenge. Determining a remedy for this problem is the main objective of the present work.

1.2. History of Modeling Two-Phase Flow in Porous Media

Liquid-vapor phase change process inside porous media is encountered in diversified scientific and engineering applications [25]. The theoretical basis for solving such problems essentially rely upon the traditional Separate Flow Model (SFM) [17, 18], where the liquid and the gaseous phases are considered as two distinct fluids with different properties, that generally assume different velocities, satisfying separate set of conservation equations. In this respect, the complete phase change process within porous media could be characterized by the presence of three distinct regions: sub-cooled, two-phase mixture and superheated vapor regions. Since SFM is most often extremely complex and perhaps inconvenient for the direct use in numerical simulations, Ramesh and Torrance [26 – 28] proposed the Separate Phase Model (SPM) in order to solve heat transfer problems involving boiling in presence of natural convection in a fluid-saturated porous medium for each of these regions while continuously tracking the interface between them using a moving boundary approach. For practical applications, however, SFM (or SPM) is considered inconvenient for numerical implementation since it requires tracking of the interfaces using a moving boundary approach and the presence of large number of coupled nonlinear equations.

Recognizing the complexities and the inherent problems of SFM (or SPM), Wang and Beckermann [29] proposed the Two-Phase Mixture Model (TPMM) based on enthalpy formulation for the phase change process through capillary porous media, where the separate phases are considered as the constituents of a binary mixture. This model is characterized by the coexistence of a two-phase zone and single-phase regions with irregular as well as moving interfaces lying in between them. The solutions could be obtained on a fixed grid, without requiring a priori knowledge (tracking) of the phase boundaries, that could be irregular in space as well as moving in time. These formulations essentially rely upon the traditional SFM and hence do not require invoking any additional assumption. The associated conservation equations for TPMM are derived specifically for addressing the phase change problems inside porous media. Based on the enthalpy values of the mixture, the state of the system inside the porous media has been identified. The inherent assumption in this model has been that the two-phase region is at a constant temperature (equal to the boiling temperature of the liquid) and hence phase change is taking place between the interfaces of the two-phase and the single phase regions. As explained latter in chapter 2, Wang et al. [30] first identified that the original formulation of Wang and Beckermann [29] is not readily suitable for numerical implementation owing to several reasons. Therefore, they proposed the first modification to the original model, by introducing the volumetric enthalpy as dependent variable on the temperature and liquid fraction for the energy conservation equation, and presented a study on boiling and natural convection in a porous layer heated from below. Later, Wang et al. [31] examined this model numerically for transient natural convection and boiling in a porous layer heated from below. Wang and Beckermann [32] then performed a numerical study on pressure-driven two-phase flow along vertical plate in a capillary porous medium as a complement to the previous work of Wang and Beckermann [29]. In their study, full two-phase similarity solutions have been obtained for both boiling and condensing flow. They observed that the boiling boundary layer has been normally wider than the one in condensing flow.

However, a closer look into the TPMM of Wang et al. [30] reveals that since some of the mixture variables and properties remain undefined for the superheated vapor phase, it cannot be employed for the prediction of complete phase change process, where phase change takes place from the sub-cooled liquid phase to the superheated vapor phase. In order to eliminate this drawback, Wang [33] proposed the second modification of TPMM [29], by introducing the modified volumetric enthalpy as dependent variable for the energy conservation equation. Nevertheless, all versions of TPMM are characterized by the coexistence within a two-phase zone, separated by the irregular as well as moving interfaces (for transient problems) of single-phase (either liquid or vapor) regions. Since these variants are obtained for fixed numerical grid, unlike SFM or (SPM), there is no requirement for the complex as well as time consuming interface tracking. Possibly owing to the generality and the ease of numerical implementation, the TPMM of Wang is by far the most widely used method for the simulation of phase change process inside porous media. In this respect, several researchers have been adopted the TPMM of Wang for simulating phase change problems under different flow conditions in order to enhance the knowledge of two-phase flow inside porous media. A further careful look into the formulation also reveals that the available formulations are valid only for Darcy flow inside an isotropic porous media [29 – 33]. Although the initial propositions of TPMM [29, 30, 33] are applicable only under the assumption of Local Thermal Equilibrium (LTE) condition, it has been extended in order to accommodate the more general Local Thermal Non-Equilibrium (LTNE) condition. For LTNE condition, the solid matrix and the fluid medium can locally coexist at different temperatures, and the respective energy conservation equations are coupled to each other through the volumetric heat exchange term.

1.3. Review of Literature and Related Work

Phase change problems inside porous media using either the forced or natural convection have attracted numerous researchers due to its implications in a wide set of technological applications. The effects of forced and natural convection on the phase change process within porous media have been studied experimentally and numerically. Thus, the following subsections provide a literature review of the previous experimental and numerical work related to the phase change process inside porous media.

1.3.1. Experimental Work

As compared to the numerical investigations, experimental studies in the field of phase change inside porous media are considerably less in number, possibly owing to the difficulty in acquiring reliable data. Udell [34], for example, obtained theoretical and experimental results for boiling within a rectangular cavity filled with a porous medium, which was heated on one side. The effects of capillarity, gravity forces, and phase change have been included. Theoretical results showed excellent agreement when compared with the experimental data. In the study, the heat transfer was increased several orders of magnitude beyond pure conduction due to evaporation, convection and condensation phenomena similar to conventional heat pipe operation. Later, Easterday et al. [35] reported experimental and numerical results for the two-phase flow and heat transfer in a horizontal porous formation with water flow and partial heating from below. In their study, experimental results have been also attained to measure temperature distributions and to visualize the two-phase flow patterns. Partial agreement between experimental and numerical results has been achieved. A combined experimental and numerical study has been providing new insight into conjugate single and two-phase flow and heat transfer in porous media. Numerical results have been obtained based on the TPMM of Wang et al. Their results showed that the two-phase structure and flow patterns are strongly dependent upon the water inlet velocity and the bottom heat flux.

Peterson and Chang [36] performed an experimental study on two-phase heat dissipation in high-conductivity porous channel heat sinks, where sub-cooled water has been used as the working fluid. The experiments have been conducted for different porous channels sizes and have been fabricated using sintered copper particles inside rectangular copper channels. The experimental results were compared to the results predicted using numerical modeling. Their results indicated that the high thermal conductivity of the porous material and the large solid-fluid contact area combined to create a highly effective, two-phase heat sink which may provide an effective mechanism for cooling high heat flux microelectronics. Zhao et al. [37], on the other hand, carried out an experimental investigation on the buoyancy-induced flow of water associated with the phase-change heat transfer inside a vertical porous tube that is heated at the wall with a constant heat flux. Their results showed that the diameter of the porous tube and the particle size of porous media have significant influence on the amount of vaporized mass of the fluid. Chen et al. [38] performed an experimental study on boiling heat transfer inside channels packed with particles having a bimodal size distribution (sintered copper bi-dispersed porous media). Their results indicated that the porous material is a highly effective two-phase heat sink that offers a lower flow resistance as compared to that of the mono-dispersed porous materials of same pore diameter.

Later, Zhao and Liao [39] conducted an experimental and theoretical modeling study on evaporative heat transfer characteristics of a capillary porous structure heated with a permeable heating source on the top. The experiments have been tested for three different typical conditions according to its heat flux. Their results showed that for small and moderate heat fluxes the whole porous structure became fully saturated with liquid except for adjacent to the horizontal heated surface where evaporation took place uniformly. For higher heat fluxes, a two-phase zone developed in the upper portion of the porous structure, while the lower portion of the porous structure became saturated with sub-cooled liquid. Theoretical results showed that the model is in good agreement with the experimental data. Yuki et al [40] verified experimentally the possibility of extremely high heat flux (over 70 MW/m^2) removal for various porous materials. The experiments have been conducted for two different porous media materials (bronze particle-sintered and copper fibers-sintered) which have high thermal conductivity to enhance the thermal diffusion in the porous material. In their study, constant heat removal against local inlet heat flux of over 70 MW/m^2 has been observed by using the bronze porous medium with high thermal conductivity. Furthermore, the evaluation of heat removal performance for various porosities and particle diameters of copper fiber porous media have been clarified, and the lower porosity material has been found to be useful for improving the evaporation rate inside porous media.

Later, Yuki et al [41] clarified experimentally and numerically the key issues to enable extremely high heat flux removal exceeding $10\,\mathrm{MW/m^2}$ of two-phase flow in particle-sintered porous media. The experiments have been also carried out for two different types of porous media (stainless steel particle–sintered and bronze particle–sintered packings). For the experiments, the effects of porous structures such as pore size and porosity on the heat transfer characteristics under some heat flux inputs have been investigated. The results suggested that liquid-vapor exchange due to capillary and pumping effects works effectively under several $\mathrm{MW/m^2}$ in this cooling system. On the other hand, the TPMM of Wang along with LTE assumptions have been used for numerical simulation of two-phase flow inside porous media in order to evaluate what kind of porous material is appropriated for higher heat removal. The results showed that utilizing a higher thermal-conductivity matrix facilitates a delay in the onset of the phase change near the heating wall and leads to much higher heat flux removal, even at the same liquid saturation, compared to the case utilizing a lower thermal-conductivity matrix. Recently, Li and Leong [42] performed an experimental and numerical investigation in order to investigate the flow boiling characteristics of water and FC-72 inside aluminum foams. With the help of their experiments, the heat transfer process prior to the onset of nucleate boiling and the hysteresis effects have been investigated. The Brinkman–Forchheimer model, along with Local Thermal Non-Equilibrium (LTNE) assumptions has been adopted for the single-phase simulations, while TPMM of Wang [33] has been employed for the two-phase predictions. Their results demonstrated reasonable agreement between the numerical and the experimental data.

1.3.2. Numerical Work

Numerical simulations can provide useful information in such complex systems with phase change processes inside porous media, and they are considered very helpful in supporting the engineering design. In many industrial applications sub-cooled water injection is commonly used in porous evaporators. Coolant phase change occurs in the solid matrix. During a complete phase change process, three distinct regions, namely, sub-cooled liquid, two-phase mixture and superheated vapor regions could be observed inside an evaporator fitted with a porous medium. The development of efficient evaporation process relies heavily on numerical modeling. This is a complex and consuming task since high nonlinearities in the problem formulation may lead to very sharp thermal and saturation fronts. Because of these rapid variations of physical quantities across the fronts, special treatment must be applied in order to achieve reasonable accuracy. The problem of modeling heat and mass transfer in a single-phase fluid flowing through a porous medium is somewhat challenging. A significantly more complicated modeling problem concerns the motion of a fluid through a porous structure which undergoes a phase change. The evaporation process has been classified as such a problem. Fluid phase change in porous media is also at the center of many technological problems. In configurations involving condensation and evaporation, regions of single-phase flow and two-phase flow often coexist within the porous medium. As far as the phase change process inside porous media is concerned, extensive studies have been carried out in the past and performed under different flow condition depending on the desired information and computational limitations.

Waite and Amin [43] used the TPMM of Wang et al in order to study the transient fluid flow and heat transfer mechanisms of two-phase flow in a side heated porous enclosure numerically. In their work, numerical results have been compared with the experimental data with good agreement. Furthermore, steady-state and transient temperature distribution as well as fluid motion have been presented for a wide range of Rayleigh numbers, imposed side heat flux on the vertical wall and fluid velocity at the bottom boundary. The observed results for certain values of the above parameters indicated bi-cellular convective flow of the fluid. Several other researchers [44 – 52, 55, 56], on the other hand, used the TPMM of Wang for the simulation of phase change process under different flow conditions inside porous media. Zhao and Liao [44] numerically investigated mixed convection boiling inside a vertically oriented capillary porous structure with asymmetric heating condition at opposing walls. In their study, different flow directions have been investigated. Liquid saturation, temperature, liquid and vapor velocity fields subjected to both superimposed aiding and opposing flows have been analyzed and presented for different values of inlet velocity. Their results showed that the direction of the incoming fluid have great influence on both the flow field and temperature distribution. Zhao et al. [45], on the other hand, conducted a numerical study on the buoyancy assisted phase change process in a symmetrically heated vertical porous channel. Their results showed that the mass flux increases as the applied heat flux is increased for both single and two-phase flow with rather low vapor fraction. However, the numerical results also indicated that the induced mass flux drops drastically and remains approximately constant afterwards when the vapor fraction is increased. Furthermore, this result was agreed qualitatively when compared with experimental data of Zhao et al. [37].

Although steady-state investigations can provide understanding of the physics behind two-phase flow problems, the transient simulation approach would be more useful since it reveals the evolution of the boiling process and the interactions between the liquid and vapor phases. In this regard, Najjari and Nasrallah [46] conducted a numerical study for the transient flow boiling with mixed convection in a vertical porous layer with localized heating from one side when the liquid is injected at the top face. In their study, temperature, pressure, velocities of the fluids, and evaporated volume fraction have been presented and analyzed for different time-space evolutions. Further, the effects of the inlet velocity, imposed heat flux, and permeability have been performed. Numerical results showed that boiling is important if the effects of both natural and forced convection are similar. Najjari and Nasrallah [47] numerically studied boiling inside an inclined porous layer, where apart from the effects of permeability and inlet velocity, different inclinations of the porous channel have been also considered. Their results showed that a critical value of the inclination angle exists which corresponds to a maximum value of the evaporated volume fraction at low inlet velocity and high permeability. Later, Najjari and Nasrallah [48 – 51] presented several case studies on the conjugate incomplete phase change problems inside a channel, with a fluid layer lying above the porous medium. They investigated the effects of distance between the heat sources, their length and the thickness of the porous layer on the complex interaction between free convection heat transfer, latent heat storage and the liquid-vapor phase change process.

An additional problem that is encountered while simulating the complete liquid-vapor phase change process (i.e., from the sub-cooled liquid phase to the superheated vapor phase) inside porous media is the occurrence of rapid, non-physical change in the predicted temperature distribution over an extremely short distance that results primarily due to the presence of the effective diffusion coefficient. Although this problem was not clearly identified in the aforementioned studies, it was remedied by Li et al. [52] who employed the "modified" Kirchhoff method [53] for calculating the effective diffusion coefficient at the control volume (CV) faces to investigate the transient behavior of two-phase flow inside porous media. The performance of this method and the conventional harmonic mean approximation [54] were compared in [52] and the former was found better in handling the rapid change in the effective diffusion coefficient. In their study, the effect of heater location on the fluid flow and heat transfer has been investigated. The results also showed that the liquid and vapor flow fields, as well as the temperature distribution and liquid saturation location exhibit distinctly different features for different heater locations. The modified Kirchhoff method was then employed by Li et al. [55, 56] in order to investigate different two- and three-dimensional transient phase change problems inside porous channels, considering symmetric and asymmetric heating as well as aiding and opposing buoyancy conditions. In their studies, the temperature distribution, liquid saturation location and velocity fields have been presented for different Rayleigh and Peclet numbers. The results showed that the liquid flow bypasses the two-phase zone, while the vapor flows primarily to the interface between the sub-cooled liquid region and the two-phase region.

On the other hand, He et al. [57] presented a series of new conservation equations for mass, momentum, and energy in order to describe the performances of fluid flow, heat absorption, and phase change inside porous media based on the enthalpy formulation of SFM. In their model, three additional assumptions have been considered: firstly, considering the compressibility of vapor in the momentum and energy equations; secondly, adding a term of the momentum transfer caused by liquid phase change into the momentum equations of vapor and liquid phases in two-phase region, and finally, the local thermal equilibrium (LTE) assumptions and the variation of enthalpy with temperature and pressure in the two-phase region. The model and numerical strategies have been validated with experiments. Numerical results showed that the pressure solutions are quite identical to experimental data. In addition, the effects of coolant injection rate and external heat flux on the distributions of temperature, pressure, and velocity have been discussed by using the validated model.

As far as the energy conservation equation for porous media is concerned, two separate models, suitable for different applications, are available according to the homogenization approach: the Local Thermal Equilibrium (LTE) and the Local Thermal Non-Equilibrium (LTNE) models. Both these models can be applied for the complete phase change process inside porous media based on the TPMM of Wang. As the name suggests, under the assumption of LTE, the heat exchange between the working fluid and the solid matrix of the porous medium is neglected [44 – 52, 55 – 57]. On the other hand, in order to consider the internal heat transfer between the fluid and the solid phases, the LTNE model has to be applied, where two separate energy conservation equations for both phases are solved. These two equations are, however, coupled to each other through the volumetric (convective) heat exchange term that takes care of the local energy transfer from the solid phase to the fluid phase and vice-versa. For single-phase problems, Wang and Wang [58] performed an investigation in order to quantify the error caused by the LTE assumption, where, in principle, LTNE model should have been employed, although, they did not comment on the applicability of LTE model for two-phase problems. Nevertheless, the use of the LTNE model is quite common in many other applications of porous media, such as, combustion inside porous media [59 – 61], where the difference between the solid and the fluid temperatures could be substantially high, particularly close to the flame-front, which cannot be neglected in order to explain the mechanism of internal heat recirculation. According to Jiang and Ren [62], the classical LTNE model was first presented approximately 80 years ago. In recent years, however, serious attention has been paid to the LTNE model for such prediction since it is more realistic for the description of underlying physical phenomena associated with the local energy transfer and hence it helps in better understanding of the mechanisms responsible for the overall heat transfer during the phase change process inside porous media [63 – 70].

Taking the internal heat exchange between the solid and fluid phases into account, Peterson and Chang [63] employed the TPMM of Wang et al along with the assumptions of the LTNE model in order to numerically investigate the phase change process from sub-cooled liquid to the saturated mixture in a high conductivity porous channel used as a heat sink. Their results indicated that the high thermal conductivity and large solid-fluid contact area of the porous channel produce a high heat transfer performance associated with two-phase heat dissipation, which may serve as a viable alternative to the existing cooling techniques for microelectronics applications, characterized by high operating heat flux. Yuki et al. [64] modified the TPMM of Wang by applying Ergun's law and the LTNE model instead of a one-energy model in order to investigate the thermo-fluid flow characteristics under high flow velocity in porous media. Their study showed that the modified equations produced more realistic and reasonable results for the two-phase flow under high velocity and high heat flux. It has been also shown that heat sinks made of porous media with high thermal conductivity and large surface area can improve heat transfer performance greatly. Furthermore, numerical results showed that in a single phase flow, the degree of thermal non-equilibrium has a positive correlation with increasing flow velocity and heat flux input, whereas in the two-phase flow, the degree of thermal non-equilibrium is remarkable in the two-phase region.

More recently, Shi and Wang [65] presented a LTNE model based mainly on the TPMM of Wang in order to investigate the transpiration cooling problems with coolant phase change within porous media. In their work, the effect of mass flow rate, heat flux, thermal conductivity, porosity, sphere diameter of the porous matrix and pressure on the temperature and liquid saturation distributions have been investigated. Numerical results showed that the effect of the transpiration cooling would be limited under high pressure due to a smaller size of two-phase region. Further, this investigation also discovered an inverse phenomenon, namely in the two-phase region, where coolant temperature could be higher than the solid temperature. Later, Xin et al. [66] numerically simulated the processes of liquid coolant flow, heat absorption, and phase change within Micro-channels, which were heated at one side by given heat fluxes in order to investigate the ability to dissipate large amounts of heat flux using TPMM. In addition, the pressure and temperature distributions obtained at different conditions have been exhibited and analyzed. Numerical results indicated that the trends predicted by this approach agree well and the modeling has been validated in some sense. Furthermore, countercurrent flows in two-phase region near the transition point have been observed.

Nevertheless, in the literature mentioned above based on the LTNE model, the coupled momentum and the energy equations have been solved separately, and neither the effect of density and pressure variations caused by phase change on the enthalpy nor the influence of varied thermal physical properties on the momentum equation have been observed. This is because these models have been based on two assumptions: the saturation temperature is constant in two-phase region and the enthalpy is only a function of temperature. As currently discovered by Wei et al. [67], these two assumptions could lead to non-veracious phenomenon in numerical simulation (i.e., a thermal insulating layer appearing within the porous matrix, which is not real because the solid matrix is made of the metal with high thermal conductivity). In order to avoid the non-veracious phenomenon, Wei et al improved the mathematical formulation of the transpiration cooling problems with boiling which is based on the Gibbs free energy of the liquid and vapor phases being equal in the two-phase region. The LTNE model and the variation of enthalpy with temperature and pressure in the two-phase region based on the TPMM of Wang have been considered. The temperature variations of the fluid and solid phases, the liquid saturation, and the pressure of the fluid within porous media have been investigated. Numerical results showed that the temperature field of the fluid and solid phases, the liquid saturation, and the pressure of the fluid within porous media are consistent, and the non-veracious issue of the thermal insulating layer has been successfully resolved. In addition, numerical study was limited for incomplete phase change process, although the mathematical formulation could be used for the simulation of complete phase change process.

Lindner et al. [68] conducted a study on multiphase flow in a porous channel with local heat input from one side. In their study, the LTNE model has been used to investigate fluid flow and heat transfer with phase change inside porous media. The effect of gravity, Stanton number of evaporation, Rayleigh number, Peclet number, and Biot number on fluid flow and heat transfer under steady-state condition for both aiding and opposing flows have been investigated. Numerical results showed that for sufficiently high heat input, opposing flow yields large differences in position of the biphasic zone and minimal liquid saturation. Furthermore, the minimal saturation increases with increasing Stanton number, Peclet number or Biot number. The Rayleigh number has an opposite effect on the minimal saturation. Xin et al. [69] developed a Modified Separate Flow Model (MSFM) to numerically investigate the heat and mass transfer with phase change behaviors in porous media. In their model the effects of capillarity, liquid phase change, non-isothermal two-phase region and the LTNE assumption have been considered. Two typical numerical examples with a one-dimension model of porous media have been studied that the high heat fluxes are vertical and parallel to the fluid flow direction, respectively. Numerical results showed that the influence of heat flux direction on heat and fluid flow behaviors in porous media is large. Furthermore, the non-isothermal assumption in the two-phase region is obvious for the former while the LTNE assumption is remarkable in the two-phase region for the latter.

A comprehensive review dealing with various aspects of the field of evaporation within porous media, have been well documented in several articles [6, 15, 22, 25] and books by Nield and Bejan [70], Kaviany [71], Vafai [72], Ingham and Pop [73], and Vadasz [74] to name a few. Interested readers should refer to them for an excellent overview. However, most of these studies as well as those mentioned in the foregoing section have been focused on homogenous and heterogeneous isotropic porous media in the steady-state solution within the frame work of one- and two-dimensional descriptions. Only in some of the investigations, the transient simulation from a single (liquid) phase to two-phase mixture region has been discussed.

A careful review of the literature reveals that almost all previous studies dealt with incomplete phase change process (i.e., from the sub-cooled liquid to the two-phase mixture) using LTE and LTNE models. According to the best of the author’s knowledge, other than the investigations of Wang [33], Shi and Wang [65] and Lindner et al. [68], there is no study that dealt with the phase change process from a sub-cooled liquid state to the superheated vapor state inside a porous medium, where the phase change takes place without any appreciable change in pressure. Hence, the saturation temperature remains the same during the complete phase change process. This assumption applies when the pressure drop through the evaporator is negligible compared to the static pressure for a given saturation temperature, which is valid for low mass flow rate applications. While Wang and Lindner et al dealt with a two-dimensional problem with a localized heater using LTE and LTNE models, respectively, Shi and Wang obtained results with a one-dimensional formulation under the LTNE condition. Nevertheless, in their studies, although the formation of superheated vapor could be numerically predicted, they are also associated with a very high temperature change within an extremely short distance. For instance, Wang presented results for porous media, composed of steel and glass beads, and reported 100^oC to 500^oC temperature difference, respectively, between two successive isotherms in the superheated vapor region, located extremely close to each other. Wang identified this zone as the dry-out region, although its existence could not be experimentally substantiated since they have been carried out only for phase change from the sub-cooled liquid to the two-phase condition. In the LTNE model of Shi and Wang, owing to the presence of volumetric heat exchange term, uniformity of temperature could be better ensured. This means that even if the predicted fluid temperature became extremely high during iteration, immediate energy transfer to the solid phase would possibly lower the fluid temperature to realistic value. Nevertheless, they also observed a very high temperature change within a very short distance in the vapor phase. Furthermore, a careful examination of results, presented by Lindner et al also shows the occurrence of a temperature difference at the interface between solid and fluid phases at the wall with a magnitude from 15^oC to 300^oC and a maximum temperature up to 1600^oC. Such a maximum temperature is higher than the melting point of bronze, which is 913^oC. Such apparently unrealistic predictions may be attributed to discontinuities in the modeled effective diffusion coefficient and effective heat capacity ratio.

Wang did not recognize the rapid change in the predicted temperature over an extremely short distance as a non-physical “jump” and hence could not identify the specific reason. In the present work, it is pointed out that the non-physical jump in the predicted temperature distribution occurs due to the rapid change (discontinuity) in the effective diffusion coefficient close to the interface between the single- and two-phase regions. The discontinuity shall henceforth be referred to as the “jump” in the remainder of the thesis. It may be noted here that the term “jump”, used in the context of the present study, has no relation to the physical density “jump” condition used in Volume of Fluid (VOF)-like methods. Nevertheless, Li et al. [52] possibly first recognized the presence of discontinuities in the modeled effective diffusion coefficient and suggested special treatment for this term. Although they proposed two different numerical schemes to avoid the “jump” in the predicted properties across interfaces, only the phase change process from the sub-cooled liquid phase to the two-phase mixture was considered in their study. In the scope of the present work, it has been attempted to extend suggestions from Li et al for simulations of phase change process from the two-phase mixture to the superheated vapor phase, but generally remained unsuccessful. The occurrence of “jump” in the predicted temperature distributions could also be avoided by assuming the saturation enthalpies ($h_{l,sat}$, $h_{v,sat}$) and the latent heat (h_{fg}) to be functions of the saturation pressure [57, 67 , 69, 75], thereby allowing explicit heat diffusion to occur solely due to the temperature gradient even in the two-phase region (since the saturation temperature depends on the local pressure). Such a remedy, however, may not perform equally well for cases where the pressure gradient is negligible owing to the extremely low mass flow rate, as in the case of present application, where the saturation temperature remains the same during the complete phase change process.

It will be evident in chapter 2 that the effective diffusion coefficient is exactly equal to zero in the two-phase region for liquid saturations $s = 0$ (fully vapor) and $s = 1$ (completely liquid) since the phase change takes place without any appreciable change in saturation temperature, whereas it remains constant for purely liquid and vapor phases owing to the assumption of constant thermo-physical properties in the single phase regions. Thus, sharp discontinuities exist in the diffusion coefficient across interfaces between single and two-phase regions that are also more severe close to the vapor phase. Such a situation often leads to a non-physical "jump" in the predicted temperature. An additional problem might also occur due to the huge difference in densities of liquid and vapor phases [33] that leads to substantial increase in velocity during phase change in a constant cross-sectional area duct, e.g., water at its saturation temperature ($100^{o}\mathrm{C}$), the liquid density ($957.85\mathrm{kg/m^3}$) is nearly 1600 times that of the vapor ($0.5978\mathrm{kg/m^3}$). A dedicated effort is, therefore, required in order to suggest the remedy for such occurrences and hence the present study is devoted towards resolving this issue using different models which guarantees that no "jump" occurs in the predicted temperature distribution during numerical simulation of complete phase change process inside porous media.

1.4. Research Objectives

Concerning the literature review presented above, it can be noted that some of the specific features of phase change processes are not clarified and require further investigation, such as characteristics of the complete phase change processes inside porous media, e.g., due to the previously mentioned large discontinuity in modeled effective diffusion coefficient and effective heat capacity ratio. Therefore, the present work aims to develop useful tools using numerical methods in order to perform a numerical study of the complete liquid-vapor phase change process inside porous media. In the first phase of this study, a two-dimensional numerical code has been developed by adopting the existing TPMM of Wang on orthogonal coordinates. This development allows for the simulation of the phase change process within porous media in both channels and pipes of constant cross-sectional area in the axial direction, while considering the densities in the single phase regions to be constant. The numerical code has been verified by comparing the simulated results with the existing numerical results for other researcher under the same condition for partial phase change process. The proposed research work shall deal with modeling and simulation of the complete phase change processes inside porous media. Thereby, the next phase of the research work is to propose a new method (smoothing algorithm) for dealing with sharp discontinuities in the modeled effective diffusion coefficient for the simulation of complete phase change process inside porous media. In order to demonstrate the effectiveness of the suggested remedy, the complete phase change process of liquid water for a one-dimensional flow situation through a constant cross-sectional area duct, filled with a porous medium has been considered. However, it will also be evident in chapter 2 that the suggested remedies are easily extendable for multi-dimensional problems involving any phase-change fluid. The outcome of this research effort is the modification approach that enables one to avoid non-physical "jump" in the predicted temperature distribution across interfaces during numerical simulations.

In this respect, the proposed investigation is expected to considerably advance the present knowledge by allowing the simulation of the complete phase change process inside porous media. The results of this work shall lead to more realistic predictions required for the description of the underlying physical phenomena associated with the local energy transfer and hence a better understanding of the mechanisms responsible for the overall heat transfer during the phase change processes inside porous media. The proposed investigation has addressed various distinct issues, pertinent to the complete phase change processes inside porous media in order to examine further the proposed smoothing algorithm for the effective diffusion coefficient that are elaborated in the following:

1. The existing formulation has been applied in order to accommodate the effect of the smoothing algorithm under LTE assumption for the simulation of complete phase change processes in both channels and pipes of constant cross-sectional area in the axial direction.

2. An alternative formulation is proposed, where the enthalpy of the phase-change fluid is treated as the dependent variable in the energy conservation equation, in order to remove the complexity in the original formulation of Wang and Beckermann for efficient numerical simulation of complete phase change process inside porous media. In the subsequent text of the present thesis, the newly proposed modification shall be referred to as the “modified enthalpy formulation”. In order to demonstrate the consistency and the accuracy of the proposed formulation, one-dimensional complete liquid-vapor phase change problem of liquid water inside a constant cross-sectional area porous evaporator with known properties has been considered by employing two different heating conditions at the evaporator wall.

3. In practical situations, however, the thermal conductivity of the solid matrix of porous media is substantially higher than that of the working fluid. As a result, the heat that is added at the duct surface is transferred to the core of the evaporator mainly through the solid struts. Particularly in the phase change region, where the fluid remains constant at the saturation temperature owing to the thermodynamic constraints, heat conduction through the solid medium plays an important role in the energy transfer process from the heated wall. The temperatures of the solid phase and the fluid medium differ from each other, although the difference in temperatures may small but substantial owing to the extremely high heat exchange coefficient between them, resulting from the small characteristic pore diameter. Most importantly, for multi-dimensional problems, the complete phase change process cannot be realistically simulated using the conventional LTE model as explained in chapter 4, owing primarily to the extremely low values of effective diffusion coefficient in the two-phase region, particularly close to the saturated liquid or vapor condition that acts as an extremely high resistance to heat transfer. For constant heat flux boundary conditions, extremely high (non-physical) temperatures are predicted at the wall/near-wall nodes. For constant wall temperature application, complete phase change cannot be realized unless the prescribed wall temperature is unrealistically high. In addition, complete phase change process cannot be simulated using LTE model for transient problems owing to the high discontinuity in the effective heat capacity ratio. In such situations, the LTNE model appears to be the more (or at all) appropriate as compared to the commonly used LTE model. In order to eliminate the drawbacks in LTE model, the present one- and two-dimensional CFD codes have been

extended to include the effects of the LTNE model for one- and two-dimensional problems, respectively, (i.e., one-dimensional pipe flow as well as channel and pipe flow models). Therefore, the main objective of this study is to investigate the complete phase change process inside porous media using the LTNE model and TPMM of Wang by extending the smoothing algorithm for the effective diffusion coefficient.

4. Another interesting aspect of evaporation inside porous media lies in the expansion of the phase change fluid that occurs due to the huge difference in the densities of the liquid and the vapor phases. Since the vapor-phase occupies a larger volume, in order to maintain the continuity of mass flow, the velocity increases considerably in a constant cross-sectional area duct. In this situation, it may be worthwhile to use a duct with increasing cross-sectional area in the axial direction. Simulation of phase change within the porous media fitted into such a variable cross-sectional area duct would, however, require employment of curvilinear coordinates and an extension of the formulation developed so far to the body-fitted coordinate system. This implicitly indicates that the method should be extended first to the non-staggered variable arrangement. Therefore, the present CFD code has been firstly extended for non-staggered grid layout on orthogonal coordinates. The modified CFD code can be used in both LTE and LTNE models, while utilizing the smoothing algorithm for the effective diffusion coefficient in order to investigate the complete phase change process of water inside a porous channel based on TPMM of Wang.

5. For the selection of the porous media in the evaporator, a higher thermal conductivity in the radial direction is desirable as compared to that in the axial direction since this will help with conductive heat transfer from the periphery to the core of the duct. A structure made of axially compressed wire mesh can serve the purpose. Simulation of complete phase change problems within such porous media would, however, require the extension of the currently available formulation for anisotropic porous media along with the LTNE model. This applies specifically to permeabilities and thermal conductivities. In order to accommodate this aspect, the two-dimensional CFD code has been further extended to include the effects of anisotropy in the porous media properties and hence the present code is capable of handling anisotropic porous media along with the LTNE model.

6. During the complete phase change process, since the density of the working fluid decreases by several orders of magnitude, porous evaporator with increasing cross-sectional area in the flow direction may be employed in order to reduce the axial velocity and hence to increase the residence time of the working fluid inside the evaporator. In this regard, an extension of the numerical model is performed in order to include the effect of increasing cross-sectional area in the axial direction to accommodate higher volume flow rates of the vapor phase, when considering complete phase change process inside porous media. For simplicity, the complete phase change process of water for a one-dimensional flow situation through a divergent porous evaporator, based on the TPMM of Wang has been investigated.

1.5. Thesis Outline

In this thesis, the complete liquid-vapor phase change process inside porous media is numerically investigated. The present thesis is divided into eight chapters which are organized in the following manner. Chapter 1 of this thesis describes the applications and the background related to two-phase flow inside porous media. A briefing on previous work in this field and the aim of this study are also presented. Chapters 2 and 3 provide the mathematical formulation and numerical aspects of the current computational models. In chapter 2, the governing equations for the fluid flow describing the conservation of mass, momentum and energy, along with the expression for the mixture properties in two-phase flow and the boundary conditions inside porous media are described. The provided description details the derived formulations for all variants of TPMM [29, 30, 33] along with the LTE assumption. A newly proposed modification of the enthalpy formulation, based on the model of Wang and Beckermann, is presented in detail. Non-dimensionalization has been carried out for all the mathematical formulations. Special method (smoothing algorithm) has been developed in order to deal with the high discontinuity in the modeled effective diffusion coefficient, and is also presented in detail. Furthermore, chapter 2 describes the mathematical formulation along with the LTNE assumptions for both isotropic and anisotropic porous media. Chapter 3 gives a detailed description of the numerical discretization method presented herein using Finite Volume Method (FVM). The numerical method for solving the conservation of momentum is discussed separately using staggered and non-staggered grid layouts. In chapter 3, computational tests to verify the numerical code for relevant problems have been carried out by comparing the simulated results with the existing numerical results for other researcher under the same condition for an incomplete phase change process.

Chapters 4, 5, 6 and 7 concern the numerical results of the complete liquid-vapor phase change process inside porous media. The strategy of the proposed smoothing algorithm introduced in chapter 2 is applied in order to avoid the non-physical “jump” in the predicted temperature distribution during the numerical simulation of the complete phase change process inside porous media. Parametric study has been performed to investigate the effects of different parameters on the flow fields and temperature distribution of the complete phase change processes. Chapter 4 presents the one-dimensional results of the complete phase change process inside a constant cross-sectional area porous evaporator. Moreover, chapter 4 provides the comparison of numerical results of the complete phase change process for one-dimensional problems based on the modified enthalpy formulation with the TPMM of Wang. In addition, chapter 4 also provides the two-dimensional results of the incomplete and complete phase change process, under steady-state condition for both channel and circular pipe flow models, based on the TPMM of Wang along with the LTE model using staggered and non-staggered grid layouts. Chapter 5 provides the one and two-dimensional results of the complete phase change process, under steady-state and transient conditions, based on the TPMM of Wang along with the LTNE model by extending the proposed smoothing algorithm for the effective diffusion coefficient, for both circular pipe and channel flow models using both staggered and non-staggered grid layouts. Chapter 6 concerns the results of the complete phase change process inside a porous channel when considering anisotropy in the properties of porous media. Chapter 7 provides detailed results of the complete phase change process inside divergent porous evaporator. Finally, chapter 8 concludes the thesis, presenting a summary of the research work, the main conclusions extracted from it, and recommendations for future related investigations.

CHAPTER 2. MATHEMATICAL FORMULATION

Two phase flow in porous media typically consists of three phases: solid, liquid and vapor phases. In addition to the transport of individual phases, there is a phase change process involved inside the porous media. Treatment of individual phases using the well known point equations of continuum physics is rather complicated and computationally expensive. In order to realize numerical flow simulation employing the modified volumetric enthalpy formulation of Two-Phase Mixture Model (TPMM) [33] flow in porous media, the strategy is to identify, to understand and finally to derive the appropriate mathematical formulations, which describe the respective flow scenarios. Since these processes mostly originate from the separate flow model (SFM), this level also poses the natural starting point of general TPMM flow analysis.

Therefore, this chapter describes the general modeling procedure of TPMM applied in the present work. The major objective is to obtain a possible remedy in order to deal with the high discontinuity in both the effective diffusion coefficient and the effective heat capacity ratio that would allow to investigate the complete phase change process inside porous media. In this regard, the mathematical formulation in this chapter is divided into five parts: Local Thermal Equilibrium (LTE) model; non-dimensionalization; special treatment for diffusion coefficient; Local Thermal Non-Equilibrium (LTNE) model and anisotropic conditions in the properties of porous media along with the LTNE model. Except for the part four, each section provides the corresponding governing equations for fluid flow inside porous media, comprising conservation of mass, momentum, energy and mixture properties in the two-phase zone along with boundary conditions. In the beginning of the first part, the derivativion of the TPMM of Wang and co-worker along with LTE model is briefly described and the physical meaning of the mixture properties in the two-phase flow is explained. Also newly proposed modification of the enthalpy formulation, termed “modified enthalpy formulation” according to the TPMM of Wang and Beckermann, is presented in detail in the first part. In the second part appropriate non-dimensionalization is provided for all the governing equations. In the third part, a special method for dealing with sharp discontinuities in the effective diffusion coefficient, which occur at the interfaces separating the single phases and the two-phase zone, is presented for the TPMM of Wang and the modified enthalpy formulation, followed by a detailed discussion. The fourth part describes the governing equations based on the TPMM of Wang along with the LTNE model. Finally, the governing equations considering anisotropy in both the mechanical and thermal properties of porous media based on the TPMM of Wang along with the LTNE model are presented in detail.

2.1. Local Thermal Equilibrium Model

As already mentioned in chapter 1, the TPMM introduced by Wang and Beckermann; Wang et al and Wang are based on the assumption of the LTE. In the LTE model, it is assumed that the temperature difference between the solid and the fluid phases can be neglected. Additionally, Darcy's law is assumed valid for both the liquid and the gas phases, the radiative heat transfer inside the porous media is neglected, and surface tension of the liquid is assumed constant. The vapor is in local thermal equilibrium with the liquid and the thermodynamic Gibbs phase equilibrium relations are assumed valid in the two-phase region. Furthermore, the properties of the porous material, like thermal conductivity and permeability etc. are assumed isotropic, although in principle, the thermal conductivity and permeability can be different in axial and longitudinal directions.

2.1.1. Original Enthalpy Formulation of Two-Phase Mixture Model

Recognizing that the SFM is not well suited for the analysis of two-phase flow in porous media with and without phase change, Wang and Beckermann proposed a TPMM for two-phase flow through capillary porous media based on enthalpy formulation that is physically well founded and practically useful. In this model, the two phases have been regarded as constituents of a binary mixture. In this definition, phases are assumed to be distinct and separable components with nonzero interfacial areas, and their mixture represents a single material with a smoothly varying aphasic composition.

In the following, a consistent TPMM, based on the familiar Separate Flow Model (SFM), has been developed, including mass, momentum and energy conservation equations. Wang and Beckermann pointed out that the TPMM has several advantages over the conventional SFM. First, significantly fewer governing equations (i.e., only those for the two-phase mixture) are required to be solved. Second, the model is a single-domain formulation in which each of the conservation equations is valid in all regions throughout the problem domain. Hence, there is no need to prescribe complex internal boundary conditions at the phase interface and to track the moving interface explicitly. Wang and Beckermann also pointed out that the interfacial area between constituent elements (phases) is no longer negligibly small but rather of finite scale for a more detailed description of the model along with the assumptions. In addition to the above conceptual definition of the TPMM, several mean mixture properties and variables need to be defined before proceeding to construct the conservation equations. To start with, the mixture density is defined as:

$$\rho = \rho_l s + \rho_v (1-s) \tag{2.1}$$

This definition implies s is the liquid volume fraction (or liquid saturation), i.e., fraction of the void space occupied by the liquid phase as:

$$s = \frac{V_l}{V_{void}} \tag{2.2}$$

If ε is the porosity of the medium and if ΔV is the total volume of a control volume, then the volume available for the fluid medium (ΔV_{void}) is given by $\Delta V_{void} = \varepsilon \Delta V$. Thus, in a two-phase mixture, volume occupied by the liquid and vapor are given as $\Delta V_l = \varepsilon s \Delta V$ and $\Delta V_v = \varepsilon (1-s) \Delta V$, respectively. On the other hand, the mixture velocity is obtained from the total momentum of the mixture,

$$\rho \mathbf{u} = \rho_l \mathbf{u}_l + \rho_v \mathbf{u}_v \tag{2.3}$$

where $\mathbf{u}$ is the superficial (or Darcian) velocity vector. The mean kinematic viscosity is defined as [29]:

$$\nu = \frac{1}{k_{rl}/\nu_l + k_{rv}/\nu_v} \tag{2.4}$$

where k_{rl} and k_{rv} are the relative permeabilities for the liquid and the vapor phases as also used in the classical SFM. Since the inertial and diffusion effects are neglected, Wang and Beckermann used a phase relative permeability weighted pressure gradient to avoid the requirement of negligible slip velocity for a two phase flow. It was observed experimentally that the relative permeability of the liquid phase increases in a nonlinear fashion from 0 to 1 as the liquid saturation increases from 0 to 1. The relative permeability were obtained using the data of both drainage and imbibition steam-water capillary pressure. These quantities have been defined as power functions involving the liquid saturation, where the irreducible liquid saturation has been taken to be zero for simplicity as [29]:

$$k_{rl} = s^n \tag{2.5a}$$

$$k_{rv} = (1-s)^n \tag{2.5b}$$

It was reported that the power index for the relative permeabilities of the liquid and vapor phases may vary between 1 and 3. Wang and Beckermann pointed out that linear functions ($n=1$) of the relative permeabilities have been usually employed for geothermal system due to their simplicity and accuracy [20, 76, 77], while cubic forms ($n=3$) have been widely used in petroleum and nuclear safety engineering [1, 78, 79]. Both these values represent the empirical parameters. Due to the importance of this issue, both these values are chosen in this work to investigate the effect of the exponent n for the relative permeabilities on the complete phase change process. The liquid and vapor mobilities are defined, respectively, as follows:

$$\lambda_l \equiv \lambda = \frac{\nu k_{rl}}{\nu_l} = \frac{k_{rl}/\nu_l}{k_{rl}/\nu_l + k_{rv}/\nu_v} \tag{2.6a}$$

$$\lambda_v = 1 - \lambda = \frac{\nu k_{rv}}{\nu_v} = \frac{k_{rv}/\nu_v}{k_{rl}/\nu_l + k_{rv}/\nu_v} \tag{2.6b}$$

Consequently,

$$\lambda_l + \lambda_v = 1 \Rightarrow \lambda_v = 1 - \lambda_l = 1 - \lambda \tag{2.7}$$

Note that the liquid mobility λ_l, also termed as λ in the following, is a dimensionless quantity. Further note that if $s=1$ fully liquid media for the liquid phase and hence $k_{rl}=1$, $k_{rv}=0$, $\nu=\nu_l$. Also, when $s=0$, which implies $k_{rl}=0$, $k_{rv}=1$, $\nu=\nu_v$. The specification of the mixture pressure is more involved because of the difference between liquid and gas pressures due to capillary forces [29]. Here, this difficulty is circumvented by using a modified Chavent's pressure variable [19, 29], where the pseudo mixture pressure (whose definition remains valid also for the single phase regions) has been defined as [19]:

$$p = \frac{p_l + p_v}{2} + \frac{1}{2}\int_0^{p_c} \left(\lambda_v - \lambda_l\right) dp \tag{2.8}$$

where, p_c is the capillary pressure, defined as:

$$p_c = p_v - p_l \tag{2.9}$$

When the capillary force is negligibly small, $p_c = 0$ and hence $p = p_l = p_v$. In the limiting case of $s = 0$ (purely vapor phase), where the liquid and vapor mobilities are $\lambda = 0$ and $\lambda_v = 1$, respectively, the pseudo mixture pressure in the first limit is defined as:

$$p = \frac{1}{2}(p_l + p_v) + \frac{1}{2}\int_0^{p_c} dp = \frac{1}{2}(p_l + p_v) + \frac{1}{2}(p_v - p_l) = p_v \tag{2.10a}$$

Similarly, the pressure of the liquid phase is retrieved for the limiting case of $s = 1$ (purely liquid phase), where $\lambda = 1$ and $\lambda_v = 0$:

$$p = \frac{1}{2}(p_l + p_v) + \frac{1}{2}\int_0^{p_c} -dp = \frac{1}{2}(p_l + p_v) - \frac{1}{2}(p_v - p_l) = p_l \tag{2.10b}$$

This implies that the definition of the single phase pressure is retrieved in both the limit [see Eqs. (2.29) – (2.32) for more details on the mixture pressure]. Having defined the basic mean properties of a two-phase mixture, the conservation equations can now be formulated starting from the governing equations for each individual phase, which are available from the SFM. In the following, the SFM is first summarized.

A. *Separate Flow Model (SFM)*

As discussed by Bear [17] or Scheidegger [18], the conventional form of the equations governing two-phase, immiscible, incompressible flow through a porous medium are:

Conservation of Mass

In order to derive the mass conservation equation, let us assume that the density, velocity and the volume fraction are given by ρ_i, $\mathbf{u}_i$ and s_i, respectively. For a fictitious *CV*, the Reynolds transport theorem can be written as:

$$\iiint_{CV} \frac{\partial}{\partial t}(\rho_i\, s_i\, \varphi\, \varepsilon)\cdot dv + \oiint_{CS} \mathbf{n}\cdot(\rho_i\, \varphi \mathbf{u})\cdot dA = \iiint_{CV} \dot{m}_i\, dv \tag{2.11}$$

where i represents the component ($i = l$ or v, for liquid or vapor); $\rho = \rho_i$; $\varphi = 1; \mathbf{u} = \mathbf{u_i}$ and $\dot{m}_i$ is the volumetric mass source or sink $(\mathrm{kg/m^3 s})$. By integration of Eq. (2.11), the mass balance for the liquid and vapor phases are given, respectively, as:

$$\frac{\partial}{\partial t}(\rho_l\, s_l\, \varepsilon) + \nabla\cdot(\rho_l \mathbf{u}_l) = \dot{m}_l \tag{2.12a}$$

$$\frac{\partial}{\partial t}\left(\rho_v\, s_v\, \varepsilon\right)+\nabla\cdot\left(\rho_v \mathbf{u}_v\right)=\dot{m}_v \tag{2.12b}$$

where $s_v = 1-s$ is the volume fraction of vapor phase and $\dot{m}_v$ is the rate of conversion of vapor mass from the liquid phase. Assuming that the porosity ε is not a function of time and the density ρ_i is constant, the mass conservation can be written according to Eq. (2.12) for the liquid phase as:

$$\rho_l\left[\varepsilon\frac{\partial s}{\partial t}+\nabla\cdot\left(\mathbf{u}_l\right)\right]=\dot{m}_l=-\dot{m}_v \tag{2.13}$$

and for the vapor phase as:

$$\rho_v\left[\varepsilon\frac{\partial(1-s)}{\partial t}+\nabla\cdot\mathbf{u}_v\right]=\dot{m}_v=-\dot{m}_l \tag{2.14}$$

Since $\dot{m}_l$ and $\dot{m}_v$ are the inter conversion terms from one phase to the other, they must balance each other in absence of any mass source or sink from external sources:

$$\dot{m}_l+\dot{m}_v=0 \tag{2.15}$$

Conservation of Momentum

The full conservation of momentum for the liquid phase can be written as:

$$\underbrace{\frac{\partial}{\partial t}\left(\rho_l\, s\mathbf{u}_l\right)}_{\textit{transient term}}+\underbrace{\frac{1}{\varepsilon}\nabla\cdot\left(\rho_l \mathbf{u}_l\, \mathbf{u}_l\right)}_{\textit{convection}}=\underbrace{-\nabla p_l}_{\textit{pressure gradient}}+\underbrace{\nabla p_{l,p}}_{\substack{\textit{additional pressure}\\ \textit{loss due to porous}\\ \textit{media}}}\underbrace{+\nabla\cdot\left(\frac{\mu_l}{\varepsilon}\nabla\mathbf{u}_l\right)}_{\textit{diffusion}}+\underbrace{\rho_l\,\mathbf{g}}_{\textit{body force}} \tag{2.16}$$

For low velocity, the term $\nabla p_{l,p}$ is given as:

$$\nabla p_{l,p}=-\frac{\mu_l}{Kk_{rl}}\mathbf{u}_l \tag{2.17}$$

where K is the absolute permeability of the porous medium. In case of extremely low velocities as assumed throughout this work, the transient, the convection and the diffusion terms are assumed to become negligibly small. After dropping those terms, the liquid velocity vector is obtained as [29]:

$$\mathbf{u}_l=-\frac{K\, k_{rl}}{\mu_l}\left(\nabla p_l-\rho_l\mathbf{g}\right) \tag{2.18}$$

Equation (2.18) represents the Darcy flow model, which relates flow velocity and phase pressure. In a similar manner, the momentum conservation equation can be written for the vapor phase as [29]:

$$\mathbf{u}_v = -\frac{Kk_{rv}}{\mu_v}(\nabla p_v - \rho_v \mathbf{g}) \qquad (2.19)$$

The capillary pressure, as given in Eq. (2.9), can be represented by Levertt's J function [80] as:

$$p_c = \left(\frac{\varepsilon}{K}\right)^{1/2} \sigma J \qquad (2.20)$$

where σ is the vapor-liquid interfacial surface tension. The capillary pressure function J is generally multi-valued. In gas-liquid systems, the experimentally obtained *J*-values typically lie between two limiting curves, known as the drainage and absorption curves [29]. In the present work, the following correlation of Levertt [29, 81] has been used as:

$$J = 1.417(1-s) - 2.120(1-s)^2 + 1.263(1-s)^3 \qquad (2.21)$$

In the limiting case of $s=1$, it follows $J=0$ and $p_c=0$, while for $s=0$, p_c is non-zero. The equations (2.13) – (2.21) constitute a full system of governing equations for the unknown velocity vectors $\mathbf{u}_l$ and $\mathbf{u}_v$, the scalar pressures p_l and p_v, and the liquid saturation s.

B. *Overall Mass Conservation*

Since the mixture density is strongly variable, the multiphase mixture flow should be categorized as compressible. By adding the phase conservation of mass from Eqs. (2.13) and (2.14), the overall mass conservation equation for the TPMM is obtained as:

$$\varepsilon \frac{\partial}{\partial t}(\rho_l s) + \nabla \cdot (\rho_l \mathbf{u}_l) + \varepsilon \frac{\partial}{\partial t}[\rho_v (1-s)] + \nabla \cdot (\rho_v \mathbf{u}_v) = \dot{m}_l + \dot{m}_v \qquad (2.22)$$

Using the definitions of mixture density ρ in Eq. (2.1) and momentum $\rho\mathbf{u}$ in Eq. (2.3) and noting that $\dot{m}_l + \dot{m}_v = 0$, the overall mass conservation equation can be written as:

$$\varepsilon \frac{\partial \rho}{\partial t} + \nabla \cdot (\rho \mathbf{u}) = 0 \qquad (2.23)$$

It may be noted here that Eq. (2.23) can be used only with the overall momentum conservation equation, and it is clear that the continuity equation is just a duplicate of the corresponding equation for single-phase mixture flow.

C. *Overall Momentum Conservation*

In order to obtain the conservation equation of momentum for the two-phase mixture, firstly, Eq. (2.18) is multiplied by ρ_l. Using the definition of the relative permeability from Eq. (2.6a), the final form of the momentum conservation equation for the liquid phase is obtained as [29]:

$$\rho_l \mathbf{u}_l = -\frac{K\lambda_l}{\nu}\left(\nabla p_l - \rho_l \mathbf{g}\right) \qquad (2.24)$$

Similarly, Eq. (2.19) is multiplied by ρ_v and using Eq. (2.6b), the momentum conservation equation for the vapor phase is obtained as [29]:

$$\rho_v \mathbf{u}_v = -\frac{K\lambda_v}{\nu}\left(\nabla p_v - \rho_v \mathbf{g}\right) \qquad (2.25)$$

By adding Eqs. (2.24) and (2.25) and using the definition of mass velocities in Eq. (2.3), the overall conservation of momentum is obtained after a few algebraic manipulations as:

$$\rho \mathbf{u} = -\frac{K}{\nu}\left[\nabla p - \rho_k \, \mathbf{g}\right] \qquad (2.26)$$

where ρ_k is the kinetic density of the mixture, which is generally different from the conventional static pressure density, ρ, as defined by Eq. (2.1) and depends on the relative permeability of the phases as follows [29]:

$$\rho_k = \lambda_l \rho_l + \lambda_v \, \rho_v = \lambda \rho_l + (1-\lambda)\rho_v \qquad (2.27)$$

From the definition of the mixture density ρ and kinematic viscosity ν, the mixture viscosity is easily defined as:

$$\mu = \rho \nu \qquad (2.28)$$

If the mobility is independent of the pressure and if can be neglected the effect of pressure, the definition of pseudo mixture pressure in Eq. (2.8) can be integrated as [29]:

$$p = \frac{1}{2}\left(p_l + p_v\right) + \frac{1}{2}\left(\lambda_v - \lambda_l\right)\left(p_v - p_l\right) \qquad (2.29)$$

After some simple algebraic manipulations, the pseudo mixture pressure in Eq. (2.29) is obtained as:

$$p = \lambda \, p_l + (1-\lambda)p_v \qquad (2.30)$$

From the definition of the mixture pressure in Eq. (2.30), the gradient of pseudo mixture pressure in Eq. (2.26) is obtained as:

$$\nabla p = \lambda_l \nabla p_l + \lambda_v \, \nabla p_v = \lambda \, \nabla p_l + (1-\lambda)\nabla p_v \qquad (2.31)$$

In order to solve for the liquid velocity $\mathbf{u}_l$ using Eq. (2.18) for the regions occupied only by the vapor phase, the momentum equation must yield zero velocity for the liquid (as there is no liquid present). In this respect, the liquid pressure can be obtained from Eq. (2.30) as:

$$p_l = \frac{p-(1-\lambda)p_v}{\lambda} \qquad (2.32)$$

For the complete vapor phase, however, $\lambda = 0$, and hence Eq. (2.32) fails to express p_l in terms of pseudo mixture pressure and hence $p_v = p$. Consider now Eq. (2.18) and since $k_{rl} = s^n$, the relative permeability for the liquid phase k_{rl} equals zero for $s = 0$. Thus, Eq. (2.3) straight away delivers $\mathbf{u}_l = 0$ for the pure vapor region.

D. Conservation of Liquid Mass and Phase Velocities

One vectorial and one scalar governing equation have been already developed for the unknowns, $\mathbf{u}$ and p. The physical properties of the two-phase mixture, as defined in Eqs. (2.1), (2.4), (2.31) and (2.32), are strongly dependent on the liquid saturation, *s*. Therefore, in order to complete the mathematical model, one also requires a governing equation for the liquid saturation, which is given by the statement for the conservation of liquid mass and phase velocities. This equation can be mathematically derived by taking the difference between the two mass conservation equations (2.13) and (2.14), and is obtained as:

$$\varepsilon\left[\frac{\partial}{\partial t}\{(\rho_l+\rho_v)s\}-\frac{\partial \rho_v}{\partial t}\right]-\nabla\cdot\left[\frac{K}{\nu}\left(\lambda\ \nabla p_l-\lambda_v \nabla p_v\right)\right]-\nabla\cdot\left[\frac{K}{\nu}\left(\lambda\ \rho_l-\lambda_v\rho_v\right)\mathbf{g}\right]=\dot{m}_l-\dot{m}_v \qquad (2.33)$$

In order to simplify Eq. (2.33), consider now the term $\lambda\ \nabla p_l - \lambda_v \nabla p_v$. From the definition of capillary pressure in Eq. (2.9), the gradient of pressure for both vapor and liquid phases are given, respectively, as follows:

$$\nabla p_v = \nabla p_l + \nabla p_c \qquad (2.34a)$$

$$\nabla p_l = \nabla p_v - \nabla p_c \qquad (2.34b)$$

Substituting ∇p_v from Eq. (2.34a) into Eq. (2.31), the following relationship is obtained as:

$$\nabla p_l = \nabla p - (1-\lambda)\nabla p_c \qquad (2.35)$$

∇p_v could be obtained by using Eqs. (2.35) and (2.34a) as follows:

$$\nabla p_v = \nabla p - (1-\lambda)\nabla p_c + \nabla p_c = \nabla p + \lambda \nabla p_c \qquad (2.36)$$

Thus, $\lambda\ \nabla p_l - \lambda_v \nabla p_v$ may be written after a few manipulations as:

$$\lambda\ \nabla p_l - \lambda_v \nabla p_v = -2\lambda(1-\lambda)p_c' \nabla s + (2\lambda - 1)\nabla p \qquad (2.37)$$

where p_c' is the derivative of p_c with respect to the liquid saturation s. Capillary pressure is only a function of liquid saturation [see Eq. (2.20)]. If the density in the single phase regions are assumed to be constant and by using mass balance for the vapor phase, as given in Eq. (2.12b) for the transient term $\left(\varepsilon\rho_v\, \partial s/\partial t\right)$, Eq. (2.33) can be written employing Eq. (2.37) after a few manipulations as:

$$\varepsilon\rho_l \frac{\partial s}{\partial t} + \nabla\cdot\left[\frac{K}{\nu}\lambda(1-\lambda)p_c'\ \nabla s\right] + \nabla\cdot\left[\frac{K}{\nu}\rho_l\lambda\,\mathbf{g}\right] - \nabla\cdot\left[\frac{K}{\nu}\lambda\nabla p\right] = \dot{m}_l \tag{2.38}$$

In Eq. (2.38), ($\lambda\nabla p$) may be substituted using the overall momentum conservation equation (2.26), while using the definition of kinetic density in Eq. (2.27). Thus, the final form of the conservation of liquid mass can be reformulated as:

$$\varepsilon\rho_l \frac{\partial s}{\partial t} + \nabla\cdot(\lambda\rho\,\mathbf{u}) = -\nabla\cdot\mathbf{j} + \dot{m}_l \tag{2.39}$$

where $\mathbf{j}$ represents the total mass flux (velocity) from one phase to the other during a phase change process inside the porous medium and may be expressed as [29]:

$$\mathbf{j} = -D\nabla s + k_{rv}\lambda\frac{K(\rho_l-\rho_v)\mathbf{g}}{\nu_v} = -D\nabla s + f\,\frac{K\,\Delta\rho}{\nu_v}\,\mathbf{g} \tag{2.40}$$

It is evident that $\mathbf{j}$ is a combination of the capillary-induced diffusive flux and the gravity-induced migrating flux. In Eq. (2.40), $\Delta\rho = (\rho_l - \rho_v)$ is the difference in densities of the liquid and the vapor phases, whereas D and f are the capillary diffusion coefficient and the hindrance coefficient, respectively, that are defined as [29]:

$$D = \frac{(\varepsilon K)^{1/2}\sigma}{\nu}\lambda(1-\lambda)\left[-\frac{dJ}{ds}\right] \tag{2.41a}$$

$$f = k_{rv}\lambda \tag{2.41b}$$

Since for the completely liquid phase $\lambda_v = 0$ and $k_{rv} = 0$, whereas for the fully vapor phase $\lambda = 0$, one readily obtains $D = 0$ and $f = 0$ for the single phase regions. The physical meaning of the coefficient f is similar to the well known hindrance coefficient in sedimentation theories, and the reader is referred to Davis and Acrivos [82]. Equation (2.39) represents the final form for the conservation of liquid mass. It may be noted here that $(\rho\mathbf{u})$ or $\mathbf{u}$ and ∇p or (p) could be solved from either Eq. (2.23) or Eq. (2.26). Under the assumption of LTNE, however, the individual mass-velocities of the liquid and the vapor phases, $\rho_l u_l$ and $\rho_v u_v$, respectively, are required, which can be obtained by employing Eq. (2.40). The mass flow rate for the liquid phase $\rho_l u_l$ may be simplified after a few manipulations using Eq. (2.24), Eq. (2.35), and the expression of $(\rho_l - \rho_k)$ from Eq. (2.27) as follows:

$$\rho_l\mathbf{u}_l = \lambda\rho\,\mathbf{u} + \mathbf{j} \tag{2.42}$$

Using the definition of mixture velocity from Eqs. (2.3) and (2.42), the mass flow rate for the vapor phase is obtained as:

$$\rho_v \mathbf{u}_v = \rho \mathbf{u} - \rho_l \mathbf{u}_l = \rho \mathbf{u} - \lambda \rho \mathbf{u} - \mathbf{j} = (1-\lambda)\rho \mathbf{u} - \mathbf{j} \tag{2.43}$$

Here, the terms $\lambda \rho u$ and $(1-\lambda)\rho u$, represent the virtual mass flow rate of the same component in the bulk stream of the whole mixture. In addition, it should be mentioned that Eqs. (2.39), (2.42) and (2.43) are only applicable with Darcy's law, and hence cannot be used for a general problem.

E. Conservation of Energy

In chapter 1, it was mentioned that two separate models are available for the conservation of energy when using the homogenization approach. In the first approach, the temperature difference between the solid and the fluid phases is neglected (i.e., LTE model), whereas in the second approach, these temperatures could be assumed to be different (i.e., LTNE model). For the latter, separate energy equations have to be solved, which are coupled with each other through the convective heat exchange. Following the SFM, the energy conservation equation for TPMM under the assumption of LTE may be written as [22, 29]:

$$\frac{\partial}{\partial t}\left[(1-\varepsilon)\rho_s h_s + \varepsilon \rho_l s h_l + \varepsilon \rho_v (1-s) h_v\right] + \nabla \cdot \left[\rho_l \mathbf{u}_l h_l + \rho_v \mathbf{u}_v h_v\right] = \nabla \cdot \left[k_{eff} \nabla T\right] + \dot{q}''' \tag{2.44}$$

where the symbols with subscript ‘s’ refer to the properties of the solid medium of the porous matrix, k_{eff} is the effective thermal conductivity of the combined medium and $\dot{q}'''$ is the volumetric heat generation (source term), which is absent for most cases. The effective thermal conductivity, k_{eff}, has been defined according to the parallel arrangement as follows [29, 83 – 87]:

$$k_{eff} = k_s(1-\varepsilon) + k_f \varepsilon = k_s(1-\varepsilon) + \varepsilon\left[k_l s + k_v(1-s)\right] \tag{2.45}$$

where for a simplistic model of a composite system consisting of solid struts and a flowing mixture, k_f is also a function of the liquid saturation. The solid, liquid, and vapor enthalpies are related to the temperatures as follows [29]:

$$h_s = h_{s,ref} + C_{ps}\left(T - T_{ref}\right) \tag{2.46a}$$

$$h_l = h_{l,sat} + C_{pl}\left(T - T_{sat}\right) \tag{2.46b}$$

$$h_v = h_{l,sat} + h_{fg} + C_{pv}\left(T - T_{sat}\right) = h_{v,sat} + C_{pv}\left[T - T_{sat}\right] \tag{2.46c}$$

where C_{ps}, C_{pl}, and C_{pv} are the specific heat for the solid, liquid, and vapor phases, respectively, whereas h_{fg} is the latent heat of vaporization and is defined as:

$$h_{fg} = (h_v - h_l)\big|_{T=Tsat} \tag{2.47}$$

The second term on the Left Hand Side (LHS) of Eq. (2.44) (i.e., advection term) can be further decomposed into contributions due to the bulk mixture motion and the intrinsic relative phase motion [29]. Using Eq. (2.42), the advection term on the LHS of Eq. (2.44) can be written as:

$$\rho_l \mathbf{u}_l h_l + \rho_v \mathbf{u}_v h_v = \rho \mathbf{u} h_k - \mathbf{j}\left(h_v - h_l\right) \tag{2.48}$$

where h_k is the kinetic enthalpy and is defined as:

$$h_k = \lambda h_l + \left(1-\lambda\right) h_v \tag{2.49}$$

On the other hand, the volumetric enthalpy of the mixture ρh is defined as:

$$\rho h = h_l \rho_l s + \left(1-s\right)\rho_v h_v \tag{2.50}$$

The specific heat is defined as $C = \partial h / \partial T$. Therefore, the kinetic specific heat and the volumetric heat capacity of the mixture are defined, respectively, as:

$$C_k = C_{pl}\lambda + \left(1-\lambda\right) C_{pv} \tag{2.51a}$$

$$\rho C = C_{pl} s \rho_l + \left(1-s\right) C_{pv} \rho_v \tag{2.51b}$$

Substituting Eqs. (2.48) – (2.50) into Eq. (2.44), the energy conservation equation (2.44) is obtained as:

$$\frac{\partial}{\partial t}\left[(1-\varepsilon)\rho_s h_s + \varepsilon \rho h\right] + \nabla\cdot\left[\rho \mathbf{u} h_k\right] = \nabla\cdot\left[k_{eff}\nabla T\right] + \nabla\cdot\left[(h_v - h_l)\mathbf{j}\right] + \dot{q}''' \tag{2.52}$$

The advection term in the energy equation (2.52) is allowable only when Darcy's law is used in the momentum equation since the definition of $\mathbf{j}$ depends on that assumption as well as the mobility. The mass flux $\mathbf{j}$ could be expressed either from Eq. (2.42) or Eq. (2.43) as:

$$\mathbf{j} = -\rho_l \mathbf{u}_l - \lambda\, \rho \mathbf{u} \tag{2.53a}$$

$$\mathbf{j} = -\rho_v \mathbf{u}_v + \lambda_v \rho \mathbf{u} \tag{2.53b}$$

In addition, Eq. (2.48) may also be rewritten after a few algebraic manipulations as:

$$\sum_\alpha \rho_\alpha u_\alpha h_\alpha = \rho \mathbf{u} h_k + \sum_\alpha (h_\alpha - h_k)\left[\rho_\alpha \mathbf{u}_\alpha - \lambda_\alpha \rho \mathbf{u}\right] \qquad \alpha = l, v \tag{2.54}$$

It can be noted here that $\rho_l \mathbf{u}_l$ and $\rho_v \mathbf{u}_v$ could also be separately obtained by solving the respective aphasic momentum equations. This simplification is not required here. The energy conservation equation (2.52) contains both kinetic enthalpy and mixture enthalpy. In order to proceed further, it would be useful to express them in terms of the mixture enthalpy, *h*. Although the form of Eq. (2.52) is quite similar to that finally adopted by Wang and Beckermann, it contains two distinct transient terms, where the first and the second terms on the LHS signify the rate of change of stored energy within the solid medium and in the fluid volume, respectively. These two terms may be combined together and could be expressed as:

$$\begin{aligned}\frac{\partial}{\partial t}\left[(1-\varepsilon)\rho_s h_s + \varepsilon\rho h\right] &= \left[\varepsilon + \frac{\rho_s C_{ps}(1-\varepsilon)}{\rho}\frac{\partial T}{\partial h}\right]\frac{\partial}{\partial t}(\rho h) - \frac{\rho_s C_{ps}(1-\varepsilon)h}{\rho}\frac{\partial T}{\partial h}\frac{\partial \rho}{\partial t} \\ &= \Omega_h \frac{\partial(\rho h)}{\partial t} - (\Omega_h - \varepsilon)\left(h\frac{\partial \rho}{\partial t}\right)\end{aligned} \tag{2.55}$$

where Ω_h is the effective heat capacity ratio and is defined as:

$$\Omega_h = \varepsilon + \frac{\rho_s C_{ps}(1-\varepsilon)}{\rho}\frac{dT}{dh} \tag{2.56}$$

At this point, Wang and Beckermann dropped the second term on the Right Hand Side (RHS) of Eq. (2.55) and used after simplification the corresponding version of Eq. (2.67) as the energy conservation equation. This term, however, should have been retained in the equation since the second term on the RHS of Eq. (2.56) is non-zero (and also positive, indicating $\Omega_h > \varepsilon$) in the single phase regions and hence if the densities in these regions are assumed to be functions of the local temperature, the second term in Eq. (2.55) would definitely be finite during a transient simulation and thereby cannot be neglected. In the two-phase region, however, this term is exactly zero since the phase change process takes place without any appreciable change in pressure, which results in $dT/dh = 0$ and hence from Eq. (2.56), one obtains $\Omega_h = \varepsilon$. To this extent, the simplification, adopted by Wang and Beckermann, is justifiable only if the densities in the single phase regions are assumed to be independent of the local temperature. Therefore, owing to the generality, the energy conservation equation (2.52) should be preferred, although it would not matter for steady-state problems considered in chapter 4, as demonstrative examples. In order to simplify the second term on the LHS of Eq. (2.52), the following relationship can be recognized as:

$$\nabla\cdot(\rho\mathbf{u}h_k) = \nabla\cdot\left(\rho\mathbf{u}h\frac{h_k}{h}\right) = \nabla\cdot(\gamma_h\,\rho\mathbf{u}h) \tag{2.57}$$

where γ_h represents the advection correction coefficient. Since it could be easily verified that in the single phase regions $\gamma_h = 1$, signifying that no correction is required when the domain is completely occupied by one of the phases, h_k may be expressed only for the two-phase mixture as $h_k = h_{v,sat} - \lambda h_{fg}$. Therefore using the definition mixture density ρ and volumetric mixture enthalpy ρh, γ_h may be expressed as:

$$\gamma_h = \frac{\rho h_k}{\rho h} = \frac{\rho\left[h_{l,sat}\lambda + h_{v,sat}(1-\lambda)\right]}{\rho_l s h_{l,sat} + (1-s)\rho_v h_{v,sat}} = \frac{\left[\rho_l s + (1-s)\rho_v\right]\left(h_{v,sat} - \lambda h_{fg}\right)}{\rho_l s h_{l,sat} + (1-s)\rho_v h_{v,sat}} \tag{2.58}$$

It is now straightforward to verify that $\gamma_h = 1$ is obtained from Eq. (2.58) by setting either $s = 1$ (i.e., completely liquid phase) or $s = 0$ (i.e., purely vapor phase), although the expression for γ_h is obtained by considering the variations only in the two-phase region. Furthermore, if the liquid saturation is known (which can be obtained iteratively from the solution of enthalpy, as shall be clarified later), Eq. (2.58) provides an explicit expression for γ_h for the entire domain. On the other hand, the first term on the RHS of Eq. (2.52) can be simplified as:

$$\nabla \cdot \left(k_{eff} \nabla T\right) = \nabla \cdot \left(k_{eff} \frac{dT}{dh} \nabla h\right) \tag{2.59}$$

Nevertheless, employing Eq. (2.40), the energy conservation equation (2.52) may be written as:

$$\begin{aligned}(1-\varepsilon)\rho_s C_{ps} \frac{\partial T}{\partial t} + \varepsilon \frac{\partial}{\partial t}(\rho h) + \nabla \cdot \left[\gamma_h \rho \mathbf{u} h\right] = \nabla \cdot \left[k_{eff} \frac{\partial T}{\partial h} \nabla T\right] - \nabla \cdot \left[D h_{fg} \nabla s\right] \\ + \nabla \cdot \left[f \frac{K \Delta\rho\, h_{fg}}{\nu_v} \mathbf{g}\right] + \dot{q}'''\end{aligned} \tag{2.60}$$

In order to further simplify Eq. (2.60), however, one requires an expression for the liquid saturation s as a function of local enthalpy, h, such that ∇s could be expressed in terms of ∇h and hence the energy conservation equation could be expressed in a form that contains h as the primary dependent variable. By noting that from the definition of the mixture density ρ, the density at the saturated vapor condition ρ_v could be expressed in terms of the liquid saturation s as:

$$\rho_v = \frac{\rho - \rho_l s}{(1-s)} \tag{2.61}$$

and using the relationship for volumetric enthalpy of mixture ρh while replacing h_l and h_v by their respective saturation values, Wang and Beckermann obtained a relationship for s as a function of the mixture density and mixture enthalpy as follows:

$$s = \frac{\rho\left(h_{v,sat} - h\right)}{\rho_l h_{fg}} \tag{2.62}$$

Nevertheless, from Eq. (2.62), ∇s may be expressed as:

$$\nabla s = -\left[\frac{\rho}{\rho_l h_{fg}} \nabla h + \frac{\left(h - h_{v,sat}\right)}{\rho_l h_{fg}} \nabla \rho\right] \tag{2.63}$$

Substituting ∇s in Eq. (2.60) and using it further, the final form of the energy conservation equation (2.60), as adopted by Wang and Beckermann [29], may be obtained as follows:

$$(1-\varepsilon)\rho_s C_{ps}\frac{\partial T}{\partial t}+\varepsilon\frac{\partial}{\partial t}(\rho h)+\nabla\cdot[\gamma_h\rho\mathbf{u}h]=\nabla\cdot[\Gamma_h\nabla h]+\nabla\cdot\left[\frac{\rho D}{\rho_l}(h-h_{v,sat})\frac{1}{\rho}\nabla\rho\right]+\nabla\cdot\left[f\,\frac{K\,\Delta\rho\,h_{fg}\,\mathbf{g}}{\nu_v}\right]+\dot{q}''' \tag{2.64}$$

where Γ_h is the effective diffusion coefficient for enthalpy and is defined as [29]:

$$\Gamma_h=\frac{\rho D}{\rho_l}+k_{eff}\,\frac{dT}{dh} \tag{2.65}$$

It is obvious that although Γ_h is represented by two terms, they are never simultaneously active for a given domain. While the first term is absent for the single phase regions as $D=0$, the second term does not play any role in the two-phase region since according to the present assumption, the phase change takes place at a constant temperature T_{sat} and hence $dT/dh=0$. Furthermore, Wang and Beckermann also represented the second term on the RHS of Eq. (2.64) as:

$$\nabla\cdot\left[\frac{\rho D}{\rho_l}(h-h_{v,sat})\frac{1}{\rho}\nabla\rho\right]=\nabla\cdot\left[\Gamma_h(h-h_{v,sat})\nabla(\ln\rho)\right] \tag{2.66}$$

This term, in its correct form as presented in Eq. (2.64), is non-zero only for the two-phase mixture since in the single phase regions $D=0$ always hold. However, if $\rho D/\rho_l$ is replaced by Γ_h which is also finite in the single phase regions, such a substitution is valid only if the densities for the liquid and the vapor phases are considered to be constant, i.e., only when $\rho_l=\rho_{l,sat}$ and $\rho_v=\rho_{v,sat}$ are assumed. Therefore, Eq. (2.64) may be considered as the final form of the energy conservation equation, without imposing any restrictive assumption with respect to densities in the single phase regions. By assuming constant density in the single phase regions, the final form of the energy conservation equation (2.64) can be written, as presented by Wang and Beckermann, as:

$$\Omega_h\frac{\partial(\rho h)}{\partial t}+\nabla\cdot[\gamma_h\rho\mathbf{u}h]=\nabla\cdot[\Gamma_h\nabla h]+\nabla\cdot[\Gamma_h(h-h_{v,sat})\nabla\ln\rho]+\nabla\cdot\left[f\,\frac{K\Delta\rho\,h_{fg}}{\nu_v}\,g\right]+\dot{q}''' \tag{2.67}$$

The term dT/dh in Eqs. (2.56) and (2.65) denotes the derivative of temperature with respect to mixture enthalpy. The relationship between enthalpy and temperature (enthalpy as a function of temperature) could also be written as:

$$T=T_{sat}+\frac{h-h_{l,sat}}{C_{pl}} \quad \text{for} \quad h\le h_{l,sat};\ T\le T_{sat} \quad \text{(liquid phase)} \tag{2.68a}$$

$$T=T_{sat} \quad \text{for} \quad h_{l,sat}<h\le h_{v,sat};\ T=T_{sat} \quad \text{(two-phase region)} \tag{2.68b}$$

$$T=T_{sat}+\frac{h-h_{v,sat}}{C_{pv}} \quad \text{for} \quad h_{v,sat}<h;\ T>T_{sat} \quad \text{(vapor phase)} \tag{2.68c}$$

The liquid saturation or the volume fraction, on the other hand, can be expressed for all regions as:

$$s = \begin{cases} 1 & h \le h_{l,sat} \\ \dfrac{\rho\left(h_{v,sat} - h\right)}{\rho_l h_{fg}} & h_{l,sat} < h \le h_{v,sat} \\ 0 & h_{v,sat} < h \end{cases} \tag{2.69}$$

From the definition in Eq. (2.68), dT/dh is obtained as:

$$\frac{dT}{dh} = \begin{cases} \dfrac{1}{C_{pl}} & h \le h_{l,sat} \\ 0 & h_{l,sat} < h \le h_{v,sat} \\ \dfrac{1}{C_{pv}} & h_{v,sat} < h \end{cases} \tag{2.70}$$

The physical meanings of all the terms appearing in Eq. (2.52) have been explained by Wang and Beckermann. They have also pointed out that this equation strongly resembles the classical formulation describing heat transfer of a single-phase multi-component mixture inside porous media. In addition, some observations can be made regarding the energy equation (2.67). The same, Eq. (2.67) represents the temperature equation in the single phase region, whereas it reduces to the liquid saturation equation in the two-phase region. It has been evident that both the temperature (may remain constant over a range of liquid saturation in the two-phase region) and the liquid saturation (may remain constant over ranges of temperature in the single phase regions) can be uniquely determined from the mixture enthalpy. Since the temperature of the solid matrix and the working fluid is assumed to be the same, and for the two-phase region the temperature remains constant (at saturation temperature) with mixture enthalpy, the solid matrix does not contribute to two-phase transport in the two-phase region. In this formulation, the effect of the solid matrix is felt only in the transient term. As mentioned before, if the temperatures of the solid matrix and the working fluid is assumed to be different and the separate energy equation is considered for the solid part, then the solid matrix can affect the phase change through the convective heat exchange term.

In Eq. (2.67), γ_h plays a role only for the two-phase region. For the single phase region $\gamma_h = 1$. Consequently, no correction is required for the advection term. For the completely liquid phase, $\lambda = 1$ and $s = 1$. This is obtained similarly for the completely vapor phase, $\lambda = 0$ and $s = 0$. Consider now the second term on the RHS of Eq. (2.67). For a single region, either $\lambda = 0$ (for vapor) or $\lambda = 1$ (for liquid), and hence the capillary diffusion D is equal to zero and the density is constant. Thus, the second term on the RHS of Eq. (2.67) disappears for the single phase regions. On the other hand, the third term on the RHS of Eq. (2.67), f is zero for either the purely liquid phase as $k_{rv} = 0$ or the purely vapor phase as $\lambda = 0$. Therefore, both the second and the third terms vanish for the single phase region. Wang and Beckermann pointed out that the equations (2.23), (2.26) and (2.67) establish a one domain formulation for flow problems in multiple regions if the two-phase region can be assumed to be isothermal and if Darcy's law is valid. From Eq. (2.26), $\rho\mathbf{u}$ has been obtained, which requires information regarding ∇p. The pressure field is to be corrected using Eq. (2.23), and the correct velocity field may be used to solve Eq. (2.67) in order to obtain the enthalpy (or temperature or volume fraction). The formulation is attractive and since there is no need to track the moving interfaces between different regions, complex interfacial boundary conditions are not required to match. The conservation of mass in Eq. (2.23) and momentum in Eq. (2.26) are readily suitable for numerical implementation [54], whereas the conservation of energy in Eq. (2.67) requires some manipulation because it is non-amenable to the solution with existing numerical algorithms.

In view of the governing energy conservation equation (2.64) along with the constitutive relations, according to the original enthalpy formulation [29], the following comments are also now in order:

1. The relationship between liquid saturation s and enthalpy h in Eq. (2.69) is implicit since it contains the mixture density ρ on the right hand side, which is an explicit function of s. During iteration, h is first obtained by solving Eq. (2.64) using semi-implicit treatment. Using the new h in the two-phase region, s is first evaluated from Eq. (2.69), since all other mixture properties explicitly depend on it. Therefore, the process would require additional computation time.
2. The second term in Eq. (2.64) on the RHS represents the diffusion of ρ in the two-phase region, which has to be accommodated as a source in the discretized equation.
3. If Eq. (2.64) is solved for the volumetric enthalpy ρh (instead of h) as the independent variable, additional problems may arise since ρh is not a monotonically increasing function of the thermodynamic state, particularly in the two-phase region [33]. This apprehension, however, would be meaningless if the mixture enthalpy h is solved from Eq. (2.64), as has been adopted for the modified enthalpy formulation in subsection 2.1.4.
4. In the two-phase region, Γ_h is obtained from Eq. (2.65) in the vicinity of $s=1$ and $s=0$ since both D and dT/dh are exactly equal to zero. Therefore, the formulation produces jumps in the predicted temperature at the phase-change interfaces, unless special care is taken. This problem, however, persists for all variants of TPMM [29, 30, 33] and may be avoided using smoothing of effective diffusion coefficient (special treatment), as will be introduced later in this thesis.

In the present work, water has been considered as the working fluid and its properties are given in Table 2.1, where the saturation temperature T_{sat} of water has been considered to be $100^{\circ}\mathrm{C}$ at atmospheric pressure. In order to evaluate the capillary diffusion coefficient porosity $\varepsilon=0.3$ and permeability $K=10^{-11}\mathrm{m}^2$ have been considered, which is typical for packed porous medium. These two quantities are required for the calculation of capillary diffusion coefficient D. In order to evaluate the effective thermal conductivity k_{eff} of the composite medium according to Eq. (2.45) (i.e., using the parallel arrangement model in addition to the porosity), the thermal conductivity of the solid matrix k_s is also required. This value has been taken as $20\,\mathrm{W/mK}$, which is typical for compressed wire-mesh structures made out of low-carbon steel [89]. Results are presented in Fig. 2.1 for different exponent n in the expression of relative permeability. Figure 2.1

represents the variations of the advection correction coefficient γ_h, hindrance coefficient f and effective diffusion coefficient Γ_h as functions of enthalpy. In the two-phase region, however, γ_h, f, and Γ_h are a strong function of the enthalpy as well as liquid saturation. Since most of these factors have appeared in the energy conservation equation for phase change problems inside porous media, it would be logically be imperative to study in detail their behavior as a function of enthalpy.

Table2.1: Thermo-physical properties of water [33, 88, 89]

Property	Liquid	Vapor
Density, ρ ($\mathrm{kg/m^3}$)	957.85	0.5978
Specific heat, C_p ($\mathrm{J/kgK}$)	4190.2	2029.0
Dynamic viscosity, μ ($\mathrm{kg/ms}$)	2.79×10^{-4}	1.202×10^{-5}
Thermal conductivity, k ($\mathrm{W/mK}$)	0.68	0.0248
Expansion coefficient, β ($\mathrm{K^{-1}}$)	5.23×10^{-4}	2.4×10^{-3}
Saturation enthalpy, h ($\mathrm{J/kg}$)	419.02×10^{3}	2676.05×10^{3}
Prandtl number $Pr=\mu C_p/k$	1.72	0.983
Latent heat of evaporation, h_{fg} ($\mathrm{J/kg}$)	2257.03×10^{3}	
Surface tension coefficient, σ ($\mathrm{N/m}$)	0.0589	

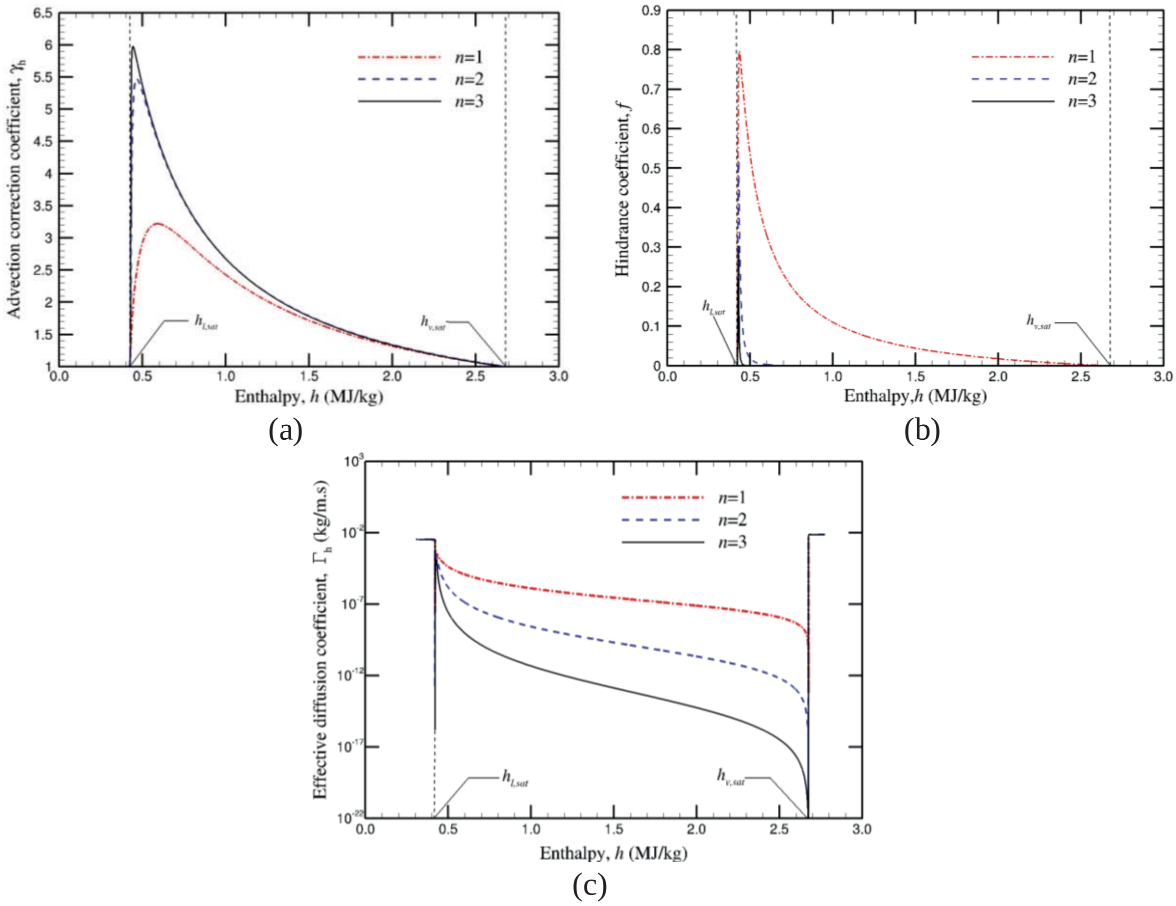

(a) (b)

(c)

Fig. 2.1: Variations (a) advection correction coefficient γ_h, (b) hindrance coefficient f and (c) effective diffusion coefficient Γ_h as functions of enthalpy h for water-steam system

Although, the advection correction coefficient and hindrance coefficient are continuous functions of enthalpy, the effective diffusion coefficient Γ_h is a strong function of enthalpy h and definitely a discontinuous function at $h_{l,sat}$ as well as at $h_{v,sat}$. This is reasonable due to the effective diffusion coefficient Γ_h has been evaluated by Eq. (2.65). The first term on the RHS of Eq. (2.65) varies smoothing in the whole range, whereas according to Eq. (2.70), dT/dh has a drastic “jump” on the phase change interfaces. Consequently, there exist sharp discontinuities in the effective diffusion coefficient across the interfaces between single and two-phase regions, which are found to be more severe closer to saturated vapor phase as shown in Fig. 2.1(c). Therefore, evaluation of Γ_h requires special care, which will be discussed later in this chapter. Based on the previous discussion, the energy conservation equation either in Eq. (2.64) or (2.67) is not readily suitable for numerical implementation [54]. It would, therefore, be worthwhile to explore alternative formulations that eliminate the aforementioned drawbacks in the original formulation of TPMM [29]. These formulations require certain modifications, as described in the next subsections of chapter 2.

2.1.2. Volumetric Enthalpy Formulation of Two-Phase Mixture Model

As claimed from subsection 2.1.1 the volumetric enthalpy (ρh) in the original formulation of Wang and Beckermann, particularly in the two-phase region, is not a monotonic function of thermodynamic state and the energy conservation equation (2.64) is not suitable for numerical implementation. Therefore, Wang et al. [30] proposed a new definition of a volumetric enthalpy as the dependent variable for the energy conservation equation to overcome the aforementioned drawbacks, which is defined as:

$$H_1 = \rho\left(h - h_{v,sat}\right) \tag{2.71}$$

In this model, the mass and momentum conservation equations remain identical as the original formulation of TPMM [29]. Except for the coefficients appearing in the energy conservation equation (2.60), i.e., advection correction coefficient γ_h and the effective diffusion coefficient Γ_h, all other mixture variables and properties remain identical in this model, based on the volumetric enthalpy formulation. Therefore, the energy conservation equation (2.52) may be written once again as:

$$(1-\varepsilon)\rho_s C_{ps}\frac{\partial T}{\partial t} + \varepsilon\frac{\partial}{\partial t}(\rho h) + \nabla\cdot\left[\rho\mathbf{u}h_k\right] = \nabla\cdot\left[k_{eff}\nabla T\right] + \nabla\cdot\left(h_{fg}\mathbf{j}\right) + \dot{q}''' \tag{2.72}$$

In order to modify the energy conservation equation from the enthalpy form to the modified volumetric enthalpy form according to the definition of H_1 in Eq. (2.71), the second transient term on the LHS of Eq. (2.72) is considered, while using the continuity equation (2.23), this term can be written in terms of H_1 as:

$$\varepsilon\frac{\partial}{\partial t}(\rho h) = \varepsilon\frac{\partial}{\partial t}\left[H_1 + \rho h_{v,sat}\right] = \varepsilon\frac{\partial H_1}{\partial t} - \nabla\cdot\left(\rho\mathbf{u}h_{v,sat}\right) \tag{2.73}$$

Using Eq. (2.73), Eq. (2.72) can be rewritten as:

$$\Omega_{H_1}\frac{\partial H_1}{\partial t}+\nabla\cdot\left[\rho\mathbf{u}\left(h_k-h_{v,sat}\right)\right]=\nabla\cdot\left[k_{eff}\nabla T\right]+\nabla\cdot\left(h_{fg}\mathbf{j}\right)+\dot{q}''' \tag{2.74}$$

where Ω_{H_1} has a similar meaning as in Eq. (2.56), but according to the present modified formulation, and hence it is derived as:

$$\Omega_{H_1}=\varepsilon+\rho_s C_{ps}\left(1-\varepsilon\right)\frac{dT}{dH_1} \tag{2.75}$$

Consider now the convective term, i.e., the second term on the LHS of Eq. (2.74). Using the definition of H_1 in Eq. (2.71), the final form of the convective term can be rewritten in terms of H_1 as:

$$\nabla\cdot\left[\rho\mathbf{u}\left(h_k-h_{v,sat}\right)\right]=\nabla\cdot\left[\rho\mathbf{u}H_1\frac{\left(h_k-h_{v,sat}\right)}{\rho\left(h-h_{v,sat}\right)}\right]=\nabla\cdot\left(\gamma_{H_1}\mathbf{u}H_1\right) \tag{2.76}$$

where γ_{H1} is still recognized as the advection correction coefficient and hence it is redefined using the definition of mixture density in Eq. (2.1) as follows:

$$\gamma_{H_1}=\frac{\rho\left(h_k-h_{v,sat}\right)}{\rho\left(h-h_{v,sat}\right)}=\frac{\rho\left(-\lambda h_{fg}\right)}{-\rho_l s h_{fg}}=\left[s+\frac{\rho_v}{\rho_l}\left(1-s\right)\right]\frac{\lambda}{s} \tag{2.77}$$

Although $\gamma_{H1}=1$ for the single phase regions, for saturated vapor condition according to Eq. (2.77) at $\lambda=s=0$, γ_{H1} is undefined.

In order to simplify the total mass flux $\mathbf{j}$ in the second term on the RHS of Eq. (2.74), an expression of ∇s in terms of ∇H_1 is required [see Eq. (2.40)]. The gradient of liquid saturation ∇s may be expressed in terms of ∇H_1 using Eq. (2.62) as:

$$\nabla s=\frac{1}{\rho_l\,h_{fg}}\nabla H_1 \tag{2.78}$$

Using the gradient of liquid saturation ∇s in Eq. (2.78), the second term on the RHS of Eq. (2.74) is obtained as:

$$\nabla\cdot\left(h_{fg}\mathbf{j}\right)=\nabla\cdot\left(\frac{D}{\rho_l}\nabla H_1\right)+\nabla\cdot\left(f\,\frac{K\,\Delta\rho\,h_{fg}\,\mathbf{g}}{\nu_v}\right) \tag{2.79}$$

On the other hand, the first term on the RHS of Eq. (2.74) can also be written in terms of H_1 as:

$$\nabla \cdot \left(k_{eff} \nabla T\right) = \nabla \cdot \left(k_{eff} \frac{dT}{dH_1} \nabla H_1 \right) \tag{2.80}$$

Using equations from (2.73) to (2.80), the final form of the modified energy conservation equation (2.74) is obtained as:

$$\Omega_{H_1} \frac{\partial H_1}{\partial t} + \nabla \cdot \left(\gamma_{H_1} \mathbf{u} H_1\right) = \nabla \cdot \left(\Gamma_{H_1} \nabla H_1\right) + \nabla \cdot \left(f \frac{K \Delta\rho\, h_{fg}\, \mathbf{g}}{\nu_v} \right) + \dot{q}''' \tag{2.81}$$

where Γ_{H_1} is also still recognized as the effective diffusion coefficient for H_1 and is redefined as:

$$\Gamma_{H_1} = \frac{D}{\rho_l} + k_{eff} \frac{dT}{dH_1} \tag{2.82}$$

It is clear from the foregoing equations that the modified energy equation (2.81) for this model is readily suited for numerical implementation only in case of an incomplete phase change process, i.e., from the sub-cooled liquid region to the two-phase zone. Wang [33] has also pointed out that the variable of H_1 becomes a monotonic function of the thermodynamic state during the transition from a single-phase region to the two-phase zone. Nevertheless, this formulation fails to predict the transition from the two-phase region to the superheated vapor region, since some of the variables (properties) remain undefined for the vapor phase. Obviously, Eq. (2.81) does reduce to the single-phase energy equation in the sub-cooled liquid region when $s = 1$. However, Eq. (2.81) is inapplicable to the superheated vapor region when $s = 0$, because γ_{H_1} given by Eq. (2.77) would become indeterminate in this limit. Consequently, this model is recommended only for the simulation of incomplete phase change process inside porous media. In order to eliminate the drawback in the TPMM of Wang et al during the simulation of complete phase change process, Wang proposed a new definition of the volumetric enthalpy as explained in the next subsection.

2.1.3. Modified Volumetric Enthalpy Formulation of Two-Phase Mixture Model

As evident from subsection 2.1.2 that the TPMM of Wang et al is inapplicable to the superheated vapor region when $s = 0$ owing to the advection correction coefficient γ_{H_1} remain undefined and hence this model cannot be used for the prediction of complete phase change process. Therefore, in order to overcome this limitation, Wang [33] proposed a new definition of the modified volumetric enthalpy in the following manner:

$$H_2 = \rho\left(h - 2h_{v,sat}\right) \tag{2.83}$$

Since the mass and momentum conservation equations for all variants of TPMM is given by Eqs. (2.23) and (2.26), respectively, the energy conservation equation for the modified volumetric enthalpy formulation, proposed by Wang, is briefly presented here for the sake of completeness. According to this formulation, the energy conservation equation (2.60) is rewritten in terms of the

H_2 as the dependent variable. In a similar manner, all the mixture variables and properties in this model remain identical to that in the formulation of TPMM of Wang et al except the variable coefficients appearing in the energy conservation equation (2.81), i.e., heat capacity ratio Ω_{H_1}, advection correction coefficient γ_{H_1}, and the effective diffusion coefficient Γ_{H_1}. Therefore, the energy conservation equation (including the evaluation of temperature and liquid saturation) and the initial/boundary conditions are obtained according to the definition of H_2 as the following:

A. *Modified formulation of Conservation of Energy*

The energy conservation equation is still represented by Eq. (2.72) in this model. Following a similar procedure for the transient term with help of the continuity equation (2.23), the transient term in Eq. (2.72) can be written in terms of H_2 as:

$$\varepsilon \frac{\partial}{\partial t}(\rho h) = \varepsilon \frac{\partial H_2}{\partial t} + 2h_{v,sat}\left[-\nabla \cdot (\rho \mathbf{u})\right] = \varepsilon \frac{\partial H_2}{\partial t} - \nabla \cdot \left(2\rho \mathbf{u} h_{v,sat}\right) \tag{2.84}$$

Using the above equation, the energy conservation equation (2.72) can be rewritten as:

$$\Omega_{H_2} \frac{\partial H_2}{\partial t} + \nabla \cdot \left[\rho \mathbf{u}\left(h_k - 2h_{v,sat}\right)\right] = \nabla \cdot \left[k_{eff} \nabla T\right] + \nabla \cdot \left(h_{fg} \mathbf{j}\right) + \dot{q}''' \tag{2.85}$$

where the equivalent effective heat capacity ratio Ω_{H_2} is derived as:

$$\Omega_{H_2} = \varepsilon + \rho_S C_{pS} (1-\varepsilon) \frac{dT}{dH_2} \tag{2.86}$$

Once again, the convective term on the LHS of Eq. (2.85) could also be written in terms of H_2 as follows:

$$\nabla \cdot \left[\rho \mathbf{u}\left(h_k - 2h_{v,sat}\right)\right] = \nabla \cdot \left[\mathbf{u} H_2 \frac{\rho\left(h_k - 2h_{v,sat}\right)}{\rho\left(h - 2h_{v,sat}\right)}\right] = \nabla \cdot \left(\gamma_{H_2} \mathbf{u} H_2\right) \tag{2.87}$$

where γ_{H_2} is the advection correction coefficient for H_2, defined as:

$$\gamma_{H_2} = \frac{\rho\left(h_k - 2h_{v,sat}\right)}{\rho\left(h - 2h_{v,sat}\right)} = \frac{\left[s + \left(\rho_v / \rho_l\right)(1-s)\right]\left[h_{v,sat}(1+\lambda) - h_{l,sat}\lambda\right]}{\left(2h_{v,sat} - h_{l,sat}\right)s + (1-s)\left(\rho_v h_{v,sat} / \rho_l\right)} \tag{2.88}$$

The second term on the RHS of Eq. (2.85) can be treated in the same manner to yields Eq. (2.79). In order to proceed further one needs to express ∇s in terms of H_2. Using the relation for ∇s in Eq. (2.62) in terms of H_2 and following relatively straightforward mathematical manipulation, the second term on the RHS of Eq. (2.85) can be represented as:

$$\nabla\cdot\left(h_{fg}\,\mathbf{j}\right)=-h_{fg}\nabla\cdot\left[-\frac{D}{\rho_l h_{fg}}\frac{1}{1+\left(1-\dfrac{\rho_v}{\rho_l}\right)\dfrac{h_{v,sat}}{h_{fg}}}\nabla H_2\right]+\nabla\cdot\left[f\,\frac{K\,\Delta\rho\,h_{fg}\,\mathbf{g}}{\nu_v}\right] \tag{2.89}$$

On the other hand, the first term on the RHS of Eq. (2.85) can also be written in terms of H_2 as:

$$\nabla\cdot\left(k_{eff}\nabla T\right)=\nabla\cdot\left(k_{eff}\,\frac{dT}{dH_2}\nabla H_2\right) \tag{2.90}$$

Similar to the previous model in subsection 2.1.2, by using equations from (2.87) to (2.90), one may obtain the applicable energy conservation equation from Eq. (2.85) as follows:

$$\Omega_{H_2}\frac{\partial H_2}{\partial t}+\nabla\cdot\left(\gamma_{H_2}\,\mathbf{u}H_2\right)=\nabla\cdot\left(\Gamma_{H_2}\,\nabla H_2\right)+\nabla\cdot\left(f\,\frac{K\,\Delta\rho\,h_{fg}\,\mathbf{g}}{\nu_v}\right)+\dot{q}''' \tag{2.91}$$

where the equivalent effective diffusion coefficient Γ_{H_2} for modified volumetric enthalpy H_2 is obtained as:

$$\Gamma_{H_2}=\frac{D\,h_{fg}}{\rho_l h_{fg}+\nabla\rho\,h_{v,sat}}+k_{eff}\,\frac{dT}{dH_2} \tag{2.92}$$

Without losing the generality, let us assume (denote) $H_2=H$, i.e., without suffix. Once again, in the single phase region $D=0$, and in the two-phase region $dT/dH\ =0$. Consequently, the second term of Eq. (2.92) plays an important role in the single phase region. In order to evaluate the value of dT/dH in Eqs. (2.86) and (2.92), relationship between H and T for all regions is required. Assuming the enthalpies of the liquid and vapor phases to be dependent only on the temperature (i.e., constant density in the single phase regions), and since the pressure drop in the porous evaporator is expected to be small owing to the extremely low flow rate, the relationship between enthalpy and temperature or liquid saturation can be written as:

For the liquid region, i.e., for $h\le h_{l,sat}$ ($T\le T_{sat}$), the enthalpy is obtained as:

$$h=h_{l,sat}-C_{pl}(T_{sat}-T) \tag{2.93}$$

According to Eq. (2.93), the modified volumetric enthalpy H for purely liquid can be written in terms of temperature T and vice versa as:

$$H\ =\rho_l h_{l,sat}-\rho_l C_{pl}\left(T_{sat}-T\right)-2\rho_l h_{v,sat} \qquad \text{for } T\le T_{sat} \tag{2.94a}$$

$$T = T_{sat} + \frac{H + \rho_l (2h_{v,sat} - h_{l,sat})}{\rho_l \, C_{pl}} \qquad \text{for } H \le -\rho_l (2h_{v,sat} - h_{l,sat}) \qquad (2.94b)$$

In order to evaluate Ω_H in Eq. (2.86) and Γ_H in Eq. (2.86), dT/dH is required. Therefore, for constant densities in the single phase regions, dT/dH is obtained from Eq. (2.94b) for the purely liquid as:

$$\frac{dT}{dH} = \frac{1}{\rho_l \, C_{pl}} \qquad (2.95)$$

For the two-phase region, i.e., for $h_{l,sat} < h \le h_{v,sat}$, the temperature is to be constant and equal to the saturation temperature as:

$$T = T_{sat} \qquad \text{for } \rho_l (h_{l,sat} - 2h_{v,sat}) < H \le -\rho_v h_{v,sat} \qquad (2.96)$$

Consequently, $dT/dH = 0$ in the two-phase region and the effective diffusion coefficient is enhanced by capillary diffusion [see Eq. (2.92) for further clarification]. For the vapor phase, on the other hand, i.e., for $h > h_{v,sat}$ ($T > T_{sat}$), the enthalpy is obtained as:

$$h = h_v + C_{pv}(T - T_{sat}) \qquad (2.97)$$

Similarly, the modified volumetric enthalpy H for purely vapor can be written in terms of temperature T according Eq. (2.97) and vice versa as:

$$H = \rho_v C_{pv} \left(T - T_{sat} \right) - \rho_v h_{v,sat} \qquad \text{for } T > T_{sat} \qquad (2.98a)$$

$$T = T_{sat} + \frac{H + \rho_v h_{v,sat}}{\rho_v \, C_{pv}} \qquad \text{for } -\rho_v h_{v,sat} < H \qquad (2.98b)$$

Similarly, dT/dH for the purely vapor is obtained as:

$$\frac{dT}{dH} = \frac{1}{\rho_v \, C_{pv}} \qquad (2.99)$$

Another important relationship that is essential, is the one between the liquid saturation s and modified volumetric enthalpy H (to be precise, s as a function of H). For purely liquid and vapor phases, the liquid saturation is assigned as $s = 1$ and $s = 0$, respectively, whereas in Eq. (2.62) along with definition of H from Eq. (2.83), the liquid saturation in the two-phase region is obtained as:

$$s = -\frac{H_2 + \rho_v h_{v,sat}}{\rho_l h_{fg} + (\rho_l - \rho_v) h_{v,sat}} \tag{2.100}$$

It may be further noted that ρ_l and ρ_v are assumed to be constants, $H_{l,sat} = -\rho_l (2h_{v,sat} - h_{l,sat})$ and $H_{v,sat} = -\rho_l h_{v,sat}$ could be substituted in Eqs. (2.94b) and (2.98b), respectively. Therefore, under this assumption, the expression for temperature in the single phase regions could be further simplified as:

$$T = T_{sat} + \frac{H - H_{l,sat}}{\rho_l \, C_{pl}} \qquad \text{for liquid phase} \tag{2.101a}$$

$$T = T_{sat} + \frac{H - H_{v,sat}}{\rho_v \, C_{pv}} \qquad \text{for vapor phase} \tag{2.101b}$$

The modified volumetric enthalpy formulation represented by Eq. (2.91) is applicable to all regions in a computational domain. This equation, along with the mass and momentum conservation equations, constitutes the basis for developing the present work. Similarly to the original formulation of TPMM, the coefficients appearing in the energy conservation equation (2.91) have been also examined at the same conditions. Therefore, water has been considered as the working fluid and its properties are given in Table 2.1. In addition, the properties of the porous medium have been taken identical to those given in the original formulation of TPMM [29], i.e., porosity $\varepsilon = 0.3$, permeability $K = 10^{-11}\,\mathrm{m}^2$, thermal conductivity of the solid $k_s = 20\,\mathrm{W/mK}$, density of the solid $\rho_s = 8000\,\mathrm{kg/m^3}$ [33] and specific heat of the solid $C_{ps} = 480\,\mathrm{J/kg\,K}$ [33]. Results are presented in Fig. 2.2 for different exponent n. Figure 2.2 displays the variations of the advection correction coefficient γ_H, hindrance coefficient f, effective diffusion coefficient Γ_H and effective heat capacity ratio Ω_H as functions of modified volumetric enthalpy H for water-steam system. The major problem in modeling the complete phase change process inside a porous medium occurs due to the presence of discontinuities in the effective diffusion coefficient at the boundaries of two-phase regions, i.e., between sub-cooled liquid region and two-phase zone as well as two-phase zone and superheated vapor region.

Figure 2.2 clearly shows that although γ_H and f are continuous functions of H, Γ_H and Ω_H are also strong functions of H and are definitely discontinuous functions at $H_{l,sat}$ and $H_{v,sat}$, whereas they assume finite constant values for the purely liquid and vapor phases. Furthermore, discontinuity problem is also associated with an additional and substantial volume expansion of the phase change fluid. This can be attributed to the huge difference in densities of the liquid and the vapor phases. It may be noted from Eq. (2.92) that Γ_H has two distinct parts. In the single phase regions, $D = 0$ (since either $k_{rv} = 0$ or $k_{rl} = 0$), whereas for the two-phase region, $dT/dH = 0$ (since the temperature is constant). Therefore, for $s = 0$ (saturated vapor) and $s = 1$ (saturated liquid), those uniquely identify the exact physical conditions (states) of the working fluid, two different values of Γ_H have been obtained with one of them, calculated from the two-phase region being exactly equal to zero as both D and dT/dH are zero for these conditions. Similarly, Ω_H has two distinct parts. In the single phase regions, Ω_H is obtained from Eq. (2.86) since $dT/dH \neq 0$, whereas in the two-phase region $\Omega_H = \varepsilon$ since $dT/dH = 0$. As it will be shortly apparent, such discontinuities, under certain conditions, can produce a non-physical "jump" in the predicted temperature distribution during the numerical simulation of complete phase change process inside porous media. In order to eliminate this problem, the Γ_H and Ω_H require special treatment, as explained in details in sections 2.3 (for Γ_H) and 2.4 (for Ω_H).

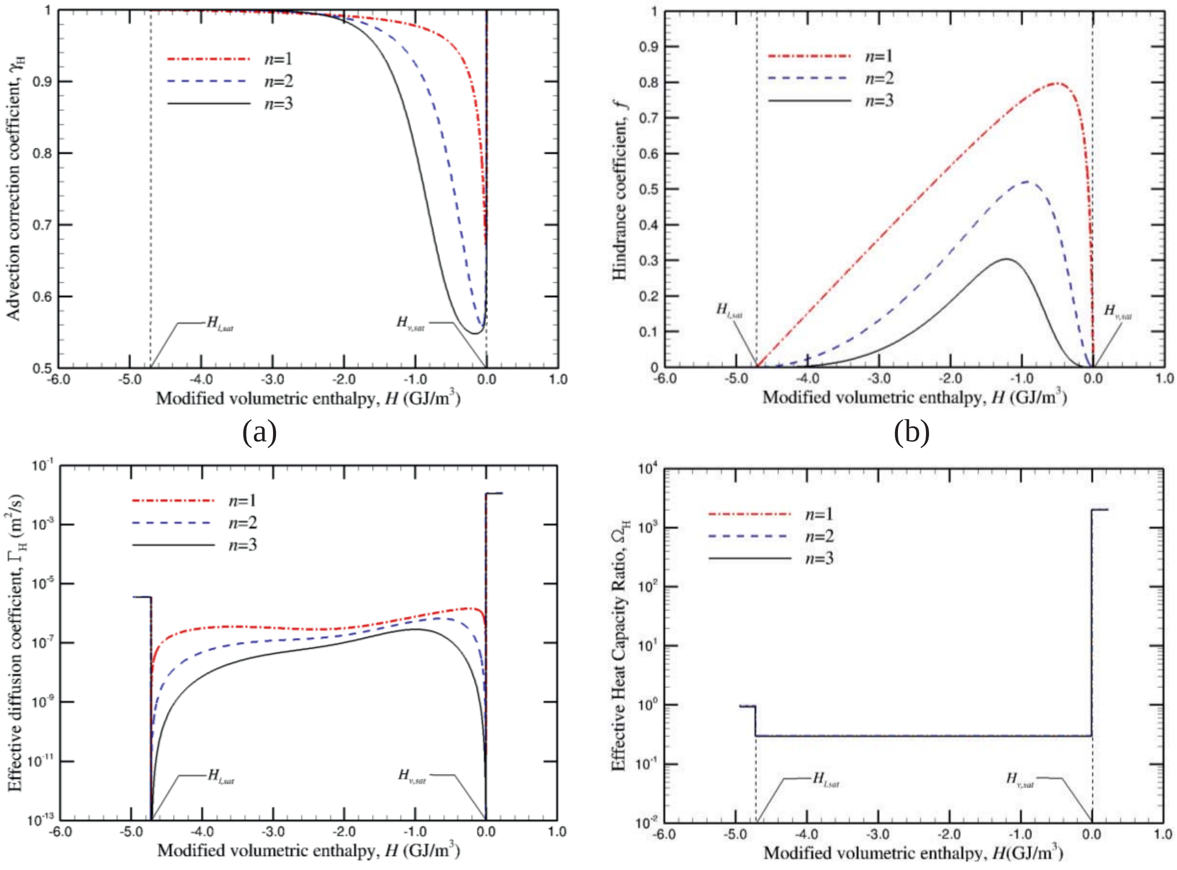

(a) (b)

(c) (d)

Fig. 2.2: Variations (a) advection correction coefficient γ_H, (b) hindrance coefficient f, (c) effective diffusion coefficient Γ_H and (d) effective heat capacity ratio Ω_H as functions of modified volumetric enthalpy H for water-steam system

B. Initial and Boundary Conditions

The initial conditions may be either specified, i.e., usually known or taken from a steady-state solution. The most common boundary condition is the impermeable condition, where there is no mass exchange through the wall. This condition is also applicable for symmetry boundary conditions. If the wall is considered to be at rest in the chosen frame of reference, this condition implies that the normal component of the two-phase mixture velocity (as well as the individual aphasic velocities) must vanish as [29]:

$$\mathbf{u} \cdot \mathbf{n} = 0 \tag{2.102}$$

It is, however, important to note that since Darcy's law is used to obtain the velocity solution instead of the complete momentum equation with diffusion term, the no-slip condition cannot be implemented on the impermeable walls. Other possible velocity boundary conditions include specified mass–flow rate (or specified velocities), specified pressure, and specified velocity gradient (fully–developed condition at the exit), etc. Implementation of these conditions is similar to any other CFD code. For the energy equation, the present formulation also requires boundary conditions for the liquid saturation. Either the liquid saturation or its gradient should be specified at the boundaries [29]. For boiling or condensing flow (i.e., for flows with complete phase change process) three separate zones often appear near the heated or cooled surface, where a two-phase region being sandwiched by two single phase regions have been found [29]. Therefore, the boundary condition for the liquid saturation at the boundary adjacent to the vapor region is set to be zero, whereas at the other boundary is unity. In addition, the liquid saturation at the boundary can be obtained by imposing the wall heat flux $\dot{q}''_w$. The foregoing discussion is made for general boundary conditions applicable on generalized curvilinear coordinates as shown in Fig. 2.3.

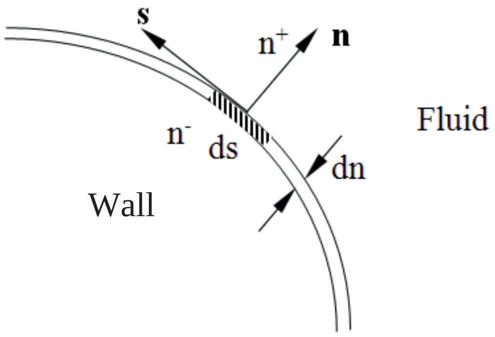

Fig. 2.3: General representation of a wall boundary condition

Consider a boundary (a curved one) as shown in Fig. 2.3, whose the unit normal vector is given as $\mathbf{n}$. The other locally orthogonal, coordinates are given as $\mathbf{s}$ (along the surface in 2D) and $\mathbf{d}$ (perpendicular to the plane of Fig. 2.3). The signs "+" and "–" indicate increasing and decreasing directions, respectively. Here, n^+ is assumed to be directed towards the fluid domain. In order to proceed further, the gradient vector may be locally defined as:

$$\nabla = \frac{\partial}{\partial s}\mathbf{s} + \frac{\partial}{\partial n}\mathbf{n} + \frac{\partial}{\partial d}\mathbf{d} \qquad (2.103)$$

In addition, according to Gauss divergence theorem, the integration of a general variable is written as:

$$\iiint_V \nabla \cdot \boldsymbol{\varphi} = \oiint_S \mathbf{n} \cdot \boldsymbol{\varphi}\, dA \qquad (2.104)$$

For example, the energy conservation equation (2.52) is integrated over the control volume of size $ds \times dn \times dd$ as shown in Fig. 2.3. When the coordinates s, n and d approaches the boundary, the transient term would disappear. The convection term would also yield zero as u_n (the normal component of the velocity) is equal zero on the boundary surface. Consequently, the energy conservation equation (2.52) can be written as:

$$\begin{aligned}&\iiint_{dV}\left[\frac{\partial}{\partial s}\left(k_{eff}\frac{\partial T}{\partial s}\right)+\frac{\partial}{\partial n}\left(k_{eff}\frac{\partial T}{\partial n}\right)+\frac{\partial}{\partial d}\left(k_{eff}\frac{\partial T}{\partial d}\right)\right]ds\,dn\,dd\\&\qquad+\iiint_{dV} h_{fg}\left[(\mathbf{j}\cdot\mathbf{s})_-^+\,dn\,dd+(\mathbf{j}\cdot\mathbf{n})_-^+\,ds\,dd+(\mathbf{j}\cdot\mathbf{d})_-^+\,ds\,dn\right]=0\end{aligned}\tag{2.105}$$

Assuming the volumetric heat generation to be zero, i.e., $\dot{q}'''=0$, and since we would like to obtain the boundary condition for a surface $n\rightarrow 0$ much faster than s or d . Thus, Eq. (2.105) yields:

$$\left[\left(k_{eff}\frac{\partial T}{\partial n}\right)_{n^+}-\left(k_{eff}\frac{\partial T}{\partial n}\right)_{n^-}\right]ds\,dd+h_{fg}\left(\mathbf{j}\cdot\mathbf{n}\right)_-^+ ds\,dd=0\tag{2.106}$$

In order to proceed further, Eq. (2.106) can be rewritten as:

$$k_{eff}\frac{\partial T}{\partial n}+\dot{q}''_w+h_{fg}\left(\mathbf{j}\cdot\mathbf{n}\right)=0\tag{2.107}$$

It may be noted here that while writing Eq. (2.107) for the wall region, the last term of Eq. (2.107) is dropped since there is no flux in the wall region resulting that:

$$-k_{eff}\left.\frac{\partial T}{\partial n}\right|_{n^-}=\dot{q}''_w\tag{2.108}$$

For a typical energy equation, the one encountered for single phase flow, for example, **j** is actually zero and Eq. (2.108) is obtained as:

$$\dot{q}''_w=-k_{eff}\frac{\partial T}{\partial n}\tag{2.109}$$

It may be noted here that $\dot{q}''_w$ is the heat added to the system and n^+ is the normal direction on the boundary that points to the fluid domain. It is, therefore, apparent that the boundary conditions can be applied with care by considering the sign convention. For an isothermal two-phase region, the energy conservation equation (2.107), at a heated or cooled surface is reduced to the following:

$$\mathbf{j}\cdot\mathbf{n}=-\frac{\dot{q}''_w}{h_{fg}}\tag{2.110}$$

If the capillary pressure, defined by Eq. (2.9), is neglected, then according to Eq. (2.41a), the capillary diffusion D equal zero. It is also important to note that Eq. (2.110) cannot be applied for single phase region. For this region, the temperature gradient is determined from the knowledge of heat flux and vice versa. In a similar manner, the integration of the energy conservation equation

(2.91) for the modified volumetric enthalpy formulation [33] over the control volume of size $ds \times dn$ as shown in Fig. 2.3 is given as:

$$\begin{aligned}\Omega_H\, dnds\frac{\partial H}{\partial t} + \gamma_H\, u_s H dn\Big|_-^+ + \gamma_H\, u_n H ds\Big|_-^+ &= \Gamma_H\,\frac{\partial H}{\partial n}\,ds\Bigg|_-^+ + \Gamma_H\,\frac{\partial H}{\partial s}\,dn\Bigg|_-^+ \\ &+ f_s\,\frac{K\,\Delta\rho\, h_{fg}}{\nu_v}\,g_s\Bigg|_-^+ dn + f_n\,\frac{K\,\Delta\rho\, h_{fg}}{\nu_v}\,g_n\Bigg|_-^+ ds\end{aligned} \tag{2.111}$$

At the surface dn goes to zero and $u_n = 0$ on the solid boundary, i.e., no blowing or suction. Consequently, Eq. (2.111) is obtained as:

$$\Gamma_H\,\frac{\partial H}{\partial n}\Bigg|_f + \left(\frac{Dh_{fg}}{\rho_l h_{fg} + \nabla\rho\, h_{v,sat}} + k_{eff}\,\frac{dT}{dH}\right)\frac{\partial H}{\partial n}\Bigg|_s + f_n\,\frac{K\,\Delta\rho\, h_{fg}}{\nu_v}\,g_n\Bigg|_f - f_n\,\frac{K\,\Delta\rho\, h_{fg}}{\nu_v}\,g_n\Bigg|_s = 0 \tag{2.112}$$

Furthermore, it can also be noted here that $Dh_{fg}/(\rho_l h_{fg} + \nabla\rho\, h_{v,sat}) = 0$, $f_n = 0$ and $-k_{eff}\,\partial T/\partial H\big|_s = \dot{q}''_w$ within the solid phase. Based on these assumptions, the wall boundary condition can be obtained from Eq. (2.112) as:

$$\dot{q}''_w = -\Gamma_H\,\frac{\partial H}{\partial n}\Bigg|_f - f_n\,\frac{K\,\Delta\rho\, h_{fg}}{\nu_v}\,g_n \tag{2.113}$$

C. *Issues Related to Density Variations*

For moderate temperature change and hence density variation in the single phase regions, the Boussinesq approximation may be invoked and hence ρ_k in the body-force term of Eq. (2.26) may be expressed as a linear function of the temperature difference [33]:

$$\rho_k = \rho_l\left[1 - \beta_l (T - T_{sat})\right]\lambda_l + \rho_v\left[1 - \beta_v (T - T_{sat})\right]\lambda_v \tag{2.114}$$

where ρ_l and ρ_v are the densities of the liquid phase and the vapor phase, respectively, at $T = T_{sat}$, whereas β_l and β_v are the isobaric expansion coefficients for the liquid and the vapor phases, respectively, at the saturation conditions. Eq. (2.114), therefore, may be recognized as an expression that considers the density variations in the single phase regions as their linear expansions with respect to the temperature difference around their respective saturation conditions. For problems, associated with large temperature difference in the single phase regions, however, more accurate and realistic models should be employed for the density variations. Nevertheless, the issues related to the substantial (realistic) variation in density for the sub-cooled liquid water and the superheated vapor, along with its implications with respect to the present problem (e.g., steady-state one-dimensional solutions), shall be taken up later in this chapter. At this point, however, it is perhaps more important to recognize that as long as the functional dependence of ρ_l and ρ_v are known, the kinetic density can be easily calculated from Eqs. (2.27) and (2.114) may never be invoked.

2.1.4. Modified Enthalpy Formulation

In view of the brief literature review on the phase change process inside porous media in chapter 1, it is now apparent that the most popular TPMM [33] use the modified volumetric enthalpy H as the dependent variable in the energy conservation equation, which may be regarded as a synthetically defined variable for the ease of numerical implementation, rather than a physical quantity. It would, therefore, be worthwhile to identify the problem associated with original enthalpy formulation of TPMM [29] and propose an alternative that would perform equally well or even better than the existing TPMM [33], where the enthalpy h of the phase-change fluid is treated as the dependent variable in the energy conservation equation. According to the TPMM of Wang and Beckermann [29], without invoking any additional assumption, the governing mass and momentum equations are derived from the conventional SFM as given in Eqs. (2.23) and (2.26), respectively. It may be noted here that Eqs. (2.23) and (2.26) remain identical for all variant of TPMM, including the modified enthalpy formulation, where the momentum equation is written by considering only the balance between the Darcy term, pressure gradient and body force. Therefore, the influences of inertia and viscous forces along with higher order effects, that is generally modeled by including the Forchheimer term in the momentum equation, are neglected in this formulation and hence it should be applicable only for cases with low mass flow rates. Nevertheless, the main underlying objective of the modified enthalpy formulation is to remove the complexities in the original model of TPMM for efficient simulation of complete phase change processes and to view the two-phase mixture as a binary mixture. Therefore, in order to eliminate the aforementioned problem in the original model of TPMM, the energy conservation equation (2.64) and the evaluation of liquid saturation in Eq. (2.62) are required special care. Furthermore, all other mixture variables maintain the same definitions according to the original formulation of TPMM, except the effective diffusion coefficient Γ_h.

A. Modified formulations of Liquid Saturation and Conservation of Energy

An explicit relation between the liquid saturation s and the mixture enthalpy h can be easily obtained by substituting the mixture density ρ as a function of s in Eq. (2.62) as follows:

$$s=\frac{\rho_v\left(h_{v,sat}-h\right)}{\rho_v\left(h_{v,sat}-h\right)+\rho_l\left(h-h_{l,sat}\right)} \qquad (2.115)$$

Therefore, the first problem associated with the original enthalpy formulation is eliminated. Since the mixture density could also be expressed as $\rho=\rho_v+\left(\rho_v-\rho_l\right)s=\rho_v+\left(\Delta\rho\right)s$, one may substitute $\nabla\rho=\left(\Delta\rho\right)\nabla s$ in Eq. (2.63) and after some simple algebraic manipulations, ∇s could be expressed as:

$$\nabla s=-\frac{\rho\nabla h}{\rho_v\left(h_{v,sat}-h\right)+\rho_l\left(h-h_{l,sat}\right)} \qquad (2.116)$$

This relation could also be derived by differentiating Eq. (2.115) in space while using the following relationship (since Eqs. (2.62) and (2.115) are two alternative expressions for s, their right hand side can be equated):

$$\rho_l \rho_v h_{fg} = \rho\left[\rho_l\left(h - h_{l,sat}\right) + \rho_v\left(h_{v,sat} - h\right)\right] \tag{2.117}$$

Nevertheless, substituting ∇s from Eq. (2.116), the alternative final form of the energy conservation equation of Eq. (2.64) may be obtained as follows:

$$(1-\varepsilon)\rho_s C_{ps}\frac{\partial T}{\partial t} + \varepsilon\frac{\partial(\rho h)}{\partial t} + \nabla\cdot\left[\gamma_h \rho \mathbf{u} h\right] = \nabla\cdot\left[\Gamma_h \nabla h\right] + \nabla\cdot\left[f\,\frac{K\Delta\rho\, h_{fg}}{\nu_v}\,g\right] + \dot{q}''' \tag{2.118}$$

where Γ_h is the modified effective diffusion coefficient for enthalpy transport h, defined as:

$$\Gamma_h = \frac{\rho D h_{fg}}{\rho_v\left(h_{v,sat} - h\right) + \rho_l\left(h - h_{l,sat}\right)} + k_{eff}\,\frac{dT}{dh} \tag{2.119}$$

Since Eq. (2.118) contains only the standard diffusion term on the RHS, the second problem, associated with the exiting enthalpy formulation, is also successfully removed. As will be shortly apparent, the formulation being general in nature could be easily extended for multi-dimensional problems involving complex geometries. Under the assumption of constant specific heats, enthalpies of the liquid and the vapor phases could be written as functions of temperature:

$$h_l = h_{l,sat} - C_{pl}\left(T_{sat} - T\right) = h_{l,sat} + C_{pl}\left(T - T_{sat}\right) \tag{2.120a}$$

$$h_v = h_{v,sat} + C_{pv}\left(T - T_{sat}\right) \tag{2.120b}$$

Therefore, from Eq. (2.120), the local temperature may be easily retrieved from the solution of enthalpy as:

$$T = T_{sat} + \frac{h - h_{l,sat}}{C_{pl}} \qquad \text{(for liquid phase, } h \le h_{l,sat}\text{)} \tag{2.121a}$$

$$T = T_{sat} + \frac{h - h_{v,sat}}{C_{pv}} \qquad \text{(for vapor phase, } h_{v,sat} < h\text{)} \tag{2.121b}$$

where the general symbol h is used for both enthalpies in liquid and vapor phases for sake of generality. Using either Eq. (2.120) or Eq. (2.121), dT/dh in Eq. (2.119) are obtained as $1/C_{pl}$ and $1/C_{pv}$ for the liquid and vapor phases, respectively. For the two-phase region, however, $dT/dh = 0$, owing to the thermodynamic constraint as mentioned before. In the rest of this thesis, the newly proposed modification shall be referred to as the “modified h-formulation”, whereas the existing modified volumetric enthalpy formulation of Wang [33] shall be referred to as the “H-formulation”. It is now evident that the expression for temperature for the modified h-formulation and the H-formulation in Eqs. (2.121) and (2.101), respectively, are remarkably similar to each other. It will, however, be shortly apparent that such similarity exists only when the densities in the single phase regions are assumed to be constant.

As mentioned earlier, all the mixture variables in the two-phase zone in this model remain identical to that in the original model of TPMM except the evaluation of liquid saturation s and the effective diffusion coefficient Γ_h. Consequently, the behaviors of the advection correction coefficient γ_h as well as the hindrance coefficient f as functions of enthalpy remain identical to that in Fig. 2.1. Thus, these results are not presented here for the sake of brevity. Figure 2.4 clearly shows that the discontinuity in the effective diffusion coefficient for the modified h-formulation at the interface between sub-cooled liquid region and two-phase zone is smaller when compared with the result obtained using the original formulation of TPMM [see Fig. 2.1(c) for the purpose of comparison]. On the other hand, the discontinuity at the saturated vapor condition (i.e., the interface between two-phase zone and superheated vapor region) still remains large as also in the original formulation of TPMM. Nevertheless, the values of Γ_h in the single phase regions remain constant regardless of the model which is in accordance with its definition, provided in Eqs. (2.65) and (2.119). Therefore, the effective diffusion coefficient Γ_h still requires special care.

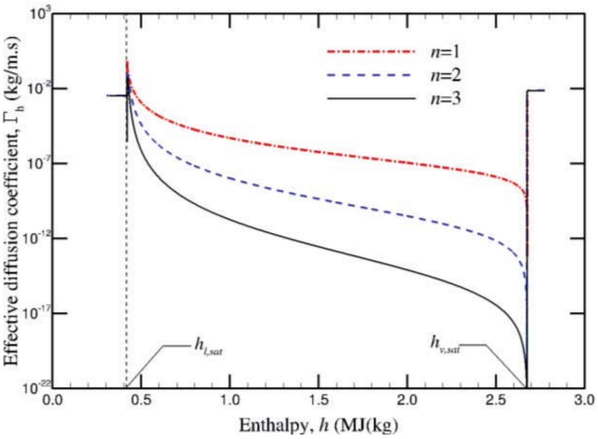

Fig. 2.4: Variations of effective diffusion coefficient Γ_h as a function of enthalpy h based on the modified enthalpy formulation for water-steam system

B. Initial and Boundary Conditions

In a similar manner, the initial conditions in this model are usually known or taken from a steady-state solution. The wall boundary condition for known heat flux is derived by the energy conservation equation (2.118) across the wall-fluid boundary is integrated over the control volume of the size $ds \times dn$ as shown in Fig. 2.3. As a result, the integration of the energy conservation equation over the control volume is written as:

$$\left((1-\varepsilon)\rho_s C_{ps} \frac{\partial T}{\partial t} - \varepsilon \frac{\partial(\rho h)}{\partial t} \right) dnds + \gamma_h\, \rho u_s h\, dn\Big|_-^+ + \gamma_h\, \rho u_n h\, ds\Big|_-^+ = \Gamma_h \frac{\partial h}{\partial n} ds\Bigg|_-^+$$
$$+ \Gamma_h \frac{\partial h}{\partial s} dn\Bigg|_-^+ + f_s \frac{K \Delta\rho\, h_{fg}}{\nu_v} g_s\Bigg|_-^+ dn + f_n \frac{K \Delta\rho\, h_{fg}}{\nu_v} g_n\Bigg|_-^+ ds + \dot{q}''' dnds \tag{2.122}$$

When the limit case approaching the wall, the above equation can be written as:

$$\gamma_h\, \rho u_s h\, dn\Big|_-^+ = \Gamma_h \frac{\partial h}{\partial n} ds\Bigg|_-^+ + f_n \frac{K \Delta\rho\, h_{fg}}{\nu_v} g_n\Bigg|_-^+ ds \tag{2.123}$$

Before proceeding further, it can be recognized the following: u_n is zero on the walls (unless there is blowing or suction, but even then the terms in the positive and negative side will cancel each other), and Γ_h contains two distinct parts as given in Eq. (2.119). On the basis of these observations, Eq. (2.123) can be rewritten as:

$$\begin{aligned}\Gamma_h \left.\frac{\partial h}{\partial n}\right|_{n^+} + \left(\frac{\rho D h_{fg}}{\rho_v\left(h_{v,sat}-h\right)+\rho_l\left(h-h_{l,sat}\right)} + k_{eff}\frac{dT}{dh}\right)\left.\frac{\partial h}{\partial n}\right|_{n^-} & \\ + f_{n^+}\frac{K\,\Delta\rho\, h_{fg}}{\nu_v}g_n - f_{n^-}\frac{K\,\Delta\rho\, h_{fg}}{\nu_v}g_n = 0 &\end{aligned} \tag{2.124}$$

Similarly, within the solid, $\rho D h_{fg} / \left[\rho_v\left(h_{v,sat}-h\right)+\rho_l\left(h-h_{l,sat}\right)\right]=0$ and $f_{n^-}=0$. Thus, the above equation may be simplified as:

$$\dot{q}''_w = -\Gamma_h \left.\frac{\partial h}{\partial n}\right|_f - f_{n^+}\frac{K\,\Delta\rho\, h_{fg}}{\nu_v}g_n \tag{2.125}$$

This is equivalent to the formulation of Eq. (2.113). Equation (2.125) can be used for the evaluation of heat flux at the wall.

2.1.5. Issues Related to Variable Properties

For extremely low mass flow rate applications, the static pressure of the fluid inside the evaporator may be taken equal to the atmospheric pressure. Therefore, the variations in ρ and h for water may now be examined at atmospheric pressure corresponding to $T_{sat}=100^{\circ}\mathrm{C}$, as presented in Figs. 2.5 and 2.6, respectively, for the single phase regions. The properties for the sub-cooled liquid and the superheated vapor phases of water in Figs. 2.5 and 2.6 have been acquired from computerized property table, for example, the one provided by Borgnakke and Sonntag [88]. It is clearly demonstrated from these figures that although enthalpy is a linear function of temperature in the single phase regions, which justifies the use of Eq. (2.120) along with the assumption of constant specific heat for all variants of TPMM, the variations in ρ in both liquid and vapor phases are non-linear functions of temperature. As a result, the modified volumetric enthalpy H also turns out to be a non-linear function of temperature. The raw data for densities in the single phase regions may be expressed in the form of following quadratic functions of temperature:

$$\rho_l = \rho_{l,sat}\left[1-\beta_l\left(T-T_{sat}\right)-a_{l2}\left(T-T_{sat}\right)^2\right] \tag{2.126a}$$

$$\rho_v = \rho_{v,sat}\left[1-\beta_v\left(T-T_{sat}\right)+a_{v2}\left(T-T_{sat}\right)^2\right] \tag{2.126b}$$

where β_l and β_v are the isobaric expansion coefficient at saturation conditions for the liquid and the vapor phases, respectively. They are defined and obtained from the fitting of raw data as:

$$\beta_l = -\frac{1}{\rho_{l,sat}}\left(\frac{\partial \rho}{\partial T}\right)_p = -\frac{1}{\rho_{l,sat}}\left(\frac{\partial \rho_l}{\partial T}\right)_p = 8\times 10^{-4} \tag{2.127a}$$

$$\beta_v = -\frac{1}{\rho_{v,sat}}\left(\frac{\partial \rho}{\partial T}\right)_p = -\frac{1}{\rho_{v,sat}}\left(\frac{\partial \rho_v}{\partial T}\right)_p = 2.47\times 10^{-3} \tag{2.127b}$$

The thermal expansion coefficient, particularly β_l, is slightly different from that used by other researchers [33, 44, 45]. The second coefficients in Eq. (2.126) are obtained as $a_{l2} = 3.4\times 10^{-6}$ and $a_{v2} = 3.25\times 10^{-6}$. Figure 2.5 also shows the variations in ρ_l and ρ_v according to the Boussinesq approximation. It is evident that since the density variation for the sub-cooled liquid phase is not substantial, the Boussinesq approximation or even the assumption of constant density for the liquid phase may not significantly affect the predicted solution.

Nevertheless, if property variation in the single phase regions are taken into account, ρ_l and ρ_v, required for different mixture properties in the two-phase region, are replaced by $\rho_{l,sat}$ and $\rho_{v,sat}$, respectively, although the rest of the h-formulation would still remain the same. For the H-formulation, however, the single phase temperatures are given only by the first part of Eqs. (2.94b) and (2.98b). Since ρ_l and ρ_v are approximated by the quadratic functions of temperature, determination of temperature from the known values of H requires solutions of cubic equations resulting from Eqs. (2.94b), (2.98b) and (2.126) and hence demands additional computation time. The expressions for dT/dH, required in Eqs. (2.86) and (2.92), are obtained as:

$$\left(\frac{\partial T}{\partial H}\right)_l = \frac{\rho_l}{\rho_l^2 C_{pl} + H\left(d\rho_l / dT\right)} \tag{2.128a}$$

$$\left(\frac{\partial T}{\partial H}\right)_v = \frac{\rho_v}{\rho_v^2 C_{pv} + H\left(d\rho_v / dT\right)} \tag{2.128b}$$

where $d\rho_l / dT$ and $d\rho_v / dT$ may be obtained from Eq. (2.126) as:

$$\frac{\partial \rho_l}{\partial T} = -\rho_{l,sat}\left[\beta_l + 2a_{l2}\left(T - T_{sat}\right)\right] \tag{2.129a}$$

$$\frac{\partial \rho_v}{\partial T} = -\rho_{v,sat}\left[\beta_v - 2a_{v2}\left(T - T_{sat}\right)\right] \tag{2.129b}$$

It is now evident that although for the modified h-formulation, the expression for the effective diffusion coefficient Γ_h still remains unaltered, Γ_H for the H-formulation turns out to be a strong function of the local properties in the single phase regions. It is, therefore, obvious that the H-formulation requires appropriate adaption in order to accommodate substantial variations in ρ in the single phase regions.

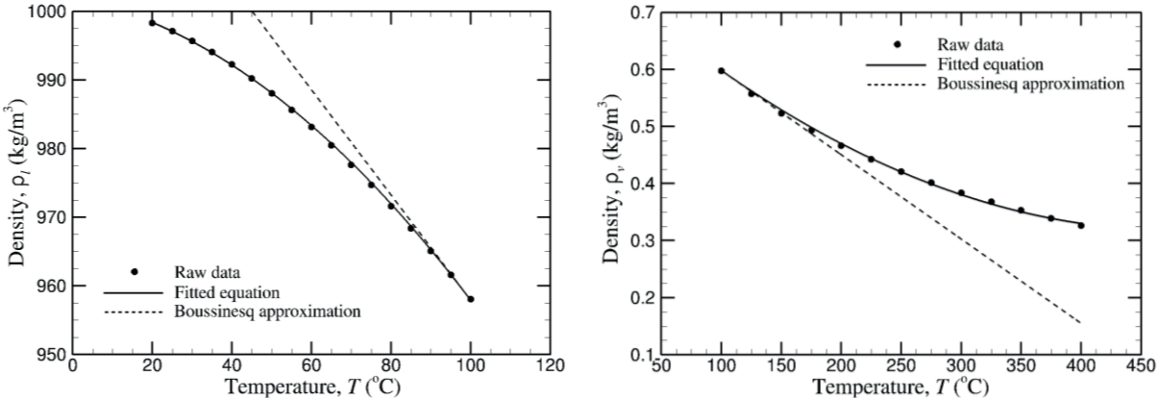

(a) (b)

Fig. 2.5: Density variations for water at atmospheric pressure in the single phase regions (a) liquid phase and (b) vapor phase

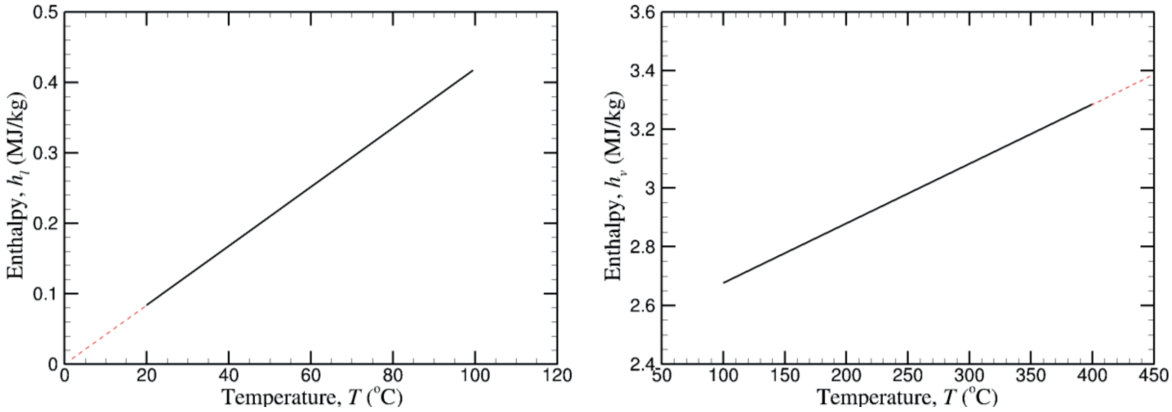

(a) (b)

Fig. 2.6: Enthalpy variations for water at atmospheric pressure in the single phase regions (a) liquid phase and (b) vapor phase

2.1.6. General Remarks on Variants of Two-Phase Mixture Model

Since the governing mass and momentum conservation equations remain invariant for all versions of TPMM and the energy conservation equations (2.91) and (2.118) for the modified h-and H-formulations, respectively, are remarkably similar to each other, they are solved in a similar manner as elaborately described in this chapter and chapter 3. However, if ρ in the single phase regions are functions of the temperature, Eqs. (2.94b) and (2.98b) turn out to be a cubic equation. Although the roots of a cubic equation may be explicitly obtained, the expressions for dT/dH in Eq. (2.128) contain additional non-linear terms. Therefore, for variable properties, the H-formulation is more complex than it was originally presented for constant densities in the single phase regions. No such additional requirement, however, could be detected for the modified h-formulation, and hence it should be preferred over the established H-formulation. For all variants of TPMM, k_{eff} of the composite medium, that consists of a solid matrix and the working fluid, is required. Although k_{eff} could be determined from a separate detailed analysis [29, 83 – 87] of the porous structure, in the present investigation, it is obtained from the simple parallel arrangement models as defined in Eq. (2.45).

Although it has been theoretically established that at least for substantial density variations in the single phase regions, the modified h-formulation should perform better than the existing H-formulation, it would be worthwhile to demonstrate that these formulations produce identical results for a given problem with constant ρ_l and ρ_v, owing to their consistency. Therefore, the complete phase change problem of water inside a constant cross-sectional area porous evaporator for the reduced one-dimensional model has been taken up in chapter 4 as a demonstrative example.

Although the pressure drop through the evaporator has been considered to be negligible in one-dimensional problem and hence the phase change process has been assumed to occur at constant saturation temperature of water corresponding to the atmospheric pressure, for multi-dimensional evaporation or for flows with substantial pressure drop, the phase change temperature is expected to vary. These issues, along with that for the variable specific heat, may also be accommodated quite easily in the present formulation by including appropriate constitutive relations, although they are left beyond the scope of the present work.

2.2. Non-Dimensionalization

Since the number of variables and parameters is quite large, the governing equations for constant densities in the single phase regions have been made dimensionless according to the definitions presented in Table 2.2, where the symbols have their usual meaning. The reference scales for different variables used in this process have been carefully chosen such that they retain all governing equations, constitutive relations and the expressions for various mixture properties in the identical form as that appear in the dimensional H-formulation and modified h-formulation. For variable density formulation, however, the liquid and vapor densities have to be replaced by their saturation values in Tables 2.2 and 2.3. In particular, for the present investigation, all spatial dimensions have been non-dimensionalized with respect to the reference length L_{ref}. The reference length L_{ref} could be considered either the inner radius of the pipe R at the inlet or the height of the channel W. On the other hand, all velocities have been scaled with respect to the average velocity at the duct inlet u_{in}. With these considerations, the governing equations for the modified h- and H-formulations for multi-dimensional problem can be written in their dimensionless form as the following:

2.2.1. Modified Volumetric Enthalpy Formulation of Two-Phase Mixture Model

The following set of governing equations has been written in dimensionless form according to the H-formulation. The mass conservation equation (2.23) is obtained as:

$$\varepsilon \frac{\partial \rho^*}{\partial t^*} + \nabla^* \cdot \left(\rho^* \mathbf{u}^* \right) = 0 \tag{2.130}$$

where the symbols with superscript '*' denote the corresponding dimensionless properties and variables. In Eq. (2.130), ρ^* and $\mathbf{u}^*$ are the dimensionless mixture density and mixture velocity vector, defined in Tables 2.2 and 2.3. Densities of pure liquid and vapor phases have been retrieved from the expansion for ρ^* by substituting $s=1$ and $s=0$, respectively. The momentum conservation equation (2.26), on the other hand, is obtained as:

$$\mathbf{u}^* = -\frac{K^*}{\mu^*}\left[\nabla^* p^* - \rho_k^* \mathbf{b}^*\right] \tag{2.131}$$

As mentioned earlier, the momentum equation considers only the Darcy's law [29, 30, 33], that accounts for additional pressure drop due to the presence of porous matrix [29] along with the body-force. In Eq. (2.131), $K^* = K / L_{ref}^2$ represents the permeability in the dimensionless form or the Darcy number, $\mu^* = \mu / (\mu_l Re_l)$ is the dimensionless viscosity and $\mathbf{b}^* = \tilde{\mathbf{b}}\, gL_{ref} / u_{in}^2 = \tilde{\mathbf{b}} / Fr^2$ is the body-force vector per unit mass in the dimensionless form. $\tilde{\mathbf{b}} = \mathbf{b}/g$ is the component of the body-force vector per unit mass that is normalized with respect to the acceleration due to gravity and hence can only assume a value between -1 and $+1$. In the definition of viscosity, $Re_l = u_{in}\, L_{ref} / \nu_l$ is the inlet Reynolds number, defined on the basis of liquid properties, inlet velocity and the reference length (i.e., the radius of the pipe or the gap between the parallel plates of the channel) such that $\mu_l^* = 1/Re_l$. Further, in the definition of $\mathbf{b}^*$, $Fr = u_{in} / \sqrt{g\, L_{ref}}$ is the Froude number, whose definition can also be found in the nomenclature section. It may be noted here that $\mathbf{b}^* = 0$ implies $Fr \to \infty$. Since definitions of both Re_l and Fr are related to each other through the following relationship $Fr = Re_l / Re_g$, where $Re_g = \rho_l \sqrt{g\, L_{ref}}\, L_{ref} / \mu_l$ may be recognized as the gravitational Reynolds number, defined on the basis of gravitational velocity $u_g = \sqrt{gL_{ref}}$, and its value remains fixed if the reference length (L_{ref}) is kept constant. In most of the previous investigations [33, 37, 39 – 45, 52, 55 – 57, 64 – 67], ρ_k^* was modeled according to the Boussinesq approximation, which considers the density variation only in the body-force term of the momentum equation and it could be expressed using the linear expressions of single-phase densities as a function of local temperature around their saturation conditions as:

$$\rho_k^* = \rho_l^*\left[1 - \beta_l^*(T^* - T_{sat}^*)\right]\lambda + \rho_v^*\left[1 - \beta_v^*(T^* - T_{sat}^*)\right]\lambda_v \tag{2.132}$$

where T^* is the temperature in the dimensionless form. In Eq. (2.132), β_l^* and β_v^* are the isobaric expansion coefficients in non-dimensional form, whereas λ and λ_v are the relative mobilities, of the liquid and vapor phases, respectively. The latter quantities are defined in Table 2.3.

The intrinsic absolute permeability of porous medium K appearing in Eq. (2.131) could be evaluated either from a separate detailed analysis (mostly desirable), where it is obtained by fully resolving the internal details of the porous structure, or by employing empirical correlation, where K could be expressed as a function of the porosity ε and the characteristic diameter d_p of the particle [70, 71]. In this respect, the Carman-Kozeny equation for packed bed of spheres, for example, is given in dimensionless form as in Eq. (2.133) [70, 71]. In an alternative manner, owing to the simplicity, the permeability of the porous medium shall be assumed to be a known quantity, by disregarding the manner in which it is obtained or prescribed.

$$K^* = \frac{d_P^{2^*}\,\varepsilon^3}{180(1-\varepsilon)^2} \tag{2.133}$$

Table 2.2: Definitions of dimensionless variables and parameters

Dimensionless variables/parameters	Expressions
Coordinates and lengths	$x^* = x/L_{ref}\ ;\ y^* = y/L_{ref}\ ;\ d_p^* = d_p/L_{ref}$
Density	$\rho^* = \rho/\rho_l\,;\ \rho_l^* = 1;\ \Delta\rho^* = (\rho_l^* - \rho_v^*)$
Velocity	$u^* = u/u_{in}$
Pressure	$p^* = p/\rho_l u_{in}^2$
Temperature	$T^* = T\,C_{pl}/h_{fg}$
Enthalpy	$h^* = h/h_{fg}\ ;\ h_{fg}^* = 1$
Modified volumetric enthalpy	$H^* = H/\rho_l h_{fg} = \rho^*(h^* - 2h_{v,sat}^*)$
Specific heat	$C_p^* = C_p/C_{pl}\,;\ C_{pl}^* = 1$
Dynamic viscosity	$\mu^* = \mu/\mu_l Re_l\ ;\ \mu_l^* = 1/Re_l\ ;\ Re_l = u_{in}\,L_{ref}/\nu_l$
Thermal conductivity	$k^* = k/\rho_l C_{pl} L_{ref}\,u_{in} = k/k_l Pe_l\,;\ k_l^* = 1/Pe_l$
Body force per unit mass	$b^* = \tilde{b}\,g\,L_{ref}/u_{in}^2 = \tilde{b}/Fr^2\,;\ \tilde{b} = b/g$
Wall heat flux	$\dot{q}_w''^{\,*} = \dot{q}_w''/\rho_l u_{in} h_{fg} = Q_w^*/Re_l\ ;\ Q_w^* = \dot{q}_w'' L_{ref}/\mu h_{fg}$
Heat exchange between fluid and solid	$\dot{q}_{sf}'''^{\,*} = \dot{q}_{sf}'''\,L_{ref}/\rho_l u_{in} h_{fg}$
Isobaric expansion coefficient	$\beta^* = \beta\,h_{fg}/C_{pl}$
Permeability (or Darcy number)	$K^* = K/L_{ref}^2$
Time	$t^* = u_{in}\,t/L_{ref}$

L_{ref} is the inner radius of the pipe R or is the gap between the parallel plate of the channel W

Finally, the energy conservation equation along with the LTE model in Eq. (2.91) can be written in the dimensionless form as:

$$\Omega_H \frac{\partial H^*}{\partial t^*} + \nabla^* \cdot (\gamma_H \mathbf{u}^* H^*) = \nabla^* \cdot (\Gamma_H^* \nabla^* H^*) + \nabla^* \cdot \left(f\,\frac{K^* \Delta\rho^*\, h_{fg}^*}{\nu_v^*}\mathbf{b}^* \right) + \dot{q}'''^{\,*} \tag{2.134}$$

where H^* is the modified volumetric enthalpy, defined in the dimensionless form as $H^* = \rho^*(h^* - 2h_{v,sat}^*)$. It is also important to recognize that $\Delta\rho^* = \rho_l^* - \rho_v^* = (1-\rho_v^*)$ and $h_{fg}^* = 1$ can be substituted in Eq. (2.134) for simplicity. However, these terms have been retained in their present form to enable the readers to use the dimensional formulation without much difficulty.

Further definitions of dimensionless mixture properties in the two-phase region appearing in Eqs. (2.130) – (2.134) are listed in Table 2.3. It can be observed from the table that the dimensionless effective diffusion coefficient for modified volumetric enthalpy Γ_H^* in Eq. (2.134) contains the effective thermal conductivity k_{eff}^* in its dimensionless form. The dimensionless effective thermal conductivity k_{eff}^* of the combined medium (that includes both solid and fluid phases) is a function of the porosity and the liquid saturation [29]. The effective thermal conductivity for such a situation can be obtained from a separate numerical and (or) experimental study [29, 83 – 87]. However, a simple estimation of k_{eff}^* [see Eq. (2.45)], which has been also adopted for the present investigation, can be written in the dimensionless form according to the parallel arrangement model as:

$$k_{eff}^* = (1-\varepsilon)k_s^* + \varepsilon\left[k_l^* s + (1-s)k_v^*\right] \tag{2.135}$$

The dimensionless effective thermal conductivity is defined as $k_{eff}^* = k_{eff} / \rho_l C_{pl} u_{in} L_{ref}$ and it retains the same form as given in Eq. (2.45) with dimensional values of k_s, k_l, and k_v being replaced by their respective dimensionless counterparts. It may be noted here that according to the present definition, the dimensionless thermal conductivity of the liquid phase is given as $k_l^* = 1/Pe_l$, where $Pe_l = \rho_l C_{pl} u_{in} L_{ref} / k_l$ is the corresponding Peclet number, defined on the basis of inlet velocity, the reference length and liquid properties. Consequently, the dimensionless thermal conductivities of the solid matrix and the vapor phase can also be obtained as $k_s^* = (k_s / k_l)/Pe_l$ and $k_v^* = (k_v / k_l)/Pe_l$, respectively. It may be further noted that the Reynolds number and the Peclet number, based on properties of the liquid phase, are related to each other as $Pe_l = Re_l Pr_l$, where $Pr_l = \mu_l C_{pl} / k_l$ is the liquid Prandtl number. Therefore, the Peclet number Pe_l is implicitly specified by fixing the Reynolds number Re_l and the working fluid Pr_l.

The source term $\dot{q}'''^*$, appearing in the energy conservation equation (2.134), represents the dimensionless volumetric heat generation, which is neglected for the most tested cases. It may be noted from Table 2.3 that f and γ_H, being already dimensionless quantities, remain unaltered as in Eqs. (2.41b) and (2.88) during the non-dimensionalization process. The dimensionless surface tension coefficient σ^*, appearing in the capillary diffusion coefficient D^* [see Table 2.3] requires special mention since this terms should be related to Re_l as follows: $\sigma^* = \sigma / \rho_l u_{in}^2 L_{ref} = \tilde{\sigma} / Re_l^2$, where $\tilde{\sigma} = \rho_l L_{ref} \sigma / \mu_l^2$ may be recognized as the normalized surface tension coefficient. From Eqs. (2.131) and (2.134), it is now evident that Fr and σ^* can be evaluated from Re_l once the gravitational Reynolds number Re_g and the normalized surface tension coefficient $\tilde{\sigma}$ are specified, respectively. Both these parameters are easy to specify as long as the working fluid and the reference length (L_{ref}) are chosen.

Table 2.3: Definitions of dimensionless properties for two-phase mixture

Variables	Expressions
Density	$\rho^* = \rho_l^* s + \rho_v^* (1-s)$
Mass velocity	$\rho^* \mathbf{u}^* = \rho_l^* \mathbf{u}_l^* + \rho_v^* \mathbf{u}_v^*$
Enthalpy	$\rho^* h^* = h_l^* \rho_l^* s + (1-s) \rho_v^* h_v^*$
Kinetic density	$\rho_k^* = \rho_l^* \left[1 - \beta_l^* \left(T^* - T_{sat}^*\right)\right] \lambda + \rho_v^* \left[1 - \beta_v^* \left(T^* - T_{sat}^*\right)\right] \lambda_v$
Dynamic Viscosity	$\mu^* = \dfrac{1}{Re_l} \left[\dfrac{\rho_l^* s + \rho_v^* (1-s)}{k_{rl}/\nu_l^* + k_{rv}/\nu_v^*} \right]$
Effective thermal conductivity	$k_{eff}^* = (1-\varepsilon) k_s^* + \varepsilon \left[k_l^* s + (1-s) k_v^* \right]$
Effective heat capacity ratio	$\Omega_H = \varepsilon + \rho_s^* C_{ps}^* (1-\varepsilon) \dfrac{dT^*}{dH^*}$
Advection correction coefficient	$\gamma_H = \dfrac{\left[s + \left(\rho_v^* / \rho_l^*\right)(1-s)\right]\left[h_{v,sat}^* (1+\lambda) - h_{l,sat}^* \lambda\right]}{\left(2h_{v,sat}^* - h_{l,sat}^*\right) s + (1-s)\left(\rho_v^* h_{v,sat}^* / \rho_l^*\right)}$
Effective diffusion coefficient	$\Gamma_H^* = \dfrac{D^* h_{fg}^*}{\rho_l^* h_{fg}^* + \nabla \rho^* h_{v,sat}^*} + k_{eff}^* \dfrac{dT^*}{dH^*}$
Capillary diffusion coefficient	$D^* = \dfrac{\left(\varepsilon K^*\right)^{1/2} \sigma^*}{\nu^*} \lambda (1-\lambda) \left[-\dfrac{dJ}{ds} \right]$
Surface tension coefficient	$\sigma^* = \dfrac{\sigma}{\rho_l u_{in}^2 L_{ref}} = \dfrac{\tilde{\sigma}}{Re_l^2}$
Relative mobilities	$\lambda = \lambda_l = \dfrac{k_{rl}/\nu_l^*}{k_{rl}/\nu_l^* + k_{rv}/\nu_v^*}$; $\lambda_v = \dfrac{k_{rv}/\nu_v^*}{k_{rl}/\nu_l^* + k_{rv}/\nu_v^*}$
Hindrance coefficient	$f = \dfrac{k_{rl}\, k_{rv}/\nu_v^*}{k_{rl}/\nu_l^* + k_{rv}/\nu_v^*}$
Relative permeabilities	$k_{rl} = s^n$, $k_{rv} = (1-s)^n$; $n = 1, 2, 3$
Capillary pressure function	$J = 1.417(1-s) - 2.120(1-s)^2 + 1.263(1-s)^3$
Pressure	$p^* = p_l^* + \int_0^s \lambda_v \left(\dfrac{dp_c^*}{ds} \right) ds = p_v^* - \int_0^s \lambda \left(\dfrac{dp_c^*}{ds} \right) ds$

It may be noted that if ρ_l^* and ρ_v^* are assumed to be constant, $H_{l,sat}^*$ and $H_{v,sat}^*$ could be substituted in Table 2.4. Therefore, the dimensionless temperature T^* in the single phase regions and the liquid saturation s in the two-phase zone can be deduced from the dimensionless modified volumetric enthalpy H^* as shown in Table 2.4. It is extremely important to note that relationships in Table 2.4 apply only when $h_{l,sat} = h + C_{pl}(T_{sat} - T)$ and $h_{v,sat} = h_{l,sat} + h_{fg}$ are set. Otherwise, a specific correction term would be necessary for the evaluation of dimensionless temperature, particularly for the liquid phase.

Table 2.4: Supplementary relations between modified volumetric enthalpy, temperature, and liquid saturation

H^*	T^*	s	dT^*/dH^*
$H^* \le H^*_{l,sat}$	$T^*_{sat} + \dfrac{H^* - H^*_{l,sat}}{\rho^*_l\, C^*_{pl}}$	1	$1/\rho^*_l\, C^*_{pl} = 1$
$H^*_{l,sat} < H^* \le H^*_{v,sat}$	T^*_{sat}	$-\dfrac{H^* - H^*_{v,sat}}{\rho^*_l h^*_{fg} + \Delta\rho^* h^*_{v,sat}}$	0
$H^*_{v,sat} < H^*$	$T^*_{sat} + \dfrac{H^* - H^*_{v,sat}}{\rho^*_v\, C^*_{pv}}$	0	$1/\rho^*_v\, C^*_{pv}$
$H^*_{l,sat} = -\rho^*_l\left(2h^*_{v,sat} - h^*_{l,sat}\right) = 2h^*_{v,sat} - h^*_{l,sat}$; $H^*_{v,sat} = -\rho^*_v h^*_{v,sat}$			

In Table 2.4, $\rho^*_l = 1$, $C^*_{pl} = 1$, $\Delta\rho^* = 1 - \rho^*_v$ and $h^*_{fg} = 1$ could also be substituted according to the present definitions. However, these terms are still retained for easy implementation of dimensional formulations. The individual dimensionless velocities of the liquid and the vapor phases can be recovered from the following relations:

$$\rho^*_l \mathbf{u}^*_l = \lambda\, \rho^* \mathbf{u}^* + \mathbf{j}^* \tag{2.136a}$$

$$\rho^*_v \mathbf{u}^*_v = (1 - \lambda\,)\rho^* \mathbf{u}^* - \mathbf{j}^* \tag{2.136b}$$

where $\mathbf{j}^*$ is the total diffusive mass flux in the dimensionless form, which can be expressed as:

$$\mathbf{j}^* = -\rho^*_l D^* \nabla^* s + f\, \frac{K^*\left(1 - \rho^*_v\right)}{\nu^*_v} \mathbf{b}^* \tag{2.137}$$

In Eqs. (2.134) and (2.137), ν^*_v is the dimensionless kinematic viscosity of the vapor phase and is defined as $\nu^*_v = \mu^*_v / \rho^*_v = 1/Re_v$, where $Re_v = \rho_v u_{in} L_{ref} / \mu_v$ is the Reynolds number based on properties of the vapor phase.

2.2.2. Modified Enthalpy Formulation

In this model, the dimensionless form for the mass and momentum conservation equations remain identical as the previous model in Eqs. (2.130) and (2.131), respectively, whereas the energy conservation equation (2.118) in the dimensionless form is obtained as:

$$(1-\varepsilon)\rho^*_s C^*_{ps} \frac{\partial T^*}{\partial t^*} + \varepsilon \frac{\partial\left(\rho^* h^*\right)}{\partial t^*} + \nabla^* \cdot \left(\gamma_h \rho^* \mathbf{u}^* h^*\right) = \nabla^* \cdot \left(\Gamma^*_h \nabla^* h^*\right) + \nabla^* \cdot \left(f\, \frac{K^* \Delta\rho^* h^*_{fg}}{\nu^*_v} \mathbf{b}^* \right) + \dot{q}'''^* \tag{2.138}$$

where h^* is the enthalpy in the dimensionless form, γ_h and Γ^*_h are obtained as:

$$\gamma_h = \frac{\left[\rho^*_l s + \rho^*_v (1-s)\right]\left(h^*_{v,sat} - \lambda_l h^*_{fg}\right)}{\rho^*_l h^*_{l,sat} s + \rho^*_v h^*_{v,sat} (1-s)} \tag{2.139a}$$

$$\Gamma_h^* = \frac{\rho^* D^* h_{fg}^*}{\rho_v^*\left(h_{v,sat}^* - h^*\right) + \rho_l^*\left(h^* - h_{l,sat}^*\right)} + k_{eff}^* \frac{dT^*}{dh^*} \tag{2.139b}$$

The relationship between enthalpy, temperature, liquid saturation and dT^*/dh^* in the dimensionless form for all regions is given in Table 2.5. It may be noted here that all other variables of the mixture which are described in Table 2.3 remain identical to the H-formulation. The individual dimensionless velocities of the liquid and the vapor phases can also be obtained from Eqs. (2.136a) and (2.136b).

Table 2.5: Supplementary relations between enthalpy, temperature, and liquid saturation based on the modified enthalpy formulation

h^*	T^*	s	dT^*/dh^*
$h^* \le h_{l,sat}^*$	$T^* = T_{sat}^* + \dfrac{h^* - h_{l,sat}^*}{C_{pl}^*}$	1	$1/C_{pl}^* = 1$
$h_{l,sat}^* < h^* \le h_{v,sat}^*$	T_{sat}^*	$\dfrac{\rho_v^*\left(h_{v,sat}^* - h^*\right)}{\rho_v^*\left(h_{v,sat}^* - h^*\right) + \rho_l^*\left(h^* - h_{l,sat}^*\right)}$	0
$h_{v,sat}^* < h^*$	$T^* = T_{sat}^* + \dfrac{h^* - h_{v,sat}^*}{C_{pv}^*}$	0	$1/C_{pv}^*$

It is now evident from the foregoing mathematical formulations in both models that other than properties of the working fluid, phase change process inside porous media also depends on its properties (K^*, ε and k_s^*), inlet flow conditions (T_{in}^* and Re_l), direction and magnitude of the body force per unit mass in the axial or transverse direction ($\tilde{\mathbf{b}}$ and Fr) and the heating condition at the wall $\dot{q}_w''^*$. The heating condition could be assumed to be maintained at a constant temperature T_w^* with specified Nusselt number Nu_o or considered to be subjected to a prescribed heat flux Q_w^*.

2.3. Special Treatment for Diffusion Coefficient

This section deals with the most important contribution of the present work. Although the solution procedure appears to be applicable for any phase change problem, it often fails to yield smooth prediction of properties during a complete phase change process and hence deserves a careful analysis. It will also be shortly apparent in Fig. 2.10 that the existing algorithm, without any modification (i.e., in its present form), can predict a temperature "jump" as high as $50^{\circ}\mathrm{C}$ (for $T_w = 160^{\circ}\mathrm{C}$) to $85\,^{\circ}\mathrm{C}$ (for $T_w = 200^{\circ}\mathrm{C}$) close to the two-phase to vapor interface within one control volume, when applied with constant wall temperature and specified heat transfer coefficient, as shown in Fig. 2.10(a). A similar prediction has been obtained for prescribed heat flux condition at the evaporator wall, as shown in Fig. 2.10(b). It may be mentioned that results, presented by Wang [33] and Shi and Wang [65], for the complete phase change problems also exhibited a rapid increase in the predicted temperature distribution within a very short distance in the vapor region. Such a high discontinuity in the predicted temperature should be considered "non-physical" since it cannot be otherwise explained. Therefore, special treatment is required in order to overcome this problem, which is systematically analyzed in this section and a successful remedy is proposed.

As mentioned earlier, for instance, a critical examination of the energy conservation equation (2.134), under steady-state condition, based on the H-formulation reveals that as compared to the conventional convection-diffusion equation, it contains three special factors (terms) in the form of γ_H, Γ_H and f. For the single-phase regions since $\gamma_H = 1$ and $f = 0$, correction to the convection term and the second term on the RHS of Eq. (2.134), respectively, are absent. Further, Table 2.3 shows that Γ_H has two distinct parts. For single-phase regions, since either $k_{rl} = 0$ or $k_{rv} = 0$, the first part of Γ_H does not exist, whereas for the two-phase region, since $dT/dH = 0$, the second part does not contribute. Since $\Gamma_{Hl} = k_{eff} / \rho_l C_{pl}$ and $\Gamma_{Hv} = k_{eff} / \rho_v C_{pv}$ for liquid and vapor phases, respectively, Γ_H is also not a function of the local temperature for single-phase regions. In the two-phase region, all these three factors are strong functions of the liquid saturation. Since they appear specifically in the energy conservation equation, it would be worthwhile to study their behavior as functions of H^*. Unlike μ^* and k^*, H^* depends only on the fluid properties and does not depend on flow conditions. In the present work, water has been considered as the phase change fluid and its properties are presented in Table 2.1. Further, for the porous medium, a typical permeability $K = 10^{-11}\,\mathrm{m}^2$ and a porosity $\varepsilon = 0.3$ have been assumed, whereas k_s has been taken as $20\,\mathrm{W/mK}$ in order to evaluate k_{eff}. Results are already presented in Fig. 2.2 for different exponent n. They clearly show that although γ_H and f are continuous functions of H, Γ_H is discontinuous at $H_{l,sat}$ as well as at $H_{v,sat}$. Without losing the generality, the following strategy is proposed in order to eliminate these discontinuities in Γ_H (for H-formulation in Fig. 2.2) and Γ_h (for modified h-formulation in Fig. 2.4) using dimensionless variables. The dimensional formulation can be easily retrieved using the dimensional counterparts.

It is imperative that since discontinuities in Γ_H^* (or Γ_h^* for generality) occur close to the saturated (either liquid or vapor) condition, special treatments are required only for these regions in two-phase and single-phase zones. The strategy for relaxation of Γ_h^* in the single-phase zones is schematically shown in Fig. 2.7. In the sub-cooled liquid region $(T^* \le T_{sat}^*)$, close to the saturated liquid condition, Γ_h^* is represented by two asymptotes: Γ_{hl}^* and $\Gamma_{h\phi,l}^*$. In order to express $\Gamma_{h\phi,l}^*$ a new variable ϕ_l is introduced as:

$$\phi_l = \frac{T_{sat}^* - T^*}{\Delta T_l^*} \tag{2.140}$$

where ϕ_l is the locally scaled temperature (closed to the saturation condition) for the liquid region and ΔT_l^* is the temperature over which Γ_h^* is relaxed in the liquid phase. Thus, when $\phi_l = 0$ (i.e., $T^* = T_{sat}^*$), $\Gamma_h^* = \psi_l \Gamma_{hl}^*$ and for $\phi_l = 1$ (i.e., $T^* = T_{sat}^* - \Delta T_l^*$), $\Gamma_h^* = \Gamma_{hl}^*$. The straight-line behavior in the range $0 \le \phi_l \le 1$ can be obtained as:

$$\Gamma_{hl,\phi}^{*} = \Gamma_{hl}^{*}\left[\psi_{l} + \phi_{l}\left(1 - \psi_{l}\right)\right] \tag{2.141}$$

where ψ_l is the factor by which Γ_{hl}^{*} is modified at $s = 1$ and Γ_{hl}^{*} is the value of Γ_h^{*} in the sub-cooled liquid phase for both constant as well as variable density formulations in the single phase regions. Therefore, using the suggestion of Churchill and Usagi [90] for two separate asymptotes, in this region, Γ_h^{*} can be modeled in this region as:

$$\Gamma_{h}^{*} = \left[\left(\Gamma_{hl}^{*}\right)^{-m_{\phi l}} + \left(\Gamma_{h\phi,l}^{*}\right)^{-m_{\phi l}}\right]^{-1/m_{\phi l}} \tag{2.142}$$

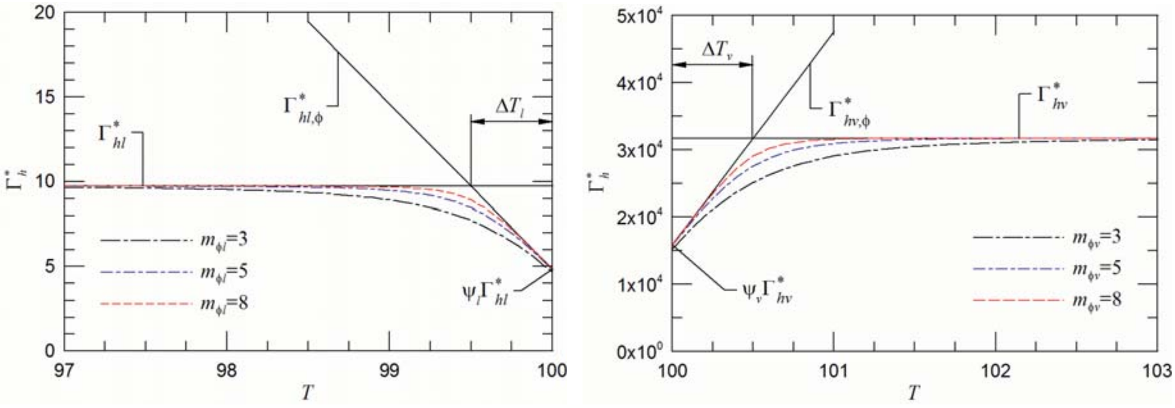

(a) (b)

Fig. 2.7: Schematic of the effective diffusion coefficient smoothing at the (a) liquid and (b) vapor regions, close to the two-phase interfaces

In Eq. (2.142), $m_{\phi l}$ is the exponent for the asymptotes that takes care for the smoothing [90]. Similarly, for the superheated vapor region ($T^{*} \geq T_{sat}^{*}$, see Fig. 2.7(b)), close to the saturated vapor condition, Γ_h^{*} is approximated by two asymptotes Γ_{hv}^{*} and $\Gamma_{h\phi,v}^{*}$ and can be represented as:

$$\Gamma_{h}^{*} = \left[\left(\Gamma_{hv}^{*}\right)^{-m_{\phi v}} + \left(\Gamma_{h\phi,v}^{*}\right)^{-m_{\phi v}}\right]^{-1/m_{\phi v}} \tag{2.143}$$

where one of the asymptotes $\Gamma_{h\phi,v}^{*}$ is calculated as:

$$\Gamma_{hv,\phi}^{*} = \Gamma_{hv}^{*}\left[\psi_{v} + \phi_{v}\left(1 - \psi_{v}\right)\right] \tag{2.144}$$

ψ_v is similar to ψ_l for the liquid phase and the new variables ϕ_v (locally scaled temperature for the vapor phase) is defined as:

$$\phi_{v} = \frac{T^{*} - T_{sat}^{*}}{\Delta T_{v}^{*}} \tag{2.145}$$

where $\phi_v = 0$ for $T^{*} = T_{sat}^{*}$, whereas $\phi_v = 1$ is retrieved for $T^{*} = T_{sat}^{*} + \Delta T_{v}^{*}$. In Eqs. (2.140) – (2.145), ΔT^{*}, ψ, and m_ϕ for liquid and vapor phases are adjustable parameters. For extremely large values of m_ϕ, smoothed Γ_h^* are represented by the selected asymptotes. Quite evidently, with $\Delta T^* \to 0$, $\psi \to 0$ and $m_\phi \to \infty$, the effect of smoothing is diminished. It is important to note that although the choice of adjustable parameters may appear arbitrary, they should be judiciously chosen such that the departure from reality due to the proposed relaxation of Γ_h^* is minimized and its effect remains undetectable.

The smoothing strategy in the two-phase region ($T^* = T_{sat}^*$) is schematically shown in Fig. 2.8. Let s_l and s_v be the cut-off liquid saturations where the true values of Γ_h^* are obtained as Γ_{h,s_l}^* and Γ_{h,s_v}^* close to saturated liquid and vapor phases, respectively. One of the asymptotes for smoothing is given by Γ_{hs}^*, which, could be obtained according to Table 2.3. In the liquid saturation ranges $s_l \le s \le 1$ (close to saturated liquid condition) and $0 \le s \le s_v$ (close to saturated vapor condition), Γ_h^* is also represented by other asymptotes $\Gamma_{hl,s}^*$ and $\Gamma_{hv,s}^*$, respectively [see Fig. 2.8]. Since in these regions the value of Γ_h^* changes by several orders of magnitude, these two asymptotes are obtained by linear interpolation in a semi-log plane as follows:

$$\log\left(\Gamma_{hl,s}^*\right) = \log\left(\psi_l \Gamma_{hl}^*\right) + \frac{1-s}{1-s_l}\left[\log\left(\Gamma_{h,s_l}^*\right) - \log\left(\psi_l \Gamma_{hl}^*\right)\right] \tag{2.146a}$$

$$\log\left(\Gamma_{hv,s}^*\right) = \log\left(\psi_v \Gamma_{hv}^*\right) + \frac{s}{s_v}\left[\log\left(\Gamma_{h,s_v}^*\right) - \log\left(\psi_v \Gamma_{hv}^*\right)\right] \tag{2.146b}$$

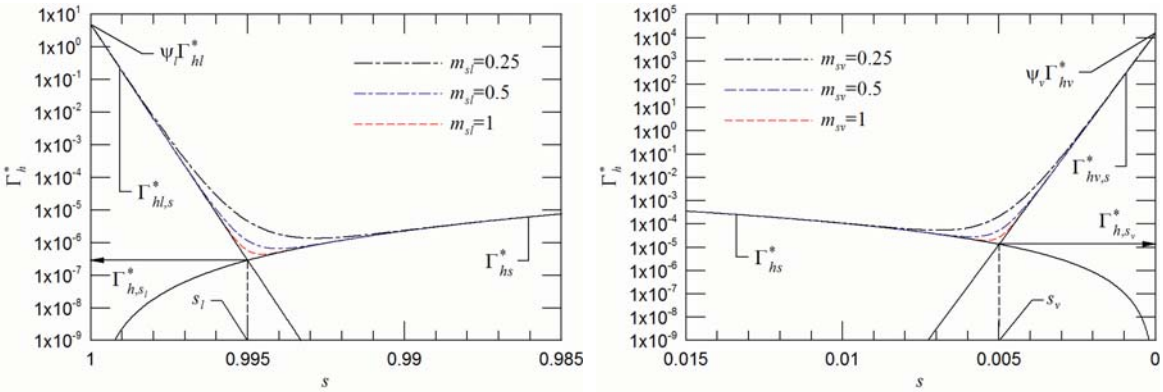

(a) (b)

Fig. 2.8: Schematic of the effective diffusion coefficient smoothing in the two-phase region, close to the (a) liquid and (b) vapor interfaces

It can be easily verified that Eq. (2.146) satisfies the essential conditions i) at $s=1$, $\Gamma_{hl,s}^* = \psi_l \Gamma_{hl}^*$; ii) at $s = s_l$, $\Gamma_{hl,s}^* = \Gamma_{h,s_l}^*$ and i) at $s=0$, $\Gamma_{hv,s}^* = \psi_v \Gamma_{hv}^*$; iii) at $s = s_v$, $\Gamma_{hv,s}^* = \Gamma_{h,s_v}^*$, respectively. Finally, following suggestions of Churchill and Usagi [90] the smoothed representation of Γ_h^* is obtained as:

$$\Gamma_h^* = \left[\left(\Gamma_{hl,s}^*\right)^{m_{sl}} + \left(\Gamma_{hs}^*\right)^{m_{sl}}\right]^{1/m_{sl}} \tag{2.147a}$$

$$\Gamma_h^* = \left[\left(\Gamma_{hv,s}^* \right)^{m_{sv}} + \left(\Gamma_{hs}^* \right)^{m_{sv}} \right]^{1/m_{sv}} \tag{2.147b}$$

where m_{sl} and m_{sv} are similar exponents for the asymptotes and Γ_{hs}^* is the diffusion coefficient that one obtains for a given value of s according to the expression in Table 2.3. Equations (2.147a) and (2.147b) represent smoothed Γ_h^* close to the saturated liquid and vapor phases, respectively. In Eqs. (2.146) and (2.147), m_{sl}, m_{sv}, s_l and s_v are the adjustable parameters that govern the smoothing of Γ_h^* in the two-phase region. Figure 2.8 shows that for large values of the m_{sl} and m_{sv}, Γ_h^* is represented by the chosen asymptotes, although their values are significantly less than $m_{\phi l}$ and $m_{\phi v}$. It is also evident that as $s_l \rightarrow 1$, $s_v \rightarrow 0$ and $m_s \rightarrow \infty$, the effect of smoothing is diminished.

In order to demonstrate the consequence of smoothing of effective diffusion coefficient for both H- and h-formulations, the following parameters have been used: $Re_l = 1.25$ (as operating condition, where $R = 25\text{mm}$ and $u_{in} = 1.45\times10^{-5}$ m/s have been assumed), $\varepsilon = 0.3$, $K^* = 10^{-8}$, $k_s^* = 8.25$ (as properties of the medium), $m_{\phi l} = m_{\phi v} \rightarrow \infty$, $m_{sl} = m_{sv} = 0.25$, $\psi_l = \psi_v = 2.5\times10^{-2}$, $\Delta T_l = \Delta T_v = 0.5^{\text{o}}\text{C}$, $s_l = 0.999$ and $s_v = 0.001$ (as the adjustable smoothing parameters). With these parameters, the consequence of smoothing is demonstrated in Fig. 2.9 for both H- and h-formulations. The figures clearly show that for both models, the effective diffusion coefficients, other than being strong functions of the dependent variables H^* and h^*, are also discontinuous at saturated liquid and vapor conditions. It can be observed from the figure that the application of smoothing algorithm, suggested in the present work restricts both Γ_H^* and Γ_h^* to finite values by preventing them from going to zero, at $s = 0$ and $s = 1$ in the two-phase region. It is also evident that the drastic change in both Γ_H^* and Γ_h^* are more prominent close to the saturated vapor condition, which perhaps explains the reason for not using the H-formulation for the simulation of phase change process inside porous media from the two-phase mixture to the superheated vapor state.

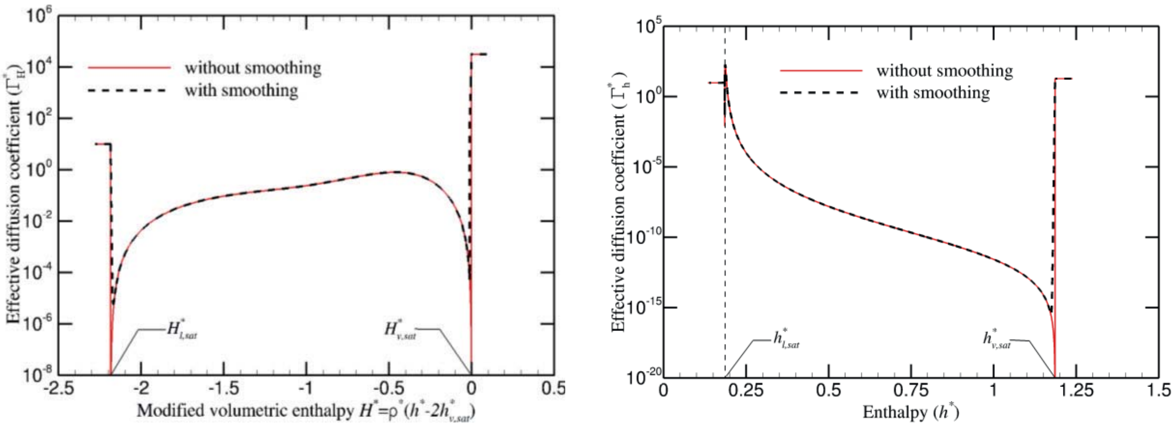

(a) (b)

Fig. 2.9: Variations in the effective diffusion coefficients with and without smoothing for $Re_l = 1.25$, $\varepsilon = 0.3$, $K^* = 10^{-8}$ and $k_s^* = 8.25$: (a) Γ_H^* as a function of H^* and (b) Γ_h^* as a function of h^*

In order to demonstrate the necessity of the proposed smoothing algorithm based on the H- and h-formulations, the complete phase change process of liquid water inside porous evaporator of known properties has been considered by employing two different heating conditions at the evaporator wall. Constant wall temperature and prescribed heat flux conditions at the evaporator wall are referred here. For the purpose of demonstration and owing to the simplicity, the cross-sectional area of the duct has been assumed to be constant in the axial (flow) direction and the flow has been considered to be one-dimensional problem. Further, a circular pipe of radius $R = 25\text{mm}$ ($R^* = 1$) and with an overall length $L = 500\text{mm}$ ($L^* = 20$) has been considered for the analysis. It has unheated inlet and exit sections lengths of $l_i^* = 0.1L^*$ and $l_e^* = 0.1L^*$, respectively. Sub-cooled liquid water at $T_{in} = 20\,^{\circ}\text{C}$ has been assumed to enter the evaporator which is subsequently heated as it flows through the porous medium. The wall of the evaporator in the heated section either has been assumed to be maintained at a constant temperature T_w (varying from $T_w = 140\,^{\circ}\text{C}$ to $T_w = 200\,^{\circ}\text{C}$), which is higher than the saturation temperature T_{sat}, or has been considered to be subjected to a prescribed uniform heat flux $\dot{q}''_w$ (varying from $2\,\text{kW/m}^2$ to $3\,\text{kW/m}^2$). In the former case, however, heat is transferred from the evaporator wall to the combined medium with a specified heat transfer coefficient. Further, a low inlet velocity $u_{in} = 2.5\times10^{-5}$ m/s has been considered corresponding to an inlet Reynolds number $Re_l = 2$. The porosity, Darcy number and thermal conductivity of the medium have been considered to be $\varepsilon = 0.3$, $K^* = 10^{-8}$ and $k_s^* = 8.25$, respectively. Other than these, $Nu_o = 4$ has been assumed. The gravitational Reynolds number Re_g and the normalized surface tension coefficient $\tilde{\sigma}$ have been taken as 4.25×10^4 and 1.8×10^7, respectively, in order to specify Fr and σ^*. Both Re_g and $\tilde{\sigma}$ have been kept fixed for the present analysis since they depend on the properties of liquid water and the pipe radius.

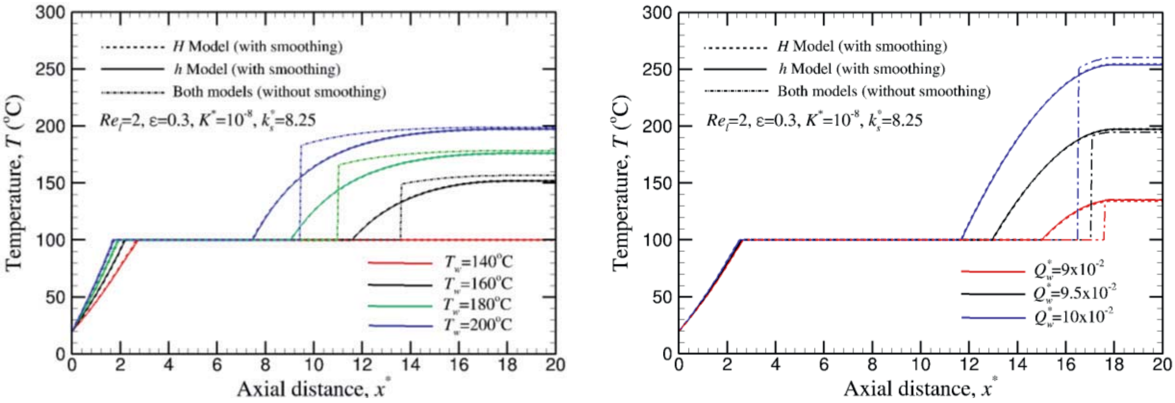

(a) (b)

Fig. 2.10: Effect of different heating conditions on the axial temperature variations for both H-and h-formulations (a) different imposed wall temperature and (b) different heat flux

Results of the effects "with" and "without" smoothing based on the H- and h-formulations for different imposed wall temperature and heat flux in the form of axial temperature distribution are presented in Fig. 2.10. It is important to note that while solutions "without" the application of a smoothing algorithm always lead to "jump" in the predicted temperature distribution, particularly close to the saturated vapor condition, no such non-physical behavior is detected for those obtained “with” applying the smoothing algorithm. It can be easily observed from the figures that the proposed smoothing algorithm proves to be essential for successfully avoiding the occurrence of “jumps” in the predicted temperature distributions. It may be noted here that the aforementioned discontinuity in the modeled Ω_H occurring when using LTE model [see Fig. 2.2(d)] is eliminated by using LTNE model [see Eq. (2.150) along with LTNE model as compared to Ω_H along with LTE model in Table 2.3]. Consequently, the smoothing algorithm is not required for Ω_H .

2.4. Local Thermal Non-Equilibrium Model

In practical situations involving phase change inside porous media, the thermal conductivity of the solid matrix of porous media is expected to be substantially higher than that of the working fluid. Therefore, heat that is supplied at the evaporator surface is transferred to the fluid medium primarily through the solid struts. Particularly in the phase change region, where the fluid temperature remains constant owing to the idealized thermodynamic constraint, heat conduction through the solid medium possibly plays the most important role in the energy transfer process from the heated wall. Temperatures of the solid and the fluid media in this region would differ from each other, although the difference in temperatures may small but substantial, since the volumetric heat exchange coefficient between them could be extremely high owing to the small characteristic pore diameter. Most importantly, for multi-dimensional problems as will be apparent in chapter 4, the complete phase change process cannot be realistically simulated using the conventional LTE model, owing primarily to the extremely lower values of effective diffusion coefficient in the two-phase region, particularly close to the saturated liquid or vapor condition, which acts as an extremely high resistance to heat transfer. In this situation, the LTNE model would be more appropriate as compared to the conventional LTE model, and hence it would definitely be worthwhile to compare the predictions obtained with both LTE and LTNE assumptions for a complete phase change process inside porous evaporator.

In order to consider the internal heat exchange between the fluid and the solid phases within the porous medium, the LTNE model considers two separate energy conservation equations for each phase, whereas the mass and momentum conservation equations remain identical. Convective heat exchange term is added in both the two equations for this purpose. For the present model, all applicable equations have been made dimensionless depending upon the dimensionless parameters, provided in Table 2.2. Further, the dimensionless mixtures properties at two-phase region are presented in Table 2.3. Consequently, the conservation of energy for both the fluid and the solid phases are given in dimensionless form as follows:

$$\Omega_H \frac{\partial H^*}{\partial t^*} + \nabla^* \cdot \left(\gamma_H \mathbf{u}^* H^*\right) = \nabla^* \cdot \left(\Gamma_H^* \nabla^* H^*\right) + \nabla^* \cdot \left(f \frac{K^* \Delta\rho^* h_{fg}^*}{\nu_v^*} \mathbf{b}^* \right) + \dot{q}_{sf}'''^* \tag{2.148}$$

$$\rho_s C_{ps} (1-\varepsilon) \frac{\partial T_s^*}{\partial t^*} = \nabla^* \cdot \left(k_{eff,s}^* \nabla^* T_s^*\right) - \dot{q}_{sf}'''^* \tag{2.149}$$

In Eq. (2.148), Ω_H is still recognized as the effective heat capacity ratio for the modified volumetric enthalpy transport, but according to the present modified formulation (i.e., LTNE model), and hence it is redefined as:

$$\Omega_H = \varepsilon \tag{2.150}$$

For the LTNE model, Γ_H^* in Eq. (2.148) contains the dimensionless effective thermal conductivity for the fluid phase $k_{eff,f}^*$ [see Eq. (2.152)]. On the other hand, $k_{eff,s}^*$ in Eq. (2.149) represents the dimensionless effective thermal conductivity of the solid phase. In the present investigation, these two quantities have been obtained according to the parallel arrangement model, where the thermal conductivities for the fluid and the solid phases can be easily decoupled from each other as follows [57, 67, 69, 75]:

$$k_{eff,f}^* = \varepsilon\left[k_l^*\, s + (1-s)k_v^*\right] \tag{2.151a}$$

$$k_{eff,s}^* = (1-\varepsilon)k_s^* \tag{2.151b}$$

where k_l^*, k_v^* and k_s^* are defined in section 2.2 as well as in Table 2.2. The effective diffusion coefficient in Eq. (2.148) is given as:

$$\Gamma_H^* = \frac{D^*\, h_{fg}^*}{\rho_l^* h_{fg}^* + \nabla\rho^*\, h_{v,sat}^*} + k_{eff,f}^* \frac{dT^*}{dH^*} \tag{2.152}$$

Quite evidently, for LTNE model, it is essential to account for the internal heat exchange between the solid and the fluid phases. Therefore, in order to incorporate the effect, $\dot{q}_{sf}^{'''*}$, appearing in Eqs. (2.148) and (2.149), has been modeled as [67]:

$$\dot{q}_{sf}^{'''*} = \left[s h_{sl}^* + (1-s)h_{sv}^*\right]a_s^*\left(T_s^* - T_f^*\right) \tag{2.153}$$

where $a_s^* = 6(1-\varepsilon)/d_p^*$ and $d_p^* = d_p/L_{ref}$ are the dimensionless specific surface area and the pore diameter of the porous medium, respectively. The convective heat transfer coefficients $h_{s\alpha}^*$ in the pores, appearing in the same equation, have been modeled as [91, 92]:

$$h_{s\alpha}^* = \left(k_\alpha^*/d_p^*\right)\left(2.0 + 1.1 Pr_\alpha^{1/3}\, Re_{p\alpha}^{0.6}\right) \tag{2.154}$$

where $\alpha = l$ stands for the liquid phase, whereas $\alpha = v$ represents the vapor phase. Although the evaluation of properties for different phases (e.g., k_α^*, $Pr_\alpha^{1/3}$, etc.) would be fairly straightforward, the Reynolds number $Re_{p\alpha}$, based on the pore diameter, the phase velocities and properties of the local phase is defined as:

$$Re_{p\alpha} = \left|\mathbf{u}_\alpha^*\right| d_p^*/\nu_\alpha^* \tag{2.155}$$

In Eq. (2.155), $\left|\mathbf{u}_\alpha^*\right|$ is the magnitude of the individual dimensionless velocities. The components of $\mathbf{u}_\alpha^*$ for the liquid and the vapor phases can be recovered from the mass velocity $\rho^*\mathbf{u}^*$

appearing in Eqs. (2.136a) and (2.136b). In order to proceed further, let us recognize the boundary condition at the heated wall when the constant heat flux along with LTNE model is applied. Similarly, integrating the energy equations for both fluid and solid phases over the solid fluid boundary by taking a control volume according to Eq. (2.113), the total heat flux $\dot{q}_w''^*$ at the wall has been assumed to be partitioned in two parts as follows:

$$\dot{q}_w''^* = \dot{q}_f''^* + \dot{q}_s''^* \tag{2.156}$$

where, $\dot{q}_f''^*$ and $\dot{q}_s''^*$ are defined as follows:

$$\dot{q}_f''^* = -\Gamma_H^* \left.\frac{\partial H^*}{\partial n^*}\right|_f - f\,\frac{K^* \Delta\rho^* h_{fg}^*}{\nu_v^*} b_n^* \tag{2.157a}$$

$$\dot{q}_s''^* = -k_{eff,s}^* \left.\frac{\partial T_s^*}{\partial n^*}\right|_{wall} \tag{2.157b}$$

In Eq. (2.156), $\dot{q}_f''^*$ and $\dot{q}_s''^*$ are the parts of the heat flux $\dot{q}_w''^*$ that are added separately to the fluid and the solid phases, respectively. The ratio of these heat fluxes may be modeled according to different idealization [92]. In the present work, five different models have been employed for this purpose and the ratio of $\dot{q}_f''^*$ and $\dot{q}_s''^*$ have been obtained as follows: Model-1: the entire amount of heat is added to the solid phase; Model-2: according to the ratio of effective thermal conductivities of the respective phase; Model-3: according to the ratio of thermal conductivities of the phases; Model-4: according to the ratio of volume fractions and Model-5: according to the porosity. These models may be summarized as follows:

$$1:\ \frac{\dot{q}_f''^*}{\dot{q}_s''^*} = 0 \tag{2.158a}$$

$$2:\ \frac{\dot{q}_f''^*}{\dot{q}_s''^*} = \frac{\varepsilon k_f^*}{(1-\varepsilon) k_s^*} \tag{2.158b}$$

$$3:\ \frac{\dot{q}_f''^*}{\dot{q}_s''^*} = \frac{k_f^*}{k_s^*} \tag{2.158c}$$

$$4:\ \frac{\dot{q}_f''^*}{\dot{q}_s''^*} = \frac{\varepsilon}{(1-\varepsilon)} \tag{2.158d}$$

$$5:\ \frac{\dot{q}_f''^*}{\dot{q}_s''^*} = \varepsilon \tag{2.158e}$$

It is also evident that the evolution of properties and mixture variables for this model, listed in Tables 2.2 and 2.3, require the liquid saturation s (in the two-phase region), or the local temperature T_f^* of the fluid phase (in the single phase region), that can also be calculated from the modified volumetric enthalpy H^* as shown in Table 2.4.

Similarly, the consequence of smoothing algorithm is also adopted for the LTNE model using identical smoothing parameters as used in Fig. 2.9. With these parameters, the consequence of smoothing is demonstrated in Fig. 2.11(b) for the LTNE model. On the other hand, Fig. 2.11(a) clearly shows that the effective diffusion coefficient, other than being a strong function of H^* for both models, is also discontinuous at saturated liquid and vapor conditions. Furthermore, the discontinuity in the effective diffusion coefficient for LTE model is also more severe than for LTNE model, which can be explained by the increase in effective thermal conductivity of the single phase regions for LTE model according to the definitions of k^*_{eff} and $k^*_{eff,f}$ [see Eqs. (2.135) and (2.151a) for clarification]. Nevertheless, in the two-phase region, Γ^*_H assumes identical values irrespective of the model, which is in accordance with its definition, provided Table 2.3. In addition, the application of smoothing algorithm, suggested in the present work restricts Γ^*_H to finite values, i.e., prevents it from going to zero at $s=0$ and $s=1$ in the two-phase region. It is also evident that the drastic change in Γ^*_H is more prominent close to the saturated vapor condition.

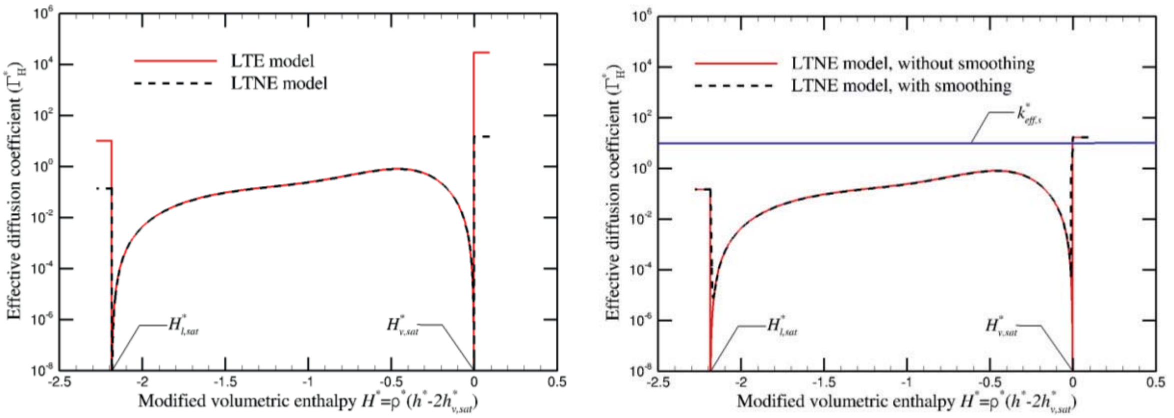

(a) (b)

Fig. 2.11: Comparison of effective diffusion coefficient (a) using LTE and LTNE models and (b) obtained with and without applying smoothing algorithm for LTNE model. ($Re_l = 1.25$, $\varepsilon = 0.3$, $K^* = 10^{-8}$ and $k^*_s = 8.25$)

2.5. Anisotropic Properties of Porous Medium Model

In many practical situations, it is reasonable to expect the porous media to be anisotropic with respect to their mechanical and thermal properties. For some applications, anisotropy may be deliberately introduced in order to achieve specific objectives [93 – 99]. For instance, while selecting the porous medium for the evaporator, a higher thermal conductivity in the radial direction is desirable as compared to that in the axial direction since this enhances the conduction heat transfer from the periphery to the core of the duct. A structure, made of axially compressed wire mesh, can possibly serve the purpose. As mentioned in chapter 1, simulation of complete phase change problems within such porous media would, however, require the extension of the currently available formulation for anisotropic porous media. A detailed analysis on liquid-vapor phase change process inside anisotropic porous media is yet to appear in the literature. However, most of the porous media are anisotropic due to the preferential orientation for enhancing heat transfer. An example is the porous evaporator application, which can be investigated as an anisotropic porous medium.

To the best of the author's knowledge, there is no numerical simulation study available in the literature, where fluid flow and heat transfer associated with phase change processes based on the H-formulation have been analyzed inside porous media considering the effect of anisotropy on the porous media properties. The effects of non-homogeneity and anisotropy in porous media only for a single phase flow based on the homogenization approach have been investigated [93 – 99]. It can be seen that anisotropy for both permeability and thermal conductivity have not been considered simultaneously, and only a few studies considered anisotropy for both permeability and thermal conductivity of the solid struts of the porous matrix which have been also limited to a specific ratio. Therefore, this section provides the required extensions along with the LTNE assumptions to include the effect of anisotropy on the porous media properties, which has been proposed earlier. Although the present procedure is an extension and supplement to the previous work, it is not straightforward. Here, the anisotropic terms which contain both velocity components and the conservation energy equation need to be handled. For the present investigation, the porous medium is considered anisotropic in both mechanically (permeability) and thermally (thermal conductivity of the struts). Thus, a generalized procedure for the governing equations in order to solve the complete liquid-vapor phase change process inside anisotropic porous medium along with LTNE model has become necessary. The longitudinal and transversal components of the permeability and thermal conductivity of the solid struts along the principle coordinate axes K_x, K_y, k_{sx}, and k_{sy} are considered, respectively. By adopting the H-formulation along with LTNE model, the mass conservation equation remains identical as in Eq. (2.130), whereas the momentum and energy conservation equations in the dimensionless form are modified and obtained as follows:

For expressing the Darcy's law along with the body-force in Eq. (2.131) for the flow in an anisotropic porous medium, the momentum conservation equation can be written as:

$$\mathbf{u}^* = -\frac{\mathbf{K}^*}{\mu^*}\left[\nabla p^* - \rho_k^* \mathbf{b}^*\right] \tag{2.159}$$

where $\mathbf{K}^*$ is the dimensionless permeability tensor and is defined as:

$$\mathbf{K}^* = \begin{bmatrix} K_{xx}^* & 0 \\ 0 & K_{yy}^* \end{bmatrix} \tag{2.160}$$

where K_{xx}^* and K_{yy}^* are defined as follows:

$$K_{xx}^* = K^* \tag{2.161a}$$

$$K_{yy}^* = K^* K_R \tag{2.161b}$$

As known, $K^* = K_x / L_{ref}^2$ represents the dimensionless permeability or Darcy number based on the axial direction, whereas $K_R = K_y / K_x$ represents the permeability ratio. In addition, all other variables are provided in Eq. (2.131) as well as Tables 2.2 and 2.3. On the other hand, the energy conservation equations for both fluid and solid phases are given as:

$$\Omega_H \frac{\partial H^*}{\partial t^*} + \nabla \cdot \left(\gamma_H \mathbf{u}^* H^*\right) = \nabla \cdot \left(\mathbf{\Gamma}^*_H \, \nabla H^*\right) + \nabla \cdot \left(f \, \frac{\mathbf{K}^* \Delta\rho^* h^*_{fg}}{\nu^*_v} \mathbf{b}^* \right) + \dot{q}'''^*_{sf} \tag{2.162}$$

$$\rho_s C_{ps} (1-\varepsilon) \frac{\partial T^*_s}{\partial t} = \nabla \cdot \left(\mathbf{k}^*_{\mathbf{eff,s}} \nabla T^*_s\right) - \dot{q}'''^*_{sf} \tag{2.163}$$

where $\mathbf{\Gamma}^*_H$ is the dimensionless effective diffusion coefficient tensor and is defined as:

$$\mathbf{\Gamma}^*_H = \begin{bmatrix} \Gamma^*_{Hx} & 0 \\ 0 & \Gamma^*_{Hy} \end{bmatrix} \tag{2.164}$$

where Γ^*_{Hx} and Γ^*_{Hy} are defined as follows:

$$\Gamma^*_{Hx} = \frac{D^*_x h^*_{fg}}{\rho^*_l h^*_{fg} + \nabla\rho^* \, h^*_{v,sat}} + k^*_{eff,f} \frac{dT^*}{dH^*} \tag{2.165a}$$

$$\Gamma^*_{Hy} = \frac{D^*_y h^*_{fg}}{\rho^*_l h^*_{fg} + \nabla\rho^* \, h^*_{v,sat}} + k^*_{eff,f} \frac{dT^*}{dH^*} \tag{2.165b}$$

In Eq. (2.165), $k^*_{eff,f}$ is the dimensionless effective thermal conductivity for the fluid phase, defined in Eq. (2.151a). The dimensionless capillary diffusion D^*_x and D^*_y in the axial and transverse directions are redefined, respectively, as follows:

$$D^*_x = \frac{\left(\varepsilon K^*\right)^{1/2} \sigma^*}{\nu^*} \lambda \, (1-\lambda) \left[-\frac{dJ}{ds}\right] \tag{2.166a}$$

$$D^*_y = \frac{\left(\varepsilon K^* K_R\right)^{1/2} \sigma^*}{\nu^*} \lambda \, (1-\lambda) \left[-\frac{dJ}{ds}\right] \tag{2.166b}$$

The local temperature T^*_f of the fluid phase in the single phase regions and the liquid saturation s in the two-phase region in this model can also be calculated from Table 2.4. Further, all other definitions for the mixture variables and properties remain unaltered according to Tables 2.2 and 2.3. In Eq. (2.163), $\mathbf{k}^*_{\mathbf{eff,s}}$ is the effective thermal conductivity for the solid phase tensor in non-dimensional form and is defined as:

$$\mathbf{k}^*_{\mathbf{eff,s}} = \begin{bmatrix} k^*_{eff,sx} & 0 \\ 0 & k^*_{eff,sy} \end{bmatrix} \tag{2.167}$$

where $k^*_{eff,sx}$ and $k^*_{eff,sy}$ are defined as follows:

$$k^*_{eff,sx} = (1-\varepsilon) k^*_{sx} \tag{2.168a}$$

$$k^*_{eff,sy} = k^*_{eff,sx} \, k_R \tag{2.168b}$$

where $k^*_{eff,sx}$ and $k^*_{eff,sy}$ are represent the dimensionless effective thermal conductivity of the solid phase in the axial and transverse directions, respectively. In Eq. (2.168), $k^*_{eff,sx}$ is defined based on the solid thermal conductivity in the axial direction, while $k_R = k^*_{sy} / k^*_{sx}$ represents the solid thermal conductivity ratio. The definition of the internal heat exchange between the solid phase and the fluid phase remains identical as in Eq. (2.153). The total diffusive mass flux in the dimensionless form that has been used in order to obtain the individual dimensionless velocities for both the liquid and the vapor phases in Eq. (2.136) are redefined in the axial and transverse directions, respectively, as follows:

$$\mathrm{j}^*_x = -\rho^*_l D^*_x \nabla^* s + f \, \frac{K^* \left(1 - \rho^*_v\right)}{\nu^*_v} b^*_x \tag{2.169a}$$

$$\mathrm{j}^*_y = -\rho^*_l D^*_y \nabla^* s + f \, \frac{K^* K_R \left(1 - \rho^*_v\right)}{\nu^*_v} b^*_y \tag{2.169b}$$

2.6. Conclusions

This chapter provided an overview on the original enthalpy formulation of TPMM proposed by Wang and Beckermann [29], which finally leads up to closed mathematical two-phase flow model. The mathematical equations for a model of complete phase change process inside porous media have been formulated based on the modified volumetric enthalpy formulation (H-formulation) of Wang [33]. After critically analyzing the drawbacks of the existing h-formulation based on the TPMM of Wang and Beckermann, a modified formulation (modified h-formulation) has been developed that can easily accommodate substantial density variations in the single phase regions as compared to the H-formulation of Wang. Since the proposed formulation (modified h-formulation) does not require the definition of any artificial variable and in view of the identified advantages, the method is strongly recommended for the further use. All the variants of TPMM have been considered based on the assumption of isotropic porous media along with the LTE condition. A critical examination of the energy conservation equation for both modified h- and H-formulations show that the major problem in modeling the complete phase change process inside porous medium occurs due to the discontinuities in the effective diffusion coefficient and effective heat capacity ratio at the boundaries of two-phase regions. In order to eliminate these discontinuities, an efficient smoothing algorithm for the effective diffusion coefficient has been proposed to avoid the non-physical “jump” in the predicted temperature distribution at the interfaces during the numerical simulation of complete phase change process. Preliminary results indicated that the smoothing algorithm successful eliminates the non-physical jump in the predicted temperature distribution without modifying the overall energy and momentum balance. The H-formulation of Wang has been also extended in order to accommodate the LTNE effect for the simulation of complete phase change process for both isotropic and anisotropic porous media. In the LTNE model, the sharp discontinuity in the effective heat capacity ratio has been eliminated, although the H-formulation for both isotropic and anisotropic porous media still requires smoothing of effective diffusion coefficient.

CHAPTER 3. NUMERICAL METHOD

Numerical simulations are expected to provide useful information about the modeled process and can therefore support the engineering design. However, difficulties encountered in numerical simulation of fluid flow with phase change process inside porous media are mainly due to the strongly nonlinear and coupled nature of the governing equations. In the present work, the governing conservation equations have been discretized on a uniform grid and subsequently solved by the Finite Volume Method (FVM). The non-linearity in the energy conservation equation has been addressed in a semi-implicit (for steady-state condition) or fully-implicit (for transient condition) manner used in conjunction with the FVM based on the SIMPLE algorithm. Details of FVM and SIMPLE algorithm can be found in many publications such as Patankar [54]. In FVM, the governing equations have been integrated over each control volume (smaller and non-overlapping sub-domains) in the flow domain. For the present work, FORTRAN was used to develop the CFD code. Therefore, this chapter presents the discretized schemes that used for solving the governing equations based on the TPMM of Wang [33] and modified enthalpy formulation. Furthermore, the grid layouts are presented for the staggered and non-staggered grid arrangments. Finally, the code verification has been included in the present chapter.

3.1. Discretization Schemes

In the present work, the first order Upwind Differencing Scheme (UDS) and the second order Central Differencing Scheme (CDS) have been employed in order to discretize the convective and the diffusive terms for the conservation of energy, respectively. Furthermore, the transient term appearing in Eqs. (2.130), (2.134) and (2.148) has been expressed employing a combination of first (two time level) and second order (three-time level) accurate scheme from Taylor series expansion. The effective diffusivities either for modified volumetric enthalpy Γ_H^* and enthalpy Γ_h^* of the combined medium (in Eq. (2.134) and (2.138), respectively, for LTE model) or Γ_H^* of the fluid phase (in Eq. (2.148) for isotropic porous medium along with LTNE model and in Eq. (2.162) for anisotropic porous medium along with LTNE model) and the effective thermal conductivities $k_{eff,s}^*$ of the solid phase (in Eq. (2.149) for LTNE model and in Eq. (2.163) for anisotropic porous medium along with LTNE model) at the cell faces have been obtained using harmonic mean approximation which ensures the balance of diffusive energy fluxes [54]. Moreover, the dynamic viscosities μ^* appearing in Eqs. (2.131) and (2.159) at the cell faces have been also obtained by harmonic mean approximation. On the other hand, several other mixture properties, e.g., the advection correction coefficient for both γ_H and γ_h, the hindrance coefficient f and the kinetic density ρ_k^* at the cell faces have been obtained using linear interpolation from the adjacent nodal values. Since the mixture properties in the two phase region are strong functions of the liquid saturation, the liquid saturation s, dT^*/dH^* (for H-formulation) and dT^*/dh^* (for h-formulation) have been iteratively updated from the previous solution of either H^* or h^*, according to the relations provided in Tables 2.4 and 2.5.

3.2. Grid Layouts

Generally, two kinds of grid arrangements have been used in order to solve the conservation of momentum either in Eq. (2.131) or Eq. (2.159) along with the conservation of mass in Eq. (2.130): staggered and non-staggered variable arrangements. Figures 3.1 and 3.2 schematically present the control volumes used for staggered grid layout, whereas Fig. 3.3 presents the control volumes used for non-staggered grid layout as explained later. For the non-staggered grid layout, all scalar variables and vector components have been stored at the same location and only one set of control volume has been employed. For staggered grid layout, on the other hand, all velocity vector components and scalar quantities have been stored at different locations, which mean it is necessary to define three types control volumes for two-dimensional problems [see Fig. 3.2]. In addition, the discretized equations for all nodes along with the boundary conditions exhibit a tri-diagonal matrix structure and hence they have been solved by the Thomas algorithm, which is actually a direct method for the solution of one-dimensional problems, but it can be applied iteratively to solve multidimensional problems and is widely used in commercial Computational Fluid Dynamics (CFD) programs [54].

3.2.1. Staggered Grid Layout

Staggered grid layout is popular because of its ability to avoid the oscillations in the pressure field that may occur when solving the governing equations with non-staggered grid layout [54]. According to Patankar, staggered grids automatically couple the grid scale pressure to the remainder of the solution, and thus they avoid the risk of obtaining an unrealistic unphysical pressure field when a pressure-velocity coupling like SIMPLE is used. In the present work, three numerical settings have been considered. First, one-dimensional pipe flow with constant cross-sectional area in the axial direction has been solved, considering both LTE and LTNE models [see Fig. 3.1(a)]. Second, one-dimensional pipe flow with increasing cross-sectional area in the axial direction has been treated, using LTE model [see Fig. 3.1(b)]. Finally, a two-dimensional problem for both channel and pipe flow models has been concerned, employing both LTE and LTNE models [see Fig. 3.2]. Figures 3.1 and 3.2 show the exemplary layout of the standard staggered grid in one- and two-dimensional coordinates, where the velocities have been stored offset from the pressure storage locations in their respective direction.

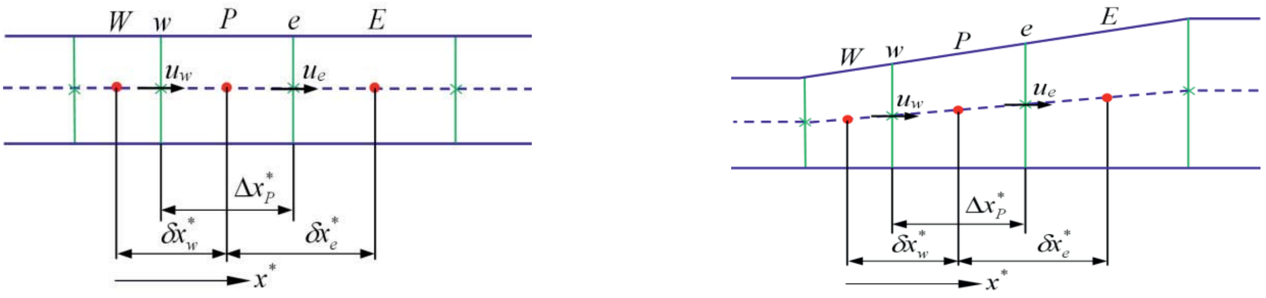

(a) (b)

Fig. 3.1: Typical control volumes used for discretization of (a) constant and (b) variable cross-sectional areas using staggered grid layout

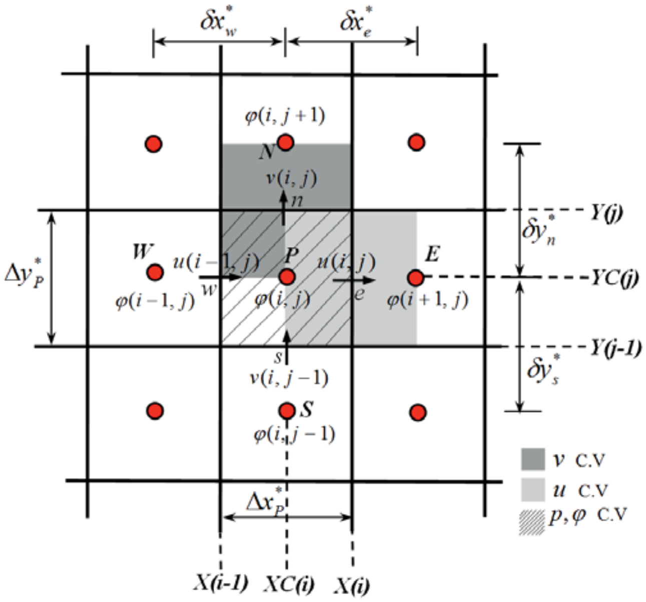

Fig. 3.2: Control volume and grid disposition for two-dimensional coordinates using staggered grid layout

3.2.2. Non-Staggered Grid Layout

The literature survey reveals that the simulations of phase change problems inside porous media available from the literature were performed only on orthogonal coordinates. However, it could be extremely useful to allow for a varying cross-sectional area of the duct in order to accommodate higher volume flow rates of the vapor phase. The respective simulations definitely require an extension of the present numerical method to non-orthogonal coordinates using non-staggered variable arrangement. In this regard, the present subsection provides a suitable discretization of the momentum equation based on a non-staggered grid layout on orthogonal coordinates. Non-staggered grid layout stores all variables at the same node locations, as shown in Fig. 3.3. However, non-staggered grid layout is prone to produce a false pressure field, i.e., a checker-board effect that adversely affects the performance of the numerical method is observed, unless special precaution has been taken [54, 100]. To remedy this problem, Peric et al. [101] developed a method to interpolate the velocities on the cell faces, which consists in creating a pseudo-equation for the cell face velocities obtained from the interpolation of the momentum equations noted down in terms of the centroids of the control volumes. For instance, the velocity at the eastern cell faces ‘ e ’ is obtained in the present work according to Peric et al as:

$$u_e^* = f_e u_E^* + (1 - f_e) u_P^* + f_e \frac{K^*}{\mu_E^*} \left(\partial p^* / \partial x^* \right)_E + (1 - f_e) \frac{K^*}{\mu_P^*} \left(\partial p^* / \partial x^* \right)_P - \frac{K^*}{\mu_e^*} \left(\partial p^* / \partial x^* \right)_e \qquad (3.1)$$

where $f_e = (x_e^* - x_P^*) / (x_E^* - x_P^*)$ is the linear interpolation factor and the velocities at the central node P and neighboring node E are written according to Eq. (2.131) as:

$$u_P^* = -\frac{K^*}{\mu_P^*} \left[\left(\partial p^* / \partial x^* \right)_P - \left(\rho_k^* b_x^* \right)_P \right] \qquad (3.2a)$$

$$u_E^* = -\frac{K^*}{\mu_E^*}\left[\left(\partial p^*/\partial x^*\right)_E - \left(\rho_k^* b_x^*\right)_E\right] \tag{3.2b}$$

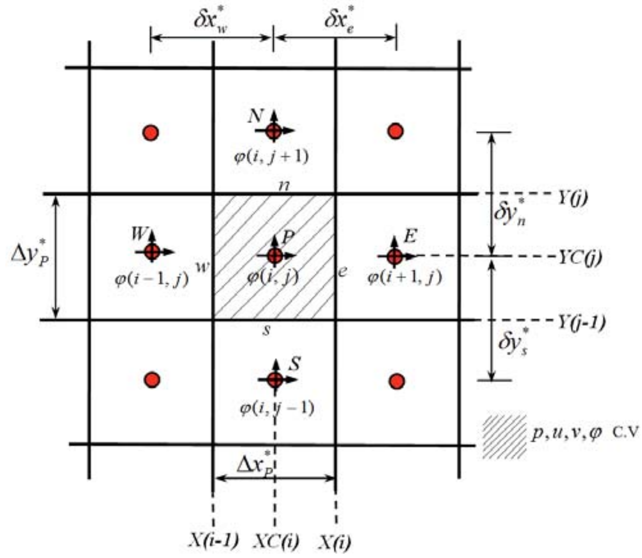

Fig. 3.3: Control volume and grid disposition for two-dimensional coordinates using non-staggered grid layout

The last term on the RHS of Eq. (3.1) may be expressed using CDS scheme as:

$$\frac{K^*}{\mu_e^*}\left(\partial p^*/\partial x^*\right)_e = \frac{K^*}{\mu_e^*}\left[\frac{p_E^* - p_P^*}{\delta x_e^*}\right] \tag{3.3}$$

Similar equations have been obtained for the other faces of the control volume. However, the mass conservation equation for a two-dimensional problem using a non-staggered grid needs four interpolations for the velocities on the ‘ e ’, ‘ w ’, ‘ s ’ and ‘ n ’ faces of the control volume. These interpolations are not unique, yet they are fundamental for the successful application of the collocated grid [102 – 104]. The pressure–velocity coupling has been obtained from the combination of the continuity equation and the momentum equation in the SIMPLE algorithm. The SIMPLE algorithm also starts with a guessed pressure field $\hat{p}^*$. The resulting velocity field at the cell faces ‘ e ’ is denoted as $\hat{u}_e^*$. Employing the preliminary values of the pressure and velocity fields at the centroids, the intermediate cell face velocity field may be written as:

$$\hat{u}_e^* = f_e \hat{u}_E^* + (1-f_e)\hat{u}_P^* + f_e \frac{K^*}{\mu_E^*}\left(\partial \hat{p}^*/\partial x^*\right)_E + (1-f_e)\frac{K^*}{\mu_P^*}\left(\partial \hat{p}^*/\partial x^*\right)_P - \frac{K^*}{\mu_e^*}\left(\partial \hat{p}^*/\partial x^*\right)_e \tag{3.4}$$

In order to proceed further, the pressure correction field p'^* is obtained by the difference between the corrected pressure field p^* and the guessed pressure field $\hat{p}^*$. In the same manner, the velocity correction for both directions, u'^* and v'^*, are obtained as: $u'^* = u^* - \hat{u}^*$ and $v'^* = v^* - \hat{v}^*$, respectively. Consequently, the velocity correction field at the east cell face is obtained as follow:

$$u'^*_e = f_e u'^*_E + (1 - f_e) u'^*_P + f_e \frac{K^*}{\mu^*_E}\left(\partial p'^* / \partial x^*\right)_E + (1 - f_e)\frac{K^*}{\mu^*_P}\left(\partial p'^* / \partial x^*\right)_P - \frac{K^*}{\mu^*_e}\left(\partial p'^* / \partial x^*\right)_e \qquad (3.5)$$

where the superscripts ^ and ′ represent the guess and the correction value, respectively. As an approximation, in the SIMPLE method only the first fourth terms in the above equation is neglected, and the corrected velocity field at the east and north faces have been obtained using the summation between the guessed velocity fields $\hat{v}^*$ and the last term in Eq. (3.5). Since the pressure equation is not solved in the present algorithm, boundary conditions for the pressure at the boundary do not required to be implemented. The pressure values at the boundary nodes have been calculated by a linear extrapolation of the values at the two nodes nearest to the boundary [see Patankar for further clarification].

3.3. Boundary Conditions

In order to solve the governing conservation equations, appropriate boundary conditions are required. In the present work, the boundary conditions occurring in one- and two-dimensional problems have been divided into four major categories: wall; inlet (prescribed), symmetry (for two-dimensional pipe flow model) and exit conditions. As mentioned before, two additional nodes have been further placed at each boundary (i.e., inlet and exit) in a one-dimensional problem as shown in Fig. 3.4 for easy implementation of boundary conditions, whereas a multiple of four additional nodes are required for a two-dimensional problem as shown in Fig. 3.5.

(a) West boundary (b) East boundary

Fig. 3.4: Control volume and grid layout for boundary conditions in one-dimensional problem

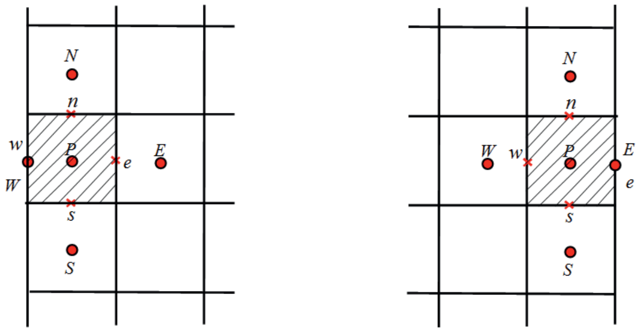

(a) West boundary (b) East boundary

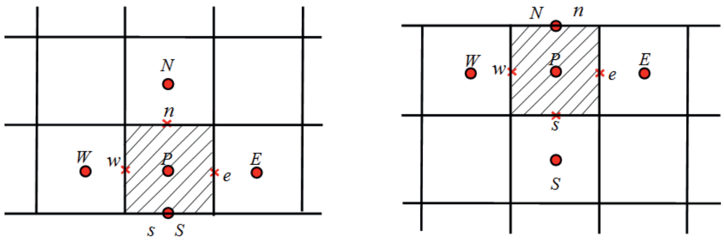

(c) South boundary (d) North boundary

Fig. 3.5: Control volume and grid disposition for boundary conditions in two-dimensional problem

A. Wall Boundary Conditions

As far as the walls are concerned, two different wall boundary conditions have been used: constant wall temperature or specified constant heat flux. For both one- and two-dimensional problems the velocity boundary conditions remain the same. Therefore, the implementation of the velocity boundary condition is first described.

Wall Boundary Condition for Velocity

Since the viscous term is dropped for the momentum equation, the no-slip boundary condition cannot be implemented in the present formulation. For an impermeable wall, the normal velocity at the wall can be set to zero. This effectively means that the normal velocity or mass flux is known at the wall. In this respect, the normal velocities are either known or pretended to be known (may be iteratively updated) at all the boundaries (inlet, symmetry or exit).

Wall Boundary Condition for the heated section

Two different types of external heat source $\dot{q}_w''^*$ have been imposed at the duct surface: specified constant heat flux $\dot{q}_w''^*$ and constant wall temperature T_w^* with specified heat transfer coefficient. During integrating the energy conservation equation over the control volume in either Fig. 3.1 or Fig. 3.2, the heat condition at the evaporator wall has been incorporated into an appropriate source term. For constant heat flux $\dot{q}_w''^*$ application, considering one-dimensional problems along with constant cross-sectional area (i.e., $A_{ce}^* = A_{cw}^* = A_c^*$) and variable cross-sectional area in the axial direction (i.e., $A_{ce}^* \neq A_{cw}^*$), the source term S^* for the wall heated condition are obtained, respectively, as:

$$S^* = \frac{P^*}{A_c^*} \Delta x_P^* \dot{q}_w''^* \tag{3.6a}$$

$$S^* = P^* \Delta x_P^* \dot{q}_w''^* \tag{3.6b}$$

In Eq. (3.6), $A_c^* = R^{*2} \big/ 2$ and $P^* = R^*$ are the cross-sectional area and perimeter per unit radian, respectively. The source term in Eqs. (3.6a) and (3.6b) are absent in the unheated section.

On the other hand, the heat source due to constant wall temperature with specified heat transfer coefficient could be modeled in dimensional form as:

$$\dot{q}_w'' = h_{co}\left(T_w - T\right) \tag{3.7}$$

In Eq. (3.7), h_{co} is the convective heat transfer coefficient at the pipe wall, which, it is assumed to be constant in the present formulation. T_w is the specified wall temperature (or surrounding temperature) and T is the local temperature of combined medium (or boundary temperature) at the axial position where heat transfer has been evaluated. In a real problem, however, h_{co} could be variable. Nevertheless, since the major objective of the present work is to demonstrate the efficiency of the newly proposed smoothing algorithm, the effect of employing a variable convective heat transfer coefficient has been not considered. The remaining treatment is similar to the case of constant heat flux condition, the only difference being the heat flux iteratively updated according to the known of boundary temperature. Thus, the non-dimensional source term S^* for the wall heated condtion is obtained for constant cross-sectional area in the axial direction as:

$$S^* = \frac{Nu_o}{Pe_l}\left(T_w^* - T_P^*\right)\Delta x_P^* \tag{3.8}$$

where $Nu_o = h_{co}\left(2R\right)/k_l$ is the Nusselt number, defined on the basis of outer pipe diameter $\left(2R\right)$ and thermal conductivity k_l of the liquid phase. It is evident from the foregoing formulation that the source term depend on either temperature T^* (in the single-phase region) or liquid saturation s (in the two-phase region) when considering constant wall temperature with specified heat transfer coefficient.

For LTE model, the total heat flux $\dot{q}_{w,x}''^*$ has been imposed directly to medium [see Eq. (2.113)], whereas for the LTNE model the total heat flux at the wall in Eq. (2.156) has been assumed to be partitioned into two parts and hence $\dot{q}_{w,x}''^* = \dot{q}_{f,x}''^* + \dot{q}_{s,x}''^*$, where $\dot{q}_{f,x}''^*$ and $\dot{q}_{s,x}''^*$ are the parts of the heat flux that are added separately to the fluid and the solid phases, respectively [see Eqs. (2.157) and (2.158)]. Thus, the source term S^* for the solid and the fluid phases, considering constant cross-sectional area in the axial direction, are obtained as:

$$S_{H^*}^* = \frac{P^*}{A_c^*}\Delta x_P^* \, \dot{q}_f''^* + \Delta x_P^* \, \dot{q}_{sf}'''^* \tag{3.9a}$$

$$S_s^* = \frac{P^*}{A_c^*}\Delta x_P^* \dot{q}_s''^* - \Delta x_P^* \dot{q}_{sf}'''^* \tag{3.9b}$$

For multi-dimensional problem, the formulation of the wall boundary condition with specified constant heat flux requires special care since the modified volumetric enthalpy at the wall is not a priori known and has to be calculated iteratively. In this case, the source terms $S_{H^*}^*$ and S_s^* for the fluid and the solid phases, considering LTNE model, are updated as:

$$S_{H^*}^* = S_{H^*}^* + a_{B,H^*}\dot{q}_f''^* \tag{3.10a}$$

$$S_s^* = S_s^* + a_{B,s^*}\dot{q}_s''^* \tag{3.10b}$$

where subscript B denotes the boundary node and a_B is the coefficient at the boundary. For LTE model, $\dot{q}_f''^* = \dot{q}_w''^*$. Since there is no diffusion term and no boundary source (such as a variation in the hindrance coefficient f) observed, all other boundary contributions to the source term should be set to zero.

B. *Inlet Boundary Condition*

The inlet boundary condition for both LTE and LTNE (either isotropic or anisotropic porous medium) models has been applied at the western wall as shown in Figs. 3.4(a) and 3.5(a), where the values of the sought quantities (T^*_s, H^*, h^* and u^*_{in}) are known. At $x^* = 0$, $H^*_{in} = \rho^*_{in}\left[h^*_{l,sat} - \rho^*_{in} C^*_{pl}\left(T^*_{sat} - T^*_{in}\right) - 2h^*_{v,sat}\right]$, $h^*_{in} = h^*_{l,sat} + C^*_{pl}\left(T^*_{in} - T^*_{sat}\right)$ and $T^*_s = T^*_{in}$ have been prescribed according to the H-formulation, h-formulation and the temperature of the solid phase, respectively. Furthermore, since sub-cooled liquid water, at a temperature $T_{in} < T_{sat}$, has been assumed to enter at the inlet of the pipe, $\rho^*_{in} = 1$ has been set. A further careful look into the continuity equation (2.130) for the one-dimensional steady-state problem reveals that the mass flow rate $\rho^*_{in} u^*_{in} = 1$ through the evaporator remains constant in the axial direction and hence its value is equal to the mass flow rate at the inlet. In this situation, the mass flow rate at the “east” boundary (i.e., at the outlet) can be set equal to the mass flow rate at the inlet and hence:

$$F^*_{m,out} = F^*_{m,in} \quad \Rightarrow \quad \rho^* u^*_x A^*_c = \rho^*_{in} u^*_{in} A^*_{c,in} = 1 \tag{3.11}$$

Since constant cross-sectional area duct ($A^*_{ce} = A^*_{c,in}$) has been considered for one-dimensional problem, and since $\rho^*_{in} = 1$ and $u^*_{in} = 1$ have been set at the pipe inlet, the integrated mass conservation in a one-dimensional pipe duct is already given in Eq. (3.11). Therefore, at the cell-face ‘e’, for example, the dimensionless axial velocity can be evaluated for both models (i.e., H-and h-formulations) due to know of the local density as $u^*_{xe} = 1/\rho^*_e$, where ρ^*_e is the density evaluated at the east cell-face using the adjacent nodal values in a linear interpolation. On the other hand, if variable cross-sectional area in the axial direction ($A^*_{ce} \neq A^*_{cw}$) has been considered, the velocity at the cell face is obtained as $u^*_{xe} = A^*_{c,in} / \rho^*_e A^*_{ce}$. For transient or multi-dimensional problems, boundary velocities at the exit should be extrapolated linearly from neighboring values at interior nodes. Boundary mass flux and hence mass flow rate are then required to be updated iteratively.

C. *Symmetry Boundary Condition*

This condition has been employed only for the pipe flow model. On the line of symmetry in a two-dimensional description for the pipe flow model as shown in Fig. 3.5(c), the normal velocity has been set to zero. The normal derivative of the general variable φ^*, i.e., modified volumetric enthalpy in this case (when considering LTE or LTNE model), has been set equal zero:

$$\frac{\partial \varphi^*}{\partial n^*} = 0 \quad \Rightarrow \varphi^*_P = \varphi^*_B \tag{3.12}$$

The boundary point has been added to the source term during the discretization of the energy conservation equation. Once a converged solution has been obtained, the boundary value may be extracted from Eq. (3.12). Similar treatment should be applied to the discretized energy equation for the solid phase when considering LTNE model.

D. *Exit Boundary Conditions*

The exit boundary condition at $x^* = L/L_{ref}$ (i.e., at the outlet) has been considered for an east boundary as shown in Figs. 3.4(b) and 3.5(b). In the present investigation, two types of the outlet boundary conditions have been used: exit with zero gradients (or fully-developed condition) and exit with zero diffusion, i.e., the second derivative has been set to zero. Both types are treated separately in details below.

Exit with Zero Gradient

The flow has been assumed to be hydro-dynamically fully-developed at the exit, which is quite reasonable for the present work owing to the presence of an unheated exit length filled with a porous medium. The local density has been calculated according to the relations provide in Table 2.3. Therefore, this condition reduces to $\partial\varphi^*/\partial x^* = 0$ for the flow in a one-dimensional problem. In the present case, the normal derivative of the velocity is zero. For a two-dimensional problem, the condition also reduces to $\partial\varphi^*/\partial n^* = 0$ for the flow variables, including the normal velocity but excluding the static pressure. Therefore, for the outlet velocity boundary conditions, the first derivative of the vertical and horizontal velocity component with respect to the axial coordinate, respectively, have been set to zero (i.e., $\partial v^*/\partial x^* = \partial u^*/\partial x^* = 0$). It may be noted here that with the help of the continuity equation, the combination would yield $\partial v^*/\partial y^* = 0$ since $\partial u^*/\partial x^* = 0$. Instead of setting $\partial v^*/\partial x^* = 0$ at the exit, Wang [33] preferred to use $\partial p^*/\partial y^* = \rho_k^* b_y^*$, which is equivalent to assuming $v = 0$ and is valid only if ρ^* is considered constant at the exit.

Exit with Zero Diffusion

For the second type of outlet boundary condition, the axial diffusion in the energy conservation equations has been neglected and hence the second derivatives of T_s^*, H^*, h^* with respect to the flow direction have been set to zero at the exit. It is important to note that the present condition may be regarded as less stringent and a better representation of the physical situation as compared to setting the first derivative to zero. Therefore, the zero diffusion boundary condition is most often used as an idealization in order to impose the outlet boundary condition [33]. As long as the assumption of fully-developed flow condition for the constant wall heat flux applications remains valid, the present condition holds for the energy transport also in the presence of shorter unheated exit length, or even in its absence. Most importantly, the widely used zero first derivative condition may be considered as a special case of the one that has been employed for the present work. Therefore, at the outlet the modified volumetric enthalpy H^*, enthalpy h^* and the temperature of the solid phase T_s^* (when considering LTNE model) have been obtained by linearly extrapolation of the values at the neighboring interior nodes that satisfy Eq. (3.13), i.e., the gradient of φ^* at the boundary is constant.

$$\frac{\partial^2\varphi^*}{\partial x^{*2}} = 0 \quad \Rightarrow \frac{\partial\varphi^*}{\partial x^*} = const. \tag{3.13}$$

The typical boundary control volumes are shown in Figs. 3.4(b) and 3.5(b). It may be noted here that the boundary node can be denoted as 'B', the node of the boundary control volume as 'P' and the internal node for the west boundary as 'W'. The distance between 'B' and 'P' is termed as Δx_B^* and the one between 'P' and 'W' as Δx_W^*. By using linear extrapolation, the exit boundary condition, for either H^*, h^* or T_s^* may be implemented in one-dimensional problem as:

$$\varphi_B^* = \varphi_P^* + \frac{\Delta x_B^*}{\Delta x_W^*}\left(\varphi_P^* - \varphi_W^*\right) = \left(1 + \frac{\Delta x_B^*}{\Delta x_W^*}\right)\varphi_P^* + \frac{\Delta x_B^*}{\Delta x_W^*}\,\varphi_W^* \tag{3.14}$$

where φ^* is the general variable, which may be either H^*or h^*or T_s^*. The same procedure has been applied along for a two-dimensional problems based on the H-formulation.

3.4. Under-relaxation

Owing to the presence of strong non-linearity in the governing conservation equations and the related constitutive relations, arising out of the interdependence of the dependent variables (e.g. ρ^*, p^*, u^*, T_s^*, H^*, h^*, etc), the discretized equations in either a semi-implicit (for steady-state condition) or fully-implicit (for transient condition) manner have been further under-relaxed and a typical relaxation factor in the range from 0.1 to 0.4 has been generally used for most of the simulations in order to achieve convergence of the iterative numerical solution.

3.5. Convergence Criteria

During the iterative numerical solutions of the direct form of the governing equations, the convergence of the solution has been checked (in every iteration) by evaluating the residuals and comparing them with prescribed tolerance. The discretized energy conservation equations, along with their boundary conditions, have been solved line-by-line in alternate directions using the Thomas algorithm [54] for tri-diagonal matrices. The sequare of residues, summed over all control volumes for a given conservation equation, has been used in order to check the convergence of the iterative solution. The solutions have been accepted as converged when this value for all conservation equations fell below 10^{-8} and the mass and energy conservation in the system has been ensured to within 0.1%, unless mentioned otherwise.

As the locations of interfaces, separating different regions, are strong functions of the flow, the heating conditions and the problem geometry and since these locations are not known a priori, only uniform control volumes have been employed for all considered cases, as illustrated in Fig. 3.6. The minmum resolution required in order to obtain reliable results and ensure their grid independence will be discussed in chapters 4 – 7 along with the numerical results separately for each problem investigated in the present work.

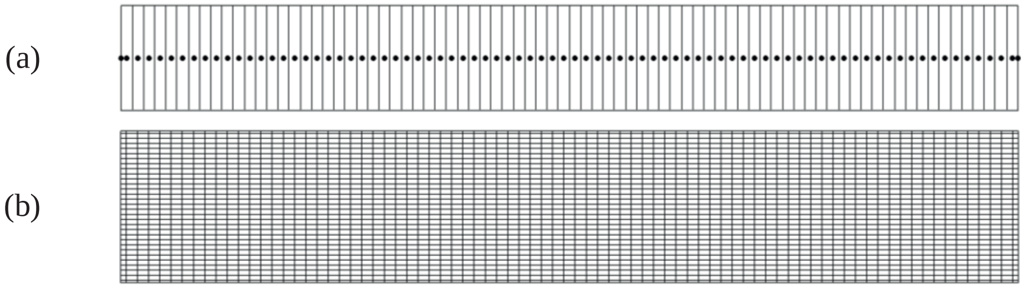

Fig. 3.6: Schematic diagram of uniform fixed grid representing of the computational domain for (a) one-dimensional and (b) two-dimensional problem

3.6. Code Verification

The present two-dimensional CFD code has been developed based on the H - formulation along with LTE model using staggered grid layout by adopting the existing two-phase flow. Thus, the current method for the solution of complete phase change process has been verified by comparing its results with the corresponding numerical results available from the literature. For this purpose, the numerical result by Najjari and Nasrallah [47] has been chosen. In this study, the porous enclosure has been heated from below. Najjari and Nasrallah provided numerical results of incomplete phase change process including temperature distribution, streamline function and liquid and vapor velocity vectors as well as the total evaporated volume fraction for an inclined channel. Their work has been carried out using the staggered grid layout for different parameters (i.e., inlet velocity, permeability and inclination angle of the channel) at $\dot{q}''_w = 3\,\mathrm{kW/m^2}$. The time step size for this simulation is $0.5\mathrm{s}$ and the total time for achieving the steady-state solution is $t = 2\times10^4\,\mathrm{s}$. The same grid resolution as used by Najjari and Nasrallah has been employed in the simulation with the staggered grid code. The comparison is presented in terms of the evaporated volume fraction ev as shown in Fig. 3.7. The evaporated volume fraction ev in the porous channel has been used to describe the importance of boiling [47]. The evaporated volume fraction has been defined in dimensional form as [30, 47]:

$$ev = \frac{1}{LW}\int_0^W\int_0^L (1-s)\,dx\,dy \qquad (3.15)$$

Najjari and Nasrallah pointed out that the evaporated volume fraction is a direct measure of the boiling strength and the extent of the resulting two-phase and vapor regions. As mentioned before, the numerical simulations have been carried out for a similar geometry with identical inclination of the channel along with identical heat flux (value), permeability and inlet velocity in the present work. Figure 3.7 shows the variation of evaporated volume fraction ev as a function of the inclination angle (in degrees) of the channel using the current method. It is clear from the figure that the volume of vapor decreases for a higher permeability value and inlet velocity as well as for an increasing angle of inclination θ . A quantitative comparison of the predicted evaporated volume fractions reveals that the values determined numerically provide excellent matches with the numerical results of Najjari and Nasrallah for different angles of inclination of the channel.

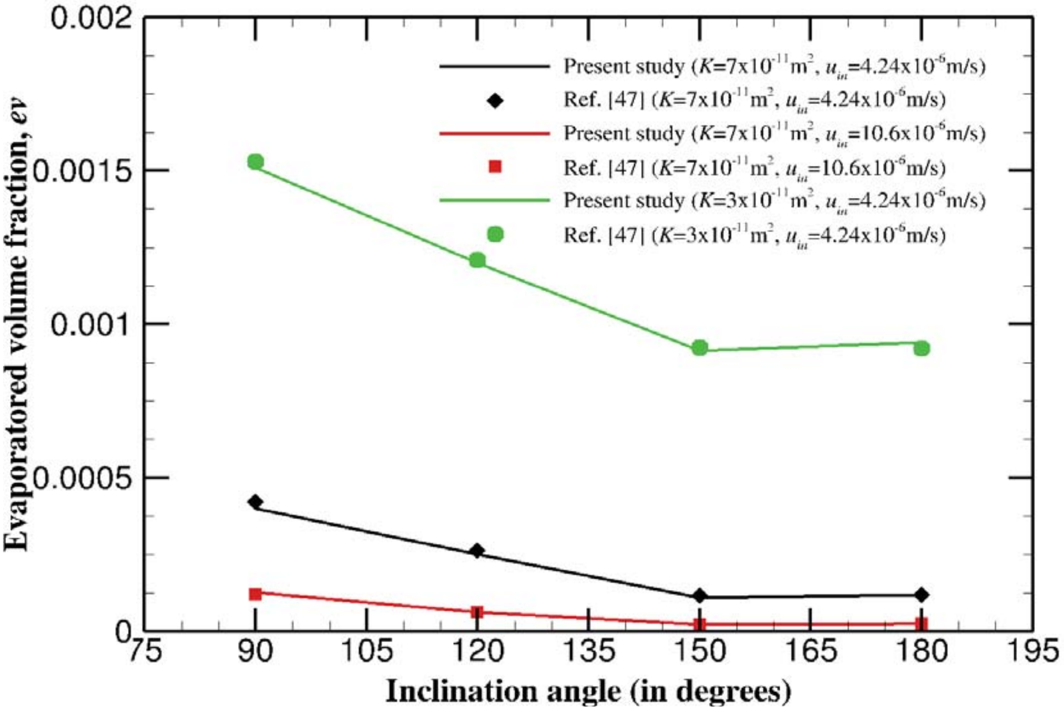

Figure 3.7: Comparison of evaporated volume fraction determined in the present study and results of Najjari and Nasrallah [47] for various inclination angles at different permeability K and inlet velocity u_{in} for $\dot{q}''_w = 3\,\mathrm{kW/m^2}$ and $t = 2\times10^4\,\mathrm{s}$

CHAPTER 4. SIMULATION OF COMPLETE PHASE CHANGE PROCESS USING LOCAL THERMAL EQUILIBRIUM MODEL

This chapter concerns the numerical results of one- and two-dimensional problems of complete liquid-vapor phase change process inside porous media along with the Local Thermal Equilibrium (LTE) model. In this chapter, numerical results of the simulation of complete phase change process in a pipe based on the H-formulation of Two-Phase Mixture Model (TPMM) [33] and modified enthalpy formulation have been obtained. On the other hand, both circular pipe and channel flow models in two-dimensional coordinates using staggered grid layout have been investigated based on the H-formulation. The main part of the simulations has been carried out by applying the proposed smoothing algorithm in order to deal with the discontinuities in the effective diffusion coefficient at the phase change interfaces and hence to obtain a smooth solution without non-physical jump in the predicted temperature distribution at the interfaces. It may be noted here that the suggested remedy is easily extendable for multi-dimensional problems involving any phase change fluid. Results for some representative cases, covering more or less the overall operating regime, are presented and discussed in this chapter in order to demonstrate the effectiveness of the suggested remedy.

As mentioned in chapter 1, the study of literature also reveals that earlier simulations were performed only on orthogonal coordinates. However, it could be extremely useful to provide a varying cross-sectional area of the duct in order to accommodate higher volume flow rates of the vapor-phase. Such simulations would definitely require an extension of the present numerical method to non-orthogonal (curvilinear) coordinates using non-staggered variable arrangements. Therefore, the present chapter also provides the comparison between results obtained using non-staggered and staggered grid layouts for the incomplete phase change process of water for a two-dimensional problem under steady-state condition inside a porous channel.

4.1. Modeling of One-dimensional Problems Based on Modified Volumetric Enthalpy Formulation of Two-Phase Mixture Model

4.1.1 Problem Description and Basic Assumptions

In order to demonstrate the usefulness of the proposed smoothing algorithm for handling sharp discontinuities in modeled transport properties, the steady one-dimensional problem of complete phase change of liquid water inside a porous evaporator has been considered in the present investigation. The problem geometry is schematically represented in Fig. 4.1. For simplicity, a pipe of constant outer radius R filled with a known porous medium has been chosen for the present analysis. The pipe has unheated inlet and exit lengths sections l_i and l_e, respectively, and the length of the heated section is l_h. The temperature at the pipe wall is constant at T_w, which is higher than the saturation temperature T_{sat}, in the heated section. Heat is transferred to the working fluid due to a specified heat transfer coefficient h_{co}. An external pressure gradient drives the sub-cooled liquid water with velocity u_{in} and at temperature T_{in} $(T_{in} < T_{sat})$ at the inlet to flow through the pipe. The liquid is heated as it passes through the pipe. When sufficient heat is added, boiling occurs, leading to the formation of a two-phase region and, subsequently, a superheated vapor region.

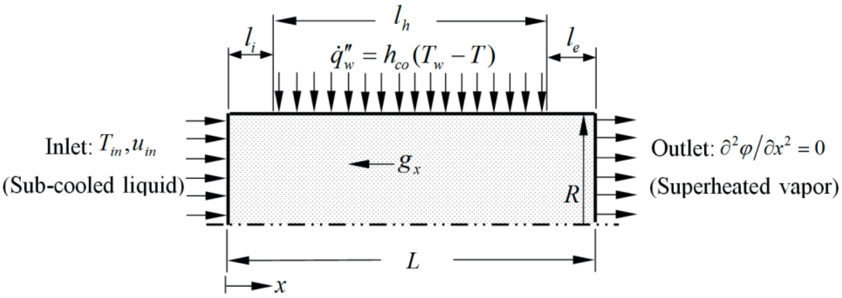

Fig. 4.1: Schematic representation of the phase change problem

The governing equations for the present problem have been obtained by adopting the H-formulation for steady-state condition. The porous medium has been considered as homogenous and a local thermal equilibrium has been assumed. The radial velocity component $v_r^* = 0$ has been assumed everywhere for the one-dimensional problem. For the problem to be axi-symmetric, $b_r^* = 0$ has been assumed. In particular, the axial direction here represents the vertical direction. With these assumptions, the non-dimensional conservation of mass in Eq. (2.130), momentum in Eq. (2.131) and energy in Eq. (2.134) for a steady-state problem, where variations exist only in the axial direction, are given as:

$$\frac{d}{dx^*}\left(\rho^* u_x^*\right) = 0 \tag{4.1}$$

$$\rho^* u_x^* = -\frac{K^*}{\nu^*}\left(\frac{dp^*}{dx^*} - \rho_k^* b_x^*\right) \tag{4.2}$$

$$\frac{d}{dx^*}\left(\gamma_H u_x^* H^*\right) = \frac{d}{dx^*}\left(\Gamma_H^* \frac{\partial H^*}{\partial x^*}\right) + \frac{d}{dx^*}\left(f\,\frac{K^* \Delta\rho^* h_{fg}^*}{\nu_v^*} b_x^*\right) + \frac{Nu_o}{Pe_l}\left(T_w^* - T^*\right) \tag{4.3}$$

where all variables appearing in Eqs. (4.1) – (4.3) are defined in chapters 2 and 3. As will be shortly apparent, for the present steady-state one-dimensional problem, the kinetic density ρ_k^* is required only when the solution for the axial pressure gradient is performed. The last term on the RHS of Eq. (4.3) acts as a special source term for the reduced one-dimensional problem, which is absent in the unheated segments. It is now apparent that in order to solve Eq. (4.3), the dimensionless temperature T^* is required since it appears explicitly in the equation, whereas Table 2.3 clearly shows that for evaluating various mixture properties in the two-phase region, the liquid saturation s is necessary. Assuming the enthalpies of liquid and vapor phases to be dependent only on temperature, since the pressure drop in the porous evaporator is expected to be small owing the extremely low mass flow rate, the relationship between enthalpy and temperature or liquid saturation can be obtained from Table 2.4.

For the present one-dimensional model, dimensionless boundary conditions for Eqs. (4.1) – (4.3) have been prescribed as follows: at the inlet, i.e., at $x^* = 0$, $T_{in}^* < T_{sat}^*$, $\rho_{in}^* = 1$, $u_x^* = u_{in}^* = 1$ and $H_{in}^* = \rho_{in}^*\left[h_{l,sat}^* - \rho_{in}^* C_{pl}^*\left(T_{sat}^* - T_{in}^*\right) - 2h_{v,sat}^*\right]$ have been specified. At the pipe outlet, i.e., at $x^* = L/R$, the second derivative of H^* has been set to zero [see Eq. (3.13)]. This condition is less stringent as compared to the fully-developed condition applicable for shorter exit lengths. Therefore, H^* at the exit has been linearly extrapolated from its neighboring values at interior nodes [see Eq. (3.14)]. For the present one-dimensional formulation, the axial velocity has been defined at the cell faces according to the staggered grid layout as shown in Fig. 3.1(a). The velocity boundary condition at the exit, however, is not required, since inlet conditions have been satisfied. Integration of the mass conservation equation (4.1), under steady-state conditions yields the simple relation given as $\rho_e^* u_{xe}^* = \rho_{in}^* u_{in}^* = 1$. Therefore, at the cell-face 'e', for example, the axial velocity u_{xe}^* has been evaluated using the local density ρ_e^* as $u_{xe}^* = 1/\rho_e^*$. As will be shortly apparent from subsection 4.1.1, the momentum equation (4.2) is also not required for the present one-dimensional problem (unless solution for the pressure field is sought), since the mass flow rate remains fixed both in time and space and the pressure variation does not affect the velocity solution. For all cases presented in this study, the convergence criterion has been set to 10^{-8}. It has been also observed that an under-relaxation factor typically in the range $0.1-0.5$ is required in order to achieve convergence of the iterative solution of Eq. (4.3).

4.1.2. Ranges of Parameters

In order to fulfil the major objective of the present work, the proposed smoothing algorithm for Γ_H^* is thoroughly tested and the results are presented in this investigation in order to derive recommendations for future use. For the purpose of demonstration, a circular duct of radius $R = 25\,\mathrm{mm}$ and of overall length $L = 500\,\mathrm{mm}$ ($L^* = 20$) has been considered for analysis, where the unheated inlet l_i and exit lengths l_e are both equal to $0.1L$. Sub-cooled liquid water at $T_{in} = 20\,^{\mathrm{o}}\mathrm{C}$ enters the pipe and the wall temperature has been varied from $T_w = 140\,^{\mathrm{o}}\mathrm{C}$ to $200\,^{\mathrm{o}}\mathrm{C}$. The mass flow rate, typically varies between $100\,\mathrm{g/h}$ and $500\,\mathrm{g/h}$, which is quite low, and hence u_{in} has been varied from 1.5×10^{-5} m/s to 7.5×10^{-5} m/s. The porosity and the permeability of the medium are also quite low and hence they have been varied from 0.2 to 0.4 and $10^{-13}\mathrm{m}^2$ to $10^{-10}\mathrm{m}^2$, respectively. On the other hand, the thermal conductivity of the solid matrix has been varied from $5\,\mathrm{W/m\,K}$ to $50\,\mathrm{W/m\,K}$ [89]. Based on these data and the properties of water given in Table 2.1, the inlet Reynolds number Re_l, dimensionless thermal conductivity of the solid matrix $k_{s,ref}^*$ and Darcy number K^* have been varied from 1.25 to 4, 2.25 to 21 and 10^{-9} to 10^{-7}, respectively.

In these definitions, $k_{s,ref}^*$, which signifies the dimensionless thermal conductivity of the solid phase under reference condition, requires a special mention. Since according to the definition in Table 2.2, k_s^* (or, for that matter, any dimensionless thermal conductivity) depends on the inlet Reynolds number, its numerical value would differ for different Re_l even if the dimensional thermal conductivity of the solid and the fluid phases are kept unaltered. In order to eliminate this problem and to enable comparison of data obtained for different inlet Reynolds number along with identical properties of the solid and the fluid phases, $k_{s,ref}^*$ has been introduced, which corresponds to k_s^* for the reference Reynolds number $Re_{l,ref} = 2$. Therefore, the true value of k_s^* for a prescribed Re_l, that is different from $Re_{l,ref}$ can be easily obtained as $k_s^* = k_{s,ref}^* Re_{l,ref} / Re_l$ and hence k_s^* is higher than $k_{s,ref}^*$ when $Re_l < Re_{l,ref}$, whereas it is lower than $k_{s,ref}^*$ for $Re_l > Re_{l,ref}$. A similar argument also applies for other dimensionless thermal conductivities in a sense that for identical thermo-physical properties of the fluid and the solid phases, the dimensionless thermal conductivities increase with a decrease in the inlet Reynolds number (may be caused by the decrease in inlet velocity for a fixed evaporator radius) and vice-versa.

The gravitational Reynolds number Re_g and the normalized surface tension coefficient $\tilde{\sigma}$ have been taken as 4.25×10^4 and 1.8×10^7, respectively, in order to specify Fr and σ^* as described in section 2.2. Both Re_g and $\tilde{\sigma}$ have been kept fixed for the present investigation since they depend only on the properties of liquid water and the pipe radius. Other than these, the exponent n of the relative permeability for both phases has been chosen as 3 [see Fig. 2.2 for clarification], whereas, $Nu_o = 4$ has been assumed. For the reference case, on the other hand, the following parameters have been used: $\varepsilon = 0.3$, $K^* = 10^{-8}$, $k_s^* = 8.25$ (for $k_s = 20\,\mathrm{W/m\,K}$ and $Re_l = 2$) as properties of the porous medium, $Re_l = 2$ according to the inlet flow condition, other than the inlet temperature $T_{in} = 20\,^{\mathrm{o}}\mathrm{C}$, which has been kept fixed, $T_w = 160\,^{\mathrm{o}}\mathrm{C}$ as the heating condition at the wall, other than $Nu_o = 4$, and the unheated inlet and exit lengths are both equal to $50\,\mathrm{mm}$, i.e., $l_i^* = l_e^* = 2$, which yields $l_h^* = 16$. In the next subsections, results are first presented for the reference case and the effects of porosity, Darcy number, thermal conductivity of the solid matrix, direction of gravity, Reynolds number and wall temperature are then discussed. As far as the smoothing of the diffusion coefficient is concerned, the following parameters have been finally used: $\Delta T_l = \Delta T_v = 0.5\,^{\mathrm{o}}\mathrm{C}$, $\psi_l = \psi_v = 2.5\times10^{-2}$, $s_l = 0.999$, $s_v = 0.001$, $m_{\phi l}, m_{\phi v} \to \infty$, such that Γ_H^* has been given by its respective asymptotes (i.e., only relaxation and no smoothing has been used), and $m_{sl} = m_{sv} = 0.25$ [see equations from (2.140) to (2.147)]. These parameters have been judiciously chosen by following the requirements that $\Delta T\,'s$ and $\psi's$ should be as small as possible, s_l and s_v should tend to 1 and 0, respectively, whereas $m's$ should be as high as possible. They have been arrived at after thorough testing with regard to satisfactorily performance for all considered cases and hence are not arbitrary, although several other choices could also produce similar results.

4.1.3. Results for the Reference Case

Results for the reference case with different number of control volumes N_{CV} are presented in Fig. 4.2. It can be readily observed that with the increase in number of control volumes, both solutions obtained “with” and “without” smoothing, nearly attain respective grid independent solutions, although without and with “jump” in the predicted temperature, respectively. The figure also shows that the temperature “jump” could be as high as $50\,^{\mathrm{o}}\mathrm{C}$, occurring within one control volume, which may be regarded as non-physical. Nevertheless, it is evident that while the axial temperature distributions obtained with $N_{CV} = 400$ and 800 are hardly distinguishable, minor variations, particularly close to the vapor phase, can be detected for the liquid saturation. Since the major objective of the present investigation is to demonstrate the performance of the proposed remedy for the smooth (i.e., without “jump”) prediction of complete phase change process inside porous media, all subsequent results have been obtained with $N_{CV} = 400$ such that they may be considered “nearly” grid independent as far as the axial temperature variation is concerned.

It may be recognized here that owing to the complex dependence of Γ_H^*, γ_H and f on H^*, the conservation of energy in Eq. (4.3) is strongly non-linear. During discretization, the non-linearity is taken care of by evaluating coefficients and sources using H^* from the previous iteration. Since a non-linear differential equation can have multiple solutions, the converged results for most of the tested cases are found to strongly depend on the initial guess. Multiple solutions are quite common for Navier-Stokes equations. In the present context, solutions with and without jump in predicted temperature can be regarded only as the evidence. The formal mathematical proof for existence of non-unique solution is, however, beyond the scope of the present investigation. During the present study, as a first approximation, the guessed temperature is always taken as that at the inlet with $u_x^* = u_{in}^* = 1$ for all axial locations. It is, however, observed that if the converged solution, obtained with the proposed smoothing algorithm, has been used as a guess to the solver that works without smoothing, the latter code not only converges very fast, but also to the nearly identical solution without any “jump” in the predicted temperature. Since these solutions are hardly distinguishable, all results, marked as “with smoothing”, have been finally obtained with the code that works “without smoothing”. The results, denoted as “without smoothing”, however, have been obtained in a conventional manner, without applying any such pre-processing.

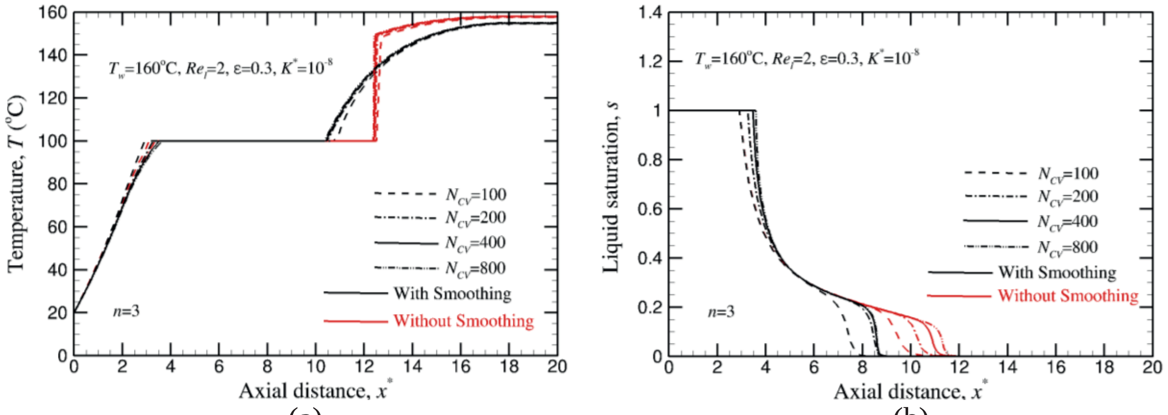

(a) (b)

Fig. 4.2: Variations in (a) temperature and (b) liquid saturation with axial distance for the reference case with different number of control volumes

It is important to note that while solutions “without” smoothing always lead to “jump” in the predicted temperature, no such non-physical behavior is detected for those obtained “with” smoothing. Since any significant change in the diffusion coefficient leads to a substantially different solution (this can be easily verified even by solving a steady one-dimensional heat conduction problem in a slab, by subjecting the left wall to a convective boundary condition, while keeping the right wall at constant temperature) and all solution have been obtained either “with” or “without” pre-processing the guessed solution, it can be safely concluded that the proposed remedy eliminates “jump” in the predicted temperature without modifying the expected solution and hence can be recommended for the simulation of complete phase change problem within porous media. It is also interesting to note that as expected from the variation of Γ_H^* in Fig. 2.2(c), prior to the “jump” in the predicted temperature close to the vapor phase, both methods (“with” and “without” smoothing) produce nearly identical solutions. Another interesting feature is that since the phase change problem inside porous media is elliptic in nature, axial diffusion plays an important role, which is present even in the two-phase region. Since H^* increases in the flow direction due to heating, energy is transferred in the upstream direction owing to axial diffusion. This results in substantial heating even in the unheated starting segment of the evaporator [$0 \le x^* \le l_i^*$, see Figs. 4.2 – 4.6].

4.1.4. Results Obtained with Parametric Variations for *n*=3

In order to test the proposed remedy, results have been also obtained by varying properties of the porous medium, flow conditions as well as heating condition. These results are summarized in Figs. 4.3 – 4.6. It is evident from these figures that the Darcy number for $n=3$ in Figs. 4.3(b) and 4.4 as well as the direction of gravity in Fig. 4.5(a) have almost insignificant influence and the porosity of the medium in Fig. 4.3(a) has only marginal effect, whereas the dimensionless thermal conductivity of the solid matrix in Fig. 4.3(c), Reynolds number in Fig. 4.5(b) and the imposed wall temperature in Fig. 4.6 have strong influences on the predicted temperature distributions. Properties of porous media affect obtained solutions by modifying only the effective diffusion coefficient which has two distinct parts [see Table 2.3 for clarification]. While the increase in porosity directly decreases k_{eff}^* [see Eq. (2.135)] in the single phase region, the capillary diffusion coefficient D^* [refer to Table 2.3] increases with the increase in both porosity and permeability of the medium in the two-phase region. In the two-phase region, k_{eff}^* has no role in the effective diffusion coefficient since $dT^*/dH^* = 0$, whereas in the single phase region, $D^* = 0$.

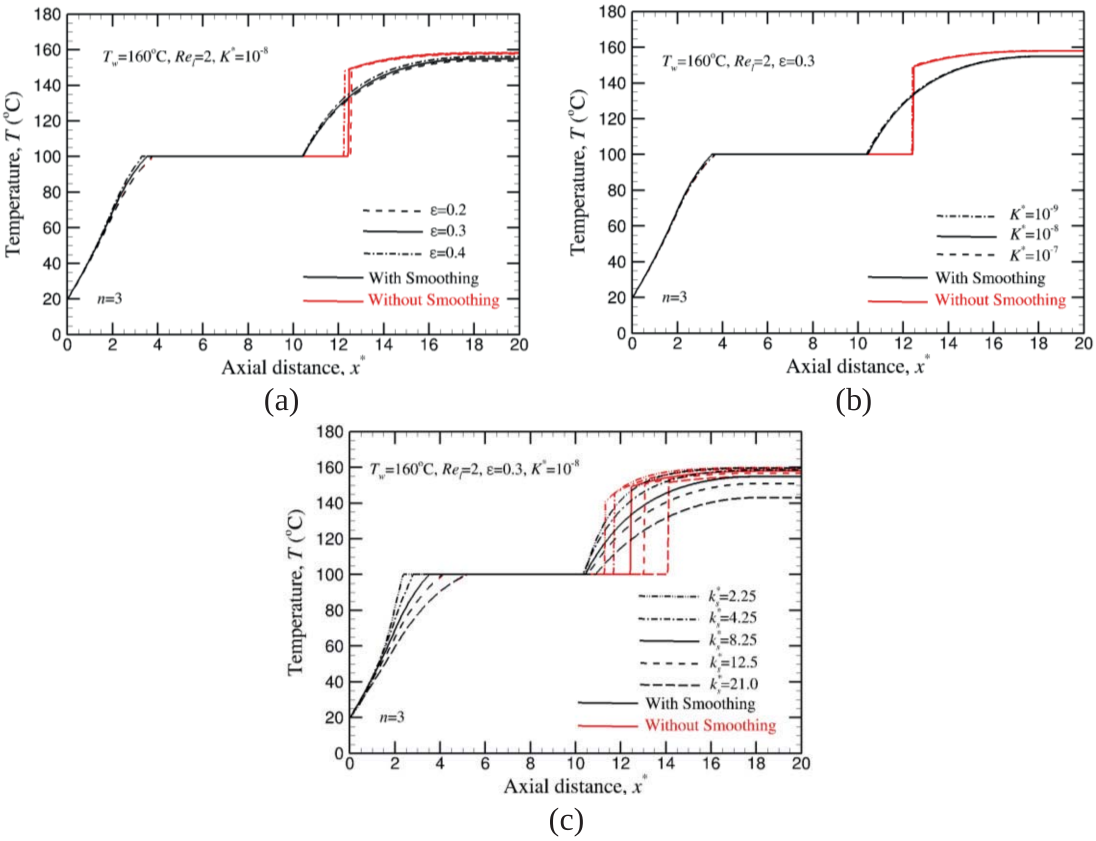

(a) (b)

(c)

Fig. 4.3: Effects of porous media properties on temperature variations as functions of axial distance for (a) different porosity, (b) different Darcy number and (c) different thermal conductivity of the solid matrix

More importantly, D^* is several orders of magnitudes lower than Γ_{Hl}^* and Γ_{Hv}^*. As a result, as compared to the permeability, which has almost negligible influence, the porosity has a more pronounced effect on the solution as may be observed from Figs. 4.3(a) and 4.3(b). Nevertheless, in order to demonstrate that the permeability does affect the axial temperature variation, further results are presented in Fig. 4.4 for $n=3$ with K^* varying from 10^{-12} to 10^{-4}. In addition, a higher thermal conductivity of the solid matrix leads to a delay of the initiation and termination of phase change process, which occurs due to an increased heat loss through the inlet [see Fig. 4.3(c)]. This trend is reasonable and can be explained by the fact that the increase in thermal conductivity of the solid struts directly increases Γ_H^* in the single phase regions, which occurs for enhanced k_{eff}^* [see Eq. (2.135)]. Furthermore, the effect of the thermal conductivity of the solid phase on the temperature distribution is more pronounced as compared to the porosity and Darcy number as may be observed from Figs. 4.3(a) – 4.3(c).

The dimensionless body-force per unit mass in the axial direction affects the energy equation only in the two-phase region, since the hindrance coefficient f is exactly equal to zero in the single-phase regions [see Fig.2.2(c)]. Furthermore, since the source term due to this force is also multiplied by a small term K^*/ν_v^*, the direction of gravity has nearly no influence on the predicted temperature [see Fig. 4.5(a)]. The pressure drop across the evaporator, however, is expected to be a strong function of the direction of gravity [refer to Eq. (4.2)]. Since the pressure variation in the present one-dimensional formulation does not affect the velocity solution and hence the energy equation, this issue of pressure variation is left out of the present study. Most prominent variations in the predicted axial temperature distributions are observed when the inlet Reynolds number [see Fig. 4.5(b)] and the wall temperature [see Fig. 4.6] are varied. The variation with Reynolds number, however, is quite expected since with the decrease in inlet velocity, the residence time of fluid inside the evaporator increases and hence phase change starts and ends early with the decrease in Reynolds number. The effect of wall temperature, as presented in Fig. 4.6, is straightforward and hence perhaps needs no further explanation.

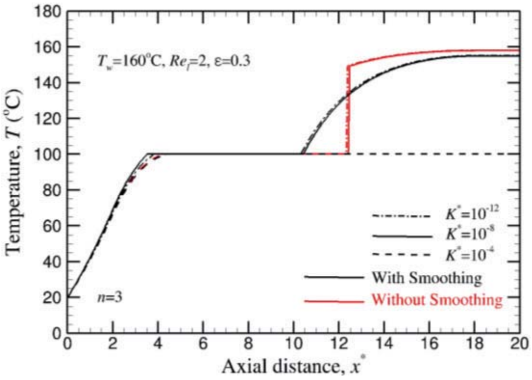

Fig. 4.4: Effects of Permeability on temperature variations as functions of axial distance for $n=3$

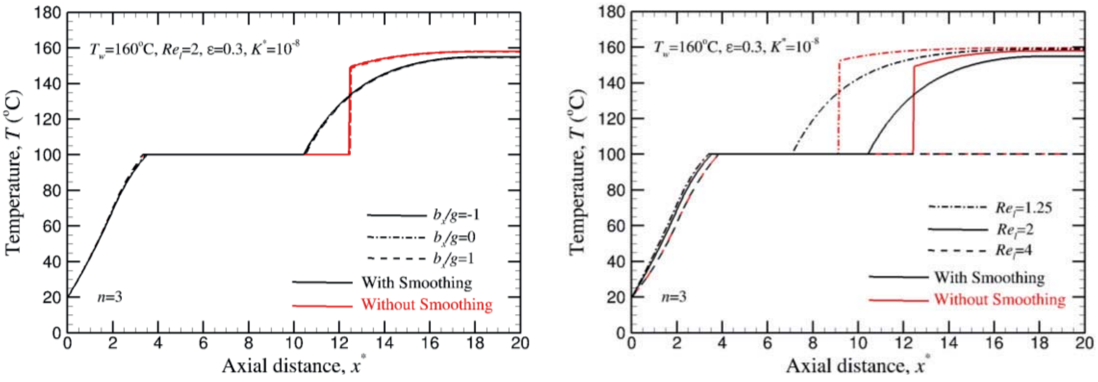

(a) (b)

Fig. 4.5: Effects of flow condition on temperature variations as functions of axial distance for (a) different directions of gravity and (b) different Reynolds number

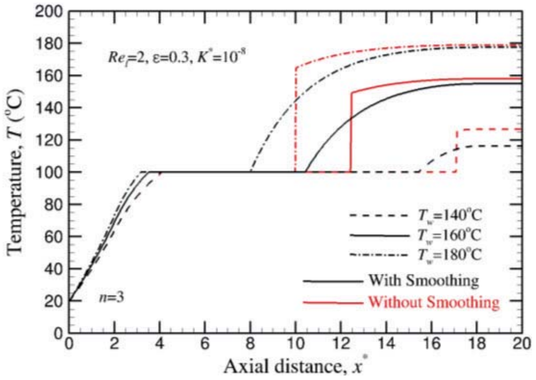

Fig. 4.6: Effect of imposed wall temperature on axial temperature variations

4.1.5. Results Obtained with Parametric Variations for *n*=1

In order to demonstrate that the exponent n either of liquid or vapor saturation in the expressions of relative permeability does affect the axial temperature distribution as well as to further establish the necessity of the proposed smoothing algorithm, results have been obtained by varying the properties of porous medium, flow conditions, and heating conditions, as shown in Figs. 4.7 – 4.9, when considering the exponent n to be equal to unity. In a manner similar to Fig. 4.2(a), results for the reference case with a different number of control volumes N_{CV} are presented in Fig. 4.7 in the form of an axial temperature distribution. It is evident from the figure that for an increase in the number of control volumes, solutions obtained “with” and “without” smoothing nearly achieve respective grid independent solutions. In addition, the axial temperature distributions obtained with $N_{CV} = 400$ and 800 are hardly distinguishable. Therefore, all the results presented in this subsection have been obtained with $N_{CV} = 400$ so they can be considered nearly grid independent as far as the comparison is concerned.

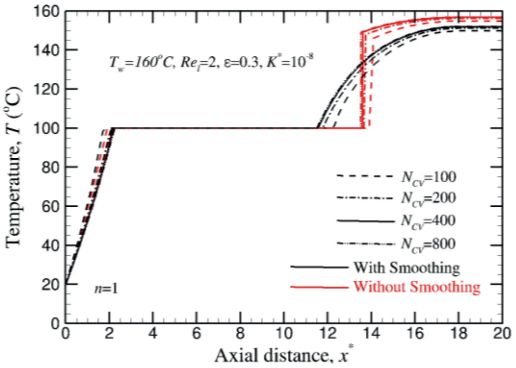

Fig. 4.7: Variations in temperature with axial distance for the reference case with different number of control volumes

Figures 4.8 and 4.9 display the effects of porous media properties, inlet flow conditions, and heating conditions for both $n = 1$ and $n = 3$. Since the main objective of the present subsection is to demonstrate the effect of the exponent n on the predictions of the complete phase change process inside a porous evaporator, all subsequent results have been finally obtained with a code that works without smoothing of Γ_H^* using the results obtained with smoothing as the guessed solution, as elaborately explained in subsection 4.1.4. Therefore, the solutions directly obtained without smoothing which are characterized by a non-physical jump in the predicted temperature distributions, are not presented here for the sake of convenience.

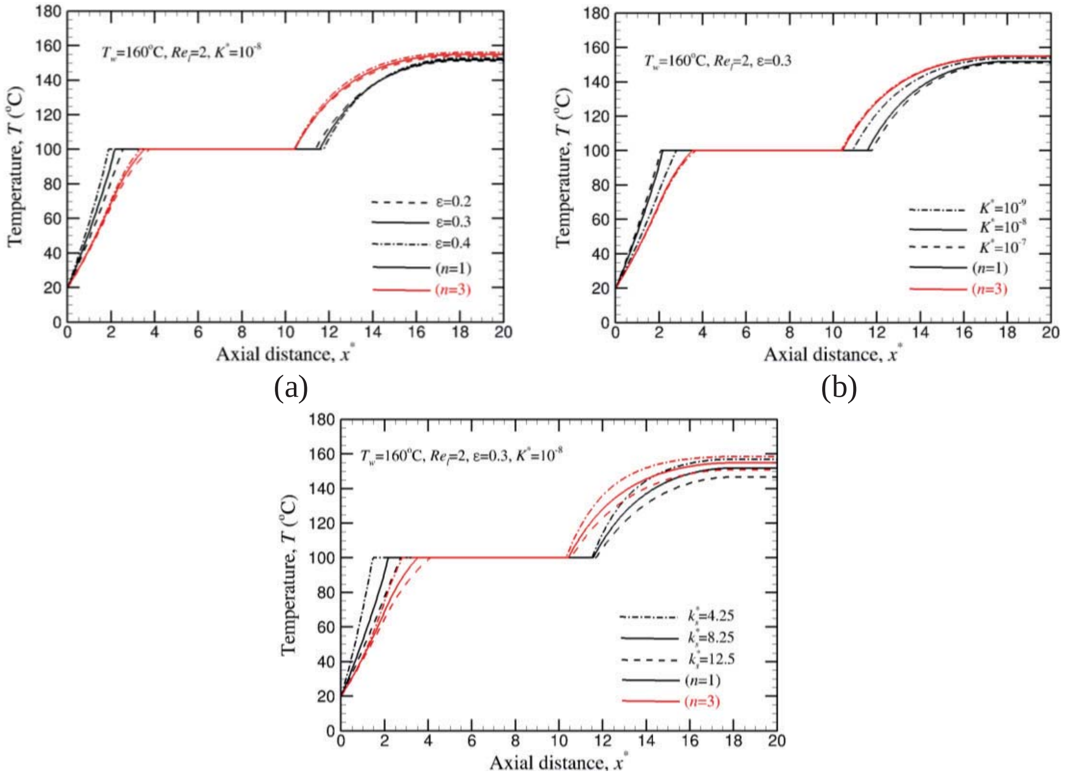

(a) (b)

(c)

Fig. 4.8: Comparison of temperature variations as a function of axial distance using smoothing algorithm for different exponent of relative permeability along with (a) different porosity, (b) different Darcy number and (c) different thermal conductivity of the solid matrix

It can be observed from the figures that the effects of porosity in Fig. 4.8(a), Darcy number in Fig. 4.8(b) and body-force per unit mass in Fig. 4.9(a) are more pronounced when the exponent of the relative permeability n equals 1 as compared to respective results obtained using $n=3$. This is reasonable since a reduction of n from 3 to 1 implies an enhanced diffusion coefficient D^* and relative permeability for both liquid and vapor phases leading to a considerable increase of Γ_H^* and f in the two-phase region [see Fig. 2.2(b), Fig. 2.2(c) and Table 2.3 for clarification]. On the other hand, the dimensionless thermal conductivity of the solid matrix in Fig. 4.8(c), Reynolds number in Fig. 4.9(b) and wall temperature in Fig. 4.9(c) strongly affect the predicted temperature distributions. The results in Figs. 4.8 and 4.9 also clearly demonstrate that the exponent n in the expression of the relative permeability has a significant effect on the initiation and termination of the phase change process. A delayed initiation of the phase change process for $n=3$ as compared to $n=1$ may be explained by the considerable decrease in the heat loss through the inlet, which occurs for decreased Γ_h^* in the two-phase region. On the other hand, the early termination of the phase change process with $n=3$ may be explained by the increase of the diffusive heat transfer from the superheated vapor phase to the two-phase mixture zone. The early termination of the phase change process for $n=3$ may also occur due to lower energy diffusion in the upstream direction from the saturated vapor to the saturated liquid. However, it is necessary to verify this phenomenon by experiments in the future. In addition, the results clearly demonstrate that the proposed smoothing algorithm is successful in avoiding the occurrence of a jump in the predicted temperature distribution for all tested cases.

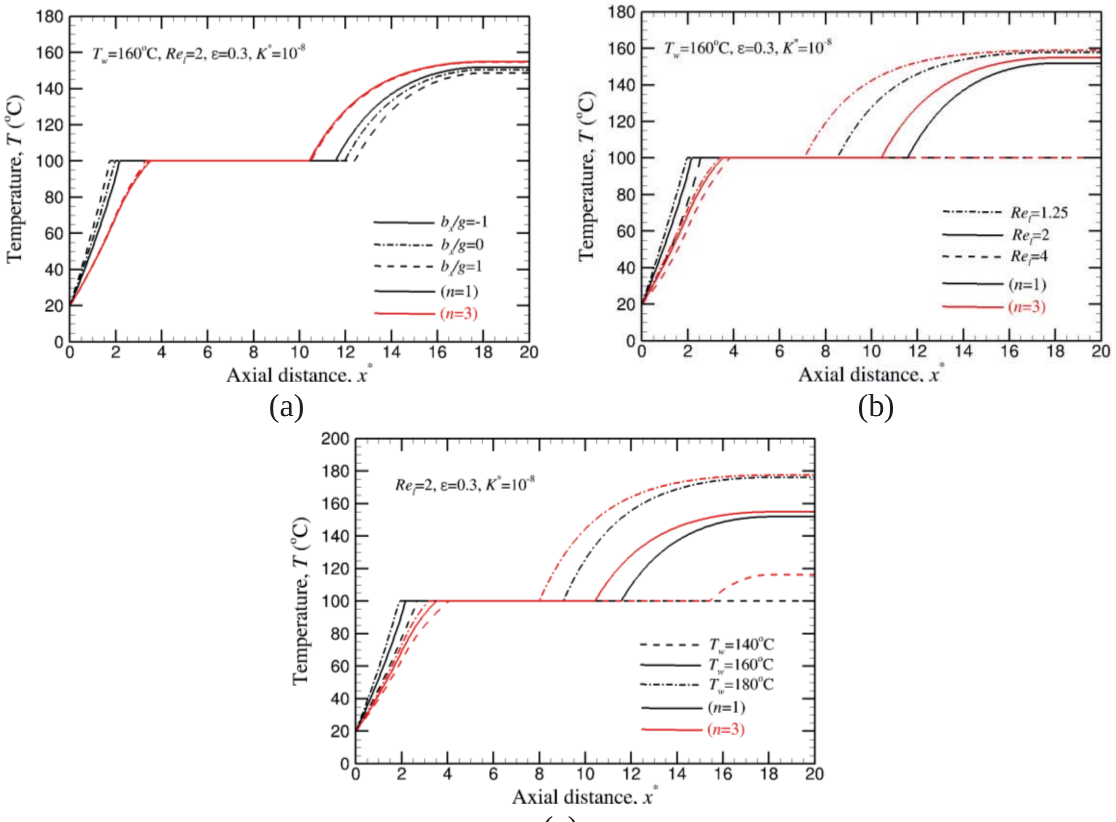

(a) (b)

(c)

Fig. 4.9: Comparison of temperature variations as a function of axial distance using smoothing algorithm for different exponent of relative permeability along with (a) different directions of gravity, (b) different Reynolds number and (c) different imposed wall temperature

4.1.6. Transient Simulation of Complete Phase Change Process

To gain additional insight into the nature of the current problem as well as to extend the previous study for the sake of completeness, transient effect is included here in order to draw meaningful conclusions regarding the transient simulation of the complete phase change process inside porous media. The study of transient fluid flow and heat transfer associated with phase change process may provide further detailed and useful information for the phase change process as it occurs in real time. In this situation, the conservation of momentum in Eq. (4.2) has to be solved, since the mass flow rate is not fixed in time, and the pressure variation affects the velocity solution. The pressure drop across the evaporator, however, is expected to be a strong function of the direction of gravity [refer to Eq. (4.2)]. After adding the transient terms to Eqs. (4.1) and (4.3), the pressure variation is influenced only through the variation in kinetic density ρ_k^*. For the present one-dimensional formulation and in order to solve the pressure equation (3.81) using staggered grid layout, the velocity boundary condition at the exit is however required to satisfy the conservation of mass in Eq. (2.130). Initial and boundary conditions are required in order to solve the governing equations. In this regard, the initial and boundary conditions for the present problem have been given as follows:

The initial conditions at the inlet, i.e., at $t^* = 0$ have been specified as:

$$u_x^* = 0 \tag{4.4}$$

$$H_{in}^* = \rho_{in}^* \left[h_{l,sat}^* - \rho_{in}^* C_{pl}^* \left(T_{sat}^* - T_{in}^* \right) - 2 h_{v,sat}^* \right] \tag{4.5}$$

After initialization, the porous medium has been assumed to be saturated with sub-cooled liquid water that enters the evaporator with uniform average velocity u_{in}^* and at constant temperature T_{in}^* at the inlet, i.e., at $x^* = 0$ and $t^* > 0$. Thus, the prescribed boundary conditions at the inlet can be written as:

$$u_x^* = u_{in}^* = 1 \tag{4.6}$$

$$H_{in}^* = \rho_{in}^* \left[h_{l,sat}^* - \rho_{in}^* C_{pl}^* \left(T_{sat}^* - T_{in}^* \right) - 2 h_{v,sat}^* \right] \tag{4.7}$$

At the outlet, i.e., at $x^* = L/R$ and $t^* > 0$, the second derivative of the modified volumetric enthalpy has been set to zero.

$$\frac{\partial^2 H^*}{\partial x^{*2}} = 0 \tag{4.8}$$

which represent an exit with zero diffusion, see Eq. (3.13) for its numerical treatment. On the other hand, the flow (velocity boundary condition) has been assumed to be hydro-dynamically fully–developed at the exit:

$$\frac{\partial u^*}{\partial x^*} = 0 \tag{4.9}$$

which corresponds to an exit with zero gradient, see Eq. (3.12). For the transient simulation of the complete phase change process, the density and specific heat of the solid matrix ($k_s^* = 8.25$, see subsection 4.1.2 for clarification) are required in the energy equation in terms of the effective heat capacity ratio, Ω_H, [see Eq. (2.134) and Table 2.3]. In the present study, $\rho_s = 8000\,\text{kg/m}^3$ and $C_{ps} = 480\,\text{J/kg K}$ have been considered [33]. Prior to obtaining results for the present investigation, a detailed grid independence study has also been carried out for the problem of plain two-phase flow. The results have been showed that at least 400 uniform control volumes with a time step size of $\Delta t = 0.5s$ (i.e., $\Delta t^* = 5\times10^{-4}$) are required to produce a grid independent solutions. Consequently, all subsequent results have been obtained with $N_{CV} = 400$ and $\Delta t = 0.5s$, so they can be considered as "nearly" grid independent as far as the axial temperature variation is concerned.

Figure 4.10(a) shows the transient behavior of liquid saturation for the incomplete phase change process at $T_w = 140\,^\circ\text{C}$ for $n=1$. Starting at $t^* = 0$, sub-cooled water enters the duct with a uniform velocity profile and the discrete heat input at the wall is activated. As heating continues until $t^* = 0.8$, the kinetic density variation is small due to a small temperature difference. Thus, the buoyancy force remains small, and its effect is not obvious. At that moment of time, the liquid saturation is unity, i.e., a sub-cooled liquid region is considered. This changes when subject to further heating.

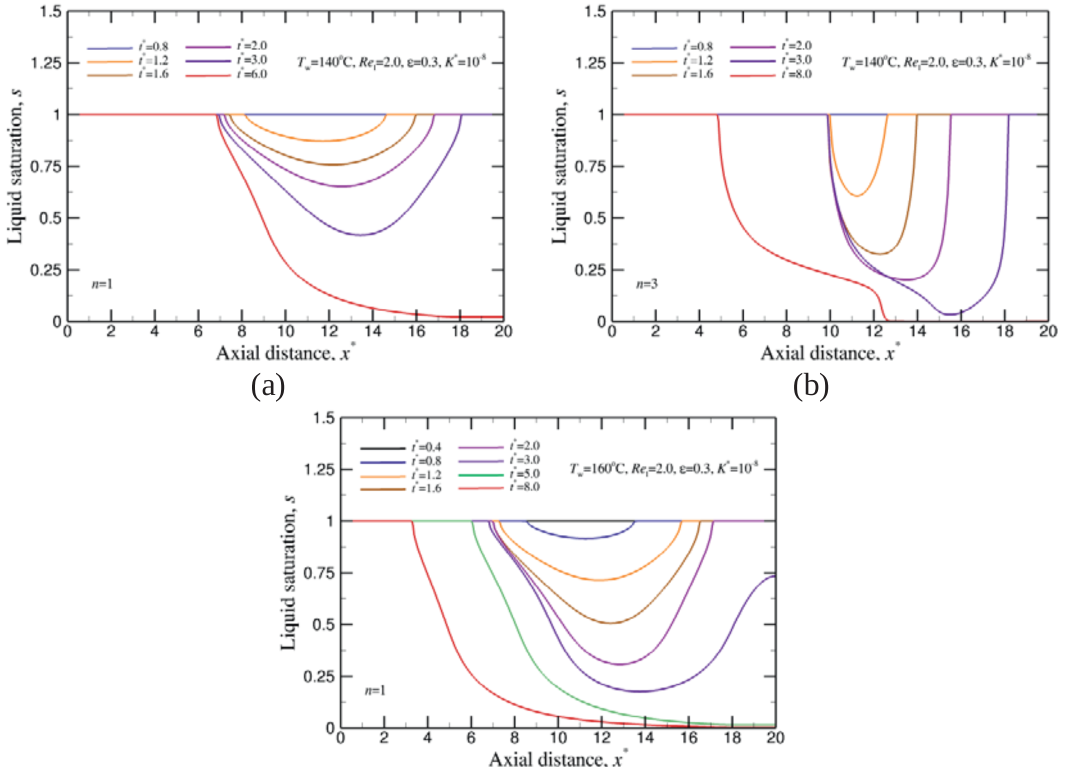

(a)

(b)

(c)

Fig. 4.10: Liquid saturation profiles obtained when applying smoothing of Γ_H^* for different points in time along with (a) $T_w = 140^\circ\text{C}, n=1$, (b) $T_w = 140^\circ\text{C}, n=3$ and (c) $T_w = 160^\circ\text{C}, n=1$

For continued heating until $t^* = 1.2$, the buoyancy force on the liquid increases and a two-phase zone forms above the heated section. The shape of the liquid saturation profile may be described as a longitudinal dome [52]. As explained before, the two-phase zone consists of both liquid and vapor coexisting. At this moment, only a small amount of liquid is vaporized and the vapor fraction is not sufficient for the complete phase change process. For continued heating until $t^* = 2$, the buoyancy force on the liquid becomes stronger and the two-phase zone expands as more liquid vaporizes. The longitudinal dome shape of the liquid saturation profile starts to slightly change and moves towards the outlet. Due to the density of the vapor being much lower than that of the liquid, the two-phase region expands. After flowing through the two-phase zone, a larger shear force is exerted on the liquid at the rearward of the two-phase zone due to accelerated main stream flow and, therefore, the liquid saturation at the outlet is increased [52]. As heating continues, the effect of buoyancy on the liquid becomes so significant at $t^* = 3$ that the two-phase zone further expands as more liquid is vaporized. With the expansion of the two-phase zone, the dome-shaped liquid saturation profile is totally changed. The liquid saturation profile declines towards the outlet due to the buoyancy force. The steady-state solution is achieved at $t^* = 6$. At this time, the minimum liquid saturation s has been found at the exit of the duct and the quantity of vapor is significantly increased.

On the other hand, Figures 4.10(b) and 4.10(c) demonstrate the transient behavior of liquid saturation for the complete phase change process at $T_w = 140\,^{\circ}\mathrm{C}$, $n = 3$ and $T_w = 160\,^{\circ}\mathrm{C}$, $n = 1$, respectively. In both cases, simulations can be performed for a very low liquid saturation level, although a complete vapor phase can never be achieved. This is possibly due to the presence of a sharp discontinuity in the modeled Ω_H, especially at the interface between two-phase and superheated vapor regions [see Fig. 2.2(d)], which cannot be eliminated using conventional treatments, and hence requires special attention. Therefore, a remedy similar to the one used for Γ_H is suggested for Ω_H in order to overcome the aforementioned problem (i.e., discontinuity in Ω_H) using the LTE model, and it is a logical extension of the work but generally remains unsuccessful. It may be noted here that the results presented in Fig. 4.10 have been finally obtained with the code that works without smoothing algorithm using the results obtained with smoothing as the guessed solution for both Γ_H and Ω_H. Thus, the aforementioned problem due to the modeled Ω_H could be eliminated for the LTNE model [see Eq. (2.150) along with LTNE model as compared to the Ω_H along with LTE model in Table 2.3] as will be discussed later in chapter 5. It is also observed from Fig. 4.10(b) that the behavior of the liquid saturation profile for $n = 3$ is quite different from the result for $n = 1$in Fig. 4.10(a). This is reasonable due to the effect of the exponent n in the expression of relative permeability as explained in subsection 4.1.5.

4.2. Modeling of One-dimensional Problems Based on Modified Enthalpy Formulation

As discussed earlier in chapter 2, a careful look into the conservation of energy for the original enthalpy formulation of TPMM proposed by Wang and Beckermann [29] reveals that this model is not readily suitable for numerical implementation due to the volumetric enthalpy not being a monotonic function of the thermodynamic state in the two-phase region and several other reasons. To avoid these difficulties, Wang [33] proposed a different form of modified volumetric enthalpy (H-formulation) for efficient numerical simulation of two-phase flow within porous media.

Nevertheless, the simulation based on the H-formulation requires significantly higher computational time in order to achieve convergence. In this situation, the original enthalpy formulation of the energy conservation equation is modified in order to remove the complexity in the volumetric enthalpy (ρh) of TPMM [29] for efficient numerical simulation of complete liquid-vapor phase change process inside porous media, i.e., with reduced computational time.

The complete phase change problem involving water as the phase change fluid inside a porous evaporator under steady-state condition has been considered as a demonstrative example in the present investigation. The schematic representation of the problem geometry is shown in Fig. 4.1 along with its relevant dimensions. For simplicity, a one-dimensional pipe, with constant cross-sectional area in the axial direction and filled with a known porous medium, has been considered for the present analysis. It has unheated inlet and exit lengths sections, l_i and l_e, respectively. The length of the heated section is l_h. The evaporator wall in the heated section has been either subjected to a prescribed $\dot{q}''_w$ or maintained at a constant temperature $T_w > T_{sat}$. In the latter case, however, heat is assumed to be transferred from the evaporator wall to the combined medium due to a specified heat transfer coefficient h_{co}. The sub-cooled liquid water at the inlet with a velocity u_{in} and at a temperature $T_{in} < T_{sat}$ flows through the evaporator due to the application of an external pressure gradient, which is then heated to the superheated vapor state.

The equations governing the respective one-dimensional formulation (where the variations occur only in the axial direction) have been obtained by integrating the multi-dimensional (axi-symmetric) conservation equations (2.130), (2.131), (2.134) and (2.138) over the evaporator cross-section for both models. For simplicity, only the steady-state phase change process within a homogenous as well as isotropic porous medium of known characteristics has been considered for both h- and H-formulations, with LTE condition. The governing mass and momentum conservation equations remain respectively identical for both formulations, as given in Eqs. (4.1) and (4.2). For constant wall heat flux applications, integration of Eq. (2.138) (for modified h-formulation) and Eq. (2.134) (for H-formulation) over the evaporator cross-section yields the following steady one-dimensional forms of the energy conservation equations:

$$\frac{d}{dx^*}\left(\gamma_h \rho^* u_x^* h^*\right) = \frac{d}{dx^*}\left(\Gamma_h^* \frac{\partial h^*}{\partial x^*}\right) + \frac{d}{dx^*}\left(f \frac{K^* \Delta\rho^* h_{fg}^*}{\nu_v^*} b_x^*\right) + \frac{P^*}{A_c^*} \dot{q}_w''^* \tag{4.10}$$

$$\frac{d}{dx^*}\left(\gamma_H u_x^* H^*\right) = \frac{d}{dx^*}\left(\Gamma_H^* \frac{\partial H^*}{\partial x^*}\right) + \frac{d}{dx^*}\left(f \frac{K^* \Delta\rho^* h_{fg}^*}{\nu_v^*} b_x^*\right) + \frac{P^*}{A_c^*} \dot{q}_w''^* \tag{4.11}$$

It may be noted here that during integration, the boundary condition at the evaporator wall has been incorporated into an appropriate source term for both one-dimensional formulations. Further, in Eqs. (4.10) and (4.11), $\dot{q}_w''^* = Q_w^* / Re_l$ with $Q_w^* = \dot{q}_w'' R / \mu h_{fg}$ is the prescribed dimensionless heat flux at the duct surface. Since all lengths have been made dimensionless with respect to the radius of the evaporator, $P^* = 1$ and $A_c^* = 1/2$ are obtained per unit radian and hence $P^*/A_c^* = 2$ may be substituted.

For constant wall temperature, on the other hand, the wall heat flux may be modeled as $\dot{q}_w'' = h_{co}(T_w - T)$, where h_{co} is the specified convective heat transfer coefficient, as described in section 4.1. For the case of prescribed wall temperature, the energy conservation equation based on the H-formulation is already given in dimensionless form by Eq. (4.3), whereas the energy conservation equation (4.10) based on the modified h-formulation may be obtained as:

$$\frac{d}{dx^*}\left(\gamma_h \rho^* u_x^* h^*\right) = \frac{d}{dx^*}\left(\Gamma_h^* \frac{dh^*}{dx^*}\right) + \frac{d}{dx^*}\left(f \frac{K^* \Delta\rho^* h_{fg}^*}{\nu_v^*} b_x^*\right) + \frac{Nu_o}{Pe_l}\left(T_w^* - T^*\right) \tag{4.12}$$

In order to solve one-dimensional conservation equations (4.1) – (4.3) and (4.10) – (4.12), boundary conditions for both h- and H-formulations are required only in the axial direction at the inlet and the exit. At the inlet, i.e., at $x^* = 0$, $u_x^* = u_{in}^* = 1$ $\rho_{in}^* = 1$, $h_{in}^* = h_{l,sat}^* - C_{pl}^*\left(T_{sat}^* - T_{in}^*\right)$ (modified h-formulation) and $H_{in}^* = \rho_{in}^*\left[h_{l,sat}^* - \rho_{in}^* C_{pl}^*\left(T_{sat}^* - T_{in}^*\right) - 2h_{v,sat}^*\right]$ (for H-formulation) have been set. At the outlet, i.e., at $x^* = L/R$, the second derivatives of h^* and H^* have been set to zero [see Eqs. (3.13) and (3.14)]. The mass flow rate at the inlet ($\rho_{in}^* u_{in}^*$) has been set to unity and hence the local velocity u_x^*, which is required for evaluating the convective terms for H-formulation, has been obtained from ρ^* as $u_x^* = 1/\rho^*$. Prior to obtaining results for the present investigation, a detailed grid independence study has been carried out and it has been observed that at least 400 uniform control volumes are required in order to obtain nearly grid independent results and further grid refinement does not significantly modify the presented solutions. During iterations, however, the discretized equations have been further under-relaxed, where typical under-relaxation factors of 0.4 and 0.1 have been used for modified h- and H-formulations, respectively, in order to achieve a converged solution for most of the simulations reported in this work. For all tested cases, the convergence criterion has been set to 10^{-6}, which has been judiciously chosen such that the choice does not significantly affect the solution.

4.2.1. Ranges of Parameters and General Remarks

The major objective of the present investigation is to obtain numerical simulations of the complete phase change process inside a porous evaporator using the modified h-formulation and to compare the predictions with those obtained using the H-formulation. All simulations, presented in this section for either modified h- or H-formulation, have been carried out under application of the smoothing strategy proposed in the present work for either Γ_h^* or Γ_H^* in order to avoid the occurrence of a non-physical “jump” in the predicted temperature distribution.

In order to demonstrate the applicability of the h-formulation, for all tested cases, a circular pipe of radius $R = 25\,\text{mm}$, i.e., $R^* = 1$, and with an overall length $L = 500\,\text{mm}$ and hence $L^* = 20$ has been considered. The length of the heated section l_h depends on the specific choice of the inlet and the exit lengths l_i and l_e, respectively. In the present investigation, l_i has been varied between 0, i.e., heating starts from the beginning of the duct, and $0.2L$, whereas l_e has been kept fixed at $0.1L$. Thus, the considered inlet and exit lengths have been given in non-dimensional form as

$l_i^* = 0-4$ (variable) and $l_e^* = 2$ (fixed). For the reference case, both l_i and l_e have been considered to equal $0.1L$ and hence $l_h = 0.8L$ has been specified. The properties of the porous medium, i.e., the porosity, the permeability and the thermal conductivity of the solid matrix, and the inlet flow condition, i.e., the inlet temperature and the inlet velocity or mass flow rate, have been taken identical to those given in subsection 4.1.5. As far as the heating condition applied only for the heated section of the evaporator $l_i^* \le x^* \le l_i^* + l_h^*$ is concerned, $\dot{q}_w''$ has been varied from $2\,\mathrm{kW/m^2}$ to $3\,\mathrm{kW/m^2}$ for the constant wall heat flux condition. On the other hand, T_w has been varied between $140\,^{\mathrm{o}}\mathrm{C}$ and $200\,^{\mathrm{o}}\mathrm{C}$ for constant wall temperature cases. Furthermore, $Nu_o = 4$ has been assumed for the latter cases, which is responsible for the heat transfer due to convection from the evaporator wall to the working fluid, as described in subsection 4.1.2. Based on the dimensional parameters given in subsection 4.1.2 and the properties of water in Table 2.1, in the present investigation, the ranges of dimensionless parameters, i.e., L^*, ε, K^*, $k_{s,ref}^*$ and Re_l, have been already given in subsection 4.1.2. These parameters are not repeated here for the sake of brevity. In addition, the value of dimensionless heat flux Q_w^* has been varied from 8.5×10^{-2} to 10.5×10^{-2}.

In the present investigation, the reference case has been specified with the following parameters: $Re_l = 2$ (the inlet condition, other than $T_{in} = 20\,^{\mathrm{o}}\mathrm{C}$), $\varepsilon = 0.3$, $K^* = 10^{-8}$, $k_s^* = 8.25$ (properties of the porous medium), $Q_w^* = 9.5\times10^{-2}$ (for constant heat flux), $T_w = 160\,^{\mathrm{o}}\mathrm{C}$ (for constant wall temperature, other than $Nu_o = 4$), $L^* = 20$, $l_i^* = l_e^* = 2$ and hence $l_h^* = 16$ (the problem geometry). These parameters have been kept unaltered for all cases, unless their effects on the phase change process have been analyzed. In the present investigation, the effects of Reynolds number, wall temperature, heat flux, porosity, Darcy number, thermal conductivity of the solid phase and inlet length of the evaporator have been investigated.

The necessity and usefulness of the proposed smoothing algorithm for the effective diffusion coefficient have been already demonstrated in section 4.1 for LTE assumption, while employing the existing *H*-formulation. For the modified *h*-formulation, it has been observed that unless the smoothing algorithm, described in chapter 2, is implemented, the solutions always exhibit a jump in the predicted temperature, particularly close to the saturated vapor condition. The results are already presented in section 2.3 and are not repeated here for the sake of convenience. It can be safely concluded that he proposed smoothing algorithm for the modified *h*-formulation provides also a successful remedy for the occurrence of “jump” in the predicted temperature distribution.

It may be mentioned here that all reported computations have been carried out on a desktop personal computer that has Intel Core i7 2.80GHz CPU with 4 cores, each consisting of 4GB DDR3 1333MHz RAM made by Hynix semiconductor, as its configuration, although its parallel processing features have not been utilized during the present investigation. The typically required computation time on this machine for the present one-dimensional phase change problems has been recorded to vary between 1 to 12 minutes.

4.2.2. Comparison of Results for both Constant Heat Flux and Wall Temperature

The predictions obtained from h- and H-formulations are compared with each other for constant heat flux applications and the results, in the form of axial temperature distributions, are presented in Figs. 4.11 – 4.13 in order to investigate the influence of various controlling parameters on the accuracy. It is quite evident from the figures that for all tested constant heat flux cases, variations in the axial temperature, as predicted by both formulations, are nearly identical and excellent agreement is obtained. For the reference case, the average absolute difference in the predicted T^* (or T) has been found to be 0.04%, which expectedly decreases with the increase in employed grid size. Particularly for this case, the modified h-formulation requires approximately 50% less computational time as compared to the existing H-formulation and hence is a better option for the simulation of the complete phase change process inside porous media. The effects of heating and flow conditions on the axial temperature distributions in Fig. 4.11 show that the increase in Q_w^* for a fixed Re_l enhances the outlet temperature, whereas with the increase in Re_l, the outlet temperature decreases considerably. It can also be observed from Fig. 4.11(a) that the effect of heat flux is more evident in the vapor phase and is less prominent for the liquid phase. Although both observations are expected, Fig. 4.11 clearly indicates that a marginal change in the operating conditions, either applied Q_w^* or Re_l, can lead to a substantial change in the exit temperature. For instance, at $Re_l = 1.25$, if a high heat flux of $Q_w^* = 9.5\times10^{-2}$ is applied, which is not even sufficient to produce complete phase change for $Re_l = 4$, see Fig. 4.11(b), the exit temperature could be higher than $600\,^{o}\mathrm{C}$. This result is not shown in the figure due to the undesirably high temperature and in order to restrict the temperature data to a reasonable range. Consequently, the results are presented for a lower Q_w^* for the low Re_l in Fig. 4.11(b).

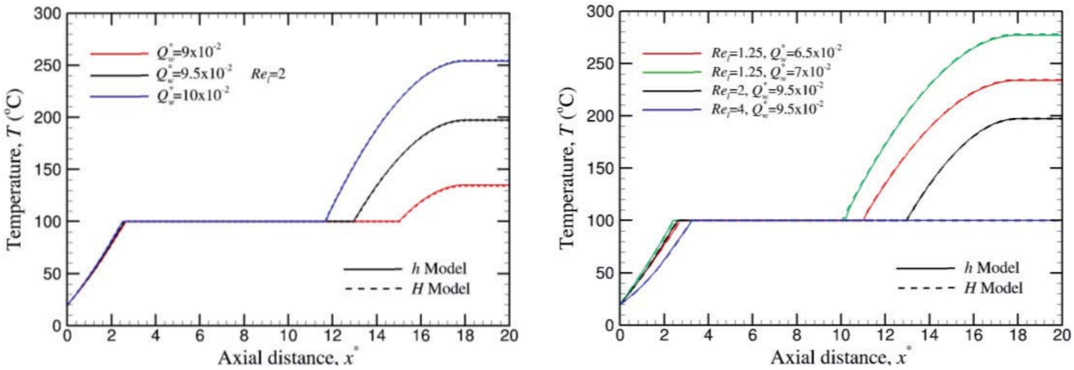

(a) (b)

Fig. 4.11: Effects of heating and flow conditions on the axial temperature distribution for constant wall heat flux cases with $\varepsilon = 0.3$, $K^* = 10^{-8}$, $k_s^* = 8.25$ and $l_i^* = 2$: (a) effect of applied heat flux for $Re_l = 2$ and (b) effect of inlet Reynolds number for different Q_w^*

Figure 4.12 shows the effects of porous media properties in the form of porosity ε in Fig. 4.12(a), permeability K^* in Fig. 4.12(b) and thermal conductivity of the solid k_s^* in Fig. 4.12(c) on the temperature variations as functions of the axial distance. It is clear from the figure that the Darcy number and the thermal conductivity of the solid phase strongly affect the temperature distribution in the evaporator, while the porosity of the medium has only marginal influence on the length of the two-phase zone and the outlet temperature. As evident from the definition of k_{eff}^{*} in Eq. (2.135), the effective diffusion coefficient Γ_h^* for modified h-formulation or Γ_H^* for H-formulation decreases in the single phase regions for an increase in porosity ε or a decrease of the solid phase thermal conductivity k_s^*. In the single phase region, k_{eff}^{*} is a linear function of ε. As a result, the effective diffusion coefficient, i.e., Γ_h^* or Γ_H^* decreases linearly with the increase in ε. In the two-phase region, on the other hand, the effective diffusion coefficient is enhanced with the increase in ε or K^* irrespective of the model. Furthermore, the effective diffusion coefficient in both models is not affected by the increase in the solid thermal conductivity due to the isothermal assumption. For the two-phase region, dT^*/dH^* and dT^*/dh^* are equal to zero. As a result, phase change initiates earlier and terminates later when the porosity and Darcy number are increased from 0.2 to 0.4 and from 10^{-9} to 10^{-7}, respectively, as shown in Figs. 4.12(a) and Fig. 4.12(b). This is due to the increase of the diffusive heat loss through the inlet. On the other hand, an increase in k_s^* leads to a delay in the initiation and termination of the phase change process due to higher heat loss through the inlet, see Fig. 4.12(c).

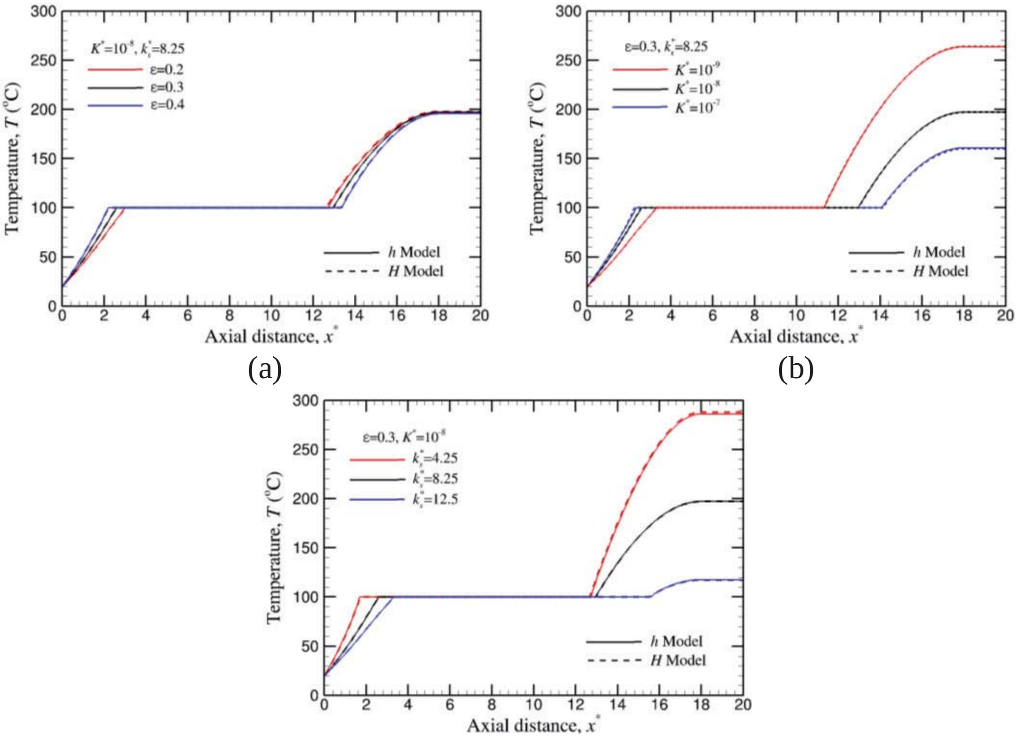

(a) (b)

(c)

Fig. 4.12: Effects of porous media properties on the axial temperature distribution for constant wall heat flux cases with $Re_l = 2$, $Q_w^* = 9.5\times10^{-2}$ and $l_i^* = 2$: (a) effect of porosity, (b) effect of Darcy number and (c) effect of thermal conductivity of the solid phase

Furthermore, the effect of the unheated starting length on the axial temperature profile, as shown in Fig. 4.13, is fairly straightforward. It is also evident from the figure that the quality of steam at the exit is extremely sensitive to the length of the heated section, and hence adequate care must be taken while designing such evaporators in order to meet the process requirements. Nevertheless, for all tested cases with considerably low mass flow rates, the axial diffusion in the upstream direction plays an extremely important role with respect to the predicted temperature distributions. Since the reasons for such occurrences have been elaborately explained in section 4.1 while obtaining the results with the conventional H -formulation, they are not repeated here for the sake of brevity.

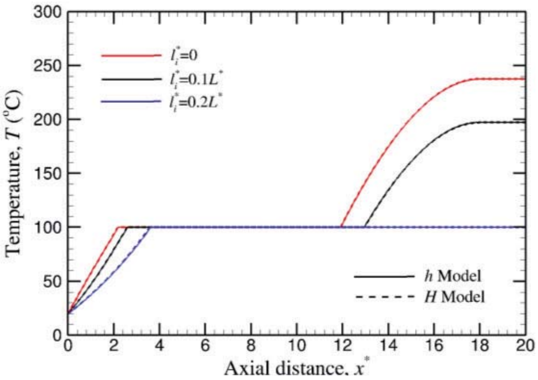

Fig. 4.13: Effect of inlet length on the axial temperature distribution for constant wall heat flux cases with $Re_l = 2$, $Q_w^* = 9.5\times10^{-2}$, $\varepsilon = 0.3$, $K^* = 10^{-8}$ and $k_s^* = 8.25$

Concerning the prescribed wall temperature cases, obtained with the modified h-formulation are compared with those predicted by the H -formulation as presented in Figs. 4.14 – 4.16. The effects of wall temperature and inlet Reynolds number are presented in Fig. 4.14, whereas the influences of porous media properties and unheated starting length are shown in Figs. 4.15 and 4.16, respectively. The figures clearly ascertain that for all tested cases with constant temperature at the evaporator wall, excellent agreement between both formulations in the predicted axial temperature distributions could be achieved, which can also be regarded as a proof of the consistency of the modified h-formulation. The average absolute difference in the predicted T^* has been recorded to be 0.08% for the reference case, for which the present formulation requires approximately 12.5% less computational time as compared to the existing H -formulation. For the present one-dimensional formulation, the heating conditions at the wall have been incorporated as source terms in Eqs. (4.3), (4.10) – (4.12) that result directly from the integration process. Therefore, constant wall temperature applications require iterative calculation of the source term and hence less computational time is saved compared to the constant Q_w^* cases, where the source term can be directly evaluated. For multi-dimensional problems, however, it is expected that problems with a Dirichlet boundary conditions (for constant T_w) in the transverse direction would require less computational time as compared to that with the Neumann boundary conditions (for constant Q_w^*) and hence the modified h-formulation would be even more beneficial. As mentioned in chapter 2, the issues related to the multi-dimensional problems are left beyond the scope of the present investigation, since they could not be addressed without substantially deviating from the major objective of the present work, and shall possibly be taken up in a separate study in the future.

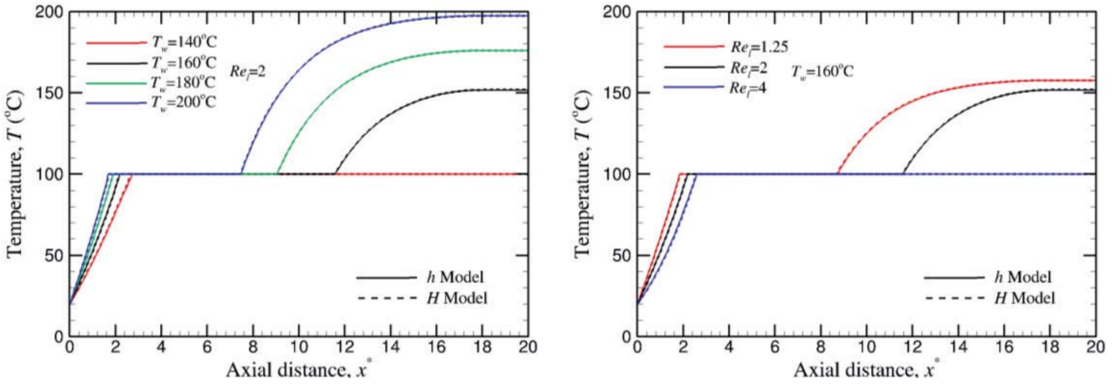

(a) (b)

Fig. 4.14: Effects of heating and flow conditions on the axial temperature distribution for constant wall temperature cases with $\varepsilon = 0.3$, $K^* = 10^{-8}$, $k_s^* = 8.25$ and $l_i^* = 2$: (a) effect of wall temperature for $Re_l = 2$ and (b) effect of inlet Reynolds number for $T_w = 160\,°\mathrm{C}$

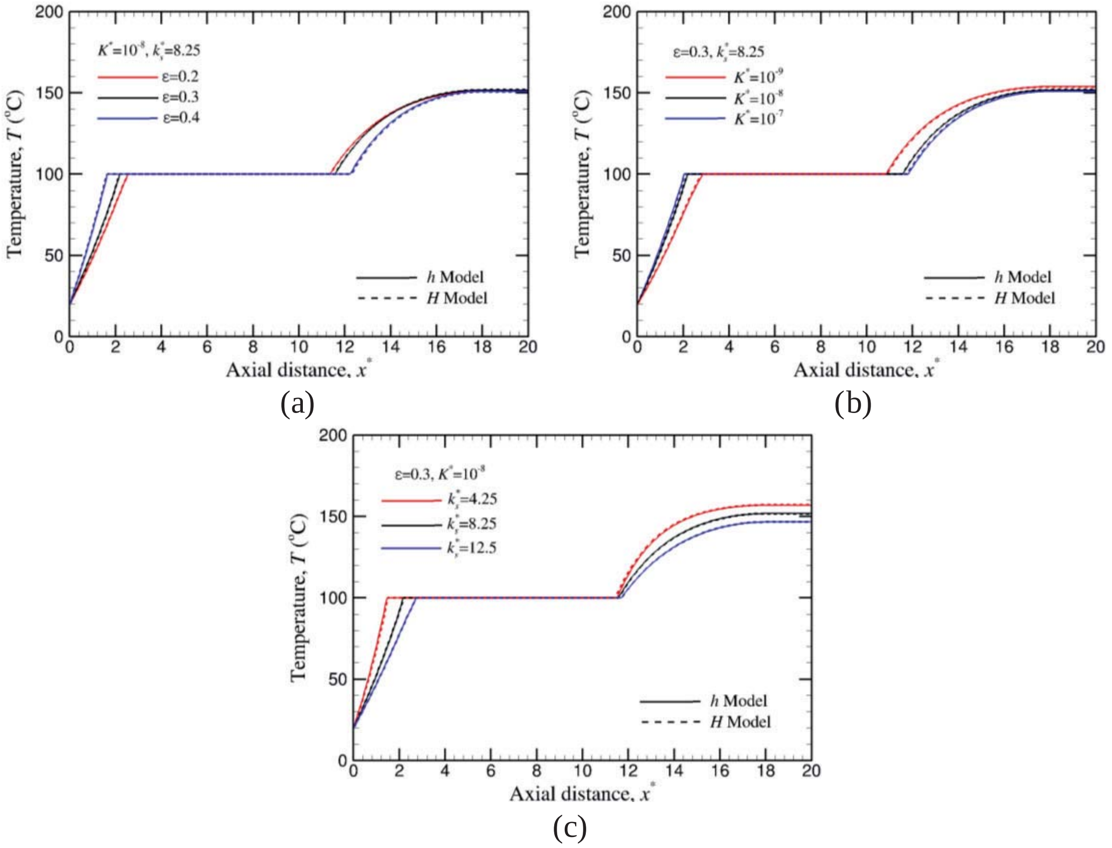

(a) (b)

(c)

Fig. 4.15: Effects of porous media properties on the axial temperature distribution for constant wall temperature cases with $Re_l = 2$, $T_w = 160\,°\mathrm{C}$ and $l_i^* = 2$: (a) effect of porosity (b) effect of Darcy number and (c) effect of thermal conductivity of the solid phase

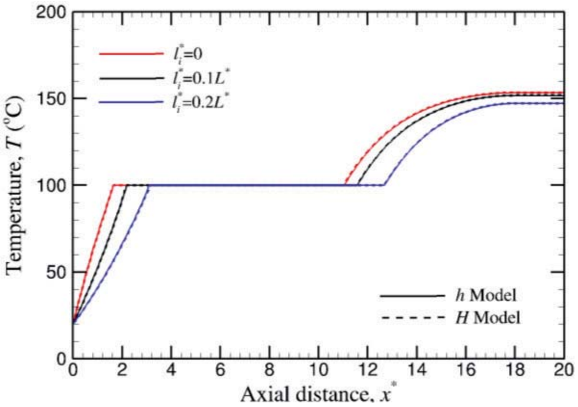

Fig. 4.16: Effect of inlet length on the axial temperature distribution for constant wall temperature cases with $Re_l = 2$, $T_w = 160\,°\mathrm{C}$, $\varepsilon = 0.3$, $K^* = 10^{-8}$ and $k_s^* = 8.25$

4.3. Modeling in Two-dimensional Coordinates using Staggered Grid Layout

Although any physical phenomenon and hence the phase change problem inside porous media is inherently multi-dimensional, steady one-dimensional idealization has been often used as simplification [57, 58, 65 – 67, 69, 75]. Such a simplification, however, may not be appropriate in the presence of asymmetry, which may occur due to flow and (or) heating conditions. Most importantly, although the cross-sectional averaged properties of the flow could still be approximately predicted by the one-dimensional model, multi-dimensional formulation would be inevitable in order to determine the local characteristics. As far as two-dimensional predictions are concerned, most of the investigations mentioned in chapter 1 dealt with incomplete phase change process inside porous medium, except Wang [33] and Lindner et al [68], they presented results employing the LTE and LTNE models, respectively, with a localized heat source on one of the walls of a parallel plate channel. For example, a careful look into the results of Wang reveals that although the formation of superheated vapor phase close to the heated surface could be clearly observed, the predictions were also associated with a substantial temperature change within a very short distance, in the range of $100^{\mathrm{o}}\mathrm{C}$ and $500^{\mathrm{o}}\mathrm{C}$ between two successive isotherms for porous media composed of steel and glass beads, respectively. Such apparently unrealistic predictions may be either attributed to the discontinuities in the effective diffusion coefficient as mentioned before, or they could have resulted from the simplified LTE assumption. In order to eliminate both these possibilities, in the present investigation, numerical simulation for the complete phase change process of water have been obtained employing the smoothing of effective diffusion coefficient for both LTE (in this chapter) and LTNE (in chapter 5) models. For this purpose, two-dimensional flow inside an asymmetrically heated parallel plate channel, similar to that adopted by Wang, and in a circular pipe, filled with a porous medium of known properties, has been considered and the results obtained for both problems have been compared with those obtained using the LTNE model (in chapter 5) for identical conditions in order to judge the applicability of the present approach.

4.3.1. Problem Description and Basic Assumptions

A schematic representation of the physical problem, along with the possible locations of the interface between the single-phase and the two-phase regions, is shown in Figs. 4.17(a) and 4.17(b) for parallel plate channels and circular pipes, respectively. The problem geometry for the channel is similar to the one adopted by Wang. Both porous parallel plate channel and circular pipe are of length L in the flow (axial) direction, while the plates are separated by a distance W and the pipe radius is R. The upper plate of the channel has been considered adiabatic, whereas the bottom plate of the channel as well as the pipe wall have unheated, i.e., adiabatic, inlet and exit lengths of l_i and l_e, respectively, complemented by a heated section of length l_h, supplying either constant heat flux or constant wall temperature with a specified heat transfer coefficient. An external pressure gradient drives the sub-cooled water, with a low temperature T_{in} and a uniform velocity u_{in} at the inlet, through the channel or pipe, compare Fig. 4.17. The temperature of water increases as it flows through the asymmetrically heated cross-section. When sufficient heat is added, boiling starts close to the heated surface of the channel or pipe and thereby a two-phase region is formed, which also spreads towards the core of the channel or pipe and extends to a larger fraction of the cross-sectional area in the downstream direction. Further addition of heat eventually leads to the formation of a superheated vapor zone. Quite obviously, the size of this region, which is also referred to as the dry-out zone [33, 52], primarily depends on both the magnitude of the heat flux and the mass flow rate through the channel or pipe. The porous medium inside the channel or pipe, on the other hand, has been considered homogenous as well as isotropic and its properties have been assumed to be known a priori.

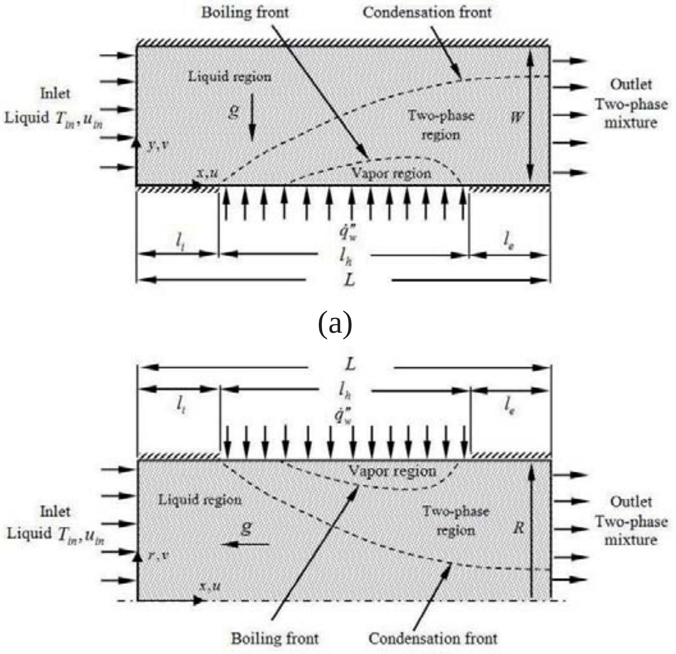

(a)

(b)

Fig. 4.17: Schematic representation of the phase change problem for (a) channel [33] and (b) pipe flows

The existing formulation based on the H-formulation, which is briefly presented here for the sake of completeness, is applied for a steady, two-dimensional complete phase change process within a porous medium due to localized asymmetric heating inside a parallel plate channel or circular pipe. Adopting the H-formulation, a set of equations governing the conservation of mass, momentum, and energy are introduced along with the assumption of the LTE model. The conservation of mass and momentum in Eqs. (2.130) and (2.131) are presented in dimensionless form for a multi-dimensional problem using cylindrical axi-symmetric coordinates as:

$$\frac{\partial}{\partial x^*}\left(\rho^* u^*\right)+\frac{1}{r^*}\frac{\partial}{\partial y^*}\left(r^* \rho^* v^*\right)=0 \tag{4.13}$$

$$\mathbf{u}^* = -\frac{K^*}{\mu^*}\left[\nabla^* p^* - \rho_k^* \mathbf{b}^*\right] \tag{4.14}$$

where the definitions of the dimensionless mixture properties ρ^*, μ^*, K^* for the two-phase flow, appearing in Eqs. (4.13) and (4.14), are given in section 2.2. In Eq. (4.13), $r^* = 1$ is used when considering channel flow, whereas $r^* = y^*$ is employed when considering pipe flow. It may be noted here that according to the TPMM formulation, the momentum equation given in Eq. (4.14) considers only Darcy's law [29, 30, 33], accounting for the additional pressure drop due to the presence of a porous matrix, and the body-force. Since the convective, or inertial, and diffusive effects have been neglected for the momentum transport, Eq. (4.14) is valid only for low mass flow rate applications, where the fluid Reynolds number based on the permeability of the porous medium, $Re_K = \rho u\sqrt{K}/\mu$, is less than unity [63]. Concerning the issues related to the substantial density variations occurring due to the significant temperature differences in the single phase regions, chapter 2 presents the modification required for the formulations based on the H-formulation in order to accommodate this behavior. Nevertheless, since the primary objective of the present study is to compare the results obtained with LTE and LTNE (in chapter 5) models for realistic prediction of the phase change process inside a porous channel or pipe, the issues related to the use of non-Boussinesq approximation for the single phase densities (i.e., for large density variations in the sub-cooled liquid and superheated vapor phases) have been left beyond the scope of the present investigation.

On the other hand, the energy conservation in Eq. (2.134) may be written for steady-state condition by dropping the transient term as:

$$\begin{aligned}\frac{\partial}{\partial x^*}\left(\gamma_H u^* H^*\right)+\frac{1}{r^*}\frac{\partial}{\partial y^*}\left(\gamma_H r^* v^* H^*\right)&=\frac{\partial}{\partial x^*}\left(\Gamma_H^* \frac{\partial H^*}{\partial x^*}\right)+\frac{1}{r^*}\frac{\partial}{\partial y^*}\left(\Gamma_H^* r^* \frac{\partial H^*}{\partial y^*}\right)\\&+\frac{\partial}{\partial x^*}\left(f\,\frac{K^*\Delta\rho^* h_{fg}^*}{\nu_v^*}\,b_x^*\right)+\frac{1}{r^*}\frac{\partial}{\partial y^*}\left(r^* f\,\frac{K^*\Delta\rho^* h_{fg}^*}{\nu_v^*}\,b_y^*\right)\end{aligned} \tag{4.15}$$

where the definitions of mixture properties and constitutive relations of quantities appearing in Eq. (4.15) are provided in Tables 2.2 and 2.3.

In order to solve the governing conservation equations (4.13) – (4.15), the fulfillment of the respective boundary conditions is required at the inlet, on the walls, and at the outlet. For the present investigation, the following conditions have been employed for both channel and pipe flow models at different boundaries of the computational domain:

At the inlet, i.e., for $x^* = 0$ and $0 \le y^* \le W^* = 1$ (or $R^* = 1$), the porous medium has been assumed to be saturated with sub-cooled liquid water that enters the evaporator with uniform velocity u_{in}^* at a specified temperature T_{in}^*, which is less than the dimensionless saturation temperature. Consequently, the boundary conditions prescribed at the inlet may be summarized as:

$$\rho_{in}^{*} = 1 \tag{4.16a}$$

$$H_{in}^{*} = \rho_{in}^{*}\left[h_{l,sat}^{*} - \rho_{in}^{*} C_{pl}^{*}\left(T_{sat}^{*} - T_{in}^{*}\right) - 2h_{v,sat}^{*}\right] \tag{4.16b}$$

$$u^{*} = u_{in}^{*} \tag{4.16c}$$

$$v^{*} = 0 \tag{4.16d}$$

At the outlet, i.e., for $x^{*} = L^{*}$ and $0 \le y^{*} \le W^{*} = 1\ (\text{or}\, R^{*} = 1)$, the second derivatives of all variables have been set to zero. For this reason, the volumetric enthalpy H^{*} at the outlet has been obtained by linearly extrapolating the values at the neighboring interior nodes to ensure $\partial^{2} H^{*} / \partial x^{*2} = 0$. On the other hand, the flow has been assumed to be hydro-dynamically fully-developed at the exit as given in Eq. (4.17), which is quite reasonable for the present investigation in the presence of an unheated exit length filled with a porous medium, and the local density has been calculated according to the relation provided in Table 2.3. In detail, the boundary condition at the exit may be written as:

$$\frac{\partial u^{*}}{\partial x^{*}} = \frac{\partial v^{*}}{\partial x^{*}} = 0 \tag{4.17}$$

Both top and bottom walls of the channel located at $y^{*} = 1$ and $y^{*} = 0$ for $0 \le x^{*} \le L^{*}$ as well as the center and the wall of the pipe at $y^{*} = 0$ and $R^{*} = 1$ for $0 \le x^{*} \le L^{*}$ have been considered to be impermeable by imposing a vanishing normal velocity component all along the axial extent of the domain. As far as the energy conservation equation is concerned, the specified heat flux boundary condition has been employed at the walls for both problems, where a vanishing local heat flux $\dot{q}_{w,x}''^{*} = \dot{q}_{w}''^{*} = 0$ has been enforced at the unheated segments, i.e., for $0 \le x^{*} \le l_{i}^{*}$ and $l_{i}^{*} + l_{h}^{*} \le x^{*} \le L^{*}$. The conditions may be formulated as:

$$-\Gamma_{H}^{*} \frac{\partial H^{*}}{\partial y^{*}} = f \, \frac{K^{*} \Delta\rho^{*} h_{fg}^{*}}{\nu_{v}^{*}} b_{y}^{*} \tag{4.18a}$$

$$v^{*} = 0 \tag{4.18b}$$

At the position of the wall being heated, either the local heat flux $\dot{q}_{w,x}''^{*} = \dot{q}_{w}''^{*}$ or the wall temperature T_{w}^{*} has been set only for the heated segment on the bottom wall of the channel or the pipe wall, i.e., for $l_{i}^{*} \le x^{*} \le l_{i}^{*} + l_{h}^{*}$. Thus, the boundary conditions may be expressed here as:

$$-\Gamma_{H}^{*} \frac{\partial H^{*}}{\partial y^{*}} - f \, \frac{K^{*} \Delta\rho^{*} h_{fg}^{*}}{\nu_{v}^{*}} b_{y}^{*} = \dot{q}_{w,x}''^{*} \tag{4.19a}$$

$$v^{*} = 0 \tag{4.19b}$$

4.3.2. Comparison of One- and Two-dimensional Models

This subsection provides the results obtained with the two-dimensional model of the incomplete phase change process for pipe flow, as shown in Fig. 4.17(b). These results are then compared with those obtained from one-dimensional simulations. Additionally, the influence of the boundary condition at the heated wall segments on the temperature distribution is considered for either constant wall temperature with a specified heat transfer coefficient or constant heat flux and is compared to the average temperature distribution as a function of the axial direction for two-phase flow, as shown in Figs. 4.18 and 4.19, respectively. A detailed grid independence study has been carried out, where it has been observed that $N_{CV} = 400 \times 20$ uniform control volumes are required for obtaining grid independent solutions. It may be noted here that the number of control volumes in the axial direction has been kept similar to the one employed for the one-dimensional problem in section 4.1. As mentioned before, the pipe radius $R = 25\,\mathrm{mm}$, i.e., $R^* = 1$ has been considered for the analysis, whereas the overall length has been fixed to $L = 500\,\mathrm{mm}$, i.e., $L^* = 20$. The unheated inlet and exit lengths have been assumed to coincide with those in the one-dimensional problem, i.e., $l_i^* = l_e^* = 2$, which yields $l_h^* = 16$. For the purpose of comparison with the respective one-dimensional results, the following parameters have been used: $\varepsilon = 0.3$, $K^* = 10^{-8}$, $k_s^* = 8.25$, $Re_l = 4$ and either $T_w = 160^{\circ}\mathrm{C}$ when using constant wall temperature at the heated wall segment, other than $Nu_o = 4$ or $Q_w^* = 9.5 \times 10^{-2}$ when using constant heat flux.

Fig. 4.18: Temperature contours for incomplete phase change process using two-dimensional pipe flow model for constant (a) wall temperature and (b) heat flux

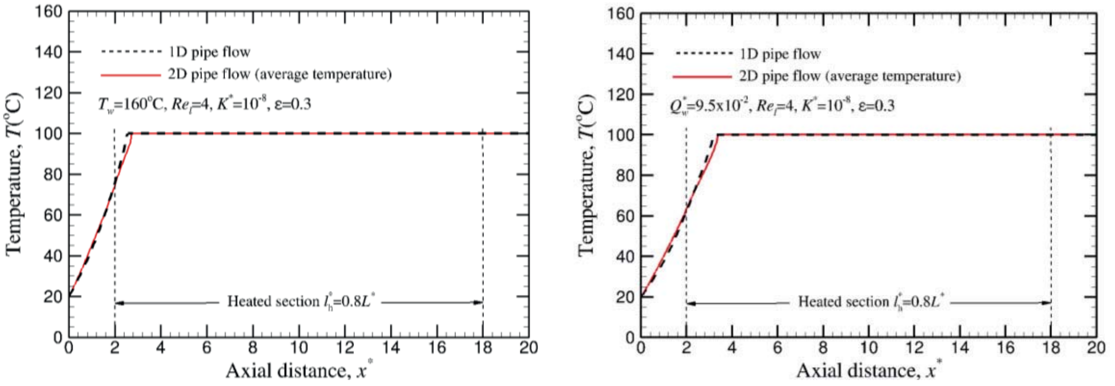

(a) (b)

Fig. 4.19: Comparison of temperature variations as a function of axial distance for one- and two-dimensional pipe flow models with constant (a) wall temperature and (b) heat flux

Figures 4.18 (a) and 4.18 (b) show the temperature distributions of incomplete phase change process obtained from the pipe flow model using either constant wall temperature with specified heat transfer coefficient or constant heat flux, respectively. It is evident from the figure that the temperature contours are approximately vertical. This is reasonable due to the very low velocity considered and the high amount of thermal energy transferred to the domain, leading to a reduced effect of convection and dominant conduction, i.e., higher conductive heat loss through the inlet owing primarily to the enhanced effective diffusion coefficient. Figures 4.19(a) and 4.19(b) display the comparison of the average temperature with respect to the axial direction between one- and two-dimensional pipe flow models. It is evident from the figures that the numerical results exhibit a very reasonable agreement between one- and two-dimensional pipe flow models for the different heating conditions, where the main difference in the resulting temperature profiles presented in Figs. 4.19 (a) and 4.19 (b) is the length of the two-phase region. In view of the foregoing discussions and the results presented in Figs. 4.18 and 4.19, the following comments explain the variations observed. At first, it is evident that while the size of the two-phase region obtained with one- and two-dimensional pipe flow models for the same heating conditions is hardly distinguishable, minor variations in the temperature profiles are observed particularly close to the saturated liquid. In this regards, it should be mentioned that the effect of buoyancy force has been included in the two-dimensional problem, whereas it has been neglected in the one-dimensional problem. This explains the small difference in the axial temperature distribution between both models. It must be recognized that comparable results for the complete phase change process are not presented here due to an extremely high discontinuity predicted in the temperature distribution in the vicinity of the wall nodes. However, the behavior of the complete phase change process will be discussed in details in the next subsections for both channel and pipe flow models.

4.3.3. Simulation of Complete Phase Change Process in Channel Flow

This subsection focuses on fluid flow and heat transfer associated with liquid-vapor phase change processes in a horizontal porous channel [see Fig. 4.17(a)]. The simulations have been carried out applying the proposed smoothing algorithm to the effective diffusion coefficient Γ_H^* in order to avoid the occurrence of a jump in the predicted temperature distribution. The consequence of using the smoothing algorithm has been demonstrated in this investigation, where the employed smoothing parameters are identical to those used in subsection 4.1.2.

A. Ranges of Parameters

For all cases studied here, the considered geometric dimensions of the channel are $L = 300\text{mm}$, i.e., $L^* = 6$ and $W = 50\text{mm}$, i.e., $W^* = 1$ [see Fig. 4.17(a)]. The unheated inlet and exit lengths have been set to $l_i = l_e = 0.2L$ ($l_i^* = l_e^* = 1.2$), the resulting length of the heated surface at the bottom wall is $l_h = 0.6L$ ($l_h^* = 3.6$). The exit length has been carefully chosen in order to avoid an affect of the exit boundary condition on the internal solution. Sub-cooled liquid water enters the channel with uniform velocity $u_{in} = 5\times10^{-4}\ \text{m/s}$ ($u_{in}^* = 1$) and $T_{in} = 20^\circ\text{C}$. As will be shortly apparent, the inlet velocity in the present study is deliberately chosen to be small enough such that the condition $Re_K < 1$ is always satisfied for both liquid and vapor phases and hence Darcy's law in Eq. (4.14) could be invoked for the solution of the velocity field [63]. With these inputs and properties of water in Table 2.1, $Re_l = 85$ has been kept fixed throughout the present investigation. For the porous medium, the average pore diameter, the porosity and the permeability have been assumed to be around $100\mu\text{m}$, 0.4 and $K = 10^{-11}\ \text{m}^2$, respectively. Therefore, the dimensionless form,

$d_p^* = 2 \times 10^{-3}$ and $K^* = 5 \times 10^{-9}$ have been kept fixed for all considered cases. Further assuming the thermal conductivity of the solid phase to vary from $k_s = 40\,\mathrm{W/m\,K}$ to $k_s = 60\,\mathrm{W/m\,K}$ [89], $k_s^* = 0.5$ ($k_s = 50\,\mathrm{W/m\,K}$) has been chosen.

At the heated section, it has been assumed that heat is added from an external source, supplying a constant heat flux $\dot{q}_w''$, ranging from $100\mathrm{kW/m^2}$ to $400\mathrm{kW/m^2}$. Therefore, the dimensionless heat flux has been fixed in the range from $Q_w^* = 8$ to $Q_w^* = 32$. In addition, the acceleration due to gravity has been assumed to act in the negative y-direction, and hence $\tilde{b}_y = -1$ and $\tilde{b}_x = 0$ have been considered for all cases. The gravitational Reynolds number Re_g, required for the calculation of the Froude number Fr, and the normalized surface tension coefficient $\tilde{\sigma}$ have been specified as 1.2×10^5 and 3.6×10^7, respectively, based on the properties of liquid water listed in Table 2.1, $g = 9.81\mathrm{m/s^2}$ and $W = 50\,\mathrm{mm}$. Finally, for the calculation of relative permeability, $n = 3$ has been adopted without any exception. Steady-state combined temperature distribution, isoline liquid saturation and velocity fields have been analyzed for various values of the heat flux.

A detailed grid independence study has been carried out using a number of $N_{CV} = 100 \times 35$, 80×25, and 60×15 control volumes to ensure the stability of the solutions that are independent of the grid size. It has been found that the utilization of $N_{CV} = 80 \times 25$ control volumes leads to sufficiently accurate results, and further grid refinement does not significantly modify the solutions. The convergence has been achieved when the criterion that the squares of the residual in the discretized governing equation using the new coefficients and source terms summed overall control volumes have been less than 10^{-5} for the modified volumetric enthalpy and pressure field. In addition, owing to the presence of strong non-linearity in Eq. (4.15), arising from the interdependent of variables H^* and $\mathbf{u}$, the discretized equation has been further under-relaxed, where a typical relaxation factor around 0.1 has been used for most of the simulations in order to achieve convergence.

B. *Effect of Smoothing of Diffusion Coefficient*

In order to demonstrate the usefulness of the proposed smoothing algorithm applied to the effective diffusion coefficient Γ_H^* for multi-dimensional problems, the predicted temperature and liquid saturation distributions for an incomplete phase change process have been obtained “with” and “without” applying smoothing to Γ_H^*. The results for a dimensionless heat flux of $Q_w^* = 16$ are presented in Fig. 4.20. It can be observed from the figure that the new solution calculated from a good guessed initial solution (marked as “with” smoothing) is identical to the one obtained “without” any smoothing. Therefore, it is concluded that the proposed smoothing algorithm does not alter the expected solution behavior, and its applicability may be extended to complete phase change problems. On the other hand, whenever there is a phase change from the saturated mixture to the superheated vapor state, the predictions obtained “without” applying the smoothing algorithm are associated with a non-physical “jump” in the predicted temperature distribution. However, these results are not presented here owing to the undesirably high temperature.

(a)

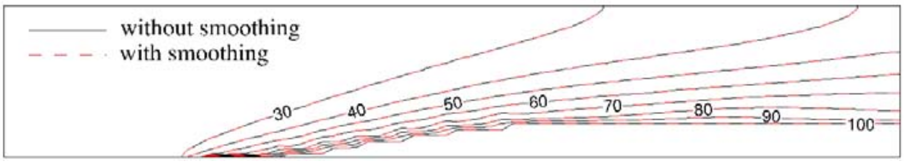

Temperature distribution $\left(T_{\max} = 100^{\circ}\mathrm{C}\right)$

(b)

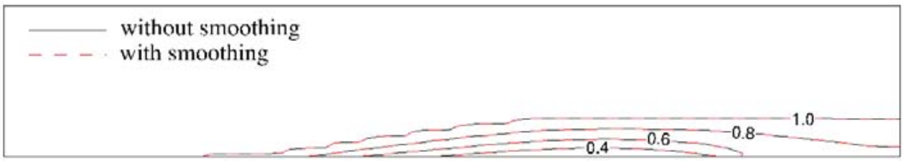

Liquid saturation distribution $\left(s_{\min} \approx 0.2\right)$

Fig. 4.20: Comparison of incomplete phase change process in channel flow using LTE model with and without applying smoothing to Γ_H^* for $Q_w^* = 16$ (a) temperature and (b) liquid saturation

C. Results Obtained with Variation of Heat Flux

In order to test the proposed remedy in case of a complete phase change process, simulations have been carried out under variation of the heat flux. The results are compiled in Figs. 4.21 – 4.24 in the form of combined medium temperature, liquid saturation and the velocity vectors in the liquid and the vapor phases. Figure 4.21 displays the numerical results of an incomplete phase change process with increased dimensionless heat flux $Q_w^* = 20$. Figure 4.21 shows that no superheated vapor zone is formed and suggests that in the zone where the phase change takes place, the two-phase region expands in the axial and transverse directions due to the increase of the heat flux at the heated surface associated with increasing buoyancy force, as compared to the solution for $Q_w^* = 16$ presented in Fig. 4.20. Most importantly, heat is transferred in the vertical (transverse) direction by both convection due to buoyancy, caused primarily by the substantial reduction in the fluid density in the phase change region, and diffusion through the combined (homogenized) medium. Although the combined temperature remains constant in the two-phase region, the diffusive energy transfer through the medium still plays its role owing to the finite values of D^*, contributing to the effective diffusion coefficient [see the definition of Γ_H^* in Table 2.3 for clarification], as well as finite spatial gradient of H^*. Since the downstream temperature is higher than that at the upstream, owing to the localized heat addition, and the mass flow rate of the water through the channel is considerably low, which is characterized by $Re_l = 85$, axial diffusion plays an extremely important role in the overall energy transfer process and eventually heats up the fluid even in the upstream direction. Considering the fact that $T_{in} = 20^{\circ}\mathrm{C}$ has been prescribed for all considered cases, this is quite evident from the location of isotherms corresponding to $T = 30^{\circ}\mathrm{C}$ for the combined medium, presented in different figures in this section.

In particular, the growth of the two-phase zone in the axial direction is prominent due to the high pressure gradient towards the outlet [33]. Furthermore, an increased heat flux leads to a reduction of the minimum liquid saturation value, occurring somewhere in the downstream part of the heated surface as indicated in Fig. 4.21(b). Wang [33] denoted the interface that separates the sub-cooled liquid region from the two-phase zone, i.e., the isoline of liquid saturation equal to unity, as a condensation front, which is appreciably inclined towards the outlet due to the incoming flow of sub-cooled liquid. Above and left of the condensation front, the sub-cooled liquid region is formed, in which isotherms have been plotted in dimensional values. The condensation front is thus the isotherm of $T_{sat} = 100^{o}\mathrm{C}$. Liquid velocity vectors shown in Fig. 4.21(c) indicate uniform flow of the sub-cooled liquid at the inlet (i.e., remain nearly parallel to the bulk flow in the axial direction). When the liquid approaches the condensation front, the flow is deflected towards the upper wall bounding the porous medium due to buoyancy force, causing it to bypass the region rich in vapor surrounding the heated surface. On the other hand, the vapor velocity vectors presented in Fig. 4.21(d) show a recognizable upward movement close to the heated surface that spreads over a large area since the vapor phase experiences a large buoyancy force owing to its significantly lower density. Nevertheless, for all considered cases, the maximum value of Re_K for both liquid and vapor phases has been found to be of the order of 10^{-2} or less, confirming the validity of Darcy law in Eq. (4.14).

(a)

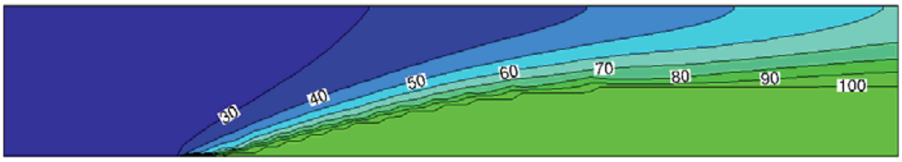

Temperature distribution $\left(T_{\max} = 100\,^{o}\mathrm{C}\right)$

(b)

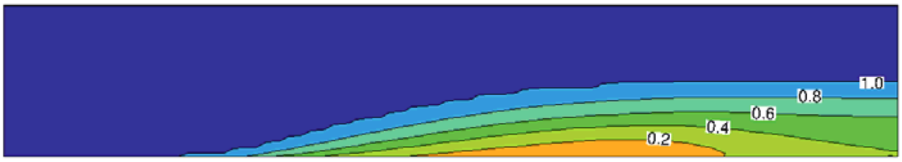

Liquid saturation distribution $\left(s_{\min} \approx 0.003\right)$

(c)

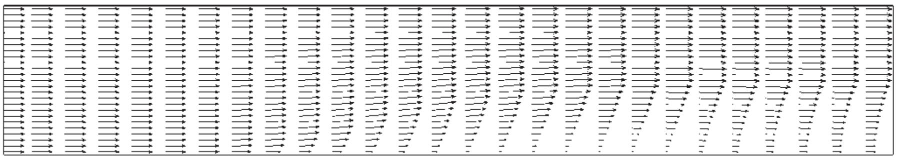

Liquid velocity vectors $\left(Re_{K,\max} = 7.32\times10^{-3}\right)$

(d)

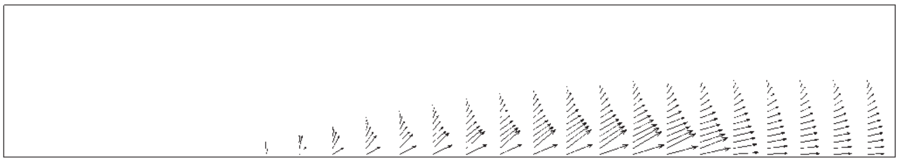

Vapor velocity vectors $\left(Re_{K,\max} = 4.75\times10^{-3}\right)$

Fig. 4.21: Solution of incomplete phase change process in channel flow using LTE model for $Q_w^* = 20$, $Re_l = 85$, $\varepsilon = 0.4$, $k_s^* = 0.5$ and $K^* = 5\times10^{-9}$

Figure 4.22 displays the results for a phase change process, where the heat flux at the heated surface is increased to $Q_w^* = 24$. This heat flux corresponds to the onset of a complete phase change process, at which zero liquid saturation is attained adjacent to the lower wall as shown in Fig. 4.22(b). It is observed that a small superheated vapor region is formed close to the bottom wall towards the end of the heated surface. Irrespective of the imposed wall heat flux and even whether incomplete or complete phase change occurs, the two-phase region occupies a large portion of the channel (flow) where the temperature remains constant at $T_{sat} = 100^{o}\mathrm{C}$. Therefore, in order to identify the interfaces separating the single and the two-phase regions, isotherms are presented for

$T_{sat} = 100 \pm 10^{-5^{\mathrm{o}}}\mathrm{C}$. Both these isotherms are, however, marked as that corresponding to $T_{sat} = 100^{\mathrm{o}}\,\mathrm{C}$ in all relevant figures, where the positive and negative sign refer to the saturation isotherms from the superheated vapor and sub-cooled liquid zones, respectively. They are often referred to as the boiling and the condensation fronts as schematically shown in Fig. 4.17(a) [33]. The liquid saturation isolines indicate that zero liquid saturation first appears at the heated surface, and very low liquid saturation surrounds the vapor phase region at the heated surface as shown in Fig. 4.22(b). Liquid velocity vectors presented in Fig. 4.22(c) have characteristics similar to the ones presented in Fig. 4.21(c) at the inlet and bypass the superheated region immediately above the heated surface. Vapor velocity vectors displayed in Fig. 4.22(d) show that the vapor flow inside the superheated vapor zone is primarily horizontal, probably due to the externally imposed horizontal pressure gradient and an upward component of the vapor velocity is results in the two-phase zone due to its low density. According to Wang, the vapor flow inside the two-phase zone is split into three components: one in the upstream direction to the front, another one flowing downstream to the back, and the remaining stream rising to the upper wall in the middle of the channel.

(a)

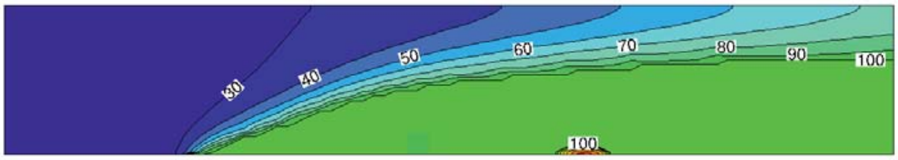

Temperature distribution $\left(T_{\max} \approx 180^{\mathrm{o}}\,\mathrm{C}\right)$

(b)

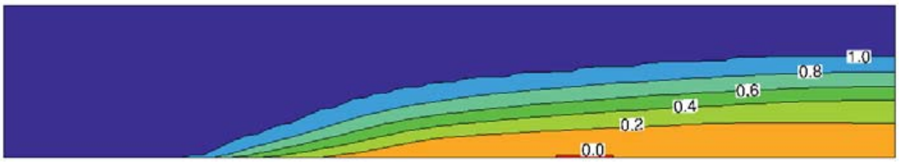

Liquid saturation distribution $\left(s_{\min} = 0\right)$

(c)

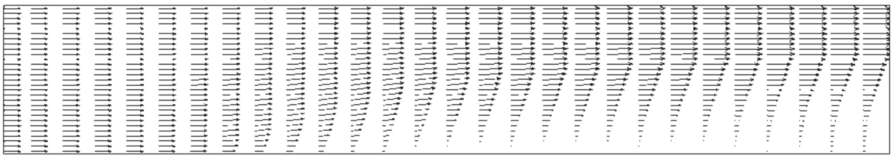

Liquid velocity vectors $\left(Re_{K,\max} = 9.11 \times 10^{-3}\right)$

(d)

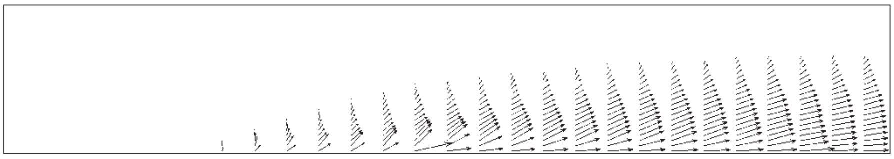

Vapor velocity vectors $\left(Re_{K,\max} = 7.5 \times 10^{-3}\right)$

Fig. 4.22: Solution of complete phase change process in channel flow using LTE model for $Q_w^* = 24$, $Re_l = 85$, $\varepsilon = 0.4$, $k_s^* = 0.5$ and $K^* = 5 \times 10^{-9}$

With further increase in the wall heat flux to $Q_w^* = 28$ and $Q_w^* = 32$, as presented in Figs. 4.23 and 4.24, respectively, it is evident that the superheated vapor zone increases in size and its first appearance is observed closer to the inlet as compared to Fig. 4.22. However, this zone is always restricted extremely close to the heated bottom surface, irrespective of the applied Q_w^*, and does not spread in the cross-flow direction due to the expected diffusive action. Most importantly, the maximum temperature of the combined medium at the heated wall is found to be as high as $180^{o}C$, $625^{o}C$ and $2000^{o}C$, for $Q_{w}^{*}=24$, $Q_{w}^{*}=28$ and $Q_{w}^{*}=32$, respectively. Depending upon the applied heat flux, different zones at the exit of the channel may be observed that are occupied by i) the sub-cooled liquid phase, observed always at the top of the channel, ii) the tow-phase mixture, observed at the middle of the channel that may be extended to the bottom of the channel for most of the cases, and iii) superheated vapor phase, observed for the highest considered heat flux corresponding to $Q_{w}^{*}=32$. Although the superheated vapor region was identified as the dry-out in the literature [33], the occurrence of such unrealistically high temperature over a short distance in the transverse direction needs further explanation.

It may be recognized here that Γ_{H}^{*} is discontinuous at the interfaces between the single and the two-phase regions, where either $s=0$ (saturated vapor) or $s=1$ (saturated liquid). These discontinuous could be eliminated for one-dimensional problems using the smoothing strategy of Γ_{H}^{*} as pointed out earlier and realistic predictions could be obtained for the axial temperature distribution. Nevertheless, since Γ_{H}^{*} for the superheated vapor phase is few orders of magnitude higher than that for the sub-cooled liquid phase and even after applying the smoothing algorithm, Γ_{H}^{*} remains quite low for the two-phase region close to $s=0$ and $s=1$, the difference in Γ_{H}^{*} is more significant across the interface separating the vapor phase and the two-phase regions. It is, therefore, evident that diffusion cannot play any significant role in the overall energy transport process, particularly from the vapor phase to the two-phase mixture, if convection is present. Since the axial velocity is significantly larger than that in the transverse direction, as may be observed from Figs. 4.21 – 4.24, the energy transport through the vapor phase due to convection is also significant higher in the flow direction. As a result, the superheated vapor zone always remains confined within narrow region close to the bottom wall, without any significant energy transfer in the transverse direction, and noticeably expands only in the axial direction with the increase in Q_{w}^{*}. Furthermore, this considerable temperature gradient occurs probably due to the implementation of the heat flux at the wall along with the LTE assumption. This also results in unrealistically high temperature at the wall obtained with LTE model, which may even exceed the melting temperature of the low carbon steel that forms the solid matrix of the porous medium. Since LTE model does not allow any realistic diffusion mechanism for energy transfer from the single phase to the two-phase mixture and vice-versa, it may be safely concluded that the model should be applied with care, or may be avoided if possible, specifically for the prediction of multi-dimensional complete phase change process inside porous media. In this situation, the LTNE model, which will be discussed in the next chapter, could be more appropriate for the simulation of complete phase change process inside a porous evaporator. The liquid saturation distributions presented in Figs. 4.23(b) and 4.24(b) exhibit similar characteristics as for the previous case in Fig. 4.22(b) with more vapor being generated at the heated surface.

(a)

Temperature distribution $\left(T_{\max} \approx 625\,^{o}\mathrm{C}\right)$

(b)

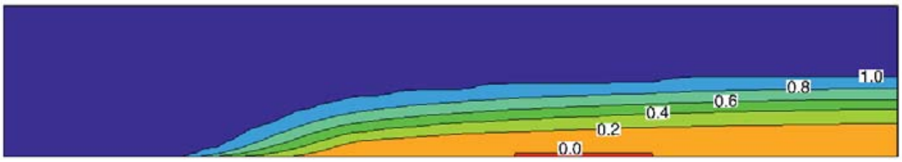

Liquid saturation distribution $\left(s_{\min} = 0\right)$

(c)

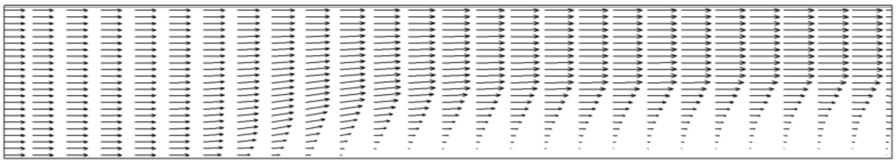

Liquid velocity vectors $\left(Re_{K,\max} = 8.06 \times 10^{-3}\right)$

(d)

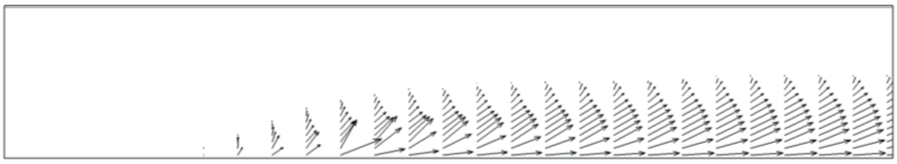

Vapor velocity vectors $\left(Re_{K,\max} = 7.9 \times 10^{-3}\right)$

Fig. 4.23: Solution of complete phase change process in channel flow using LTE model for $Q_w^* = 28$, $Re_l = 85$, $\varepsilon = 0.4$, $k_s^* = 0.5$ and $K^* = 5 \times 10^{-9}$

(a)

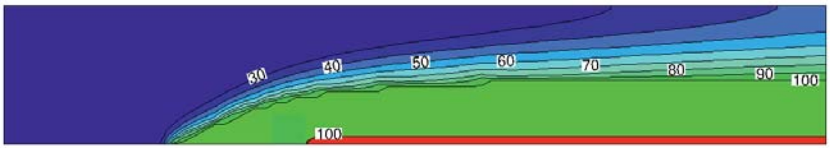

Temperature distribution $\left(T_{\max} \approx 2000^{o}\,\mathrm{C}\right)$

(b)

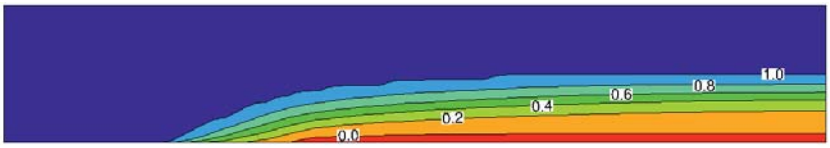

Liquid saturation distribution $\left(s_{\min} = 0\right)$

(c)

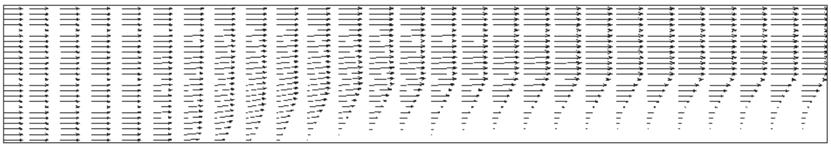

Liquid velocity vectors $\left(Re_{K,\max} = 7.9 \times 10^{-3}\right)$

(d)

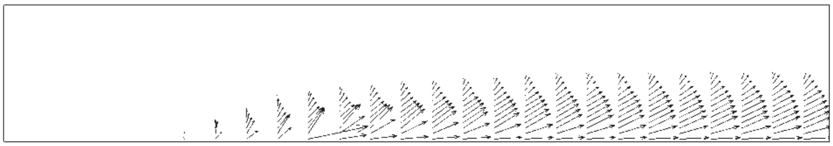

Vapor velocity vectors $\left(Re_{K,\max} = 9.57 \times 10^{-3}\right)$

Fig. 4.24: Solution of complete phase change process in channel flow using LTE model for $Q_w^* = 32$, $Re_l = 85$, $\varepsilon = 0.4$, $k_s^* = 0.5$ and $K^* = 5 \times 10^{-9}$

4.3.4. Simulation of Complete Phase Change Process in Pipe Flow

This subsection describes the complete phase change process of water under steady-state condition for pipe flow as shown in Fig. 4.17(b), using cylindrical axi-symmetric coordinates. The simulations have been performed using a staggered grid layout and parameter values identical to those used in channel flow, keeping the same hydraulic diameter $(D_h = 2W)$. Consequently, the pipe radius $R = 50\,\mathrm{mm}$ has been considered for the present analysis. Figures 4.25 – 4.28 present the obtained numerical solutions in terms of the temperature and liquid saturation distributions as well as velocity fields for $\varepsilon = 0.4$, $k_s^* = 0.5$, $K^* = 5\times10^{-9}$ and $Re_l = 85$ independence of the imposed heat flux that has been varied from $Q_w^* = 10$ to $Q_w^* = 20$. Other parameters have been considered: $l_i^* = l_e^* = 1.2$, i.e., $l_h^* = 3.6$, $\tilde{b}_x = -1$ and $\tilde{b}_r = 0$. As shown in Figs. 4.25(a) and 4.26(a), the two-phase zone is present on the pipe wall for the dimensionless heat flux value $Q_w^* = 10$. On the other hand, at the inlet and the center of the pipe, the working fluid is in sub-cooled liquid state. It should be noted that the onset of the phase change process takes place for a value of the dimensionless heat flux below $Q_w^* = 10$. As the liquid passes the heated surface, it absorbs heat and its temperature increases, leading to a reduced fluid density. It is evident from Fig. 4.25 that the two-phase zone expands further towards the center and the outlet of the pipe for an increased heat flux due to enhanced heat diffusion in the upstream direction and consequently, more heat transfer in the domain. On the other hand, sub-cooled liquid zone contracts with a more pronounced temperature gradient adjacent to the condensation front due to the backward axial diffusion associated with enhanced heat loss through the inlet. As the heat flux is further increased, the acceleration of the main stream due to buoyancy force becomes so significant that the flow structure changes [see Fig. 4.25(c)]. The temperature distribution characterizing the complete phase change process for a still further increased heat flux of $Q_w^* = 20$ is presented in Fig. 4.25(d). It is evident from the figure that extremely high temperatures occur in the superheated vapor region close to the heated surface similar to those observed previously in channel flow. This occurrence may be also identified as the non-physical "jump" in the predicted temperature distribution, which could not be resolved using the LTE model. It is expected that the LTNE model could be more realistic for the simulation of complete phase change process in pipe flow.

The isolines of the liquid saturation are presented in Fig. 4.26 for identical values of the heat flux as in the previous figure. The two-phase zone forms as a thin layer close to the heated surface for an imposed heat flux of $Q_w^* = 10$. This can be noticed at the relevant location adjacent to the heated surface in Fig. 4.29(a). It is observed from Figs. 4.26(b) and 4.26(c) that the liquid saturation close to the heated surface decreases as the heat flux is gradually increased. Given the incoming sub-cooled liquid, the two-phase zone becomes significantly thinner towards its end facing the inlet, whereas it gradually grows in the axial direction due to the buoyancy force, the diffusive heat flux in the upstream direction as well as the heat loss through the inlet. Since heat is increasingly transferred by diffusion, the temperature difference of the combined medium near the two-phase zone is reduced [see Figs. 4.25(d) and 4.26(d)], along with its density difference. This gradually leads to an augmented heat transfer and the expansion of the two-phase zone towards the center of the pipe, although it continuously expands along the flow direction. The different features of the liquid and vapor velocity vector fields for a variation in the imposed heat flux are presented in Figs. 4.27 and 4.28. Acted upon by the buoyancy force, the heated liquid adjacent to the wall flows slightly faster than inside the pipe away from the heated surface.

The quantity of generated vapor is sufficiently small so that its effect on the velocity field shown in Fig. 4.28(a) is also less prominent. For an increased heat flux, the vapor flows in a similar manner as compared to low heat flux in an elongated region [see Fig. 4. 28(b)]. As the heat flux is further increased to $Q_w^* = 14$, the vapor phase becomes much more pronounced along with the two-phase zone and is pushed downwards to the center of the duct and to the outlet, as shown in Figs. 4. 27(c) and 4. 28(c). It is interesting to note in Fig. 4. 27(d) that the liquid velocity is nearly annihilated close to the heated surface as the heat flux is still further increased to $Q_w^* = 20$. This is reasonable due to the nearly vanishing liquid saturation and needs no further explanation.

(a)

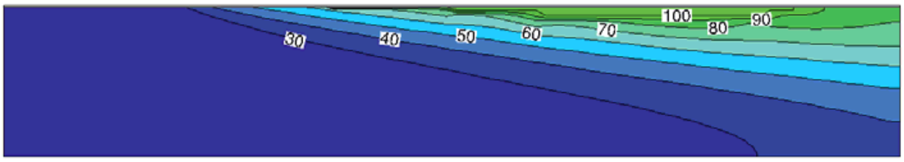

$Q_w^* = 10$, $T_{\max} = 100^{\circ}\mathrm{C}$

(b)

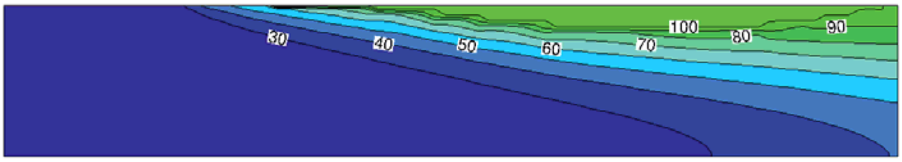

$Q_w^* = 12$, $T_{\max} = 100^{\circ}\mathrm{C}$

(c)

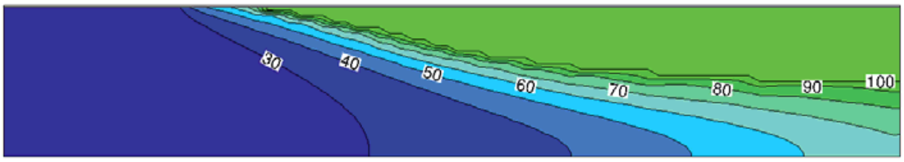

$Q_w^* = 14$, $T_{\max} = 100^{\circ}\mathrm{C}$

(d)

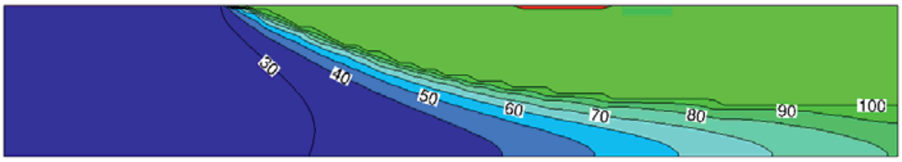

$Q_w^* = 20$, $T_{\max} \approx 730^{\circ}\mathrm{C}$

Fig. 4.25: Temperature distributions of complete phase change process in pipe flow using LTE model for different dimensionless heat fluxes for $Re_l = 85$, $\varepsilon = 0.4$, $k_s^* = 0.5$ and $K^* = 5\times10^{-9}$

(a)

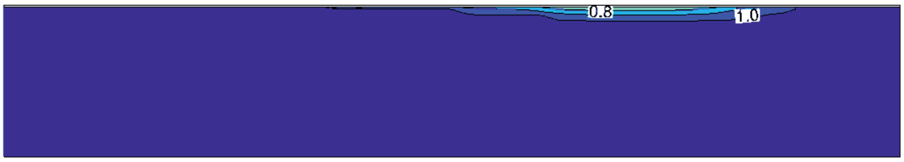

$Q_w^* = 10$, $s_{\min} \approx 0.7$

(b)

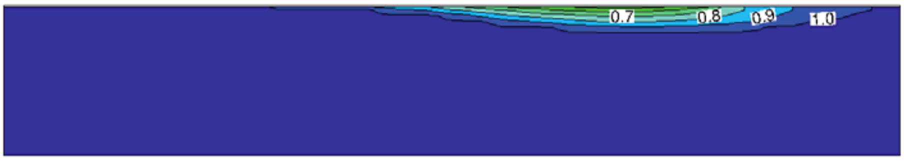

$Q_w^* = 12$, $s_{\min} \approx 0.45$

(c)

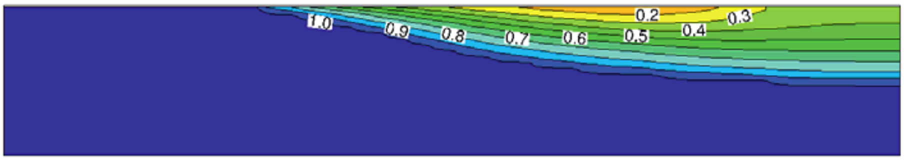

$Q_w^* = 14$, $s_{\min} \approx 0.18$

(d)

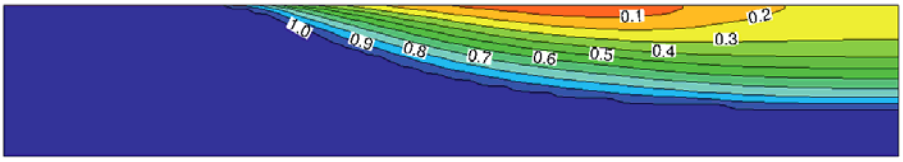

$Q_w^* = 20$, $s_{\min} = 0$

Fig. 4.26: Liquid saturation distributions of complete phase change process in pipe flow using LTE model for different heat fluxes for $Re_l = 85$, $\varepsilon = 0.4$, $k_s^* = 0.5$ and $K^* = 5 \times 10^{-9}$

(a)

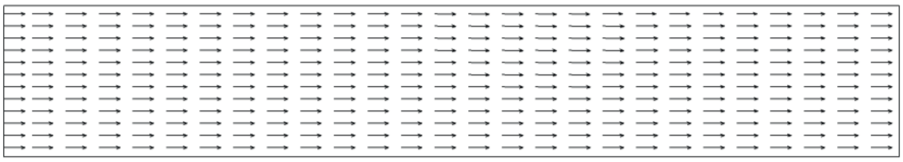

$Q_w^* = 10$, $Re_{K,\max} = 5.53 \times 10^{-3}$

(b)

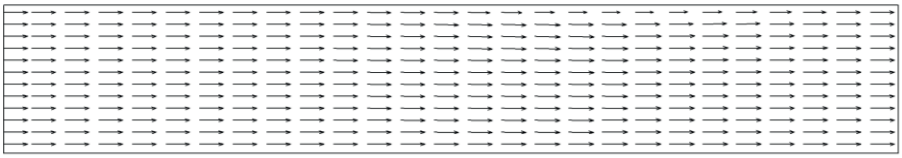

$Q_w^* = 12$, $Re_{K,\max} = 5.9 \times 10^{-3}$

(c)

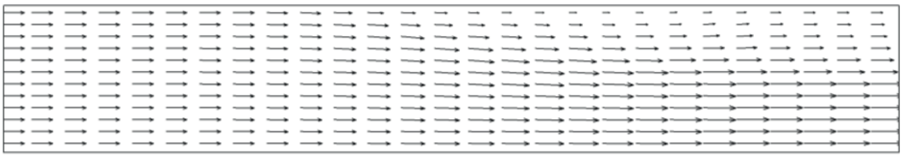

$Q_w^* = 14$, $Re_{K,\max} = 8.5 \times 10^{-3}$

(d)

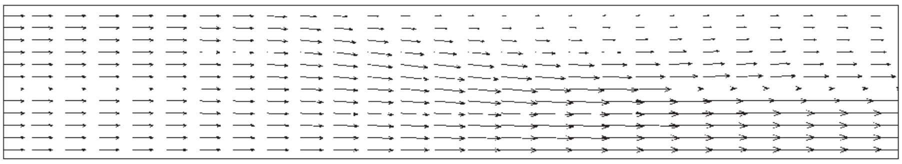

$Q_w^* = 20$, $Re_{K,\max} = 1.2 \times 10^{-2}$

Fig. 4.27: Liquid velocity vectors of complete phase change process in pipe flow using LTE model for different heat fluxes for $Re_l = 85$, $\varepsilon = 0.4$, $k_s^* = 0.5$ and $K^* = 5 \times 10^{-9}$

$Q_w^* = 10$, $Re_{K,\max} = 7.5\times10^{-4}$

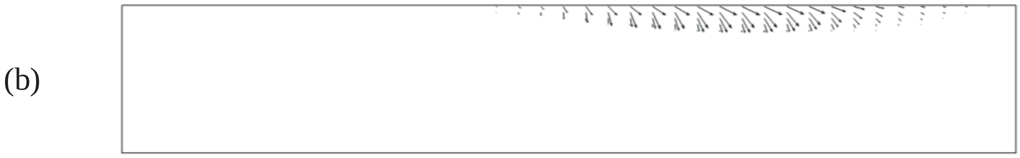

$Q_w^* = 12$, $Re_{K,\max} = 1.54\times10^{-3}$

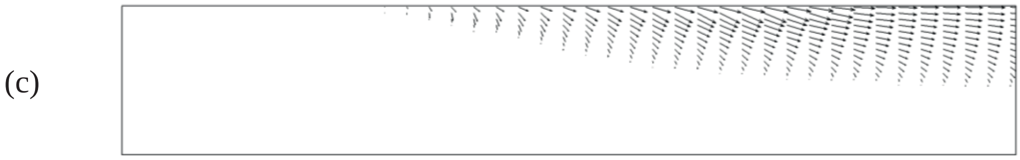

$Q_w^* = 14$, $Re_{K,\max} = 4.25\times10^{-3}$

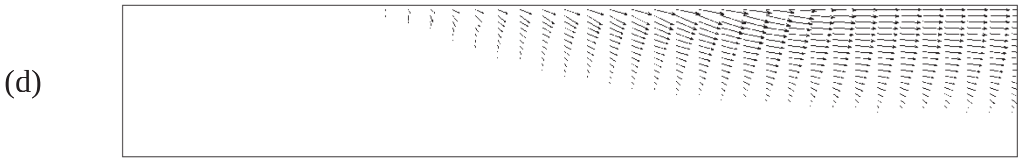

$Q_w^* = 20$, $Re_{K,\max} = 6.8\times10^{-3}$

Fig. 4.28: Vapor velocity vectors of complete phase change process in pipe flow using LTE model for different heat fluxes for $Re_l = 85$, $\varepsilon = 0.4$, $k_s^* = 0.5$ and $K^* = 5\times10^{-9}$

4.4. Modeling in Two-dimensional Coordinates using Non-Staggered Grid Layout

In order to accommodate variations in the cross-sectional area of the evaporator, a method of solution in generalized curvilinear coordinates is required. Therefore, the present CFD code has been extended to non-staggered grid layouts, while using the smoothing algorithm for the effective diffusion coefficient. The results obtained in this section using a non-staggered grid layout along with LTE model have been compared with those computed using a staggered grid layout for channel flow under steady-state condition. For the purpose of comparison, the simulations have been performed using the same number of control volumes, i.e., $N_{CV} = 80\times25$, and parameter values identical to those used for the staggered grid layout in channel flow [see subsection 4.3.3 for details]. The major objective of the present study is to demonstrate the applicability of a non-staggered grid layout for the numerical simulation of incomplete phase change process inside a porous channel. The comparison of results obtained for an incomplete phase change process of water using either non-staggered or staggered grid layout are presented in terms of temperature and liquid saturation distributions for two different values of the heat flux imposed at the heated surface, $Q_w^* = 12$ and $Q_w^* = 16$, in Figs. 4.29 and 4.30 respectively. Other parameters have been employed: $\varepsilon = 0.4$, $K^* = 5\times10^{-9}$, $k_s^* = 0.5$ as properties of the porous medium, other than $n = 3$, $Re_l = 85$ for the inlet flow condition along with $T_{in} = 20^{\circ}\mathrm{C}$ and the unheated inlet and exit lengths $l_i^* = l_e^* = 1.2$,i.e., $l_h^* = 3.6$. A comparison of the numerical results obtained for an incomplete phase change process using either non-staggered or staggered grid layout reveals that an excellent matching, since the predicted results are hardly distinguishable. Therefore, the successful application of the non-staggered grid layout could be extended towards complete phase change problems. The effect of a variation in the heat flux on the temperature and liquid saturation distributions have been discussed in details in the previous sections, and are hence not repeated here for the sake of brevity. The comparison of results obtained for a complete phase change process is also not presented here due to the extremely high unphysical temperature rise occurring in the superheated vapor region close to the heated surface. In this respect, a detailed study is provided in the next chapter using the LTNE model to establish the performance of non-staggered grid layouts for the simulation of the complete phase change process inside a porous channel as compared with staggered grid layouts.

(a)

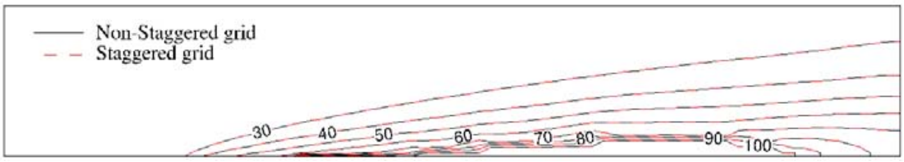

Temperature distribution $\left(T_{\max} = 100\,^{\circ}\mathrm{C}\right)$

(b)

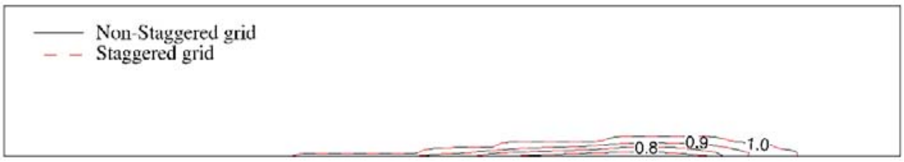

Liquid saturation distribution $\left(s_{\min} \approx 0.6\right)$

Fig. 4.29: Comparison of non-staggered and staggered grid results for two-phase flow in channel using LTE model for $Q_w^* = 12$, $\varepsilon = 0.4$, $K^* = 5\times10^{-9}$ and $k_s^* = 0.5$

(a)

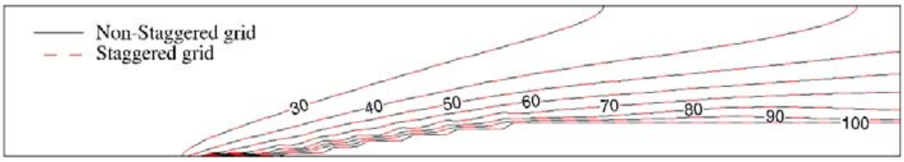

Temperature distribution $\left(T_{\max} = 100\,^{\circ}\mathrm{C}\right)$

(b)

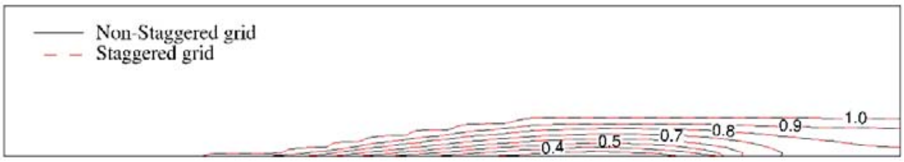

Liquid saturation distribution $\left(s_{\min} \approx 0.2\right)$

Fig. 4.30: Comparison of non-staggered and staggered grid results for two-phase flow in channel using LTE model for $Q_w^* = 16$, $\varepsilon = 0.4$, $K^* = 5\times10^{-9}$ and $k_s^* = 0.5$

4.5. Conclusions

Fluid flow and heat transfer associated with complete phase change process utilizing H-formulation of Wang [33] and modified h-formulation along with the assumption of LTE condition have been investigated within this chapter. The main part of the simulations has been carried out by applying the proposed smoothing algorithm in order to deal with the discontinuities in the effective diffusion coefficient at the phase change interfaces and hence to obtain a smooth solution without non-physical jump in the predicted temperature distribution at the interfaces. For the purpose of demonstration, the one-and two-dimensional phase change problems inside porous evaporator operated in the Darcy flow regime have been considered. The present investigation of the complete phase change process inside porous media, based on the H-formulation, shows that the conventional treatment of effective diffusion coefficient leads to a non-physical “jump” in the predicted temperature distribution, particularly close to the interface between the two-phase and the superheated vapor regions. A thorough parametric study for a one-dimensional problem indicates that the adoption of the proposed smoothing algorithm successfully eliminates non-physical “jump” in the predicted temperature distribution without modifying the overall energy and momentum balance. All tested cases, covering applicable ranges of parametric variations, could be physically interpreted. Therefore, the methodology is recommended for future simulations of complete phase change processes within porous media. The results also indicated that the effect of decreasing the exponent n in the expression for the relative permeability from 3 to 1 leads to substantial change in the predicted temperature distribution due to considerable enhancement in the effective diffusion coefficient Γ_H^* and hindrance coefficient f in the two-phase region. Since both these values represent the empirical parameters, therefore, it is necessary to verify this phenomenon by the experiments in the future. Complete phase change process along with LTE model could never be achieved in a transient simulation due to the presence of sharp discontinuity in the effective heat capacity ratio, which could not be eliminated using conventional treatments.

In this chapter, the results for steady one-dimensional complete phase change problems of water inside a porous evaporator, obtained from the modified h- and the existing H-formulations, have been compared and excellent agreements have been observed for all tested cases, irrespective of the employed heating conditions at the evaporator wall. Additionally, it has been also observed that the modified h-formulation requires significantly less computation time, although all variants of TPMM require smoothing of effective diffusion coefficient in order to avoid “jump” in the predicted temperature. Since the proposed formulation does not require the definition of any artificial variable and in view of the identified advantages, the method is strongly recommended for the future use of simulation of complete phase change process inside porous media.

On the other hand, it has been observed that the LTE model, even after employing the smoothing algorithm, fails to produce realistic predictions for multi-dimensional complete phase change problems for both channel and pipe flow models since the superheated vapor has been observed to be confined to a zone extremely close to the heated wall and the predicted maximum temperature of the combined medium at the wall has been recorded to be unrealistically high. These observations could be attributed to the extremely lower values of the effective diffusion coefficient in the two-phase mixture zone, close to the superheated vapor region, that restricts any recognizable diffusive energy transport across the interface in between. Therefore, the use of the LTE model should be avoided as far as possible. A comparison of the numerical results of the incomplete phase change process obtained using either the non-staggered grid layout or the staggered grid layout shows that the results are identical.

CHAPTER 5. SIMULATION OF COMPLETE PHASE CHANGE PROCESS USING LOCAL THERMAL NON-EQUILIBRIUM MODEL

In the present chapter, the smoothing algorithm for the effective diffusion coefficient employed in the H-formulation of Two-Phase Mixture Model (TPMM) [33] is extended for Local Thermal Non-Equilibrium (LTNE) model. Consequently, numerical simulations of complete phase change process inside porous media with LTNE assumptions using the proposed smoothing algorithm have been performed under different flow conditions in order to demonstrate the necessity and the usefulness of the algorithm for handling sharp discontinuities in the effective diffusion coefficient to avoid the non-physical “jump” in the predicted temperature distribution. In particular, steady-state one-dimensional pipe flow with constant cross-sectional area in the axial direction, as well as two-dimensional problems under both steady-state and transient conditions have been investigated. The latter problems include both channel and circular pipe flow models through porous media, applying constant heat flux at different locations using staggered grid layout. In addition, the present LTNE results were compared with those obtained with the conventional Local Thermal Equilibrium (LTE) model. Furthermore, effects of parameters, such as properties of porous medium, operating condition and partitioning of the wall heat flux, on the predicted temperature distribution, liquid saturation and velocity fields have been investigated in this chapter. Furthermore, this chapter also presents the comparison between results obtained using non-staggered and staggered grid layouts for the incomplete and complete phase change process for a two-dimensional problem under steady-state condition inside a porous channel.

5.1. Modeling of One-dimensional Problem

5.1.1. Problem Description and Basic Assumptions

The complete phase change of liquid water inside a porous evaporator under steady-state condition has been considered in the present work as a demonstrative example. For numerical simulation, the H-formulation along with the assumption of LTNE, have been used. The model has been applied for a one-dimensional pipe flow with constant cross-sectional area in the axial direction. The problem geometry is shown in Fig. 5.1 along with its dimensions. It has unheated starting and exit lengths of l_i and l_e, respectively. The length of the heated section is l_h, where a constant heat flux $\dot{q}''_w$ has been applied on the duct surface. The entire pipe is filled with a porous medium of known properties. An external pressure gradient drives the sub-cooled liquid water at the inlet, with a temperature T_{in} and a velocity u_{in}, to flow through the pipe. Water is heated to the superheated vapor state as it passes through the duct when sufficient heat is added.

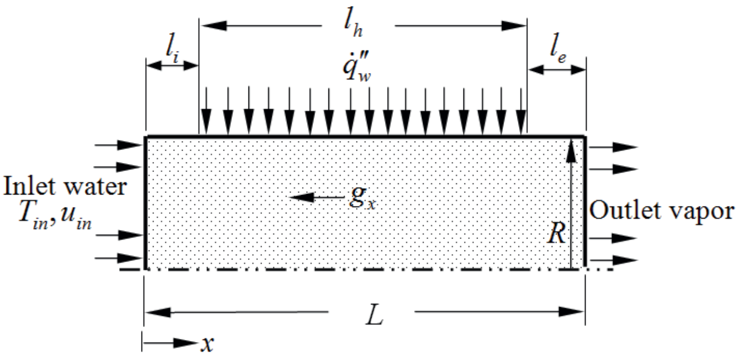

Fig. 5.1: Schematic representation of the porous evaporator

The LTNE model has been considered here owing to the large difference in thermal conductivities between the solid and the fluid phases. For the purpose of comparison, the conventional LTE model has been also considered. With these assumptions and considering that the variation remain only in the axial direction, the governing one-dimensional conservation equations of mass in Eq. (2.130), momentum in Eq. (2.131) and energy in Eq. (2.134) in dimensionless form for LTE model are obtained as:

$$\frac{d}{dx^*}\left(\rho^* u_x^*\right)=0 \tag{5.1}$$

$$\rho^* u_x^* = -\frac{K^*}{\nu^*}\left(\frac{dp^*}{dx^*}-\rho_k^* b_x^*\right) \tag{5.2}$$

$$\frac{d}{dx^*}\left(\gamma_H u_x^* H^*\right)=\frac{d}{dx^*}\left(\Gamma_H^*\,\frac{dH^*}{dx^*}\right)+\frac{d}{dx^*}\left(f\,\frac{K^*\Delta\rho^*\,h_{fg}^*}{\nu_v^*}\,b_x^*\right)+\frac{P^*}{A_c^*}\,\dot{q}_w''^{*} \tag{5.3}$$

In the present investigation, the axial dimension extends in the vertical direction. As will be shortly apparent, for the present steady-state one-dimensional problem, the kinetic density ρ_k in Eq. (5.2) is required only when the solution for the axial pressure gradient is required and hence all the variables appearing in Eqs. (5.1) – (5.3) are provided in section 2.2. Further in Eq. (5.3), $\dot{q}_w''^{*} = Q_w^*/Re_l$ with $Q_w^* = \dot{q}_w'' R/\mu h_{fg}$ is the dimensionless heat flux at the duct surface, which has been set to zero for the unheated segments, i.e., for $0 \le x^* \le l_i^*$ and $l_i^* + l_h^* \le x^* \le L^*$. According to Table 2.3, the effective diffusion coefficient Γ_H^* in Eq. (5.3) contains the effective thermal conductivity k_{eff}^* in its dimensionless form [see Eq. (2.135)].

In order to consider the internal heat exchange between the fluid and the solid phases within the porous medium, the LTNE model considers two separate energy conservation equations, one for each phase. Finally, the energy conservation equations for the fluid in Eq. (2.148) and the solid in Eq. (2.149) phases along with LTNE model are given as follows:

$$\frac{d}{dx^*}\left(\gamma_H u_x^* H^*\right)=\frac{d}{dx^*}\left(\Gamma_H^*\,\frac{dH^*}{dx^*}\right)+\frac{d}{dx^*}\left(f\,\frac{K^*\Delta\rho^*\,h_{fg}^*}{\nu_v^*}\,b_x^*\right)+\frac{P^*}{A_c^*}\,\dot{q}_f''^{*}+\dot{q}_{sf}'''^{*} \tag{5.4}$$

$$\frac{d}{dx^*}\left(k_{eff,s}^*\,\frac{dT_s^*}{dx^*}\right)+\frac{P^*}{A_c^*}\,\dot{q}_s''^{*}-\dot{q}_{sf}'''^{*}=0 \tag{5.5}$$

For LTNE model, the mass and momentum conservation equations remain identical to Eqs. (5.1) and (5.2), respectively. Furthermore, Γ_H^* in Eq. (5.4) contains the dimensionless effective thermal conductivity for the fluid phase $k_{eff,f}^*$ [see Eq. (2.151a)]. In Eqs. (5.4) and (5.5), the internal heat exchange $\dot{q}_{sf}'''^{*}$ between phases is defined by Eq. (2.153). In order to obtain the internal heat exchange, the heat transfer coefficient requires the phase velocities [see Eqs. (2.153) – (2.155)]. Consequently, the phase velocities $u_{x\alpha}^*$ appearing in Eqs. (5.1) – (5.3) can be calculated from the mass flux $\rho^* u_x^*$ using the individual velocity in Eq. (2.136) and the diffusive mass flux j_x^* in Eq. (2.137) as follows:

$$\rho_l^* u_{xl}^* = \lambda\ \rho^* u_x^* + j_x^* \tag{5.6a}$$

$$\rho_v^* u_{xv}^* = (1-\lambda\ )\rho^* u_x^* - j_x^* \tag{5.6b}$$

$$j_x^* = -\rho_l^* D^* \frac{ds}{dx^*} + f\,\frac{K^*\left(1-\rho_v^*\right)}{\nu_v^*} b_x^* \tag{5.6c}$$

The boundary conditions for both LTE and LTNE models have been prescribed as follows. At the inlet, i.e., at $x^* = 0$, $u_x^* = 1$, $\rho_{in}^* = 1$, $H_{in}^* = \rho_{in}^*\left[h_{l,sat}^* - \rho_{in}^* C_{pl}^*\left(T_{sat}^* - T_{in}^*\right) - 2h_{v,sat}^*\right]$ and $T_s^* = T_{in}^*$ have been specified. On the other hand, at the outlet, i.e., at $x^* = L/R$, the second derivatives of H^* and T_s^* have been set to zero (exit with zero diffusion) as described in chapter 3. This condition is considered to be less stringent as compared to the fully-developed condition for shorter exit lengths. Under steady-state condition and since the present problem deals with a porous evaporator of constant cross-sectional area in the axial direction, the mass flow rates at all cell faces can be set equal to that at the inlet as: $u_{xe}^*\ \rho_e^* = u_{in}^*\ \rho_{in}^* = 1$. Therefore, the cell face velocity can be directly obtained as $u_{xe}^* = 1/\rho_e^*$ [see section 3.3 for further clarification]. At the position of the pipe wall that is heated with constant dimensionless heat flux, where $l_i^* \le x^* \le l_e^*$, five different models along with LTNE model have been employed according to ratio of $\dot{q}_f''^*$ and $\dot{q}_s''^*$ [see Eqs. (2.156) – (2.158) for clarification].

5.1.2. Ranges of Parameters

For all considered cases, the radius and the length of the evaporator have been taken as $R = 25\text{mm}$ and $L = 400\text{mm}$. Hence, in the dimensionless form, $R^* = 1$ and $L^* = 16$ have been set for all simulations, reported in the present work. The length of the heated section l_h, however, depends on the specific choice of l_i and l_e. In the present investigation, l_i has been varied between 0 and $0.2L$, whereas l_e has been always kept fixed at $0.1L$. This unheated exit length has been deliberately provided as a part of the computational domain in order to avoid the influence of exit boundary condition on the internal solution.

Sub-cooled liquid water at $T_{in} = 20\ ^{\text{o}}\text{C}$ has been assumed to enter the evaporator, which is then heated as it flows through the porous medium. At the heated section, heat is added from an external source, supplying a constant heat flux, ranging from 2kW/m^2 to 4.5kW/m^2, to the out surface of the evaporator. Depending upon the heat addition and the operating conditions, boiling occurs and subsequently, a superheated vapor zone is formed. In a typical application of porous media evaporator, the mass flow rate of water is usually quite low and varies between 100g/h and 500g/h. Therefore, in the present investigation, the average inlet velocity of water has been varied from 0.015mm/s to 0.075mm/s. The average pore diameter of the porous medium, typically used for evaporator and required for the calculation of $\dot{q}_{sf}'''^*$ [see Eqs. (2.154) and (2.155)], and the porosity have been varied from $100\mu\text{m}$ to 1mm and 0.2 to 0.4, respectively. For the present demonstrative examples, the permeability of the porous medium has been assumed to follow the Carman-Kozeny relation [70, 71] for packed bed of spheres, as given in the dimensionless form in Eq. (2.133). Therefore, the permeability could be varied from $5\times10^{-13}\,\mathrm{m}^2$ to $10^{-9}\,\mathrm{m}^2$. The thermal conductivity of the solid phase, on the other hand, has been varied between $10\,\mathrm{W/m\,K}$ and $30\,\mathrm{W/m\,K}$ [89]. Therefore, using the aforementioned dimensional values for different influencing variables, the following ranges of dimensionless parameters have been considered in the present study as given in Table 5.1.

Table 5.1: Ranges of dimensionless parameters used for one-dimensional problem along with LTNE model

Parameters	Ranges of dimensionless values
Starting length, l_i^*	$0-3.2$
Inlet Reynolds number, Re_l	$1.25-5$
Heat Flux, Q_w^*	$8.5\times10^{-2}-13\times10^{-2}$
Porosity, ε	$0.2-0.4$
Darcy number K^*	$10^{-9}-10^{-7}$
Solid thermal conductivity, $k_{s,ref}^*$	$4.25-12.5$

In Table 5.1, $k_{s,ref}^*$ signifies the dimensionless thermal conductivity of the solid phase under reference condition. It can be noted here that since the definition of k_s^* (or any dimensionless thermal conductivity) in Table 2.2 depends on the inlet Reynolds number, its numerical value would differ for different Re_l even if the dimensional thermal conductivity of the solid and the fluid phases have been kept unaltered. In order to eliminate this problem and to enable comparison of data obtained for different inlet Reynolds number for identical properties of the solid phase, $k_{s,ref}^*$ has been introduced, which corresponds to k_s^* for $Re_{l,ref}=2$. Therefore, the true value of k_s^* for a prescribed Re_l, that is different from $Re_{l,ref}$, could be obtained as $k_s^*=k_{s,ref}^*Re_{l,ref}\big/Re_l$.

From Fig. 5.1, it is evident that l_h^* can be calculated from $L^*=16$ (fixed), and l_i^* and $l_e^*=1.6$ (fixed). Other than the fixed values, the reference case has been chosen with the following parameters: $l_i^*=1.6$, $Re_l=2$, $Q_w^*=12.5\times10^{-2}$, $d_p^*=5.75\times10^{-3}$, $\varepsilon=0.3$, $K^*=10^{-8}$ and $k_s^*=8.25$, along with Model-2, given by Eq. (2.158b), for partitioning of the wall heat flux. These parameters have been kept fixed for all cases, unless otherwise mentioned and they have been varied only when their effects on the phase change process has been investigated. Prior to carrying out detailed investigation, considerable effort has been devoted in order to ensure grid independence of the results presented in this study. Through a systematic study, it has been recognized that 500 uniform control volumes are sufficient for this purpose and further grid refinement does not significantly modify the solutions. As mentioned in chapter 3, owing to the presence of strong non-linearity in Eqs. (5.3) and (5.4), arising out of the interdependence of dependent variables H^*, s and u_x^*, the discretized equations have been further under-relaxed and a relaxation factor of 0.1 has been generally used for most of the simulations in order to achieve convergence. For all cases presented in this study, the convergence criterion has been set to 10^{-6}.

5.1.3. Consequence of Smoothing of Diffusion Coefficient

In order to demonstrate the necessity of proposed smoothing algorithm for the effective diffusion coefficient using LTNE model, the predicted temperature distributions along the evaporator length, with and without applying the proposed smoothing algorithm, have been first obtained for varying porosity with a low heat flux $Q_w^* = 11.5 \times 10^{-2}$ and for different heat fluxes with $\varepsilon = 0.3$, where the other parameters have been taken the same as that for the reference case. The results are presented in Figs. 5.2(a) and 5.2(b), respectively. It may be noted that the solutions marked as "with smoothing" have been finally obtained with a code that works "without smoothing" of effective diffusion coefficient, while using the results obtained "with smoothing" as the guessed solution, as elaborately described before in chapter 4. These new solutions (with "good" guesses), however, could not be distinguished from their guessed solutions and hence it can be concluded that the proposed smoothing algorithm does not modify the expected solution. The figure clearly shows that the phase change from the sub-cooled liquid state to the saturated mixture could always be simulated without the occurrence of "jumps" in the predicted temperature for both low and high heat flux applications. On the other hand, it is evident from Fig. 5.2(b) that whenever is phase change from the saturated mixture to the superheated vapor state, the predictions obtained without applying the smoothing algorithm are always associated with the non-physical "jump" in the axial temperature distribution. This justifies the use of proposed smoothing algorithm even for LTNE model for the simulation of complete phase change process within porous media.

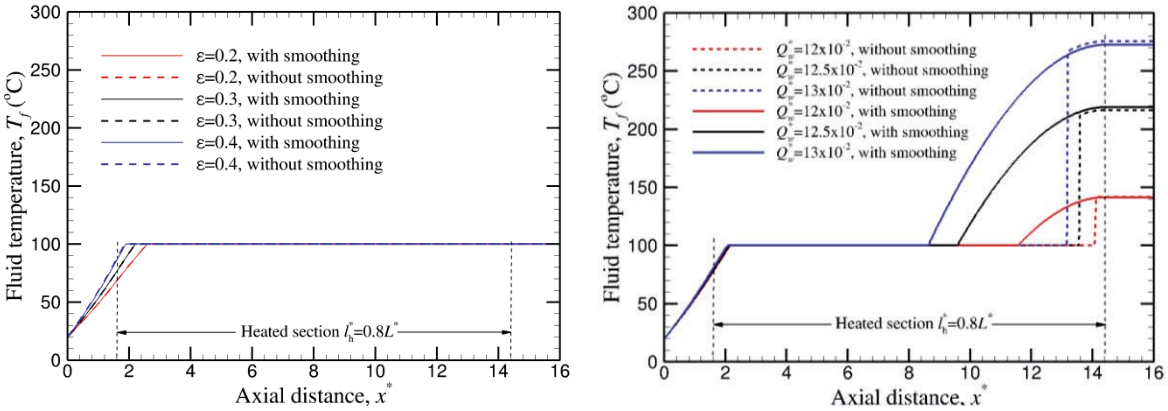

(a) (b)

Fig. 5.2: Comparison of axial temperature distributions using LTNE model with and without applying smoothing of Γ_H^* (a) incomplete phase change for different porosities with $Q_w^* = 11.5 \times 10^{-2}$ and (b) complete phase change for different heat fluxes with $\varepsilon = 0.3$. Other parameters: $Re_l = 2$, $K^* = 10^{-8}$ and $k_s^* = 8.25$

Another interesting feature that can be observed not only from Fig. 5.2, but also from all subsequent figures presented in this investigation, is the effect of axial diffusion on the temperature distribution in the unheated starting length. Since the mass flow rate for the present application is extremely low (this is characterized by $1.25 \le Re_l \le 5$), the process in the unheated segments is dominated by the presence of heat conduction (addition) in the downstream direction, resulting in a nearly linear temperature variation in the starting length for all cases under consideration. This issue has been discussed further in details in subsection 5.1.5 while dealing with the effects of porous media properties on the axial temperature distribution.

5.1.4. Effects of Operating Conditions

Figure 5.3 displays the effects of heat addition Q_w^* and inlet Reynolds number Re_l on the predicted temperature distributions for both LTNE and LTE model. It can be observed from Fig. 5.3(a) that the difference between the solid and the fluid temperatures is hardly recognizable, irrespective of the operating condition, owing to the extremely high convective heat transfer coefficient between these phases [see Eqs. (2.154) and (2.155) for clarification]. The fluid temperature for LTNE model is represented by T_f in Fig. 5.3 in order to distinguish it from the temperature of the medium T, obtained with the LTE model. As a result, only the fluid temperature T_f and the temperature of the medium T for LTNE and LTE models, respectively, are presented in Fig. 5.3(b). Nevertheless, it is also evident from the figure that the temperature distributions, predicted by LTNE model, are noticeably higher particularly in the superheated vapor region as compared to that obtained by LTE model, although the difference in predictions decreases with the decrease in heat flux and the increase in Reynolds number. While the effects of heat flux and Reynolds number on the difference in predicted temperatures are quite expected and hence probably need no further explanation, the lower exit temperature, obtained using LTE model, can be attributed to the higher conduction heat loss through the inlet, owing primarily to the enhanced temperature gradient. Reasons for such occurrence shall be elaborated later in this section.

It is also interesting to note that the phase change process initiates early when LTE model is used, as may be observed from Fig. 5.3(b) for $Re_l = 1.25$, although it still occurs, but hardly distinguishable for higher Reynolds number. This observation may be explained by the fact that according to LTE model, the entire amount of heat is directly added to the fluid phase in the two-phase region, in contrast to the combined medium in the single phase region, since Γ_H^* has no contribution from the thermal conductivities of any of the phases [see the definition in Table 2.3]. On the other hand, for LTNE model, owing to the partitioning of heat flux [see Eq. (2.158)], a part of the heat that is added to the solid phase can be transferred to the fluid phase only when the solid phase temperature is higher than that of the fluid medium. More importantly, as will be shortly apparent from Fig. 5.4, heat can even be transferred in the reverse direction, i.e., from the fluid phase to the solid phase, particularly close to the saturated liquid condition. Quite evidently, the difference in the initiation of phase change process, predicted by LTE and LTNE models, diminishes with the decrease in imposed wall heat flux and the increase in inlet Reynolds number (since convective transport starts playing its role), which is consistent with the observations from Fig. 5.3. It is also interesting to note from Fig. 5.3 that a marginal change in the operating condition (either applied heat flux or Reynolds number) can lead to a substantial change in the exit temperature. For example, at $Re_l = 1.25$, if a high heat flux of $Q_w^* = 12.5 \times 10^{-2}$ is applied, which is not even sufficient to produce complete phase change for $Re_l = 5$ [see Fig. 5.3(b)], the exit temperature could be as high as $665^{\mathrm{o}}\mathrm{C}$, although the result is not shown in the figure owing to the undesirably high temperature and in order to restrict the temperature data to a reasonable range. Therefore, the operating conditions are required to be appropriately designed in order to achieve the desired objective. Nevertheless, the results presented in Fig. 5.3 clearly demonstrate that wherever applicable, LTNE model should be used in lieu of the traditional LTE model, e.g., for lower Reynolds number and higher heat input to the system, in order to avoid prediction of considerably lower exit temperature of the working fluid.

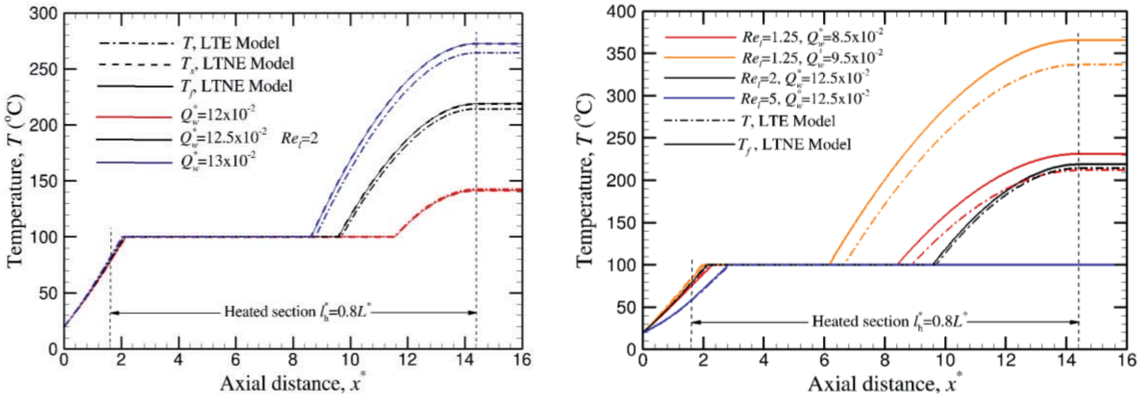

(a) (b)

Fig. 5.3: Effects of (a) applied heat flux and (b) inlet Reynolds number on axial temperature distributions using LTNE and LTE models. Other parameters: $\varepsilon = 0.3$, $K^* = 10^{-8}$ and $k_s^* = 8.25$

As mentioned before, from the data in Fig. 5.3(a), it is nearly impossible to distinguish the solid temperature from the fluid temperature obtained using LTNE model. Therefore, the absolute differences between these temperatures $\Delta T_{sf} = T_s - T_f$ are shown in Fig. 5.4 for the same cases presented in Fig. 5.3. Since in reality, ΔT_{sf} can be either positive or negative and since its magnitude remains quite small (the maximum being of the order of $1\,^{\mathrm{o}}\mathrm{C}$) over a large range of the axial distance x^* to be appreciated on a linear scale, the absolute value of ΔT_{sf} is plotted on a logarithmic scale as the ordinate in Fig. 5.4. It may be noted from Fig. 5.4 that for a complete phase change process $\left|\Delta T_{sf}\right|$ is characterized by the existence of two peaks, where the first peak, characterized by $T_s < T_f$, corresponds to the conversion from the sub-cooled liquid to the two-phase mixture and the second peak, with $T_s > T_f$, represents phase change from the two-phase mixture to the superheated vapor. Complete phase change occurs for all cases, except for $Re_l = 5$ and $Q_w^* = 12.5 \times 10^{-2}$, for which the phase change occurs only from the sub-cooled liquid state to the two-phase mixture. It is also obvious that since ΔT_{sf} changes sign in the phase change region, it must go to zero somewhere within the heated section (phase change region), although $\Delta T_{sf} = 0$ has never been predicted anywhere in the computational domain except at the inlet, where the Dirichlet boundary conditions on the energy conservation equations for both fluid and solid phases have been enforced. However, had that been the case, those points should have been eliminated from Fig. 5.4 in order to enable plotting $\left|\Delta T_{sf}\right|$ on a logarithmic scale. Nevertheless, the observation in Fig. 5.4

can be explained by considering the energy transfer through the fluid and the solid phases in the downstream and the upstream directions. It should also be recognized that the modeled effective diffusion coefficient for the two-phase mixture close to the saturated (either liquid or vapor) condition, even after applying the proposed smoothing algorithm, is several orders of magnitude lower than that for the single phase conditions, which acts as an enhanced resistance to the axial energy transfer. Most importantly, the temperature of the fluid phase remains unaltered in the two-phase region (in accordance with the thermodynamic constraints, imposed due to the present assumptions) where only the solid temperature is allowed to adjust itself in order to satisfy the overall energy balance. This explains the occurrence of two peaks for $\left|\Delta T_{sf}\right|$, as observed in Fig. 5.4.

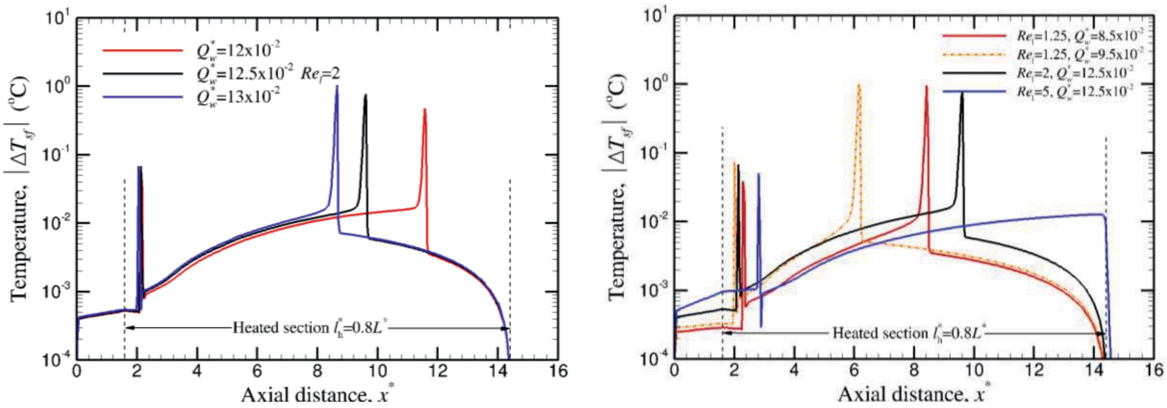

(a) (b)

Fig. 5.4: Variations of $\left|\Delta T_{sf}\right| = \left|T_s - T_f\right|$ obtained using LTNE model for (a) applied heat flux and (b) inlet Reynolds number. Other parameters: $\varepsilon = 0.3$, $K^* = 10^{-8}$ and $k_s^* = 8.25$

The variation of $\left|\Delta T_{sf}\right|$ and the delayed initiation of the phase change process obtained with LTNE model also explain the prediction of lower evaporator exit temperature predicted by LTE model. In order to elaborate this issue further, the overall energy balance of the evaporator for a complete phase change process (with liquid phase at the inlet and vapor phase at the exit) may be considered. Recognizing that at the evaporator exit, the temperature gradient is nearly zero and hence no heat is added (or lost) through the exit, the energy conservation may be written as:

$$\dot{m}_{out} C_{pv} T_{out} = \dot{m}_{in} C_{pl} T_{in} + \dot{q}''_w R l_h - \dot{q}_{cond} \tag{5.7}$$

where the suffix 'out' stands for the evaporator exit condition and $\dot{q}_{cond}$ is the heat loss through the evaporator inlet due to axial conduction, which may be expressed by Eqs. (5.8a) and (5.8b) for LTE and LTNE models, respectively:

$$\dot{q}_{cond} = k_{eff} \left(\frac{R^2}{2} \right) \left. \frac{dT}{dx} \right|_{in} \tag{5.8a}$$

$$\dot{q}_{cond} = \frac{R^2}{2} \left(k_{eff,f} \left. \frac{dT_f}{dx} \right|_{in} + k_{eff,s} \left. \frac{dT_s}{dx} \right|_{in} \right) \tag{5.8b}$$

In Eq. (5.8), the effective thermal conductivities are given by Eqs. (2.135) and (2.151) for LTE and LTNE models, respectively. Noting that under steady-state condition, the mass flow rate through the evaporator remains the same at any axial location and according to Eq. (3.50) it is given by $\dot{m}_{in} = \dot{m}_{out} = \rho_l u_{in} R^2/2$, Eq. (5.7) along with Eq. (5.8) may be partially non-dimensionalized using the definitions of dimensionless variables listed in Table 1. Therefore, expressions for the evaporator exit temperatures for LTE and LTNE models may be obtained from Eqs. (5.9a) and (5.9b), respectively, as follows:

$$T_{out} = \frac{1}{C_{pv}^*}\left[T_{in} + 2\left(\frac{Q_w^*}{Re_l}\right)\frac{h_{fg} l_h^*}{C_{pl}} - \left\{\varepsilon k_l^* + (1-\varepsilon) k_s^*\right\}\left.\frac{dT}{dx^*}\right|_{in}\right] \tag{5.9a}$$

$$T_{out} = \frac{1}{C_{pv}^*}\left[T_{in} + 2\left(\frac{Q_w^*}{Re_l}\right)\frac{h_{fg} l_h^*}{C_{pl}} - \left\{\varepsilon k_l^* \left.\frac{dT_f}{dx^*}\right|_{in} + (1-\varepsilon) k_s^* \left.\frac{dT_s}{dx^*}\right|_{in}\right\}\right] \tag{5.9b}$$

Comparing Eqs. (5.9a) and (5.9b), it is evident that first two terms on the RHS of these equations remain the same for both LTE and LTNE models. The difference in predictions of the evaporator exit temperature, therefore, results from the rest of the terms in Eq. (5.9). Since according to the definition $T_s = T_f + \Delta T_{sf}$, where ΔT_{sf} could either be positive or negative, Eq. (5.9b) may be further expressed as:

$$T_{out} = \frac{1}{C_{pv}^*}\left[T_{in} + 2\left(\frac{Q_w^*}{Re_l}\right)\frac{h_{fg} l_h^*}{C_{pl}} - \left\{\varepsilon k_l^* + (1-\varepsilon) k_s^*\right\}\left.\frac{dT_f}{dx^*}\right|_{in} - (1-\varepsilon) k_s^* \left.\frac{d(\Delta T_{sf})}{dx^*}\right|_{in}\right] \tag{5.10}$$

Noting that the gradient of ΔT_{sf} with respect to the axial coordinate x^* at the inlet is nearly zero and further recognizing that the temperature variation remains nearly linear in the liquid phase up to the initiation of phase change process, particularly for low Reynolds number applications, the axial temperature gradient at the inlet may be approximated as:

$$\left.\frac{dT}{dx^*}\right|_{in} \approx \frac{T_{sat} - T_{in}}{l_{sat}^*} \tag{5.11}$$

where T is the medium temperature for LTE model, whereas it represents the fluid phase temperature T_f for LTNE model and l_{sat}^* is the axial distance required for the initiation of the phase change process. Therefore, the predicted outlet temperature for both LTE and LTNE models in Eqs. (5.9a) and (5.10), respectively, may be expressed as:

$$T_{out} \approx \frac{1}{C_{pv}^*}\left[T_{in} + 2\left(\frac{Q_w^*}{Re_l}\right)\frac{h_{fg} l_h^*}{C_{pl}} - \left\{\varepsilon k_l^* + (1-\varepsilon) k_s^*\right\}\frac{T_{sat} - T_{in}}{l_{sat}^*}\right] \tag{5.12}$$

It is now apparent that since the phase change process initiates early for LTE model (as explained before) and hence l_{sat}^* is less than that obtained with the LTNE model, the predicted evaporator exit temperature is less for the LTE model as compared to that for the LTNE model. It is also evident that since the difference in l_{sat}^* increases with the decrease in inlet Reynolds number as well as the increase in imposed heat flux and for identical thermo-physical properties, k^* (for all phases) increases with the decrease in Reynolds number, the difference in predicted outlet temperatures also increases for these cases. However, if this argument is true, for identical operating conditions (inlet Reynolds number Re_l, applied heat flux Q_w^*, etc.), as well as lengths of the heated (l_h^*) and exit sections (l_e^*), the difference in the predicted evaporator exit temperatures should decrease with the increase in inlet length l_i^*. This has been demonstrated in Fig. 5.5 for $Re_l = 1.25$ for two different inlet lengths $l_i^* = 1.6$ (when $L^* = 16$) and $l_i^* = 3.6$ (when $L^* = 18$) with $Q_w^* = 8.5 \times 10^{-2}$, which clearly demonstrates that the difference in T_{out} decreases with the increase in l_i^* and is hardly visible for $l_i^* = 3.6$.

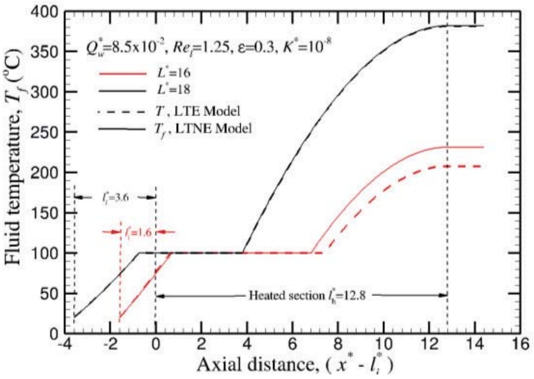

Fig. 5.5: Effects of inlet length on axial temperature distributions

5.1.5. Effects of Porous Media Properties

Figure 5.6 presents the effects of porous media properties (in the form of porosity ε in Fig. 5.6(a), permeability K^* in Fig. 5.6(b) and thermal conductivity of the solid matrix k_s^* in Fig. 5.6(c)) on the axial temperature distribution in the porous evaporator, predicted with LTNE model. According to LTNE model, the total energy transport per unit cross-sectional area of the evaporator through the solid and the fluid phases due to axial diffusion in the upstream direction can be obtained as:

$$q_{x,diff}^* = \Gamma_H^* \frac{dH^*}{dx^*} + k_{eff,s}^* \frac{dT_s^*}{dx^*} = q_{x,f}^* + q_{x,s}^* > 0 \tag{5.13}$$

where the first and the second parts, i.e., $q_{x,f}^*$ and $q_{x,s}^*$ represent the heat flux due to axial diffusion through the fluid and the solid media (phases), respectively. Since both H^* and T_s^* increase in the downstream direction (while H^* increases even in the two-phase region, $T_s^* \approx T_f^*$ remains nearly constant during the phase change process, owing to the present assumptions as demonstrated in Figs. 5.3 and 5.4) due to external heat addition, the axial diffusion effectively adds energy and heats up the medium in the upstream direction. Variations in the diffusive heat fluxes in the upstream direction $q_{x,f}^*$, $q_{x,s}^*$ and $q_{x,diff}^*$ are presented in Fig. 5.7 for the same cases shown in Fig. 5.6. Before analyzing the results in Figs. 5.6 and 5.7, however, it would be useful to study the behavior of effective diffusivity and thermal conductivities for different phases, involved in the diffusive energy transport process.

The definition of Γ_H^*, $k_{eff,f}^*$, $k_{eff,s}^*$ are presented in Eqs. (2.152), (2.151a) and (2.151b), respectively. For the single phase regions, since $D^*=0$ and $k_{eff,f}^*$ is a linear function of ε, Γ_H^* increases linearly with the increase in ε, whereas it is independent of K^*. Furthermore, since in these regions $\Gamma_H^*=k_{eff,f}^*\left(dT^*/dH^*\right)$, $q_{x,f}^*$ is given by $k_{eff,f}^*\left(dT^*/dx^*\right)$, which, as expected, is similar to the expression for $q_{x,s}^*$ in Eq. (5.13). In the two-phase region, however, $\Gamma_H^*\sim\left(\varepsilon K^*\right)^{1/2}$ follows a square-root dependence on both ε and K^*. On the other hand, $k_{eff,s}^*$ remains identical for both single and two-phase regions since it decreases and increases linearly with the increase in ε and k_s^*, respectively. It may be noted here that although $k_{eff,s}^*$ is few orders of magnitude higher than Γ_H^* in the two-phase region, conduction heat transfer through the solid phase in the upstream direction is considerably less in this region since T_s^* remains nearly constant and hence $dT_s^*/dx^*\approx 0$ [refer to Figs. 2.11, 5.3 and 5.4 for clarification].

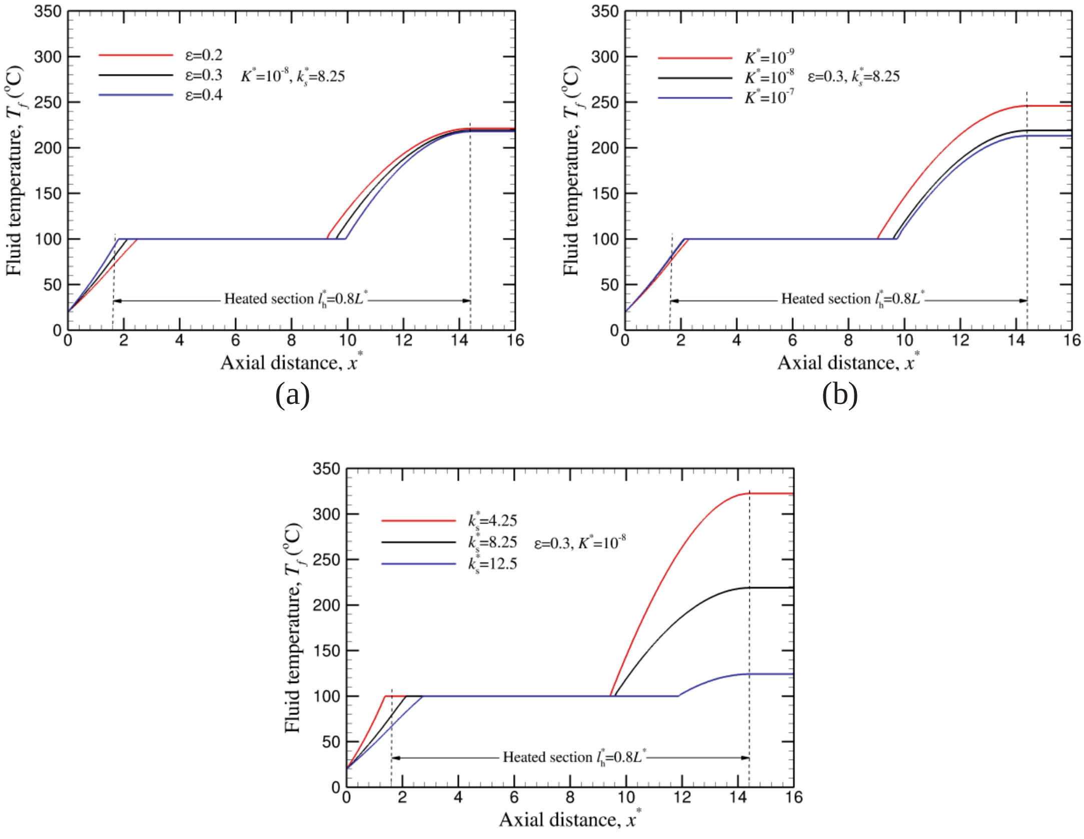

(a) (b)

(c)

Fig. 5.6: Effects of (a) porosity, (b) permeability (Darcy number) and (c) thermal conductivity of the solid matrix on the axial temperature distributions using LTNE model. Other parameters: $Re_l=2$ and $Q_w^*=12.5\times10^{-2}$

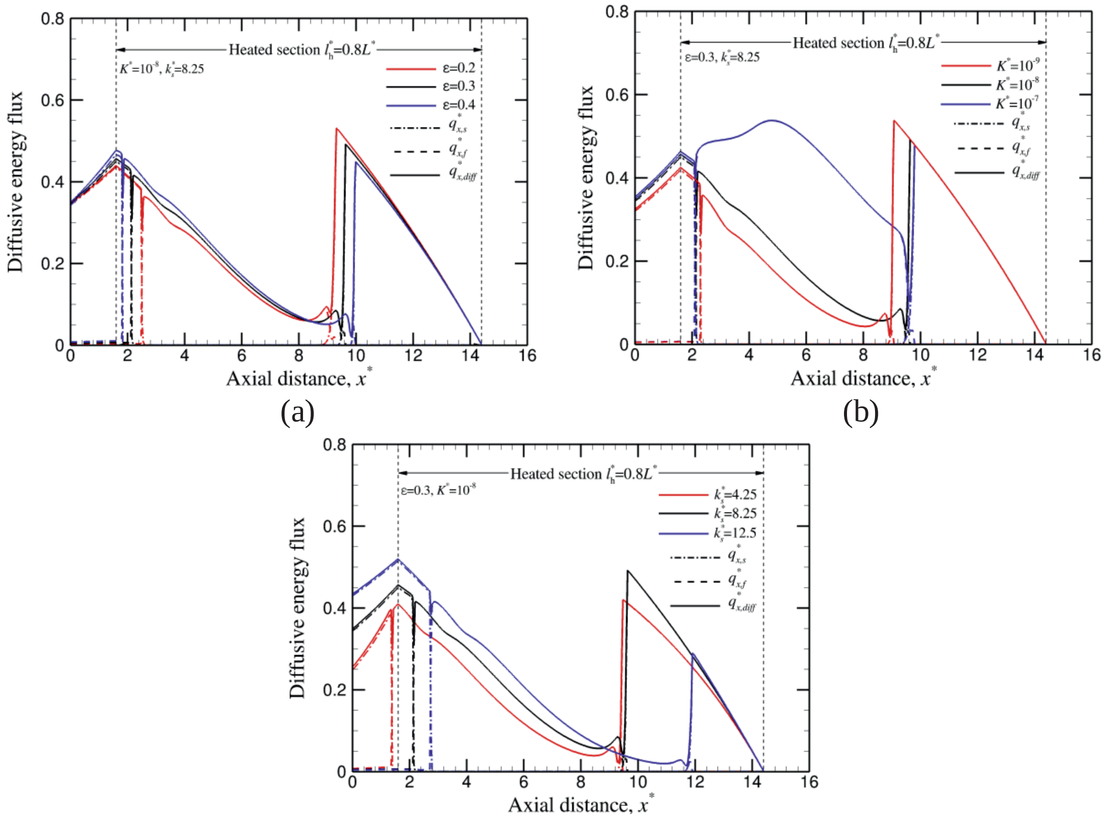

(a) (b)

(c)

Fig. 5.7: Effects of (a) porosity, (b) permeability (Darcy number) and (c) thermal conductivity of the solid matrix on axial diffusion in the upstream direction using LTNE model. Other parameters: $Re_l = 2$ and $Q_w^* = 12.5\times10^{-2}$

In view of the foregoing discussions and the results presented in Fig. 5.7, the following comments that also explain the variations, observed in Fig. 5.6, are now in order.

1. For the single phase regions, since $k_{eff,s}^*$ is several orders of magnitude higher than $k_{eff,f}^*$ and since $T_s^* \approx T_f^*$ holds for the entire length of the evaporator, the total diffusive energy flux $q_{x,diff}^*$ is dominated by $q_{x,s}^*$. The difference between $q_{x,s}^*$ and $q_{x,f}^*$ is even higher for the superheated vapor phase since k_v^* is approximately 27.4 times lower than k_l^* [refer to the thermo-physical properties of water in Table 2.1].
2. In the two-phase region, since $dT_s^*/dx^* \approx 0$ and hence $q_{x,s}^* \to 0$, $q_{x,diff}^*$ is represented by the diffusive flux through the fluid medium $q_{x,f}^*$.
3. Since there is no heat loss through the outlet of the evaporator, as indicated in Fig. 5.7 by $q_{x,diff}^* \to 0$ beyond the heated section (i.e., for $x^* > l_i^* + l_h^*$), a global energy balance of the evaporator suggests that an increase in the diffusive heat loss through the inlet for the same external heat addition and the mass flow rate is directly related to the reduced outlet temperature. This observation can be verified for all cases reported in Figs. 5.6 and 5.7.
4. Considerably higher heat loss through the inlet that occurs for higher k_s^*, as may be observed from Fig. 5.7(c), is responsible for the delayed (at larger axial distance from the inlet)

initiation of the phase change process from the sub-cooled liquid state to the two-phase mixture [see Fig. 5.6(c)]. The early initiation of the phase change process may also be associated with an early termination of the phase change process from the two-phase mixture to the superheated vapor as may be observed from Fig. 5.6(c).

5. An early initiation of the phase change process depends not only on the diffusive heat loss through the inlet, but also on the amount of energy diffused in the upstream direction through the two-phase region. Since this latter diffusive energy flux increases with both ε and K^*, the phase change process initiates early for higher values of ε [see Fig. 5.6(a)] and K^* [see Fig. 5.6(b)].
6. An early termination of the phase change process for $\varepsilon = 0.2$ as compared to $\varepsilon = 0.4$ [see Fig. 5.6(a)] and shorter two-phase region for $k_s^* = 8.25$ as compared to $k_s^* = 4.25$ [see Fig. 5.6(c)] can be explained by the increased diffusive heat transfer from the superheated vapor phase to the two-phase mixture region, which occurs for enhanced $k_{eff,s}^*$ (lower ε and higher k_s^*). The early termination of the phase change process may also occur due to lower energy diffusion in the upstream direction from the saturated vapor phase to the saturated liquid phase (through the two-phase mixture), as may be observed from Fig. 5.6(b) for lower values of K^*.

5.1.6. Effects of Inlet Length and Partitioning of Wall Heat Flux

The effects of inlet length (i.e., length of the heated section since the exit length has been kept fixed) and portioning of the wall heat flux according to different models presented in Eq. (2.158) are summarized in Fig. 5.8 for the LTNE model. It is easy to recognize from Fig. 5.8(a) that for a constant wall heat flux, a decrease in the inlet length is directly associated with an increase in the total heat supplied to the evaporator, which in turn, enhances the exit temperature of the working fluid. On the other hand, Fig. 5.8(b) demonstrates that different models for partitioning of the wall heat flux have almost no influence on the axial temperature distribution owing to the extremely high convective heat transfer coefficient between the solid and fluid phases, which nearly equates the temperatures of these phases, as demonstrated in Figs. 5.3 and 5.4. These models, however, could be important for other porous media with larger characteristic pore diameter and higher porosity.

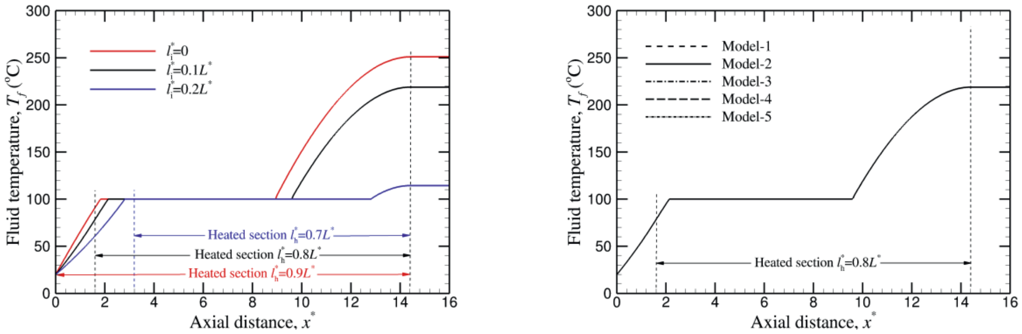

(a) (b)

Fig. 5.8: Effects of (a) inlet length and (b) partitioning of fluid and solid heat fluxes on axial temperature distributions using LTNE model. Other parameters: $Re_l = 2$, $Q_w^* = 12.5 \times 10^{-2}$, $\varepsilon = 0.3$, $K^* = 10^{-8}$ and $k_s^* = 8.25$

5.1.7. Results Obtained with Parametric Variations for *n*=3

This subsection describes the implementation of the complete phase change process inside porous evaporator for different exponent n in the expression of relative permeability. Figure 5.9 displays the effects of operating conditions (in the form of heat flux in Fig. 5.9(a) and Reynolds number in Fig. 5.9(b)) and properties of porous medium (in the form of porosity in Fig. 5.9(c) and Darcy number in Fig. 5.9(d)) on the axial temperature distribution for the fluid phase in the porous evaporator for both $n=1$ and $n=3$, predicted with LTNE model. It is evident from the figure that considerable quantitative differences in the predicted temperature distributions are found when comparing the results to the ones obtained using $n=1$. This is reasonable and has been already explained in chapter 4. Nevertheless, it can also be observed from the figure that the Darcy number in Fig. 5.9(d) has almost no influence on the axial temperature distribution when considering $n=3$, whereas the heat flux in Fig. 5.9(a), Reynolds number in Fig. 5.9(b) and porosity in Fig. 5.9(c) have significant effects on the exit predicted temperature distributions as compared with respective results that obtained using $n=1$.

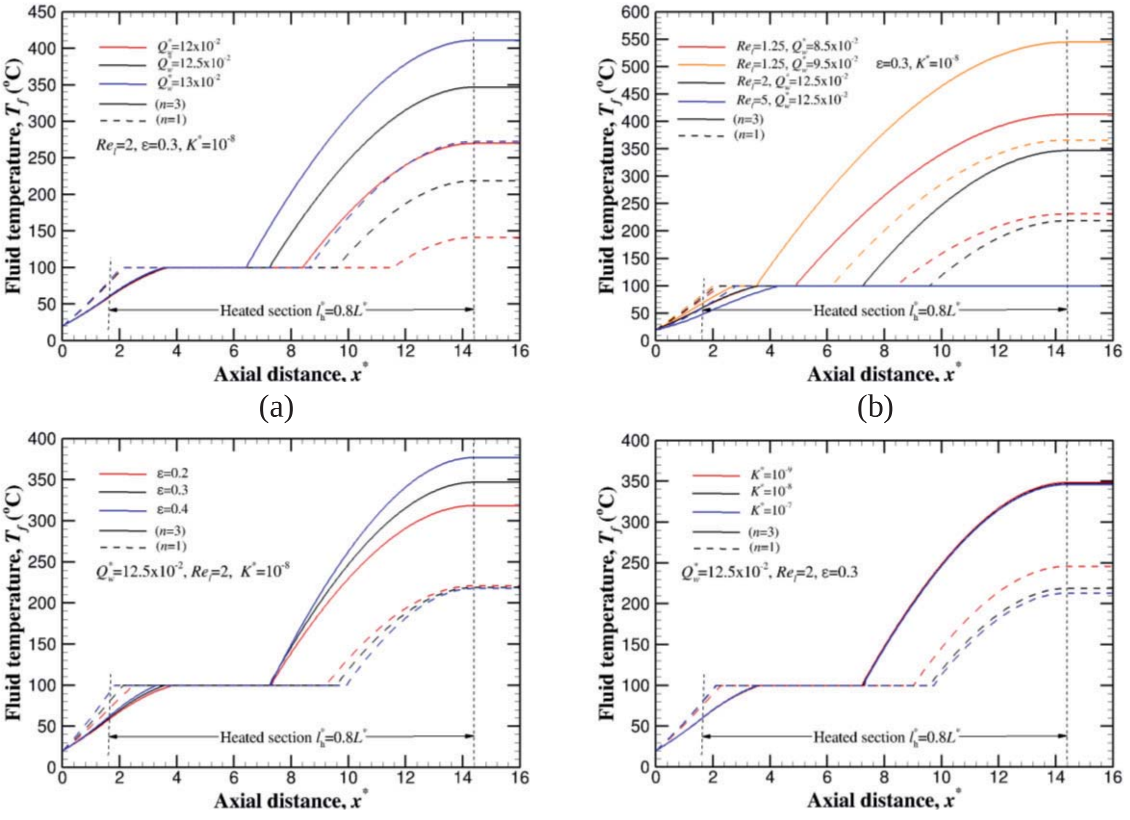

(c) (d)

Fig. 5.9: Comparison of fluid temperature variations as a function of axial distance using the smoothing algorithm with LTNE model for (a) different heat flux (b) different Reynolds number, (c) different porosity and (d) different Darcy number

An early initiation of phase change process for $n=1$ as compared to $n=3$ can be explained by the higher diffusive heat loss through the inlet, which occurs due to the higher Γ_H^* in the two-phase region. On the other hand, the delayed termination of phase change process for $n=1$ as compared to $n=3$ can also be explained by the lower energy diffusion in the upstream direction from the saturated vapor phase to the saturated liquid phase through the two-phase mixture region. In addition, the results clearly demonstrate that the present smoothing algorithm for the effective diffusion coefficient is successful in avoiding the occurrence of jump in the predicted temperature distribution for all tested cases.

5.2. Modeling in Two-dimensional Coordinates using Staggered Grid Layout

As far as the two-dimensional predictions along with LTE model are concerned, a further careful look into the results presented in chapter 4 reveals that although the formation of superheated vapor phase close to the heated surface could be clearly observed, the predictions are associated with a very high temperature change within a very short distance. Such apparently unrealistic predictions may be attributed to the discontinuities in the effective diffusion coefficient and effective heat capacity ratio (for transient problems) as mentioned before, or they could have resulted from the simplified LTE assumption, which prohibits the local (internal) heat transfer from the solid phase to the fluid phase and vice-versa. In the present investigation, the numerical simulations for the complete phase change process of water have been obtained employing the smoothing for effective diffusion coefficient along with the LTNE model in order to eliminate both excessively high temperature change and suppression of heat transfer between the solid phase and fluid phase, considering similar physical problems to that adopted in chapter 4 and the results obtained from both models (i.e., LTE and LTNE models) have been compared with each other for identical conditions in order to determine their applicability.

5.2.1. Problem Description and Basic Assumptions

The physical geometry and properties of the working fluid as well as the solid medium have been chosen to be similar to those given in chapter 4 for the purpose of comparison. The problem under investigation is a complete phase change process of water inside isotropic porous media, under steady-state condition, which has been considered as a demonstrative example. The schematic representation of the problem geometry is shown in Fig. 4.17 along with its dimensions. The models have been applied for a two-dimensional parallel plate channel ($L \times W$) and circular pipe ($L \times R$), filled with a porous medium of known properties, where an asymmetric heat source has been located on the bottom wall of the channel [see Fig. 4.17(a)] and on the outer surface of the pipe [see Fig. 4.17(b)], which is insulated elsewhere. The existing model, which is briefly presented here for purpose of comparison, considers a steady, two-dimensional complete phase change process within isotropic porous medium due to localized asymmetric heating inside either parallel plate channel or circular pipe duct. By assimilating the above assumptions, the system of the mass, momentum conservation equations are given in Eqs. (4.13) and (4.14), respectively. On the other hand, the energy conservation equations for both the fluid in Eq. (2.148) and the solid in Eq. (2.149) phases, where the volume-averaged internal heat exchange within porous matrix is added in both phases, are introduced for a steady two-dimensional coordinates in non-dimensional form, respectively, as:

$$\begin{aligned}\frac{\partial}{\partial x^*}\left(\gamma_H u^* H^*\right)+\frac{1}{r^*}\frac{\partial}{\partial y^*}\left(\gamma_H r^* v^* H^*\right)=\frac{\partial}{\partial x^*}\left(\Gamma_H^* \frac{\partial H^*}{\partial x^*}\right)+\frac{1}{r^*}\frac{\partial}{\partial y^*}\left(\Gamma_H^* r^* \frac{\partial H^*}{\partial y^*}\right)\\ +\frac{\partial}{\partial x^*}\left(f\frac{K^*\Delta\rho^* h_{fg}^*}{\nu_v^*}b_x^*\right)+\frac{1}{r^*}\frac{\partial}{\partial y^*}\left(r^* f\frac{K^*\Delta\rho^* h_{fg}^*}{\nu_v^*}b_y^*\right)+\dot{q}_{sf}^{\prime\prime\prime *}\end{aligned} \tag{5.14}$$

$$\frac{\partial}{\partial x^*}\left(k^*_{eff,s}\frac{\partial T_s^*}{\partial x^*}\right)+\frac{1}{r^*}\frac{\partial}{\partial y^*}\left(k^*_{eff,s}\, r^*\frac{\partial T_s^*}{\partial y^*}\right)-\dot{q}'''^{*}_{sf}=0 \tag{5.15}$$

where all the definitions of mixture properties and constitutive relations appearing in Eqs. (5.14) and (5.15) are provided in sections 2.2 and 2.4.

For the steady-state problem, the boundary conditions for the present investigation for both channel and pipe flow models have been employed at different boundaries of the computational domain as follows:

At the inlet $x^*=0$, the porous medium has been saturated with sub-cooled liquid water that enters the evaporator with uniform velocity u^*_{in} and specified constant temperature of the fluid T^*_{in}, which is less than the saturation temperature and hence $\rho^*_{in}=1$ has been set. Further at the inlet, the solid and fluid phases have been assumed to be in equilibrium. Therefore, the prescribed boundary conditions at the inlet may be summarized as:

$$H^*_{in}=\rho^*_{in}\left[h^*_{l,sat}-\rho^*_{in}C^*_{pl}\left(T^*_{sat}-T^*_{in}\right)-2h^*_{v,sat}\right] \tag{5.16a}$$

$$T_s^*=T^*_{in} \tag{5.16b}$$

$$u^*=u^*_{in} \tag{5.16c}$$

$$v^*=0 \tag{5.16d}$$

On the other hand, at the outlet (exit), i.e., at $x^*=L^*$ and for $0\le y^*\le W^*=1$ or $R^*=1$, the second derivatives of all variables have been set to zero. Therefore, the modified volumetric enthalpy H^* and the temperature of the solid phase T_s^* at the outlet have been obtained by linearly extrapolating the values at the neighboring interior nodes, whereas the hydrodynamic flow condition has been assumed to be fully-developed at the exit as follows:

$$\frac{\partial u^*}{\partial x^*}=\frac{\partial v^*}{\partial x^*}=0 \tag{5.17}$$

On the entire top wall of the channel (i.e., at $y^*=1$ and for $0\le x^*\le L^*$) and the center of the pipe (i.e., at $y^*=0$ and for $0\le x^*\le L^*$) as well as on the unheated segments of the bottom wall for the channel at $y^*=0$ and the pipe wall at $R^*=1$, i.e., for $0\le x^*\le l_i^*$ and $l_i^*+l_h^*\le x^*\le L^*$, the boundary conditions have been considered similar to that given in chapter 4 as follows [see Eq. (4.18) for clarification]:

$$-\Gamma^*_H\frac{\partial H^*}{\partial y^*}=f\,\frac{K^*\Delta\rho^*\,h^*_{fg}}{\nu^*_v}\,b^*_y \tag{5.18a}$$

$$k^*_{eff,s}\frac{\partial T_s^*}{\partial y^*}=0 \tag{5.18b}$$

$$v^*=0 \tag{5.18c}$$

At the position of the wall that is heated with constant heat flux, $\dot{q}''^{*}_{w,x}$, i.e., for $l_i^* \leq x^*$ and $x^* \leq l_i^* + l_h^*$ for the channel flow at $y^* = 0$ or for the pipe flow at $R^* = 1$, four different models have been employed according to the ratio of $\dot{q}''^{*}_{f,x}$ and $\dot{q}''^{*}_{s,x}$, where the applied heat flux $\dot{q}''^{*}_{w,x}$ at the wall have been added separately to the fluid and solid phases [see Eqs. (2.156) – (2.158d)]. Consequently, the boundary conditions can also be mathematically written as follows:

$$-\Gamma_H^* \frac{\partial H^*}{\partial y^*} - f \frac{K^* \Delta\rho^* h_{fg}^*}{\nu_v^*} b_y^* = \dot{q}''^{*}_{f,x} \tag{5.19a}$$

$$-k_{eff,s}^* \frac{\partial T_s^*}{\partial y^*} = \dot{q}''^{*}_{s,x} \tag{5.19b}$$

$$v^* = 0 \tag{5.19c}$$

5.2.2. Simulation of Complete Change Process in Channel Flow using Heat Flux at Lower Wall

A. Ranges of Parameters

As discussed earlier, the present study focuses on the complete phase change process of water inside a porous channel, considering LTNE model in order to eliminate the non-physical “jump” in the predicted temperature distribution close to the heated surface at the wall that has been obtained when using LTE model. In the present study, uniform fixed grids have been chosen and using identical number of control volumes $N_{CV} = 80 \times 25$ as used with LTE model for the purpose of comparison. In addition, similar values for the adjustable smoothing parameters have been used with LTNE model to those employed in LTE model. In the same manner, the discretized equations have been further under-relaxed and a relaxation factor of 0.1 has been generally used for most of the simulations in order to achieve convergence of the iterative solution. For all cases presented in this study, the convergence criterion has been set to 10^{-5}, which has been judiciously chosen such that the choice does not significantly affect the final solution.

The numerical simulations have been carried out for similar geometry as used with LTE model in chapter 4. Thus, the geometric parameters of the channel $L = 300\text{mm}$ ($L^* = 6$) and $W = 50\text{mm}$ ($W^* = 1$) have been considered for the present analysis. The unheated starting and exit length are both equal to 60mm ($l_i^* = l_e^* = 1.2$, which yields $l_h^* = 3.6$). The inlet velocity u_{in} has been allowed to vary between $2 \times 10^{-4}\ \text{m/s}$ and $8 \times 10^{-4}\ \text{m/s}$ for the entire study. These values have been chosen in order to satisfy the criterion of the fluid Reynolds number $Re_K < 1$ for the velocity fields for both the liquid and vapor phases. Furthermore, for the porous medium, average pore diameter, porosity and permeability have been varied from $50\mu\text{m}$ to $300\mu\text{m}$, 0.3 to 0.5 and $5 \times 10^{-12}\text{m}^2$ to $5 \times 10^{-11}\text{m}^2$, respectively. On the other hand, the thermal conductivity of the solid phase has been varied from 30W/mK to 80W/mK [65, 89].

The results have been obtained only for different values of heat flux, Reynolds number Re_l, Darcy number K^*, porosity ε, thermal conductivity of the solid matrix k_s^*, and different models for partitioning of the wall heat flux. At the heated surface, heat is added from an external source, supplying a constant heat flux $\dot{q}''_w$, ranging from $100\mathrm{kW/m^2}$ to $400\mathrm{kW/m^2}$ at the bottom wall of the channel. In addition, the acceleration due to gravity vector has been assumed to act only in the negative y^*-direction and hence $\tilde{b}_y=-1$ has been considered for all the cases. Based on this, the following ranges of dimensionless parameters have been considered in the present work as given in Table 5.2:

Table 5.2: Ranges of dimensionless parameters used for two-dimensional channel flow along with LTNE model

Parameters	Ranges of dimensionless values
Inlet Reynolds number, Re_l	$70-120$
Heat Flux, Q_w^*	$8-32$
Porosity, ε	$0.3-0.5$
Darcy number K^*	$10^{-9}-10^{-8}$
Solid thermal conductivity, $k_{s,ref}^*$	$0.3-0.8$

Other than the fixed values, the reference case has been chosen with the following parameters: $Fr=1.2\times10^5$, $\tilde{\sigma}=3.6\times10^7$, $Re_l=85$, $d_p^*=2\times10^{-3}$, $\varepsilon=0.4$, $K^*=5\times10^{-9}$ and $k_s^*=0.5\,(50\,\mathrm{W/mK})$, along with Model-1 for the partitioning of wall heat flux. These parameters have been kept fixed for all cases and they have been varied only when their effects on the phase change process have been investigated.

B. Results Obtained with Variation of Heat Flux

In view of the discussions made so far in chapter 4 for multi-dimensional problems, the performance of the LTNE model for the simulation of the present problem may now be critically examined. The predicted temperature distributions for both fluid and solid phases, the liquid saturation distribution, and the liquid as well as the vapor velocity vectors have been obtained for different values of the heat flux. The results are summarized in Figs. 5.10 – 5.12. These figures display the numerical results of the complete phase change process obtained with the LTNE model when the heat flux imposed at the heated surface is varying from $Q_w^*=24$ to $Q_w^*=32$, since with the LTE model unrealistic predictions are obtained only at higher heat fluxes, associated with the formation of superheated vapor zone. In order to obtain these results, the imposed wall heat flux has been partitioned according to Model-1, where the entire amount of heat has been assumed to be added only to the solid phase [see Eq. (2.158a)]. Since the common features, observed for the liquid-vapor phase change process inside an asymmetrically heated horizontal porous channel, have been elaborately discussed in chapter 4, they are not repeated here. On the other hand, the difference in predictions, observed specifically with LTNE model as compared to those obtained for LTE model, is only considered here for further discussion.

Figure 5.10 shows the numerical results of complete phase change process for $Q_w^*=24$, while other conditions have been kept fixed to those of the reference case. It is clear from the figure that the fluid and solid temperatures locally exceed the saturation temperature. The aforementioned heat flux corresponds to the onset of the complete phase change process, at which a vanishing liquid saturation first appears close to the heated surface as shown in Fig. 5.10(b). It is observed from Fig. 5.10(a) that a small superheated vapor region is formed close to the bottom wall towards the end of the heated surface. It can also be observed from the figure that the degree of superheating decreases and the size of superheated vapor region is extended somewhat at the heated surface, whereas the two-phase mixture zone is contracted, as compared to the LTE model at the same conditions [see Fig. 4.22(a) for comparison]. Figure 5.10(c) displays the solid temperature distribution, where a pronounced similarity to the temperature distribution in the fluid phase shown in Fig. 5.10(a) can be observed. Inside the domain, the temperature difference between the solid and the fluid phases is hardly recognizable. A difference occurs close to the heated surface, owing to the extremely high convective heat transfer coefficient between these phases [see Fig. 5.4 for clarification]. The liquid saturation distribution is shown in Fig. 5.10(b), which retains similar characteristic to the previous case for LTE model presented in Fig. 4.22(b) with little more growth of superheated vapor region at the heated surface. Liquid and vapor velocity vectors are shown in Figs. 5.10(d) and 5.10(e), which also retain similar characteristics to those presented in Figs. 4.22(c) and 4.22(d), respectively, and hence need no further explanation.

(a)

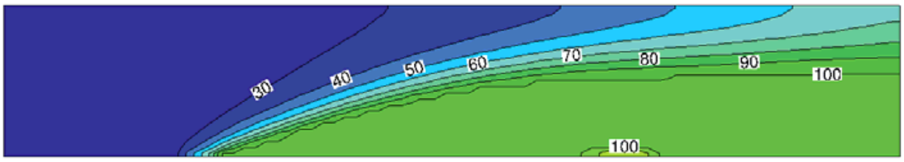

Fluid temperature distribution $\left(T_{f,\max} \approx 112\,^{\circ}\mathrm{C}\right)$

(b)

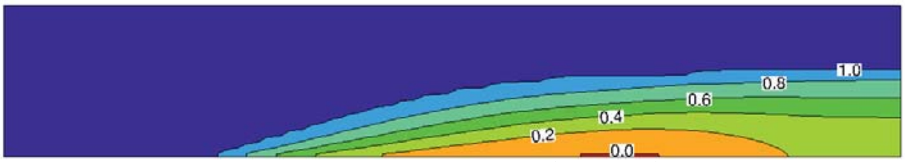

Liquid saturation distribution $\left(s_{\min} = 0\right)$

(c)

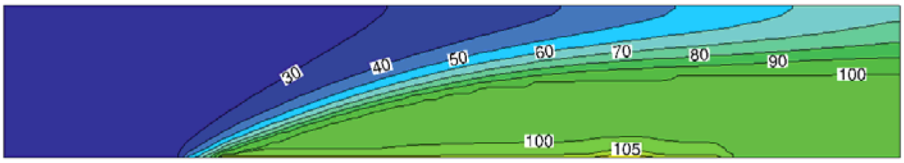

Solid temperature distribution $\left(T_{s,\max} \approx 123^{\circ}\,\mathrm{C}\right)$

(d)

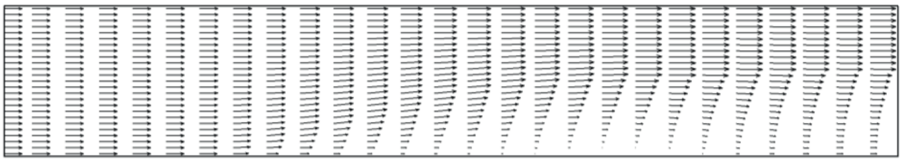

Liquid velocity vectors $\left(Re_{K,\max} = 8.09 \times 10^{-3}\right)$

(e)

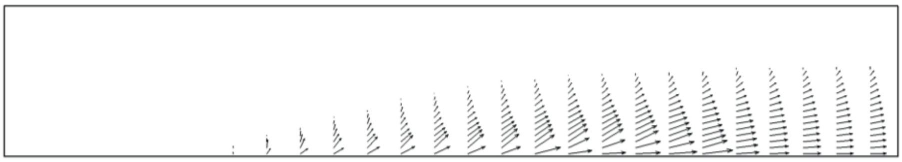

Vapor velocity vectors $\left(Re_{K,\max} = 6.58 \times 10^{-3}\right)$

Fig. 5.10: Solution of complete phase change process in channel flow using LTNE model along with Model-1 for partitioning of the wall heat flux for $Q_w^* = 24$, $Re_l = 85$, $\varepsilon = 0.4$, $k_s^* = 0.5$, and $K^* = 5 \times 10^{-9}$

With further increase in the heat flux to $Q_w^* = 28$ and $Q_w^* = 32$, as presented in Figs. 5.11 and 5.12, it is evident that the superheated vapor region above the heated surface is more extended in the axial and transverse directions and penetrates deeper towards the center of the channel as compared to the previous case in Fig. 5.10(a). It is also evident from the figures that the superheated vapor zone never extends to the exit of the channel, as observed in Fig. 4.24 with LTE model for $Q_w^* = 32$. Most importantly, the locations of the boiling and the condensation fronts obtained from LTNE model may be clearly identified in Figs. 5.10 – 5.12, as compared with LTE model in Figs. 4.22 – 4.24, not only from the distribution of fluid temperature, but also from the velocity vectors in the liquid and the vapor phases, respectively. A higher heat transfer between the solid and fluid phases, which counteracts the incoming sub-cooled liquid flow, leads to a stronger upward vapor flow and the condensation front is shifted in the upstream direction. The liquid saturation distribution inside the two-phase zone in Figs. 5.11(b) and 5.12(b) retains similar characteristics as in the previous case in Fig. 5.10(b). The liquid and vapor velocity vectors shown in Figs. 5.11(d), 5.12(d), 5.11(e) and 5.12(e) also show similar characteristics to the previous case in Figs. 5.10(d) and 5.10(e)), however, with a more horizontal orientation of vapor velocity inside the superheated vapor region. The liquid velocity vector is once again parallel to the side walls at the inlet and then bypasses the superheated vapor region immediately above the heated surface.

Most importantly, it can be observed from Figs. 5.10 – 5.12 that the maximum temperatures of the fluid and the solid phases predicted by LTNE model are significantly lower, particularly in the superheated vapor region at the heated surface, as compared to those obtained with LTE model for the same Q_w^*, which appears to be more realistic. Further, irrespective of the imposed wall heat flux, neither of them exceeds the melting temperature of the solid matrix of the considered porous medium [see Figs. 4.22(a) – 4.24(a) for comparison]. In detail, with LTNE model, $T_{\max,f}$ has been obtained as $112^{\circ}\mathrm{C}$, $160^{\circ}\mathrm{C}$ and $214^{\circ}\mathrm{C}$ in contrast to $T = 180^{\circ}\mathrm{C}$, $625^{\circ}\mathrm{C}$ and $2000^{\circ}\mathrm{C}$, obtained from LTE model, whereas $T_{\max,s}$, which can be predicted only with LTNE model, has been obtained as $123^{\circ}\mathrm{C}$, $172^{\circ}\mathrm{C}$ and $227^{\circ}\mathrm{C}$ for $Q_w^* = 24$, $Q_w^* = 28$ and $Q_w^* = 32$, respectively, and hence $T_{\max,s}$ has been invariably observed to be greater than $T_{\max,f}$. This observation is quite expected and may be explained in view of the fact that the results, presented in Figs. 5.10 – 5.12, have been obtained employing Model-1 for the partitioning of wall heat flux, i.e., by assuming the entire heat to be added to the solid phase at the wall and hence T_s increases more than T_f in the vicinity of the wall, where the maximum temperatures occurs. The temperature of the fluid phase also eventually increases and the phase change process is initiated at the wall due to the volumetric heat exchange $\dot{q}_{sf}'''^*$ from the solid phase to the fluid phase. While the effects of heat flux on the difference in the predicted temperatures are quite expected, the lower predicted temperature at the heated surface, obtained using LTNE model, can be attributed to the higher conduction heat loss through the inlet, owing primarily to the enhanced effective diffusion coefficient. In order to explain the aforementioned differences in observations, the additional diffusive heat transfer mechanisms, available for LTNE model, may now be critically examined. According to this model, energy may diffuse through both solid structures and fluid phase, whereas for LTE model, heat diffusion can occur only through the combined medium due to the gradient in H^*. Nevertheless, like Γ_H^* for LTE model, Γ_H^* for LTNE model also remains quite low in the two-phase region close to $s=0$ and $s=1$ even after applying the smoothing algorithm, although the difference in Γ_H^* within LTNE model across the interfaces separating the single and the two-phase regions are considerably less severe than that obtained for LTE model. Therefore, even for LTNE model, diffusion through the fluid medium cannot play any significant role in heat transfer from the superheated vapor phase to the two-phase mixture.

(a)

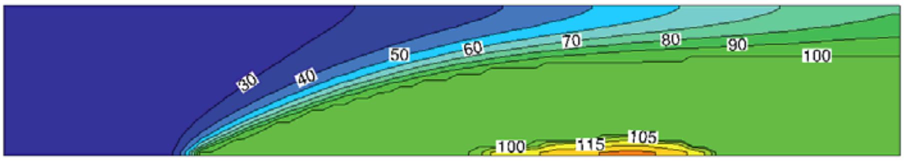

Fluid temperature distribution $\left(T_{f,\max} \approx 160\,^{\circ}\mathrm{C}\right)$

(b)

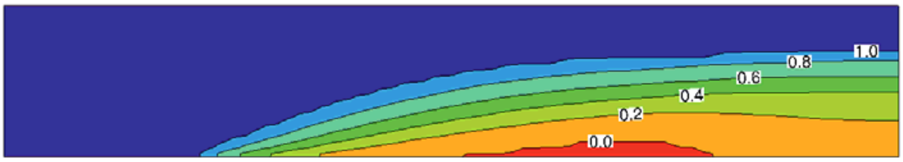

Liquid saturation distribution $\left(s_{\min} = 0\right)$

(c)

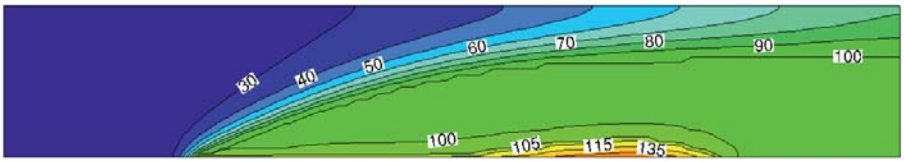

Solid temperature distribution $\left(T_{s,\max} \approx 172\,^{\circ}\mathrm{C}\right)$

(d)

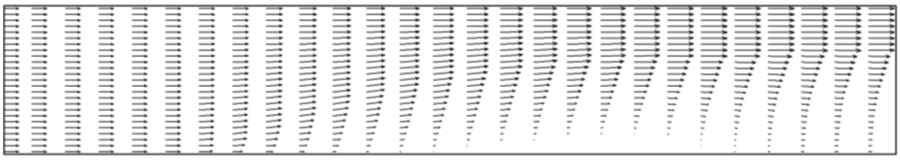

Liquid velocity vectors $\left(Re_{K,\max} = 9.6014\times10^{-3}\right)$

(e)

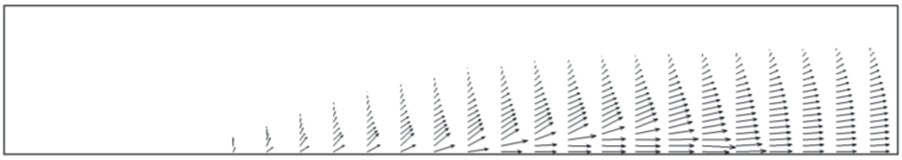

Vapor velocity vectors $\left(Re_{K,\max} = 7.98\times10^{-3}\right)$

Fig. 5.11: Solution of complete phase change process in channel flow using LTNE model along with Model-1 for partitioning of the wall heat flux for $Q_w^* = 28$, $Re_l = 85$, $\varepsilon = 0.4$, $k_s^* = 0.5$, and $K^* = 5\times10^{-9}$

(a)

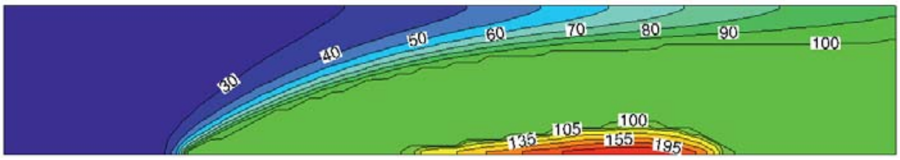

Fluid temperature distribution $\left(T_{f,\max} \approx 214^{\circ}\mathrm{C}\right)$

(b)

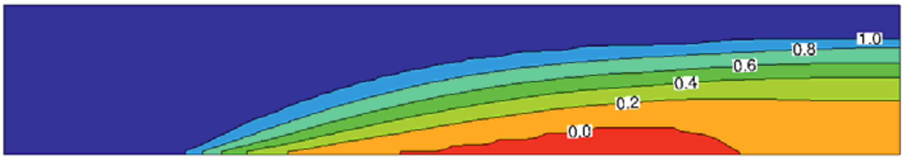

Liquid saturation distribution $\left(s_{\min} = 0\right)$

(c)

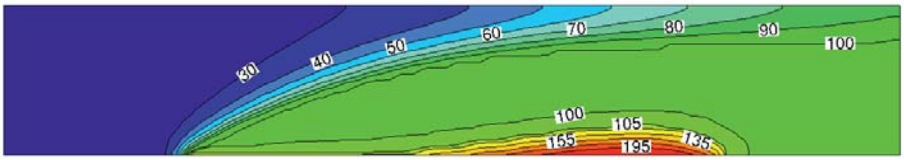

Solid temperature distribution $\left(T_{s,\max} \approx 227^{\circ}\mathrm{C}\right)$

(d)

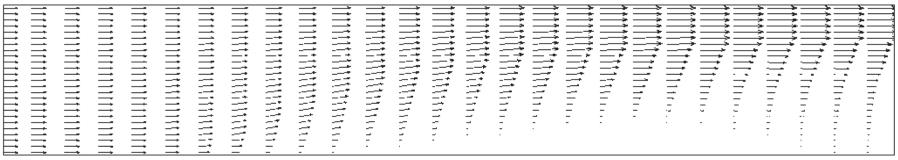

Liquid velocity vectors $\left(Re_{K,\max} = 1.12\times10^{-2}\right)$

(e)

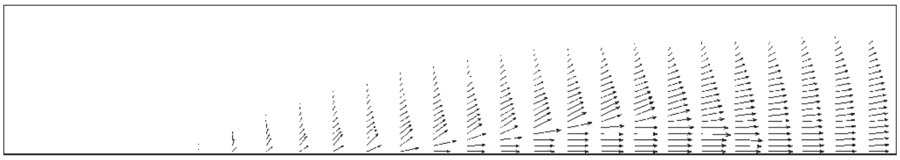

Vapor velocity vectors $\left(Re_{K,\max} = 8.63\times10^{-3}\right)$

Fig. 5.12: Solution of complete phase change process in channel flow using LTNE model along with Model-1 for partitioning of the wall heat flux for $Q_w^* = 32$, $Re_l = 85$, $\varepsilon = 0.4$, $k_s^* = 0.5$, and $K^* = 5\times10^{-9}$

In this situation, heat conduction through the solid phases, which is governed by Eq. (5.15) and is driven by the gradient of T_s^* according to LTNE model, assumes the dominant role and transports energy across the boiling and the condensation fronts. Close to the interface between the superheated vapor and the two-phase mixture region, particularly where $s \approx 0$, the marginally heated solid phase then transfers energy to the relatively colder fluid phase due to the internal heat exchange mechanism, which is available only for LTNE model. Nevertheless, owing to the small pore diameter $d_p = 100\,\mu\mathrm{m}$ (or $d_p^* = 2\times10^{-3}$) for all test cases in Figs. 5.10 – 5.12, the convective heat exchange between the solid and the fluid phases is extremely high according to Eqs. (2.153) and (2.154), and hence the effects of conduction heat transfer through the solid phase is clearly visible from the isotherms in Figs. 5.10 – 5.12 only close to the boiling front. Everywhere else, however, $T_s^* \approx T_f^*$ is observed except at the wall, where the maximum temperatures occur for both solid and fluid phases. These additional mechanisms, incorporated in LTNE model for conduction heat transfer through the solid phase and subsequent heating of the two-phase mixture due to internal energy exchange, are responsible for i) expansion of the superheated vapor zone in the transverse direction and ii) prediction of lower maximum temperatures for both fluid and solid phases that appears to be reasonable. Therefore, LTNE model is strongly recommended for the realistic prediction of complete liquid-vapor phase change process within porous media, in lieu of using the conventional LTE model, although the former may appear to be more complex as far as the numerical implementation is concerned.

C. Results Obtained along the Flow and Transverse Directions

In order to further examine the characteristics of complete phase change process inside porous media, the variations in liquid saturation, fluid temperature and solid temperature for different values of Q_w^* are presented in Figs. 5.13 and 5.14 as functions of transverse (y^*) and axial (x^*) coordinates, respectively, considering Model-1for the partitioning of wall heat flux. While the results in Fig. 5.13 are presented at $x^* = 0.7L^*$, Fig. 5.14 shows the distributions at the wall i.e., at $y^* = 0$. Further in Figs. 5.13 and 5.14, the boiling and the condensation fronts for $Q_w^* = 32$ are shown as ‘BF’ and ‘CF’, respectively. These fronts may be easily identified from the variations of s and T_f^* for other wall heat fluxes, although they are not marked in these figures for the sake of brevity.

It is evident from the Fig. 5.13 that with the increase in Q_w^*, both boiling and condensation fronts move upward, confirming that both superheated vapor and two-phase mixture regions expand more in the transverse direction. These observations are quite expected and can be explained in view of the discussions already made so far. Figure 5.13(b) also shows that the maximum difference between T_s^* and T_f^* occurs at the wall, which may be attributed to the model employed for the portioning of imposed wall flux that assumes entire heat to be added only to the solid phase. The difference in solid and fluid phase temperatures reduces remarkably within a very short distance away from the wall in the transverse direction and hence $T_s^* \approx T_f^*$ is obtained almost everywhere else, owing to the extremely high volumetric heat exchange between the solid and the fluid phases, as explained earlier. Close to the boiling front, however, T_s^* is observed to be marginally higher than T_f^* in order to allow for necessary energy transport across the interface separating the superheated vapor and the two-phase mixture regions.

The variation in s and T_f^*, as presented in Fig. 5.14, clearly show the existence of one condensation front and two boiling fronts, which is in agreement with the observed isotherms for the fluid phase in Figs. 5.10 – 5.12. The presence of considerable heat transfer due to axial conduction in the upstream direction is also clearly demonstrated in Fig. 5.14(b) by the positive gradients of both solid and fluid temperatures in the axial direction even in the unheated upstream section of the evaporator, which is mostly filled with sub-cooled liquid phase. The contribution of axial conduction to the overall local energy transport increases with the increase in Q_w^* and hence the condensation front moves towards the inlet of the evaporator, as may be observed from the variations of s in Fig. 5.14(a). Owing to the same reason, for the maximum considered heat flux

$Q_w^* = 32$, the phase change process initiates in the unheated segment and the two-phase mixture is observed even before the heat flux is actually introduced at the wall starting from $l_i^* = 1.2$.

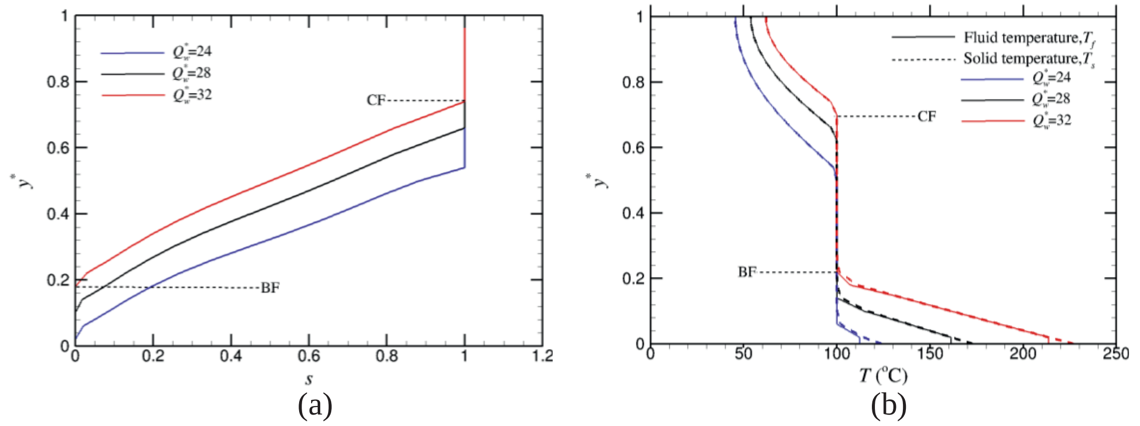

(a) (b)

Fig. 5.13: Effects of Q_w^* on the variation of (a) liquid saturation and (b) temperature distributions for both solid and fluid phases as functions of y^* at $x^* = 0.7L^*$ obtained using LTNE model with wall heat flux partitioned according to Model-1

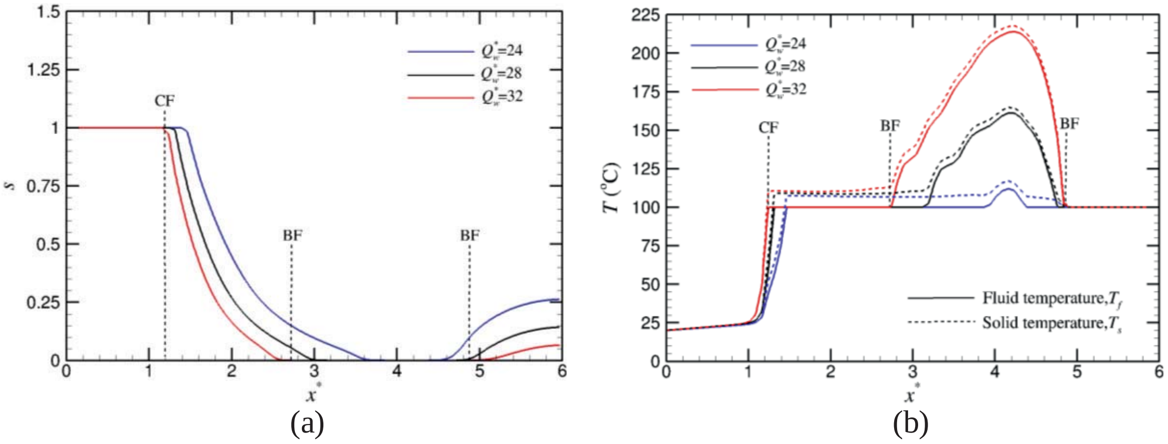

(a) (b)

Fig. 5.14: Effects of Q_w^* on the variation of (a) liquid saturation and (b) temperature distributions for both solid and fluid phases as functions of x^* at $y^* = 0$ obtained using LTNE model with wall heat flux partitioned according to Model-1

After the initiation of phase change process for a given Q_w^*, as more heat is added to the evaporator through the wall, a superheated vapor region is formed, marked by the first boiling front from the inlet in Fig. 5.14. Owing mainly to the configuration and the heating condition for the present problem, however, the maximum solid and fluid temperatures at the wall occur around $x^* \approx 4.2 = 0.7L^*$ irrespective of Q_w^*. With further increase in the axial distance, both T_s^* and T_f^* drop remarkably, thereby allowing for the heat loss from the superheated vapor region to the two-phase mixture zone that occupies most of the areas at the exit of the evaporator. As a result, a second boiling front is formed. It is also expected and evident from Fig. 5.14 that the of superheated vapor region at the wall increases with the increase in Q_w^*, which is in accordance with the variations of T_f^* in Figs. 5.10 – 5.12.

It is also interesting to note from Figs. 5.10 – 5.14 that over most of the two-phase region except close to the wall and the boiling front, $T_s^* \approx T_f^* = T_{sat}^*$ is observed and hence $\delta T_s^* \big/ \delta x_j^* \approx 0$ is obtained. Consequently, in this region, heat conduction through the solid phase is negligible in all directions and the total diffusive energy transport is represented only by that through the fluid medium, which is driven by the finite of H^*, although $\delta T_f^* \big/ \delta x_j^* = 0$. On the other hand, in the single phase regions, since $k_{eff,s}^*$, is several orders of magnitude higher than $k_{eff,f}^*$ and since $T_s^* \approx T_f^*$ holds, which implies $\delta T_s^* \big/ \delta x_j^* \approx \delta T_f^* \big/ \delta x_j^*$ almost everywhere in these regions except in the vicinity of the wall and the boiling front, the total energy transfer due to heat conduction is dominated by that through solid phase.

D. *Effects of Partitioning of Wall Heat Flux*

The effects of partitioning of the wall heat flux according to the different models given in Eq. (2.158) are summarized in Figs. 5.15 and 5.17. These results are shown only for $Q_w^* = 32$, while other conditions have been kept fixed to those of the reference case, since the maximum difference in predictions, due to the applied model for portioning of Q_w^* is best exhibited at the highest considered heat flux. It may be noted here that for the chosen porosity $\varepsilon = 0.4$ and thermal conductivities of the fluid and the solid phases, $\dot{q}_f'' \big/ \dot{q}_s''$ has been obtained as 0 and $2/3$ for Models-1 and 4, respectively, whereas it has been obtained allowed to vary approximately from 3.3×10^{-4} to 9×10^{-3} and 5×10^{-4} to 1.2×10^{-2} for Models-2 and 3, respectively, where the lower and the upper limits correspond to the properties of vapor ($k_f^* = k_v^*$) and liquid ($k_f^* = k_l^*$) phases, respectively. It is, therefore, evident that the modeled fraction of Q_w^* added directly to the fluid phase at the wall increases as the employed model for the portioning of the wall heat flux is changed from Model-1 to Model-4.

Comparison of results in Figs. 5.12 and 5.15 – 5.17, obtained employing different models for the partitioning of wall heat flux, clearly shows that their overall features remain nearly identical and hence they are hardly distinguishable from each other. Most of the variations are restricted extremely close to the wall, where the differences in predicted $T_{s,\max}$ and $T_{f,\max}$ have been recorded to be approximately $13^{\circ}\mathrm{C}$, $3^{\circ}\mathrm{C}$, $-6^{\circ}\mathrm{C}$ and $-15^{\circ}\mathrm{C}$ for Models-1, 2, 3 and 4, respectively, owing mainly to the higher fraction of heat addition to the fluid phase at the evaporator wall. Everywhere else, even close to the boiling front, however, almost identical solutions are obtained, irrespective of the employed model. In order to further clarify this issue, the variations in s and T_f as functions of y^* at the exit of the evaporator are presented in Fig. 5.18, which clearly confirms that the solutions for all models, at least at the exit, are indeed identical. In this figure, the identical solutions are demonstrated by the distributions of s in the two-phase region and that in the sub-cooled liquid phase are exhibited by the variations in T_f. The temperature distributions in the solid phase are, however, not shown in figure since it could not be distinguish from T_f, as mentioned earlier. A closer inspection of the data in Fig. 5.13(b) reveals that other than the region extremely close to the heated wall, the maximum difference in T_s and T_f occurs near the boiling front. This difference has been found to be approximately $3.5^{\circ}\mathrm{C}$ for all models, although similar results are not presented in this thesis for the sake of brevity. Therefore, Model-2 appears to be the most realistic, although Model-1 has been found to be the most stable. On the other hand, Models-3 and 4 predict negative differences between T_s and T_f at the wall, even in the superheated vapor region, which may be considered unrealistic, although the interior solutions remain nearly identical to that obtained employing the other realistic or stable models, identified as Models-1 and 2, respectively.

(a)

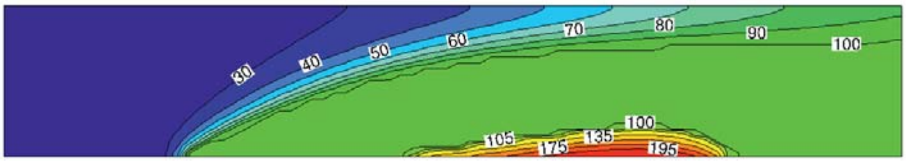

Fluid temperature distribution $\left(T_{f,\max} \approx 227\,^{\circ}\mathrm{C}\right)$

(b)

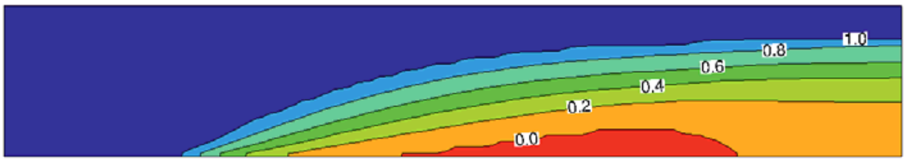

Liquid saturation distribution $\left(s_{\min} = 0\right)$

(c)

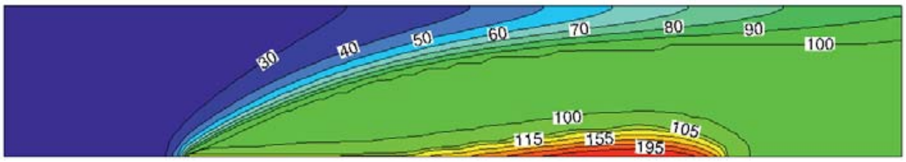

Solid temperature distribution $\left(T_{s,\max} \approx 230\,^{\circ}\mathrm{C}\right)$

Fig. 5.15: Solution of complete phase change process in channel flow using LTNE model along with Model-2 for partitioning of the wall heat flux for $Q_w^* = 32$, $Re_l = 85$, $\varepsilon = 0.4$, $k_s^* = 0.5$, and $K^* = 5 \times 10^{-9}$

(a)

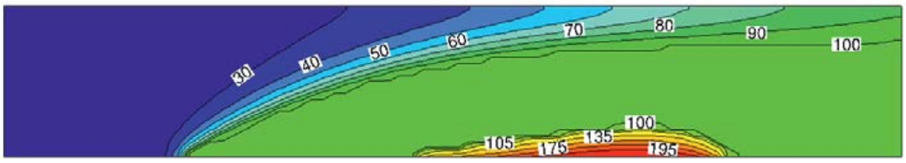

Fluid temperature distribution $\left(T_{f,\max} \approx 233\,^{\circ}\mathrm{C}\right)$

(b)

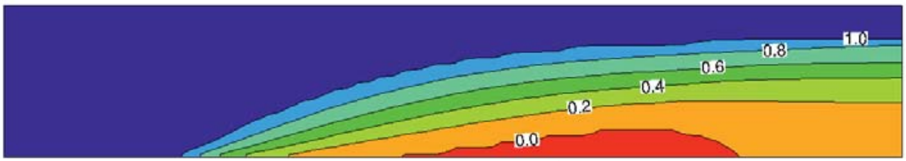

Liquid saturation distribution $\left(s_{\min} = 0\right)$

(c)

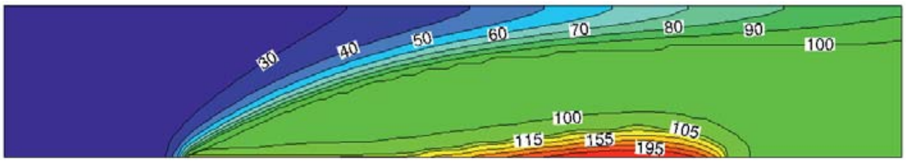

Solid temperature distribution $\left(T_{s,\max} \approx 227\,^{\circ}\mathrm{C}\right)$

Fig. 5.16: Solution of complete phase change process in channel flow using LTNE model along with Model-3 for partitioning of the wall heat flux for $Q_w^* = 32$, $Re_l = 85$, $\varepsilon = 0.4$, $k_s^* = 0.5$, and $K^* = 5 \times 10^{-9}$

(a)

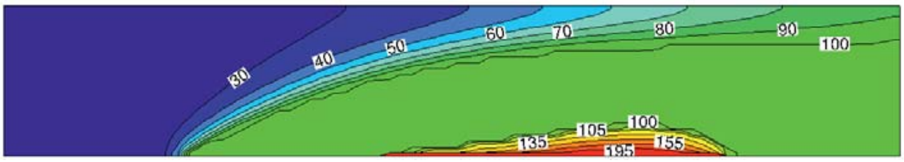

Fluid temperature distribution $\left(T_{f,\max} \approx 237\,^{\circ}\mathrm{C}\right)$

(b)

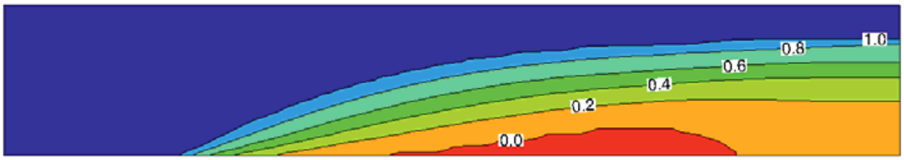

Liquid saturation distribution $\left(s_{\min} = 0\right)$

(c)

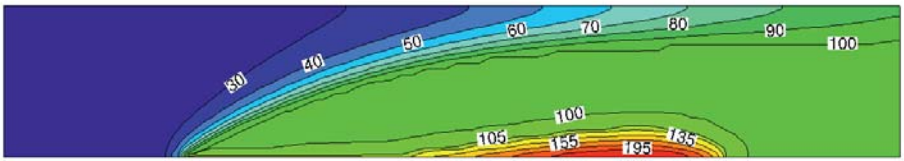

Solid temperature distribution $\left(T_{s,\max} \approx 222\,^{\circ}\mathrm{C}\right)$

Fig. 5.17: Solution of complete phase change process in channel flow using LTNE model along with Model-4 for partitioning of the wall heat flux for $Q_w^* = 32$, $Re_l = 85$, $\varepsilon = 0.4$, $k_s^* = 0.5$, and $K^* = 5 \times 10^{-9}$

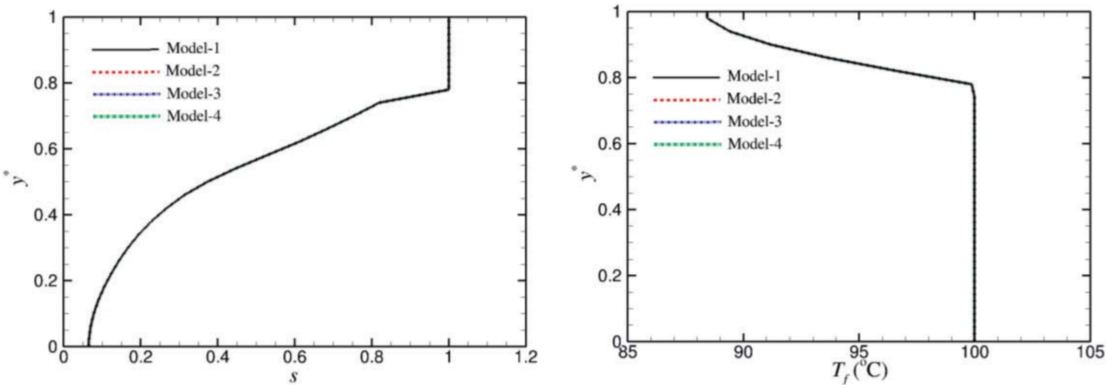

(a) (b)

Fig. 5.18: Effects of different models for partiontioning of wall of heat flux on the variations of (a) s, (b) T_f as functions of y^* at the evaporator exit obtained using LTNE model

E. Result Obtained with Parametric Variations

In this subsection, the effect of parametric variations on fluid flow and heat transfer associated with complete phase change process using staggered grid layout will be presented, employing Model-1 for the partitioning of wall heat flux. Figure 5.19 displays the numerical results representative of the complete phase change process of the fluid temperature distribution for different Reynolds number, when the heat flux at the bottom wall is $Q_w^* = 32$, while other parameters have been kept the same as that for the reference case. It can be observed that an extensive two-phase zone develops inside the channel above the superheated vapor region for $Re_l = 70$ as compared to $Re_l = 120$. The decrease in Reynolds number leads to an extension of the two-phase region towards the upper wall at the exit of the channel and increases the size of superheated vapor region due to increases the residence time of fluid inside the channel. Furthermore, it can also be found from the figure that the superheated vapor region expands in the transverse and axial directions without occurrence of jump in the predicted temperature distribution. The effect of Reynolds number on the difference in predicted temperatures is quite expected and hence needs no further explanation. Most importantly, it is evident from the Fig. 5.19 that a marginal change in the flow condition leads to a substantial change in the predicted temperature distribution. Therefore, operating conditions require to be satisfactorily designed in order to achieve the desired objective.

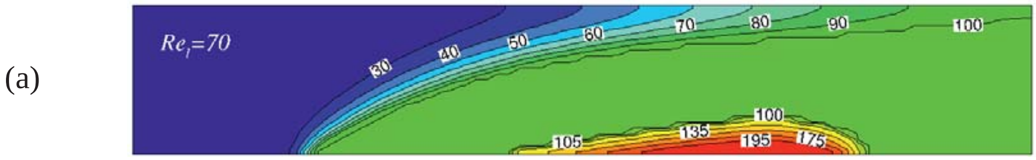

Fluid temperature distribution $\left(T_{f,\max} \approx 245\,^{\text{o}}\text{C}\right)$

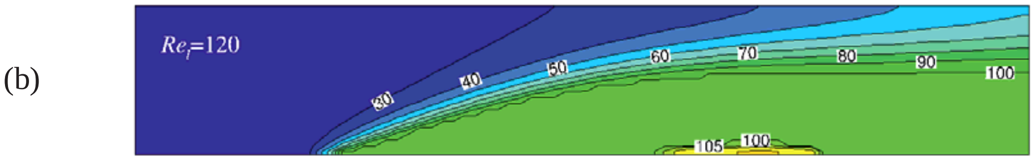

Fluid temperature distribution $\left(T_{f,\max} \approx 140^{\text{o}}\text{C}\right)$

Fig. 5.19: Solution of complete phase change process in channel flow using LTNE model along with Model-1 for partitioning of the wall heat flux for different Reynolds number for $Q_w^* = 32$, $\varepsilon = 0.4$, $k_s^* = 0.5$ and $K^* = 5 \times 10^{-9}$

Figures 5.20 – 5.22 present the effects of porous media properties (in the form of Darcy number K^* in Fig. 5.20, porosity ε in Fig. 5.21 and thermal conductivity of the solid matrix k_s^* in Fig. 5.22) on the fluid temperature distribution when the heat flux at the heated surface is $Q_w^* = 32$. As Darcy number is decreased, while keeping ε constant, the obstruction of the flow field increases, resulting in reduction of pressure drop. Therefore, the complete phase change process initiates earlier and the size of superheated vapor region is extended in the axial and transverse directions with the decrease in K^*, as may be observed from Fig. 5.20(a). An early initiation of phase change processes for $K^* = 10^{-9}$ as compared to $K^* = 10^{-8}$ may also be explained by the reduced capillary diffusion affecting the effective diffusion coefficient in the two-phase region. In contrast to high K^*, the two-phase region is more extended in the upstream direction for low K^* due to higher heat transfer coefficient between the solid phase and the fluid phase, owing primarily to the reduced pore diameter of the porous medium [see Eqs. (2.133) and (2.154)].

It is clear from Fig. 5.21 that the porosity has only marginal effect on the complete phase change process. As a result, phase change process initiates earlier for $\varepsilon = 0.5$ as compared to $\varepsilon = 0.3$. It is also observed from Fig. 5.21 that the isotherms of fluid, predicted for $\varepsilon = 0.5$, are noticeably higher in the superheated vapor region at the heated surface as compared to that obtained for $\varepsilon = 0.3$ and $\varepsilon = 0.4$ (in Fig. 5.12). This can be explained by the reduced effective thermal conductivity of the solid phase $k_{eff,s}^*$ due to the increase in ε [see Eq. (2.151)] leading to a decrease in the diffusive heat loss through the inlet and increase in the amount of energy diffused in the upstream direction, which enhances the temperatures of the solid and fluid phases at the heated surface. In addition, according to Eq. (2.133), when the Darcy number is constant, a larger porosity leads to a decrease in the average pore diameter of the solid matrix, leading to an increase in the heat transfer coefficient between the solid phase and the fluid phase [see Eq. (2.154)]. This means that the convective heat transfer between the solid phase and the fluid phase increases with an increase in porosity while keeping the Darcy number fixed.

(a)

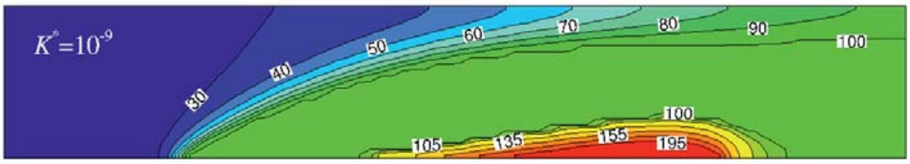

Fluid temperature distribution $\left(T_{f,\max} \approx 255\,^{\circ}\mathrm{C}\right)$

(b)

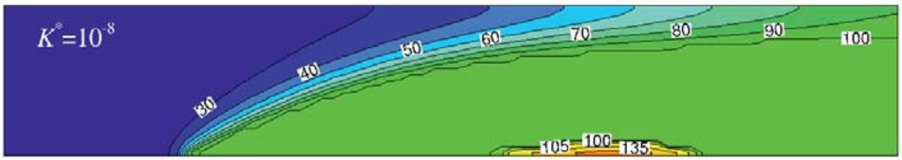

Fluid temperature distribution $\left(T_{f,\max} \approx 162\,^{\circ}\mathrm{C}\right)$

Fig. 5.20: Solution of complete phase change process in channel flow using LTNE model along with Model-1for partitioning of the wall heat flux for different Darcy number for $Re_l = 85$, $Q_w^* = 32$, $\varepsilon = 0.4$ and $k_s^* = 0.5$

(a)

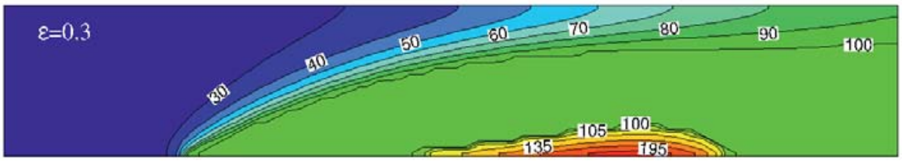

Fluid temperature distribution $\left(T_{f,\max} \approx 204^{\circ}\mathrm{C}\right)$

(b)

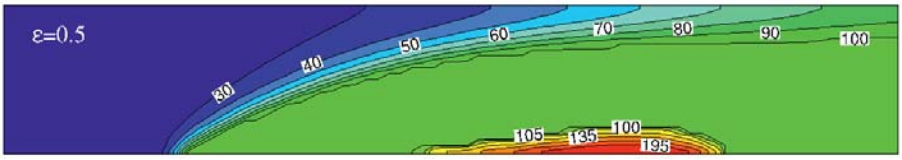

Fluid temperature distribution $\left(T_{f,\max} \approx 230^{\circ}\mathrm{C}\right)$

Fig. 5.21: Solution of complete phase change process in channel flow using LTNE model along with Model-1for partitioning of the wall heat flux for different porosity for $Re_l = 85, Q_w^* = 32$, $k_s^* = 0.5$ and $K^* = 5\times10^{-9}$

On the other hand, it can be observed from Fig. 5.22 that a shorter superheated vapor region is formed for $k_s^* = 0.8$ as compared to $k_s^* = 0.3$. This can be explained by the increased diffusive heat transfer from the superheated vapor region to the two-phase mixture region, which occurs for enhanced $k_{eff,s}^*$. The early termination of phase change process may occur due to lower energy diffusion in the upstream direction from the boiling front to the condensation front (through two-phase mixture region), as may be observed from Fig. 5.22(a) for lower values of k_s^*. Furthermore, the increase in k_s^* leads to a delay in the initiation of complete phase change process from the two-phase mixture to the superheated vapor state, as may be observed from Fig. 5.22(b), due to higher heat loss through the inlet as compared to $k_s^* = 0.3$ in Fig. 5.22(a). The early initiation of the phase change process may also be associated with an early termination of the phase change process from the two-phase mixture to the superheated vapor region, as may be observed from Fig. 5.22(a). For the sub-cooled liquid region, $k_{eff,s}^*$ is several orders of magnitude higher than $k_{eff,f}^*$ and since $T_s^* \approx T_f^*$ holds for the entire domain of the channel, the total diffusive energy flux is dominated by the heat flux due to the axial and transverse diffusivities through the solid phase at the wall.

(a)

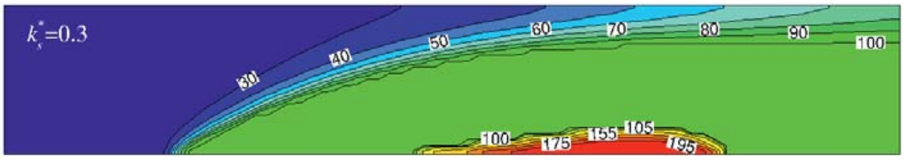

Fluid temperature distribution $\left(T_{f,\max} \approx 271^{\circ}\mathrm{C}\right)$

(b)

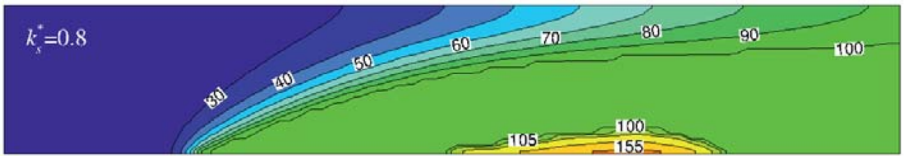

Fluid temperature distribution $\left(T_{f,\max} \approx 160^{\circ}\mathrm{C}\right)$

Fig. 5.22: Solution of complete phase change process in channel flow using LTNE model along with Model-1for partitioning of the wall heat flux for different thermal conductivity of the solid phase for $Re_l = 85$, $Q_w^* = 32$, $\varepsilon = 0.4$ and $K^* = 5 \times 10^{-9}$

5.2.3. Transient Simulation of Complete Phase Change Process in Channel Flow

As explained in chapter 4, for transient simulations of one-dimensional problems along with LTE model, results could be obtained only for very low liquid saturation levels and complete phase change could never be achieved as shown in Fig. 4.10 due to the presence of a sharp discontinuity in the modeled effective heat capacity ratio (Ω_H) at the boiling front. In the LTNE model, the sharp discontinuity in the modeled Ω_H is not present [see Eq. (2.150)] in contrast to the LTE model [see Table 2.3]. Consequently, the simulations have been carried out by applying the proposed smoothing algorithm both for the Γ_H and Ω_H for the LTE model [see subsection in 4.1.6 for clarification], whereas only the former is smoothed in case of the LTNE model. In this regard, a two-dimensional CFD code according to the staggered grid layout has been extended in order to accommodate the effect of transient term to Eqs. (4.13), (5.14) and (5.15) for the investigation of complete phase change process within porous media. The study of transient heat transfer and fluid flow associated with liquid-vapor phase change process can, therefore, provide further detailed and useful information for the phase change process as it occurs in real time. While modeling the transient simulation of complete phase change process along with the assumption of LTNE, density and specific heat of the solid phase are required for the energy conservation equation of the solid phase, and hence in the present study $\rho_s = 8000 \mathrm{kg/m^3}$ and $C_{ps} = 480 \mathrm{J/kg.K}$ have been considered [33]. On the other hand, the effective heat capacity ratio for the energy conservation equation of the fluid phase is only depended on the porosity [see Eq. (2.150)]. The simulations have been carried out using a number of control volumes identical to the one in the previous study, i.e., $N_{CV} = 80 \times 25$, whereas the time step size $\Delta t = 0.5\text{s}$, i.e., $\Delta t^* = 5 \times 10^{-3}$, has been considered. All other parameters have been taken as: $l_i^* = l_e^* = 1.2$, $l_h^* = 3.6$, $Re_l = 85$, $\varepsilon = 0.4$, $K^* = 5 \times 10^{-9}$ and $k_s^* = 0.5$:

In order to solve the governing equations, the required initial and boundary conditions for the present investigation have been given in the following:

The initial conditions at the inlet, i.e., at $x^* = 0$ and $t^* = 0$ have been specified as:

$$H_{in}^* = \rho_{in}^* \left[h_{l,sat}^* - \rho_{in}^* C_{pl}^* \left(T_{sat}^* - T_{in}^* \right) - 2h_{v,sat}^* \right] \tag{5.20a}$$

$$T_s^* = T_{in}^* \tag{5.20b}$$

$$u^* = 0 \tag{5.20c}$$

$$v^* = 0 \tag{5.20d}$$

After initialization, the boundary conditions at the inlet, i.e., at $x^* = 0$ and $t^* > 0$, and at the outlet, i.e., at $x^* = L^*$ and $t^* > 0$, have been given same as Eqs. (5.16) and (5.17), respectively. On the other hand, at the adiabatic wall, i.e., $y^* = 1$; $y^* = 0$, $l_i^* \geq x^* \geq l_i^* + l_h^*$ and $t^* > 0$, and the segment of the wall that is heated with constant heat flux, i.e., $y^* = 0$, $l_i^* \leq x^* \leq l_i^* + l_h^*$ and $t^* > 0$, the boundary conditions have been given same as Eqs. (5.18) and (5.19), respectively.

Figures 5.23 – 5.25 show the transient behavior of the temperature for both fluid and solid phases and liquid saturation distributions for the complete phase process in channel flow of water for $Q_w^* = 32$. At $t^* = 0$, water flows into the channel with a uniform velocity profile and the heat flux at the bottom wall is activated. The solution at $t^* = 0.1$ represents the two-phase flow where the buoyancy force on the liquid increases and gives a larger temperature difference as shown in Figs. 5.23(a), 5.24(a) and 5.25(a). Prior to this, the isotherms for both the fluid and solid phases have approximately the longitudinal dome shape [52] covering the heated surface as shown in Figs. 5.23(a) and 5.24(a). The liquid upstream of the heated surface flowing towards the outlet is lifted upwards due to higher temperature and lower density. The liquid deflects downward slightly after flowing past the heated surface [see Fig. 5.23(a)]. The two-phase region is expanded above the heated surface and the quantity of vapor phase is increased. The onset of complete phase change process occurs around $t^* = 0.25$ as shown in Fig. 5.23(b). An extremely thin superheated vapor region is formed with a short distance above the heated surface and the dome-shaped temperature distribution is totally changed. The isotherms in the leading edge of the heated surface are inclined in an upward fashion towards the outlet [see Figs. 5.23(b) and 5.24(b)] due to the incoming sub-cooled liquid and the buoyancy force. The two-phase region is expanded towards the upper wall and the outlet of the channel as shown in Fig. 5.25(b). Furthermore, the buoyancy force on the liquid becomes stronger that it changes the flow structure and its effect on the flow field is now obvious. The quantity of vapor at this time is increased so that its effect on the velocity field is obvious and only a small amount of liquid becomes fully vapor at this time as shown in Fig. 5.25(b). With continued heating, at $t^* = 0.5$, the effect of buoyancy and the axial as well as transverse diffusive heat flux in the liquid region increase due to the greater extent of energy transferred to the domain.

Their effect on liquid saturation becomes evident, and the increased vaporization of liquid leads to an expansion of the two-phase and superheated vapor regions as shown in as shown in Fig. 5.25(c). The density of the vapor being much lower than that of the liquid, the generated vapor flows upwards due to the buoyancy force, which leads to an expansion of the superheated vapor and two-phase regions at the same time.

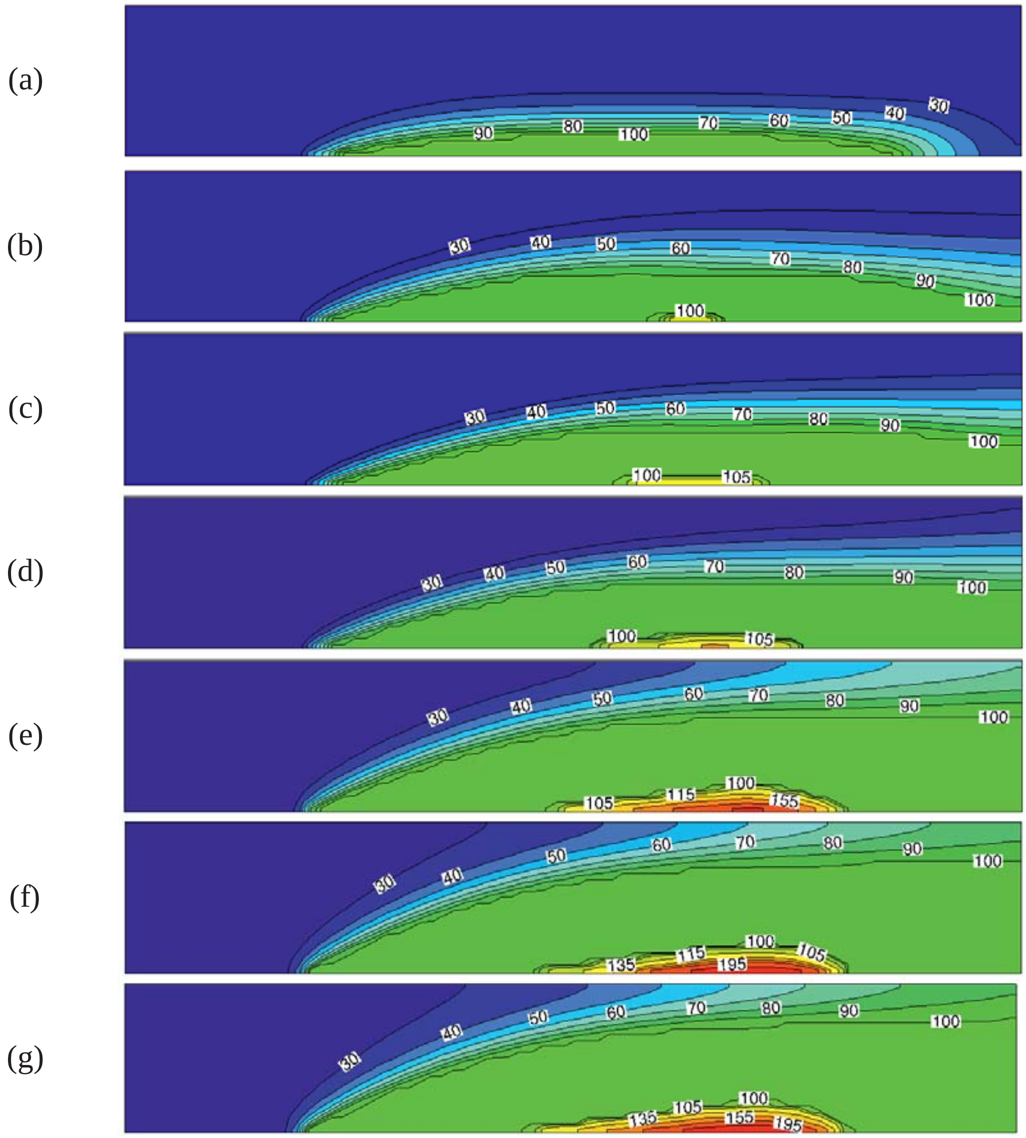

Fig. 5.23: Fluid temperature distributions of complete phase change process in channel flow using LTNE model along with the Model-1for partitioning of the wall heat flux for different: (a) $t^* = 0.1$, (b) 0.25, (c) 0.5, (d) 1, (e) 4, (f) 10 and (g) 16 for $Re_l = 85$, $Q_w^* = 32$, $\varepsilon = 0.4$, $k_s^* = 0.5$ and $K^* = 5 \times 10^{-9}$

At $t^* = 1$, the superheated vapor and the two-phase regions are further expanded and the quantity of vapor is sufficiently increased. As heating continues at $t^* = 4$, the superheated vapor region further expands and the density difference between the liquid from the incoming upstream and the liquid adjacent to the condensation front is further increased. Li et al. [52] pointed out that the vapor formed in the two-phase zone partially occupies the pores, thereby reducing the permeability for liquid flow. Consequently, this also supports an upward deflection of the liquid flow. After flowing through the superheated vapor region, the accelerated main stream flows downward and exerts a larger shear force on the liquid at the rearward of the two-phase region. At $t^* = 10$, the effect of buoyancy on the liquid, in particular on the liquid saturation and fluid flow, becomes more prominent, causing the two-phase and superheated vapor regions to expand further as more liquid vaporizes. The vapor is driven by both capillary and buoyancy forces, flows strongly up towards the upper wall and to the outlet of the channel. The majority of the vapor above the unheated surface flows directly upwards due to the buoyancy force [see Fig. 5.25(f)]. A steady-state solution is achieved at $t^* = 16$ and presented in Figs. 5.23(g), 5.24(g) and 5.25(g). At this time, the minimum liquid saturation s found above the heated surface with the expansion of the two-phase and superheated vapor regions. It can be safely concluded that the heterogeneous energy equation and the proposed smoothing algorithm are indeed successful in dealing with the rapid change in the modeled Ω_H and Γ_H, which may promote undesirable jump in the predicted temperature profiles.

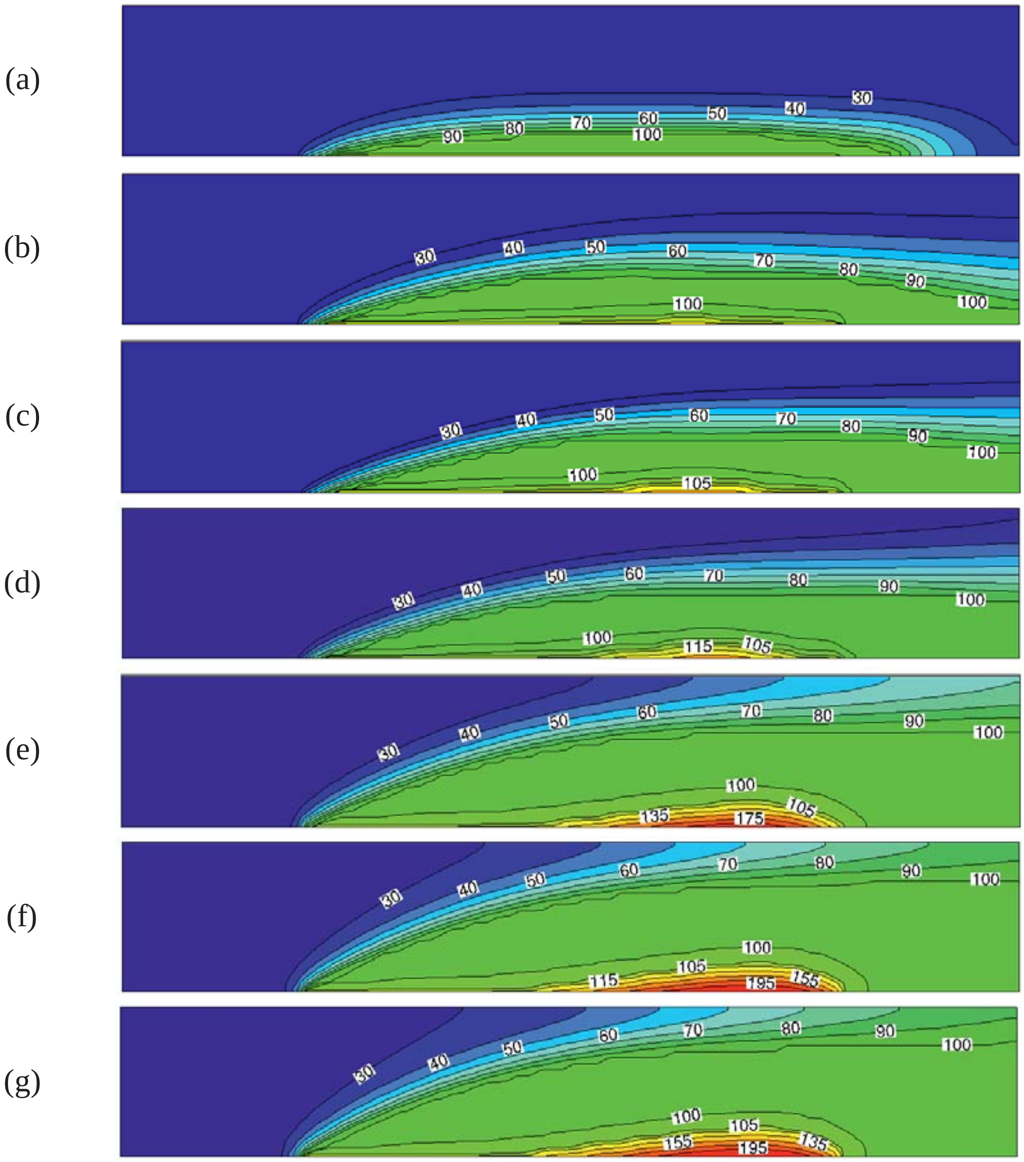

Fig. 5.24: Solid temperature distributions of complete phase change process in channel flow using LTNE model along with the Model-1for partitioning of the wall heat flux for different: (a) $t^* = 0.1$, (b) 0.25, (c) 0.5, (d) 1, (e) 4, (f) 10 and (g) 16 for $Re_l = 85$, $Q_w^* = 32$, $\varepsilon = 0.4$, $k_s^* = 0.5$ and $K^* = 5\times10^{-9}$

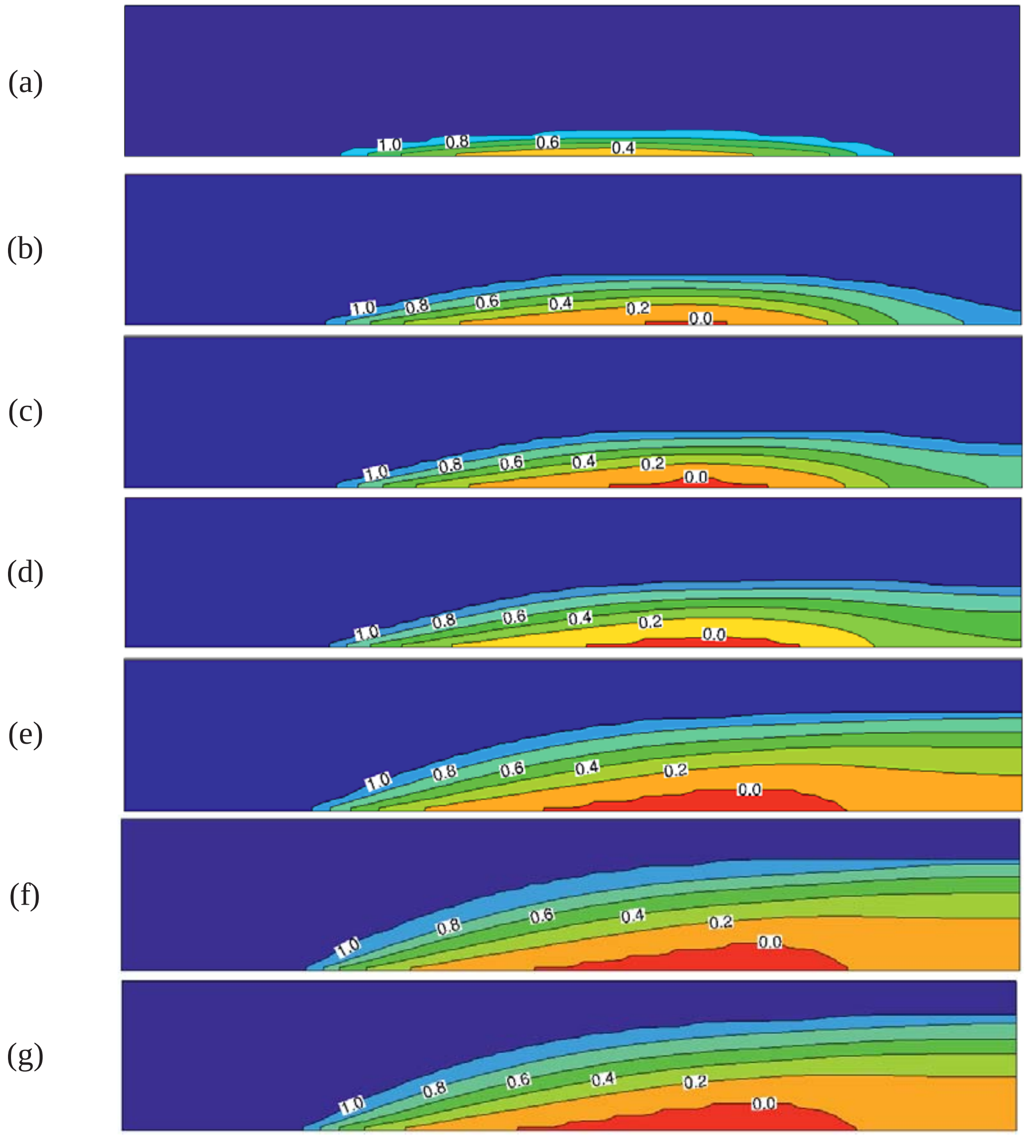

Fig. 5.25: Liquid saturation distributions of complete phase change process in channel flow using LTNE model along with the Model-1for partitioning of the wall heat flux for different: (a) $t^* = 0.1$, (b) 0.25, (c) 0.5, (d) 1, (e) 4, (f) 10 and (g) 16 for $Re_l = 85$, $Q_w^* = 32$, $\varepsilon = 0.4$, $k_s^* = 0.5$ and $K^* = 5\times10^{-9}$

5.2.4. Simulation of Complete Phase Change Process in Channel Flow using Heat Flux at Different Locations

A. Discrete Heat Flux at the Upper Wall

This subsection provides the numerical results of complete phase change process in channel flow, under steady-state condition, when the heater supplying identical heat flux, is moved from the lower to the upper wall. For the purpose of comparison, the geometric parameters, operating conditions and porous media properties remain identical as that for the reference case for lower heat flux case when using heat flux at the lower wall. Figure 5.26 shows the numerical results of complete phase change process of the temperature for both fluid and solid phases and liquid saturation distributions as well as velocity fields for the maximum value of the heat flux $Q_w^* = 32$, considering Model-1 for the partitioning of wall heat flux for $Re_l = 85$, $\varepsilon = 0.4$, $k_s^* = 0.5$ and $K^* = 5\times10^{-9}$.

It is observed from the figure that the temperature distribution behavior for both phases show the reversed shape [see Figs. 5.26(a) and 5.26(c)] as compared with that for the localized heater at the lower wall [see Figs. 5.12(a) and 5.12(c)]. The buoyancy force drives the high temperature fluid to flow towards the heated surface at the upper wall, reducing the heat exchange between the heated surface and the liquid below, which in turn increase the temperature at the upper wall for both phases. As a result, phase change process somewhat initiates earlier for this case as compared with the localized heater at the lower wall. After the onset of complete phase change process as shown in Fig. 5.26(b), the generated vapor with lower density raises on the top of the heated surface due to the buoyancy force. Consequently, the maximum temperature for both phases (i.e., fluid and solid phases) is more increased as compared with that for the localized heater at the lower wall due to the buoyancy force. For instance, the maximum temperature of the fluid and the solid phases at the present results approximately reaches $229^{\circ}\mathrm{C}$ and $242^{\circ}\mathrm{C}$, respectively, whereas the maximum temperatures for the fluid and the solid phases when supplying the heat flux at lower wall approximately reaches to $214^{\circ}\mathrm{C}$ and $227^{\circ}\mathrm{C}$, respectively.

(a)

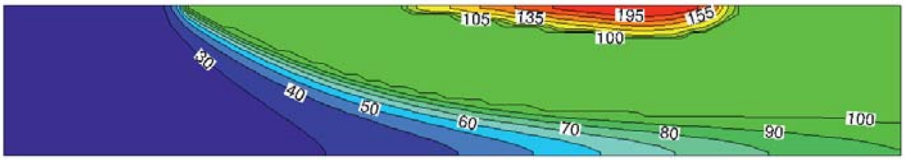

Fluid temperature distribution $\left(T_{f,\max} \approx 229\,^{\circ}\mathrm{C}\right)$

(b)

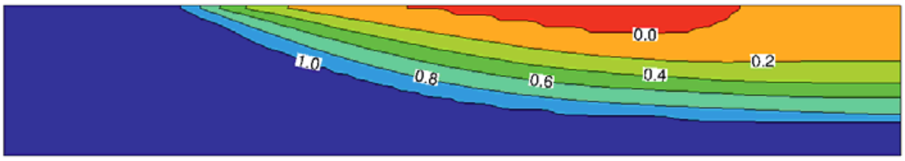

Liquid saturation distribution $\left(s_{\min} = 0\right)$

(c)

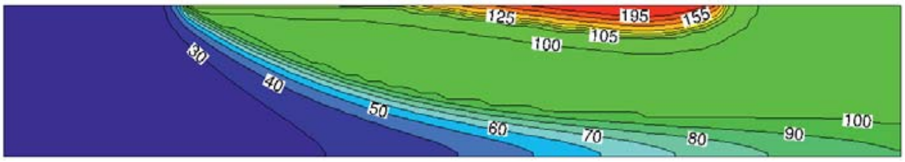

Solid temperature distribution $\left(T_{s,\max} \approx 242^{\circ}\,\mathrm{C}\right)$

(d)

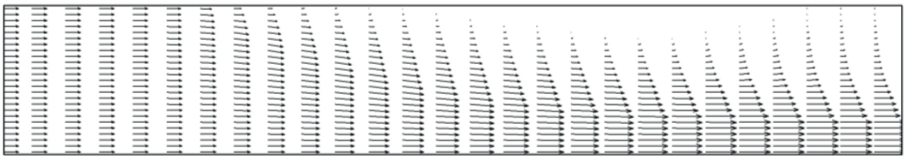

Liquid velocity vectors $\left(Re_{K,\max} = 1.144\times10^{-2}\right)$

(e)

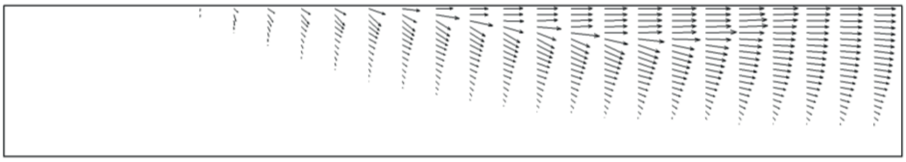

Vapor velocity vectors $\left(Re_{K,\max} = 8.1\times10^{-3}\right)$

Fig. 5.26: Solution of complete phase change process in channel flow using LTNE model along with the Model-1for partitioning of the wall heat flux discrete at upper wall for $Re_l = 85$, $Q_w^* = 32$, $\varepsilon = 0.4$, $k_s^* = 0.5$ and $K^* = 5\times10^{-9}$

It is also clear from the figure that the superheated vapor region assumes the shape of a convex which is similar to the reversed shape that is formed when the heat flux is supplied at the bottom wall. The resulting shape is not only affected by gravity, but also by the upward flow of the vapor phase as it approaches the boiling front. The velocity vectors of the liquid and vapor phases can be clearly seen in Figs. 5.26(d) and 5.26(e), respectively. The main stream, coming from the upstream boundary flows downward to bypass the heated surface. It is also interesting to note that the vapor density is much smaller than that of the liquid, leading the liquid in the two-phase region to flow downward towards the outlet [see Fig. 5.26(d)]. Most importantly, it can be concluded from this study that a marginal difference in the temperature distribution could be observed due to the buoyancy force and the quality of steam is somewhat sensitive to the location of the heated surface. Nevertheless, adequate care must be also taken while designing such evaporator in order to meet the process requirement.

B. Discrete Heat Flux at both the Lower and Upper Walls

This subsection concerns with the numerical results of fluid flow and heat transfer associated with phase change process inside porous media, under steady-state condition, when the same heat input is divided and supplied through two identical heaters located at the same axial distance on the upper and lower walls. As mentioned before, the value of the heat flux allowed at the upper heat flux case is $Q_w^* = 32$. Consequently, the heat flux at the lower and upper heated surfaces has been set to $Q_w^* = 16$, resulting in a total heat flux of $Q_w^* = 32$. For the studied case, all others parametric values (i.e., geometric parameters, porous media properties, and operating conditions) have been set to the same values as that for the reference case when the heat flux has been located at the lower wall for the purpose of comparison. Figure 5.27 shows the numerical results of temperature distributions for both fluid and solid phases and velocity fields as well as liquid saturation distributions for $Q_w^* = 16$. As the liquid flows across the heated surfaces, it absorbs heat from the solid portion of the porous medium through the convective heat exchange between both phases. Buoyancy force drives the higher temperature fluid upward towards the heated surface of the upper wall. In this situation, the convective heat transfer coefficient of the fluid at the upper wall is decreased, which leads to a reduction of the heat exchange between the solid and fluid phases, due to the effect of buoyancy force. This situation leads to a higher fluid temperature in the vicinity of the upper wall. It is, however, interesting to note that when the same heat input is divided and supplied through two identical heaters located at the same axial distance on the upper and the lower walls, a nearly symmetric temperature profile is obtained, indicating that the buoyancy force has only minor influence [see Figs. 5.27(a), and 5.27(c)]. Phase change at the upper wall initiates slightly earlier than at the bottom wall [see Fig 5.27(b)]. Thus, the minimum liquid saturation occurs at the upper wall prior to that at the lower wall. An extremely small layer of the two-phase region covers a part of both heated surfaces as shown in Fig. 5.27(b), and the two-phase mixture region expands towards the outlet and transverse directions. Consequently, the liquid flow is bounded between the condensation front at the upper and lower walls up to the outlet as a jet shape profile as shown in Figs. 5.27(b), 5.27(d) and 5.27(e). This will, however, change further with the increase in the heat flux. Most importantly, complete phase change process does not occur although the total heat input to the evaporator remains the same. The spreading of the heat, as shown in Fig.5.27, reduces the temperature difference for both the fluid and solid phases close to the heated surface at the walls and at the downstream of the heated surface as compared with either lower or upper heat flux cases for the same total amount of heat flux [see Figs. 5.12(a), 5.12(c), 5.26(a) and 5.26(c) when the imposed heat flux is $Q_w^* = 32$]. Therefore, complete phase change process can be obtained by further increasing the heat flux on both the walls.

(a)

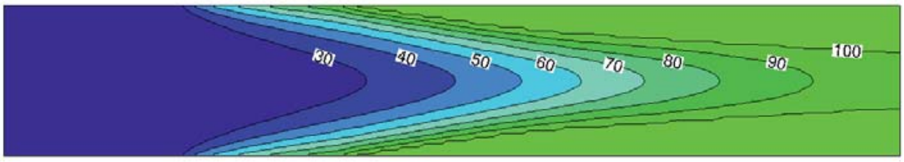

Fluid temperature distribution $\left(T_{f,\max} = 100\,^{\circ}\mathrm{C}\right)$

(b)

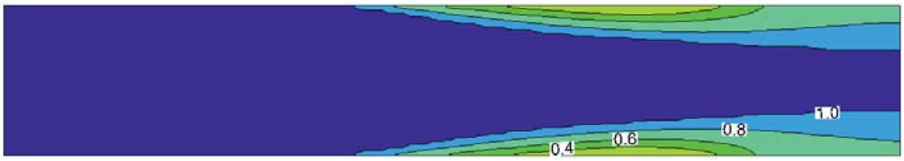

Liquid saturation distribution $\left(s_{\min} \approx 0.23\right)$

(c)

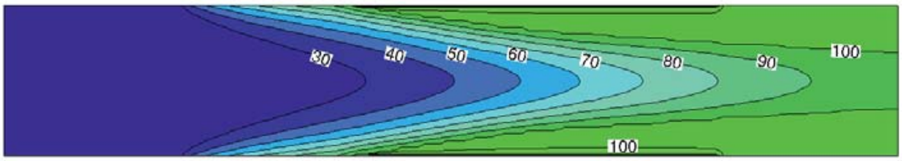

Solid temperature distribution $\left(T_{s,\max} \approx 108\,^{\circ}\mathrm{C}\right)$

(d)

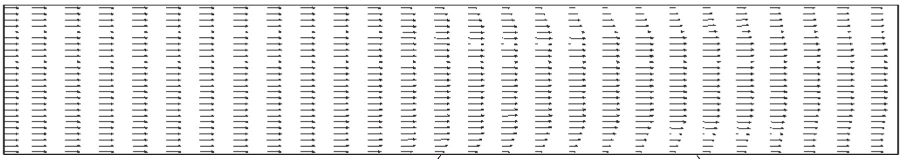

Liquid velocity vectors $\left(Re_{K,\max} = 6.63 \times 10^{-3}\right)$

(e)

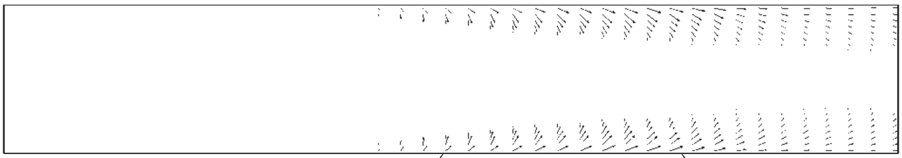

Vapor velocity vectors $\left(Re_{K,\max} = 3.5 \times 10^{-3}\right)$

Fig. 5.27: Solution of incomplete phase change process in channel flow using LTNE model along with the Model-1for partitioning of the wall heat flux discrete at both upper and lower walls for $Re_l = 85$, $Q_w^* = 16$, $\varepsilon = 0.4$, $k_s^* = 0.5$ and $K^* = 5 \times 10^{-9}$

5.2.5. Simulation of Complete Phase Change Process in Pipe Flow

This subsection provides the numerical results of the complete phase change process under steady-state condition for pipe flow as shown in Fig. 4.17(b), using cylindrical axi-symmetric coordinates. This study has been carried out by applying the proposed smoothing algorithm for the effective diffusion coefficient in order to complement the previous investigation for the channel flow and to compare the results with that obtained using LTE model for identical conditions. Liquid saturation and fluid and solid phase temperatures for different values of the heat flux have been analyzed. Comparison of the results between the LTNE and LTE models have been performed using staggered grid layout and identical parametric values as the ones used in channel flow, while keeping the same hydraulic diameter $(D_h = 2W)$ as well as identical number of control volumes. Consequently, the pipe radius $R = 50\,\text{mm}$ and the pipe length $L = 300\,\text{mm}$ have been considered for the present analysis. Other than that, different parameters have been used: $l_i^* = l_e^* = 1.2$, $l_h^* = 3.6$, $\tilde{b}_x = -1$, $\tilde{b}_r = 0$, $Re_l = 85$, $\varepsilon = 0.4$, $k_s^* = 0.5$ and $K^* = 5 \times 10^{-9}$. The heat flux imposed at heated surface has been set to vary from $Q_w^* = 20$ to $Q_w^* = 32$, along with the Model-1 for the partitioning of wall heat flux.

Figure 5.28 displays the comparison of numerical results between combined medium temperature (for LTE model) and fluid temperature (for LTNE model) for $Q_w^* = 20$. It is evident from the figure that the incoming sub-cooled liquid flow from the upstream within LTNE model is heated earlier as compared with that obtained using LTE model, while keeping all the other parameters fixed. One such comparison is presented in Fig. 5.28, which shows that, although LTNE model predicts earlier initiation of phase change, no superheated vapor region could be detected as compared with LTE model. These predictions are quite reasonable because the total heat flux within LTNE is imposed to the solid phase and is then diffused to the domain due to the higher thermal conductivity of the solid phase, and hence the fluid is heated through a convective heat exchange between the solid and fluid phases. Consequently, the temperature rise close to the heated surface at the wall is suppressed and the temperature becomes higher than that of the LTE model in the upstream direction. Most importantly, the comparison of the temperature distributions reveals that the numerical result obtained within LTNE model is more convenient than that of LTE model due to the elimination of the non-physical jump in the predicted temperature distribution close to the heated surface at the pipe wall.

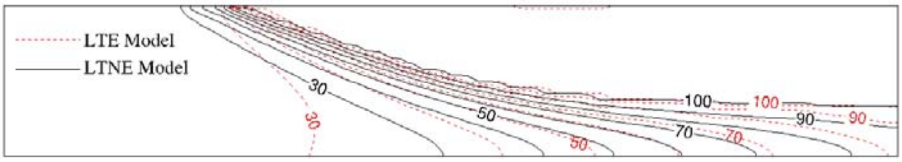

Fig. 5.28: Comparison of temperature distribution during phase change process in pipe flow using LTE and LTNE models for $Q_w^* = 20$

Figures 5.29 – 5.31 display the numerical results of complete phase change process when the heat flux is increased from $Q_w^* = 22$ to $Q_w^* = 32$, respectively. These figures present the temperature for both fluid and solid phases as well as liquid saturation distributions. With the increase of the heat flux to $Q_w^* = 22$ as shown in Fig. 5.29(a), the complete phase change process is observed within a very short distance somewhere close to the heated surface at the wall without any sharp gradient in the predicted fluid temperature distribution. In addition, the solid temperature distribution exceeds the saturation temperature [see Fig. 5.30(a)] and the two-phase region covers a large portion of the heated surface. As the heat flux is increased and since the vapor density is much smaller than of the liquid, the volume of vapor expands further, leading to the expansion of the superheated vapor region as shown in Fig. 5.29. The two-phase region moves simultaneously downward towards the center of the pipe and to the outlet, resulting in a long condensation front [see Fig 5.31].

(a)

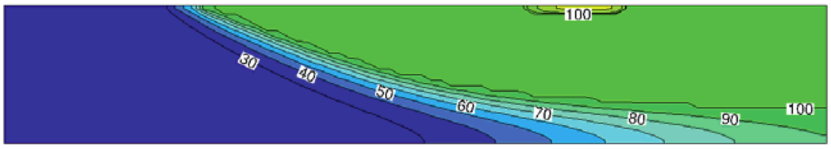

$Q_w^* = 22$, $T_{f,\max} \approx 120\,^{\circ}\mathrm{C}$

(b)

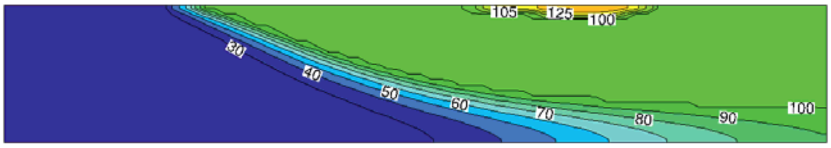

$Q_w^* = 24$, $T_{f,\max} \approx 153\,^{\circ}\mathrm{C}$

(c)

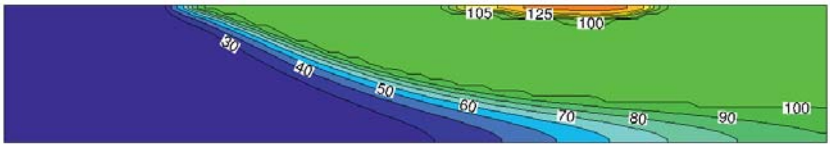

$Q_w^* = 28$, $T_{f,\max} \approx 167\,^{\circ}\mathrm{C}$

(d)

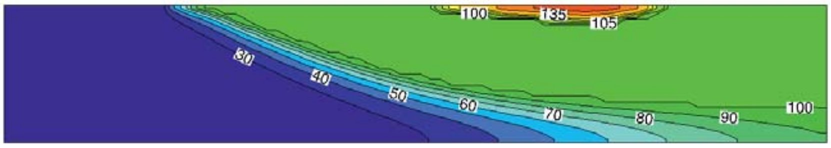

$Q_w^* = 32$, $T_{f,\max} \approx 194\,^{\circ}\mathrm{C}$

Fig. 5.29: Fluid temperature distributions of complete phase change process in pipe flow using LTNE model for different dimensionless heat fluxes for $\varepsilon = 0.4$, $Re_l = 85$, $k_s^* = 0.5$ and $K^* = 5\times10^{-9}$

(a)

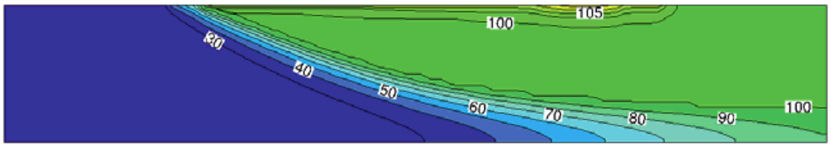

$Q_w^* = 22$, $T_{s,\max} \approx 130\,^{\circ}\mathrm{C}$

(b)

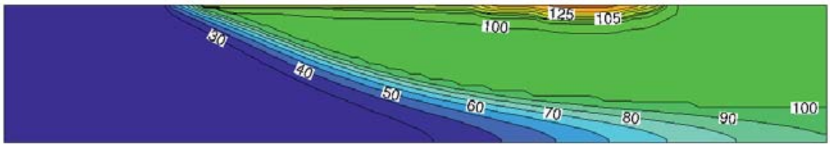

$Q_w^* = 24$, $T_{s,\max} \approx 165\,^{\circ}\mathrm{C}$

(c)

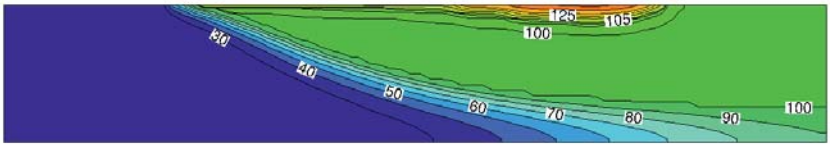

$Q_w^* = 28$, $T_{s,\max} \approx 181^{\circ}\mathrm{C}$

(d)

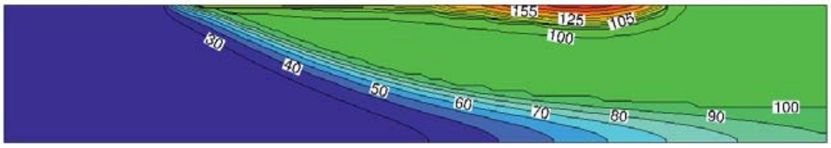

$Q_w^* = 32$, $T_{s,\max} \approx 209\,^{\circ}\mathrm{C}$

Fig. 5.30: Solid temperature distributions of complete phase change process in pipe flow using LTNE model for different dimensionless heat fluxes for $\varepsilon = 0.4$, $Re_l = 85$, $k_s^* = 0.5$ and $K^* = 5\times10^{-9}$

It is also observed from Fig. 5.29 that, with the increase of the heat flux, the sub-cooled liquid and the two-phase regions have only minor influence at the center of the pipe. The solid temperature distribution behavior in Fig. 5.30 is very similar to that of the fluid although the solid temperature at the superheated vapor region is slightly higher than that of the fluid phase as shown in Fig. 5.29. The velocity vectors for both liquid and vapor phases show a similar fashion as compared with the ones for pipe flow using LTE model for identical conditions. These results are not shown here for sake of brevity. It is interesting to note that the pipe flow solution based on the LTNE model predicts earlier initiation the superheated vapor region as compared with the channel flow model for the same heat flux values. Similarly, the proposed smoothing algorithm along with LTNE model is indeed successful in dealing with the rapid change in the effective diffusion coefficient, which may eliminate the occurrence of “jumps” in the predicted temperate distribution close to the heated surface at the wall as compared with the pipe flow using LTE model.

(a)

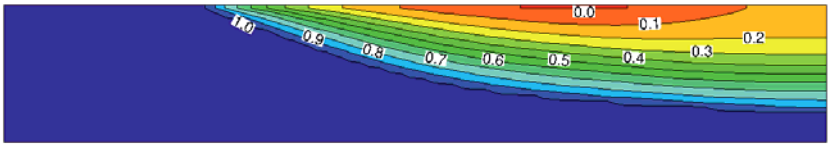

$Q_w^* = 22,\ s_{\min} = 0$

(b)

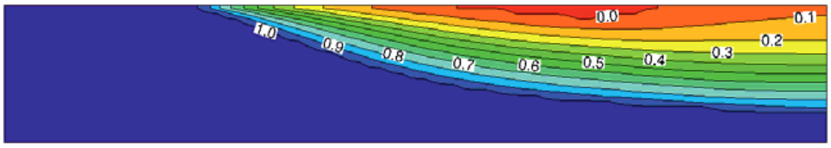

$Q_w^* = 24,\ s_{\min} = 0$

(c)

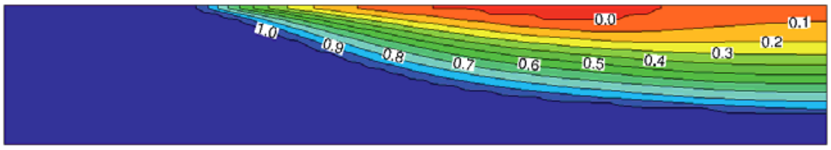

$Q_w^* = 28,\ s_{\min} = 0$

(d)

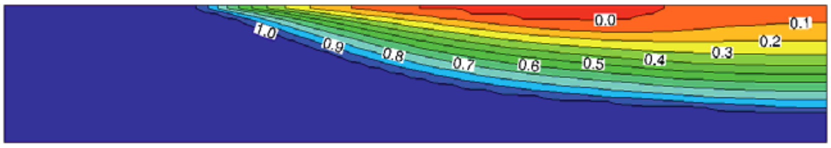

$Q_w^* = 32,\ s_{\min} = 0$

Fig. 5.31: Liquid saturation distributions of complete phase change process in pipe flow using LTNE model for different dimensionless heat fluxes for $\varepsilon = 0.4$, $Re_l = 85$, $k_s^* = 0.5$ and $K^* = 5 \times 10^{-9}$

5.3. Modeling in Two-dimensional Coordinates using Non-Staggered Grid Layout

This section presents the comparison of numerical results obtained using non-staggered and staggered uniform grid layouts, considering the problems of incomplete and complete liquid-vapor phase change process inside a porous medium, under steady-state condition. The CFD code developed in this study has been applied using the same grid refinement, solution algorithm and convergence criterion for both grid arrangements. As a demonstrative example, numerical results of incomplete and complete phase change process have been obtained for identical conditions to that in subsection 5.2.2, for the purpose of comparison. To assess the performance of non-staggered and staggered grid layouts on the temperatures and liquid saturation solutions within LTNE model, different cases of the heat flux and total evaporated volume fraction have been investigated.

For all considered cases, the geometric parameters of the channel $L = 300\text{mm}$ ($L^* = 6$) and $W = 50\text{mm}$ ($W^* = 1$) have been considered for the present analysis. The unheated inlet and exit lengths are both equal to $l_i^* = l_e^* = 1.2$, i.e., $l_h^* = 3.6$. The inlet velocity u_{in} of liquid water has been considered to be $5 \times 10^{-4}\,\text{m/s}$ for the entire study at a constant temperature of $T_{in} = 20^\circ\text{C}$. The average pore diameter, porosity, permeability and thermal conductivity of the solid phase k_s have been considered to be $100\mu\text{m}$, 0.4, 10^{-11}m^2 and 50W/mK, respectively. At the heated surface, heat is added from an external source, supplying a constant heat flux $\dot{q}''_w$, ranging from 150kW/m^2 to 400kW/m^2, to the bottom wall. Based on these data and properties of water given in Table 2.1, the following range of dimensionless heat flux from $Q_w^* = 12$ to $Q_w^* = 32$ has been considered. Other than the fixed values, the reference case has been chosen with the following parameters: $Re_l = 85$, $d_p^* = 2 \times 10^{-3}$, $\varepsilon = 0.4$, $K^* = 5 \times 10^{-9}$ and $k_s^* = 0.5$, along with Model-1 for the partitioning of wall heat flux.

As the location of interfaces, separating different regions, are strong functions of the flow, the heating conditions and the problem geometry and since these locations are not known a priori, only uniform control volumes have been employed for all considered cases. For transient simulations, the locations of interfaces are also functions of time. Nevertheless, before performing simulations for different cases, a careful gird independence study has been carried out using four different numbers of uniform control volumes ($80 \times 25, 100 \times 35, 120 \times 45$ and 140×55) for two different values of heat flux. It has been observed that the use of $N_{CV} = 80 \times 25$ control volume produce sufficiently accurate results and further grid refinement does not significantly modify the solutions. Additionally, computation time is severely increased by using the 100×35 control volumes. Owing to the strong non-linearity in the conservation equations and the constitutive relations, the discretized equations have been further under-relaxed in order to achieve convergence and typical relaxations factor around 0.1 have been often used for most of the simulations. The solutions have been accepted as converged when this value for all conservation equations fell below 10^{-5}, since further lowering of the convergence criterion does not appreciably modify the accepted solution. In addition, the adjustable smoothing parametric values have been used with LTNE model similar to those employed along with LTE model.

5.3.1. Comparison of Non-Staggered and Staggered Grids Solutions

This subsection provides the comparison between the results obtained using non-staggered and staggered grid layouts for the incomplete and complete phase change process inside porous media. The results have been obtained for different Q_w^* that are summarized in Figs. 5.32 – 5.35 in the form of fluid and solid phase temperatures as well as liquid saturation. Figure 5.32 compares the results of incomplete phase change process between the non-staggered and the staggered grid layouts for $Q_w^* = 20$. On the other hand, Figs. 5.33 – 5.35 compare the results of complete phase change process between both methods when the heat flux imposed at the heated surface is varying from $Q_w^* = 24$ to $Q_w^* = 32$, respectively. The figures show that the non-staggered grid provides identical results in comparison to staggered grid solutions. In other words, the accuracy of the non-staggered and the staggered grid layouts are identical. The average absolute difference in the predicted temperatures for both fluid and solid phases have been found to be 0.01%, which expectedly decreases with the increase in employed grid size. In Particular, the non-staggered grid layout requires approximately 3% less computational time as compared to the staggered grid layout. On the other hand, the staggered grid layout has been found to be more stable during the convergence when dealing with very high heat flux values and complete phase change process. The effects of varying the input heat flux on the behavior of phase change process inside porous channel have been elaborately discussed earlier in subsection 5.2.2 and hence they are not repeated here for the sake of brevity.

(a)

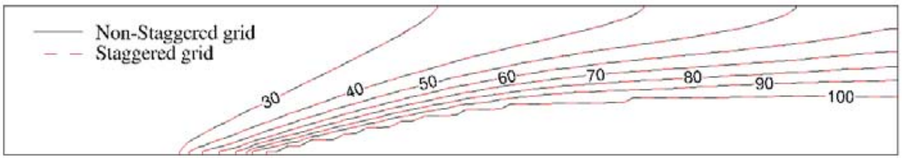

Fluid temperature distribution $\left(T_{f,\max} = 100\,^{\circ}\mathrm{C}\right)$

(b)

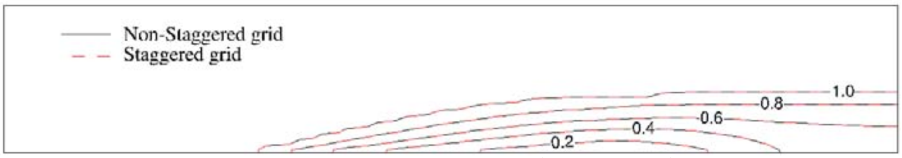

Liquid saturation distribution $\left(s_{\min} \approx 0.09\right)$

(c)

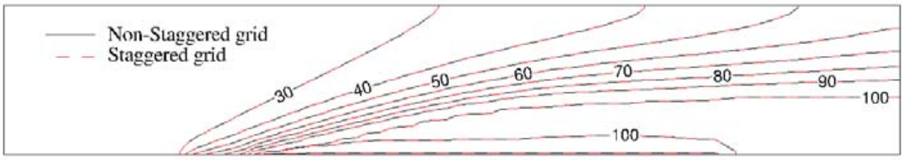

Solid temperature distribution $\left(T_{s,\max} \approx 110\,^{\circ}\mathrm{C}\right)$

Fig. 5.32: Comparison of non-staggered and staggered grid results of incomplete phase change process using LTNE model along with Model-1 for partitioning of the wall heat flux for $Re_l = 85$, $Q_w^* = 20$, $\varepsilon = 0.4$, $k_s^* = 0.5$ and $K^* = 5 \times 10^{-9}$

(a)

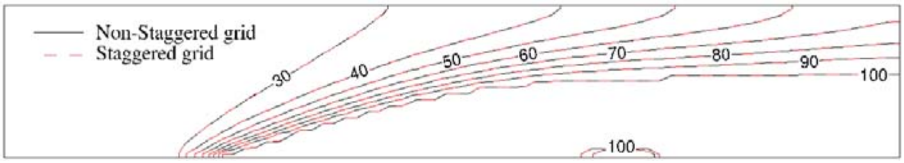

Fluid temperature distribution $\left(T_{f,\max} \approx 112^{\circ}\mathrm{C}\right)$

(b)

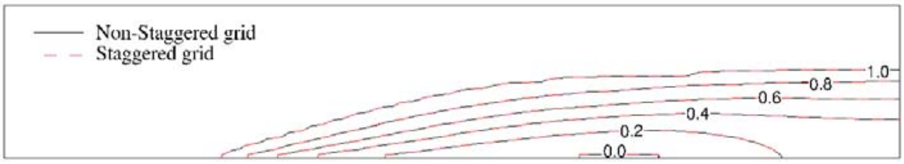

Liquid saturation distribution $\left(s_{\min} = 0\right)$

(c)

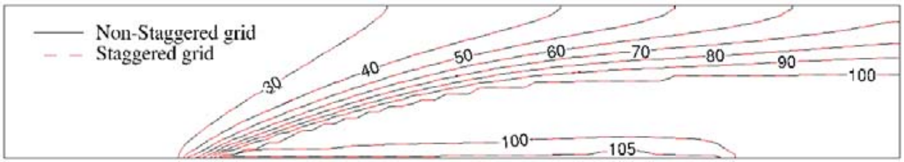

Solid temperature distribution $\left(T_{s,\max} \approx 123^{\circ}\mathrm{C}\right)$

Fig. 5.33: Comparison of non-staggered and staggered grid results of complete phase change process using LTNE model along with Model-1 for partitioning of the wall heat flux for $Re_l = 85$, $Q_w^* = 24$, $\varepsilon = 0.4$, $k_s^* = 0.5$ and $K^* = 5 \times 10^{-9}$

(a)

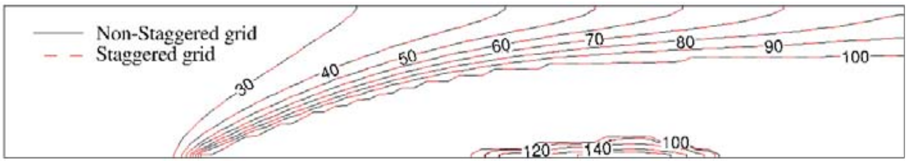

Fluid temperature distribution $\left(T_{f,\max} \approx 160^{\circ}\mathrm{C}\right)$

(b)

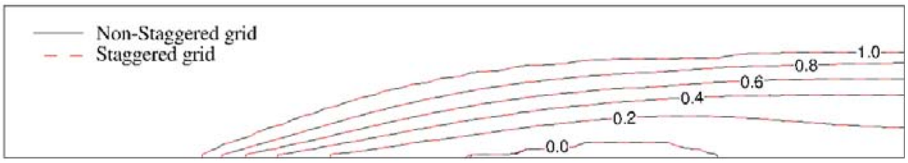

Liquid saturation distribution $\left(s_{\min} = 0\right)$

(c)

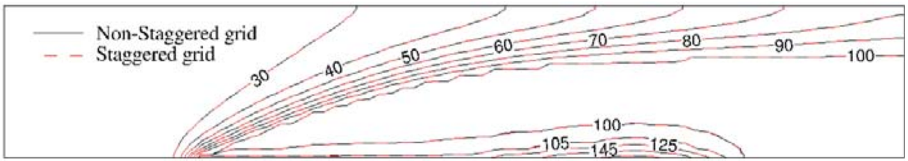

Solid temperature distribution $\left(T_{s,\max} \approx 172^{\circ}\mathrm{C}\right)$

Fig. 5.34: Comparison of non-staggered and staggered grid results of complete phase change process using LTNE model along with Model-1 for partitioning of the wall heat flux for $Re_l = 85$, $Q_w^* = 28$, $\varepsilon = 0.4$, $k_s^* = 0.5$ and $K^* = 5 \times 10^{-9}$

(a)

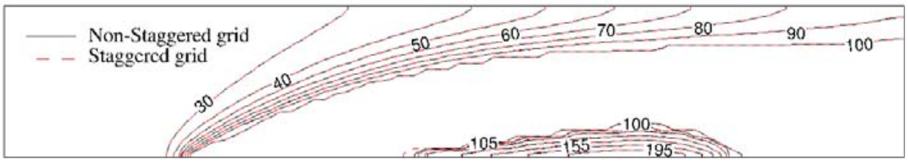

Fluid temperature distribution $\left(T_{f,\max} \approx 214^{\mathrm{o}}\mathrm{C}\right)$

(b)

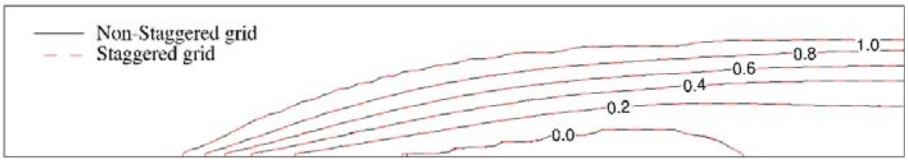

Liquid saturation distribution $\left(s_{\min} = 0\right)$

(c)

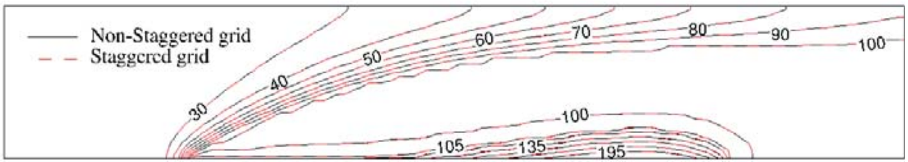

Solid temperature distribution $\left(T_{s,\max} \approx 227^{\mathrm{o}}\mathrm{C}\right)$

Fig. 5.35: Comparison of non-staggered and staggered grid results of complete phase change process using LTNE model along with Model-1 for partitioning of the wall heat flux for $Re_l = 85$, $Q_w^* = 32$, $\varepsilon = 0.4$, $k_s^* = 0.5$ and $K^* = 5 \times 10^{-9}$

5.3.2. Evaporated Volume Fraction

As mentioned in chapter 3, the evaporated volume fraction ev in the entire porous channel has been used to describe the importance of boiling [30, 47]. The evaporated volume fraction is defined in dimensionless form as:

$$ev = \frac{W^*}{L^*} \int_0^1 \int_0^{L^*/W^*} (1 - s)\, dx^* dy^* \tag{5.15}$$

Figure 5.36 shows the variation of the evaporated volume fraction ev as a function of dimensionless heat flux imposed at the heated surface of the bottom wall. This figure displays the comparison between the numerical results obtained using non-staggered and staggered grid layouts for different models for the partitioning of wall heat flux [see Eq. (2.158)]. It has been already explained the difference in the solutions obtained with these different partitioning models and hence, these results are not presented here for the sake of brevity. Comparison of the evaporated volume fraction reveals that the present numerical results are similar to the ones with staggered grid layout for different heat fluxes. Different models for the partitioning of the wall heat flux have almost no influence on the total evaporated volume fraction owing to the extremely high convective heat transfer coefficient between the solid phase and the fluid phase.

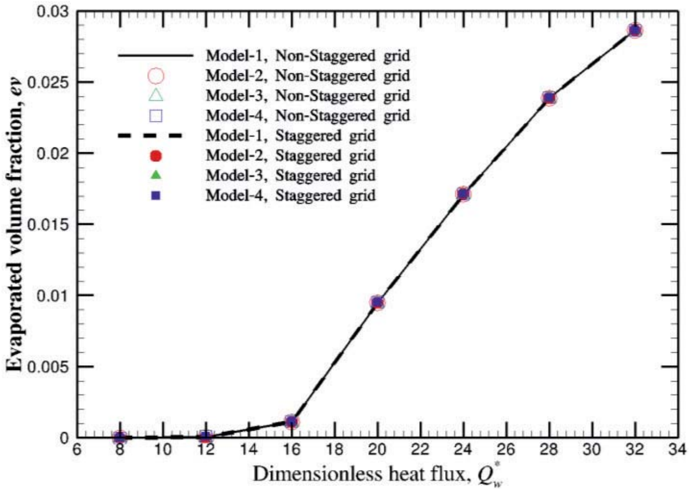

Fig. 5.36: Comparison of non-staggered and staggered grid results of the evaporated volume fraction as a function of the dimensionless heat flux using LTNE model for different models for partitioning of the wall heat flux for $Re_l = 85$, $\varepsilon = 0.4$, $k_s^* = 0.5$ and $K^* = 5\times10^{-9}$

To the best of the author's knowledge, the complete phase change process has not been modeled before based on the H-formulation with LTNE assumption, which enables suppression of temperature jump in the superheated vapor region when using the smoothing strategy, using non-staggered grid layout. Most importantly, it can be concluded from the present study that, for the problem of complete phase change process, the use of either non-staggered or staggered grid layout can be recommended, since both methods can be applied successfully. The non-staggered grid has an important role, especially for simulations in more complex geometries, for instance, it would be useful to provide a varying cross-sectional area of the duct in order to accommodate higher volume flow rates of the vapor phase. Such simulations would require extension of the numerical method in non-orthogonal (curvilinear) coordinates using non-staggered grid layout.

5.4. Conclusions

In this chapter, numerical simulations have been carried out in order to investigate the complete liquid-vapor phase change process of water inside an asymmetrically heated porous evaporator employing LTNE assumption. For all numerical simulations, formulations based on TPMM of Wang [33] have been used by extending the proposed smoothing algorithm for the effective diffusion coefficient. For the purpose of demonstration, the complete phase change process of water through a one-dimensional pipe flow and two-dimensional channel and pipe flows operated in the Darcy flow regime have been considered.

For one-dimensional problems, without applying the smoothing algorithm for the effective diffusion coefficient, even the LTNE model results in "jump" in the predicted temperature field, which demonstrates the necessity of a remedy. Since the LTNE model captures the true physical condition better than the commonly used LTE model, the difference in the predicted fluid temperature and combined medium temperature at the evaporator outlet using LTNE and LTE models suggests that the former should be applied wherever applicable, although the temperature of the fluid and the solid phases attain nearly the same temperature when LTNE model is used. The effect of employing different models for the partitioning of wall heat flux using the LTNE model has been found negligible owing to the extremely high convective heat transfer coefficient between the solid and the fluid phases that results from smaller characteristic pore diameter. A representative parametric study suggests that the diffusive energy transport process in the upstream direction through the solid and the fluid phases has a strong influence on the initiation and termination of the phase change process.

The use of a smoothing algorithm for the effective diffusion coefficient along with LTNE model successful eliminates the “jump” in the predicted temperature distribution, even for numerical predictions of multi-dimensional complete phase change problems inside porous media (for both channel and pipe flow models), which could not be removed using LTE model. The conduction heat transfer through the solid phase and the internal heat exchange between the solid and fluid phases across the interface separating the superheated vapor and the two-phase mixture regions constitute two additionally required mechanisms for realistic predictions of LTNE model. The LTNE model is more appropriate and necessary for the accurate estimation of the wall heat flux, and hence strongly recommended for the simulation of the complete phase change process inside porous media. Different models for the partitioning of wall heat flux using the LTNE model have negligible influence on the overall predictions, except in the vicinity of the wall. A closer inspection of the results reveals that Model-2 appears to be the most realistic, whereas Model-1 has been found to be the most stable. Models-3 and 4, on the other hand, should be avoided since they produce negative values of $(T_s - T_f)$ at the wall. The results also show that the Reynolds number, the Darcy number and the thermal conductivity of the solid phase have a strong effect on the predicted temperature distributions, whereas the porosity has only a marginal effect.

Furthermore, the results show that the LTNE model and the smoothing algorithm are successful in dealing with the rapid change in the modeled effective heat capacity ratio and effective diffusion coefficient in transient simulations of the complete phase change process, which may otherwise promote an undesirable jump in the temperature distribution. The temperature of steam is slightly sensitive to the location of the heated surface as can be observed when the heater is moved from the lower to the upper wall of the channel and supplies identical heat flux, indicating that the buoyancy force has only minor influence. In a circular pipe flow model, the LTNE model predicts early initiation of the phase change process as compared to the results obtained using LTE model for identical conditions. A comparison of the numerical results of the incomplete and complete phase change process obtained using either the non-staggered grid layout or the staggered grid layout shows that the results are identical. Therefore, the results clearly demonstrate that, for the problem of complete evaporation process, the use of either non-staggered or staggered grid layout can be recommended, since both methods can be applied successfully.

CHAPTER 6. SIMULATION OF COMPLETE PHASE CHANGE PROCESS USING ANISOTROPIC MODEL

Although, additional effects in the form of anisotropy in the porous media properties, along with Local Thermal Non-Equilibrium (LTNE) model for phase change inside porous media could be quite important for a number of practical applications, the literature review shows that most of the earlier studies were performed only on the assumption of isotropic porous media. In many practical applications involving large temperature differences between the fluid and solid phases, the assumption of LTE is inadequate. In such circumstances, it is pertinent to take into account the effects of the LTNE assumption. Realizing this fact, investigations have been carried out in the previous chapter to investigate the effects of LTNE assumption on the complete phase change process within isotropic porous medium. However, in accurate modeling of complete phase change process within anisotropic porous medium, LTNE model prevails in most of the circumstances to avoid the occurrence of non-physical "jump" in the predicted temperature distribution.

Based on the above observations, the present chapter presents the numerical results of complete phase change process considering anisotropy in mechanical and in thermal properties of the porous medium. In particular, steady-state two-dimensional channel flow has been investigated, applying constant heat flux boundary conditions at the bottom wall and using staggered grid layout. The flow in the porous medium has been adopted by the Two-Phase Mixture Model (TPMM) of Wang [33] along with LTNE model. The proposed smoothing algorithm for the effective diffusion coefficient has been extended and applied for the anisotropic model. The results of incomplete and complete phase change processes obtained using the anisotropic model have been compared with that obtained from the isotropic model. Furthermore, the effect of variations in the thermal conductivity of the solid phase and in the Darcy number have been investigated for fixed values of k_R and K_R.

6.1. Problem Description and Basic Assumptions

The problem of complete, stationary phase change of liquid water inside a porous channel has been examined in the present study as a demonstrative example. The schematic representation of the problem geometry, as well as the coordinates system, is shown in Fig. 4.17(a) along with its dimensions. For simplicity, a two-dimensional parallel plate channel filled with a known porous medium has been chosen for the present analysis. The porous medium has been considered anisotropy in both mechanical and thermal properties. A partitioning constant heat flux $\dot{q}''_w$ has been applied on the bottom wall according to the model-1 for partitioning of the wall heat flux, given by Eq. (2.158a). An external pressure gradient drives the sub-cooled liquid water with a uniform velocity u_{in} and at a temperature lower than the saturation temperature $T_{in} < T_{sat}$ at the inlet to flow through the channel. The examined conditions have been considered identical to those given in chapter 5 for the purpose of comparison. By adopting the H-formulation along with LTNE model, the conservation of mass in Eq. (2.130), momentum in Eq. (2.159) and energy for both fluid and solid phases in Eqs. (2.162) and (2.163), respectively, are introduced under steady-state condition by dropping the transient term, respectively. The individual velocities of liquid and vapor phases can be recovered from the Eqs. (2.169a) and (2.169b), respectively. The boundary conditions for the present study are given similar to that in Eqs. (5.16) – (5.19) by including the anisotropic effect (i.e., Γ^{*}_{Hy} and $k^{*}_{eff,sy}$).

6.2. Ranges of Parameters and Numerical Results

The physical geometry of the channel has been chosen to be similar to that used for LTNE model in chapter 5, with parameters $L = 300\text{mm}$ ($L^{*} = 6$) and $W = 50\text{mm}$ ($W^{*} = 1$). Present predictions have been compared with respective results that were obtained using the isotropic model when the same heat input has been supplied through an identical heater located at the same axial distance at the bottom wall, as presented in chapter 5, for $\dot{q}''_w = 400\text{kW/m}^2$, $\varepsilon = 0.4$, $u_{in} = 5\times10^{-4}\,\text{m/s}$ and $K = 10^{-11}\text{m}^2$. In addition, uniform grid has been employed as well, and identical number of control volumes $N_{CV} = 80\times25$. From the anisotropic relations, it is possible to find many limiting ranges for the porous medium properties by changing the permeability and thermal conductivity ratios of different directions in the solid struts. In detail, the present investigation demonstrates the effect of the permeability ratio K_R, the thermal conductivity ratio k_R, the thermal conductivity of the solid phase k^{*}_{sx} by keeping k_R fixed as well as the Darcy number by keeping K_R fixed on the complete phase change process. For the porous medium, the average pore diameter is required to evaluate the heat transfer coefficient $h^{*}_{s\alpha}$ [see Eq. (2.154)] and has been assumed to vary from $30\mu\text{m}$ to $400\mu\text{m}$, whereas the porosity has been considered to be 0.4. For the present demonstrative examples, the longitudinal component of permeability K_x could be varied from 10^{-12}m^2 to 10^{-10}m^2. The thermal conductivity of the solid phase k_s, on the other hand, has been varied between $20\,\text{W/m K}$ and $250\,\text{W/m K}$. Based on these data and the properties of water given in Table 2.1, the following ranges of dimensionless parameters that have been considered for this study are summarized in Table 6.1:

Table 6.1: Ranges of dimensionless parameters used for two-dimensional problem along with LTNE model inside anisotropic porous channel

Parameters	Ranges of dimensionless values
Permeability ratio, K_R	$1-10$
Thermal conductivity ratio, k_R	$1-5$
Thermal conductivity of the solid phase, k^{*}_{sx}	0.2 – 0.8
Darcy number, K^{*}	$5\times10^{-10} - 5\times10^{-8}$

Additionally, the reference case has been chosen to be isotropic with the following parameters: $Re_l = 85$, $Q^{*}_w = 32$, $\varepsilon = 0.4$, $d^{*}_p = 2\times10^{-3}$, $K^{*} = 5\times10^{-9}$ (i.e., $K = 10^{-11}\text{m}^2$), $k^{*}_{sx} = 0.5$ (i.e., $k_{sx} = 50\,\text{W/m K}$), $k_R = 1$ and $K_R = 1$ along with the Model-1 for the partitioning of wall heat flux. In the present investigation, the effects of anisotropy in permeability and thermal diffusivity, on the complete phase change process, are discussed separately. Results are presented in terms of temperature for both fluid and solid phases and liquid saturation distributions to understand the phase change physics.

6.2.1. Effects of Solid Thermal Conductivity Ratio (k_R)

This subsection presents the numerically predicted, fluid and solid temperatures as well as liquid saturation distributions for the complete phase change process, respectively. In this case the solid thermal conductivity ratio k_R has been varied from 1 to 5. These results are presented in Figs. 6.1 – 6.3. The temperature and liquid saturation patterns corresponding to a porous medium with an isotropic thermal conductivity ($k_R = 1$) are depicted in Figs. 6.1(a) – 6.3(a), which have been already presented in chapter 5 [see Fig. 5.12]. It can be observed from Figs. 6.1 and 6.2 that the maximum temperatures for both fluid and solid phases and the steam quality are decreased with an increase in k_R irrespective of K_R. Furthermore, it is also observed from the figures that the areas of two-phase and superheated vapor regions are reduced with the increase in k_R as compared with the isotropic case [see Fig. 6.3]. This is reasonable and can be explained by the increase in the diffusive heat transfer in the transverse direction from the superheated vapor phase to the two-phase mixture region, which occurs for enhanced $k^*_{eff,sy}$.

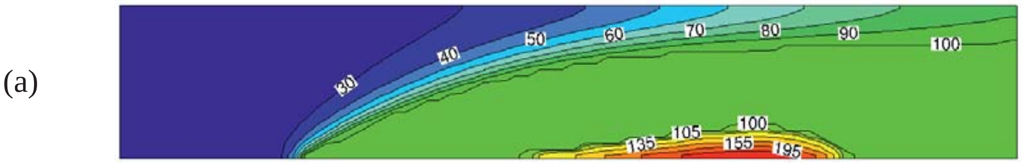

$k_R = 1$, $T_{f,\max} \approx 214\,^\circ\mathrm{C}$

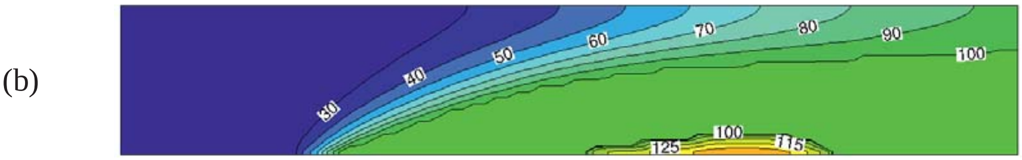

$k_R = 2$, $T_{f,\max} \approx 143\,^\circ\mathrm{C}$

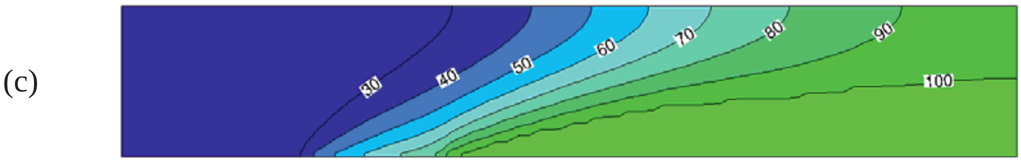

$k_R = 5$, $T_{f,\max} = 100\,^\circ\mathrm{C}$

Fig. 6.1: Fluid temperature distributions for different solid thermal conductivity ratio for $K_R = 1$, $Re_l = 85$, $Q^*_w = 32$, $\varepsilon = 0.4$, $k^*_{sx} = 0.5$ and $K^* = 5\times 10^{-9}$

It is also clearly seen from Figs. 6.1(c) – 6.3(c) that the superheated vapor region vanishes due to higher energy diffusion in the upstream and upward directions, from the two-phase zone to the saturated liquid phase. Another reason for this is the considerable diffusive heat loss through the inlet for higher $k^*_{eff,sy}$. The absence of temperature gradients in the transverse direction is due to the fact that the thermal conductivity in that direction is much higher than in the axial direction. It can also be seen that the isotherms are now considerably inclined towards the outlet near the upper wall for $k_R = 1$ [see Figs. 6.1(a) and 6.2(a)]. This is expected since the diffusive heat transfer in the transverse direction from the saturated vapor to the saturated liquid (through two-phase region) decreases when k_R is reduced. On the contrary, the isotherms are further inclined towards the inlet with increasing in k_R. This is due to increase in the thermal conductivity of the solid phase in the transverse direction, indicating the heat transport mechanism is dominated by conduction, as may be observed from Figs. 6.1(c) and 6.2(c). Due to relatively larger thermal conductivity in the transverse direction, the temperature gradients for the working fluid for $k_R = 5$ is smaller than for $k_R = 2$ and 1. The increase in k_R causes higher flow intensity in the channel resulting in a reduction of the maximum temperature. It can be concluded that the anisotropy in thermal properties has significant influence on the complete phase change process.

(a)

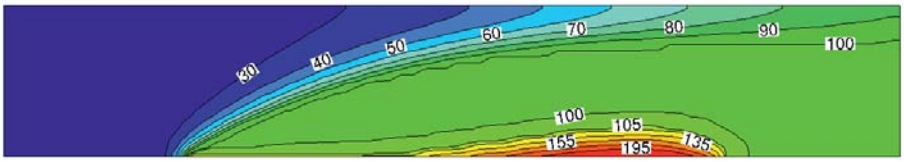

$k_R = 1$, $T_{s,\max} \approx 227\,^{\circ}\mathrm{C}$

(b)

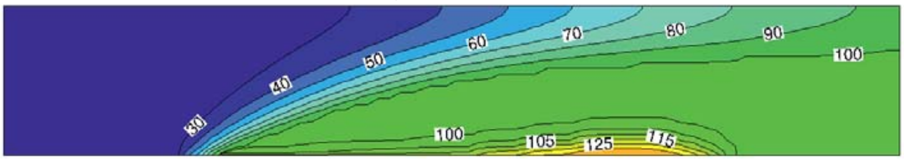

$k_R = 2$, $T_{s,\max} \approx 151\,^{\circ}\mathrm{C}$

(c)

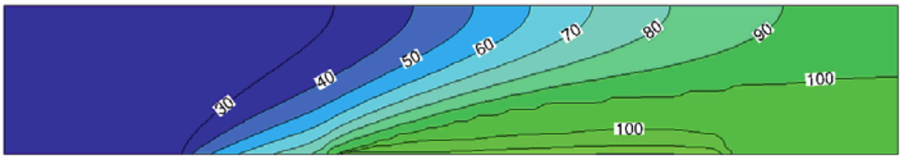

$k_R = 5$, $T_{s,\max} \approx 106\,^{\circ}\mathrm{C}$

Fig. 6.2: Solid temperature distributions for different solid thermal conductivity ratio for $K_R = 1$, $Re_l = 85$, $Q_w^* = 32$, $\varepsilon = 0.4$, $k_{sx}^* = 0.5$ and $K^* = 5\times10^{-9}$

(a)

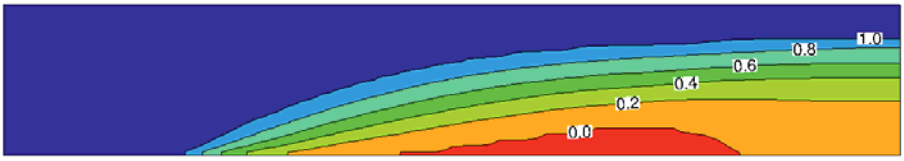

$k_R = 1$, $s_{\min} = 0$

(b)

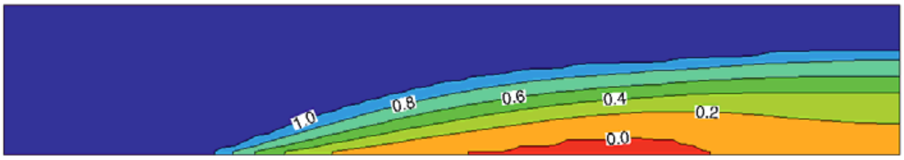

$k_R = 2$, $s_{\min} = 0$

(c)

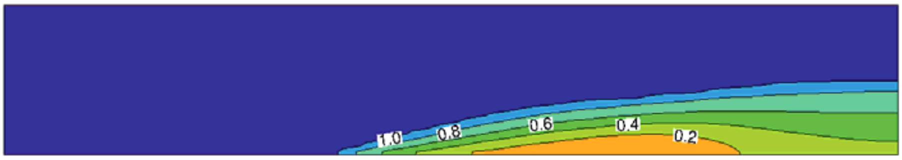

$k_R = 5$, $s_{\min} \approx 0.009$

Fig. 6.3: Liquid saturation distributions for different solid thermal conductivity ratio for $K_R = 1$, $Re_l = 85$, $Q_w^* = 32$, $\varepsilon = 0.4$, $k_{sx}^* = 0.5$ and $K^* = 5\times10^{-9}$

6.2.2. Effects of Permeability Ratio (K_R)

This subsection is concerned with numerical results for the complete phase change process inside anisotropic porous media for various permeability ratios. Figures 6.4 – 6.6 illustrate the temperature for both fluid and solid phases and liquid saturation distributions, respectively, for various K_R, ranging from 1 to 10. Similarly, the numerical results for the isotropic model are presented in Figs. 6.4(a) – 6.6(a). It is observed from the figures that the maximum temperatures for both fluid and solid phases are decreased with the increase in K_R due to increase in the diffusive energy flux in the transverse direction. The decrease of maximum temperature with an increase in K_R, being connected with an increased effective diffusion coefficient in the transverse direction, is caused by an enhanced diffusive energy flux in the transverse direction from the boiling front to the condensation front, which is responsible for a delayed initiation of the superheated vapor region [see Figs. 6.6(a) and 6.6(d)]. As K_R greater than 1, Figs. 6.4(b) and 6.5(b) show that the strength of convection is higher compared to $K_R = 1$. This can be explained by the fact that an increase in K_R corresponds to increase in the permeability K_y, the effective diffusion coefficient in the transverse direction is increased, resulting in a stronger overall heat transfer. Furthermore, the onset of complete phase change process can be observed for $K_R = 5$ when the boiling front begins to emerge [see Fig. 6.6(c)].

(a)

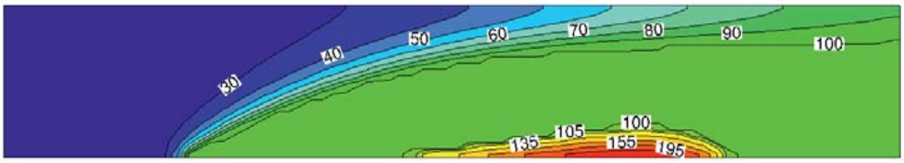

$K_R = 1$, $T_{f,\max} \approx 214\,^{\circ}\mathrm{C}$

(b)

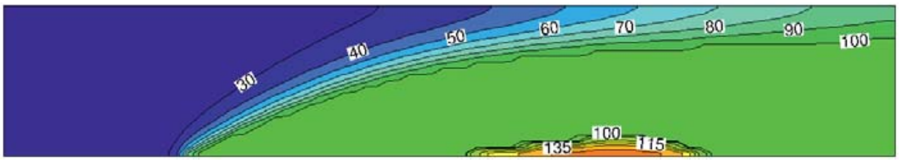

$K_R = 2$, $T_{f,\max} \approx 171\,^{\circ}\mathrm{C}$

(c)

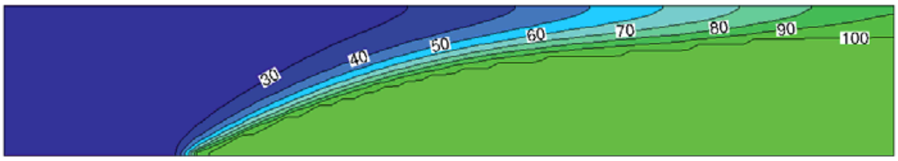

$K_R = 5$, $T_{f,\max} = 100\,^{\circ}\mathrm{C}$

(d)

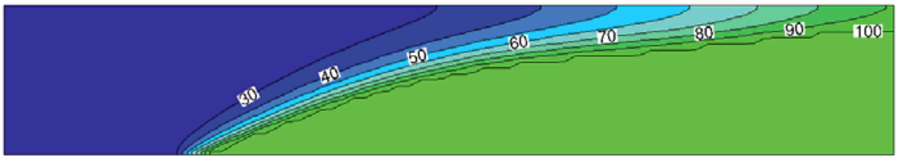

$K_R = 10$, $T_{f,\max} = 100\,^{\circ}\mathrm{C}$

Fig. 6.4: Fluid temperature distributions for different permeability ratio for $k_R = 1$, $Re_l = 85$, $Q_w^* = 32$, $\varepsilon = 0.4$, $k_{sx}^* = 0.5$ and $K^* = 5 \times 10^{-9}$

The increase in K_R progressively weakens the steam quality due to increase the amount of energy diffusing in the transverse direction from the saturated vapor state to the saturated liquid state [see Figs. 6.4(d) and 6.5(d)]. For this situation, the permeability in the axial direction is now much lower than that in the transverse direction, thus, spreading in the transverse direction is non-uniform as the axial direction. However, due to the relatively low permeability in the axial direction, the vertically flowing fluid is strongly channeled along the end of upper wall. Indeed, the isotherms as shown in Figs. 6.4 and 6.5 illustrate that gradual decrease in the magnitude of the temperature for both fluid and solid phases is observed with the variation of K_R from 1 to 10. For $K_R = 10$, Figs. 6.4(d) and 6.5(d) show that an increment of the permeability ratio has very little influence on the temperature behavior, whereas the quality of vapor inside the two-phase region is significantly reduced [see Fig. 6.6(d)]. Due to the relatively high permeability in the transverse direction, the two-phase zone is further extended towards the downstream direction and the upper wall [see Figs. 6.6(a) – 6.6(d)]. Therefore, it is also concluded that the anisotropy in hydrodynamic properties has also significant influence on the complete phase change process.

(a)

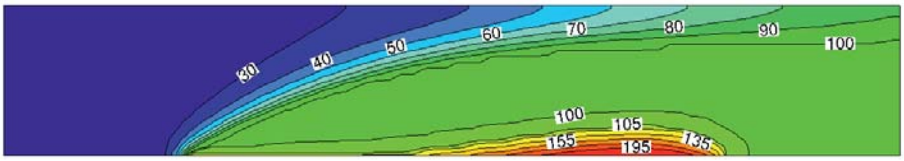

$K_R = 1$, $T_{s,\max} \approx 227^{\circ}\mathrm{C}$

(b)

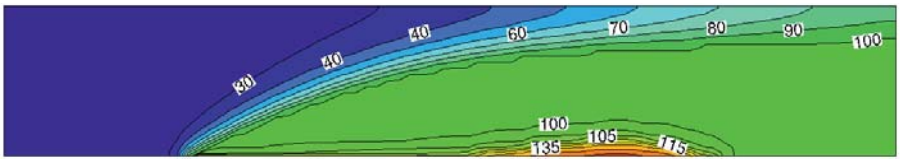

$K_R = 2$, $T_{s,\max} \approx 185^{\circ}\mathrm{C}$

(c)

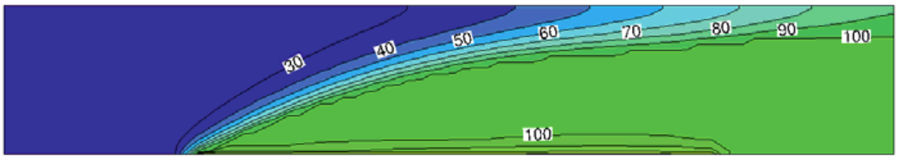

$K_R = 5$, $T_{s,\max} \approx 119^{\circ}\mathrm{C}$

(d)

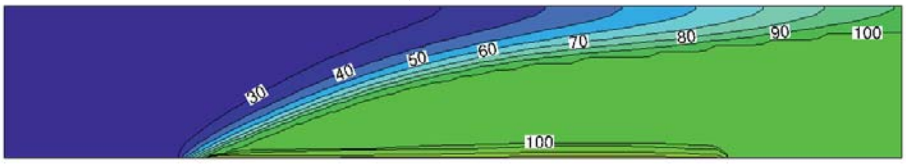

$K_R = 10$, $T_{s,\max} \approx 116^{\circ}\mathrm{C}$

Fig. 6.5: Solid temperature distributions for different permeability ratio for $k_R = 1$, $Re_l = 85$, $Q_w^* = 32$, $\varepsilon = 0.4$, $k_{sx}^* = 0.5$ and $K^* = 5 \times 10^{-9}$

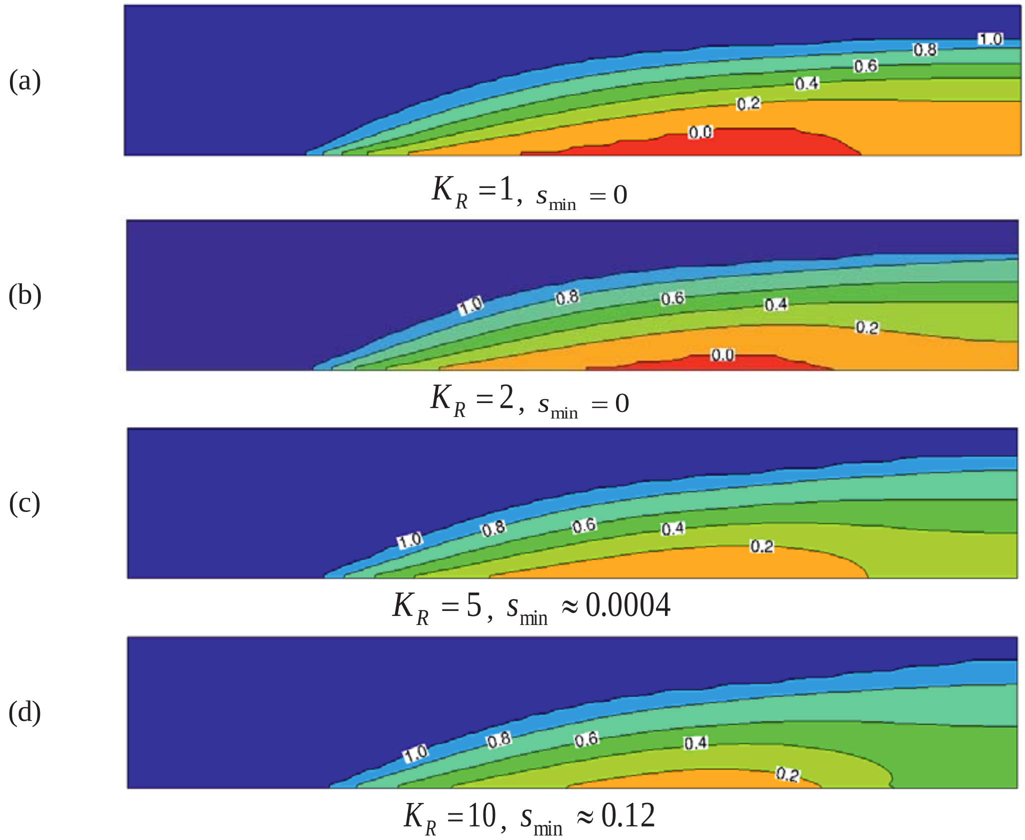

(a) $K_R = 1$, $s_{\min} = 0$

(b) $K_R = 2$, $s_{\min} = 0$

(c) $K_R = 5$, $s_{\min} \approx 0.0004$

(d) $K_R = 10$, $s_{\min} \approx 0.12$

Fig. 6.6: Liquid saturation distributions for different permeability ratio for $k_R = 1$, $Re_l = 85$, $Q_w^* = 32$, $\varepsilon = 0.4$, $k_{sx}^* = 0.5$ and $K^* = 5 \times 10^{-9}$

6.2.3. Effects of Solid Thermal Conductivity (k_{sx}^*)

This subsection describes the implementation of complete phase change process for different thermal conductivities of the solid phase in the axial direction k_{sx}^*, while keeping the solid thermal conductivity ratio fixed. Figures 6.7 – 6.9 illustrate the variations of temperature for both fluid and solid phases and liquid saturation distributions, respectively, for various k_{sx}^* (0.2 – 0.8) at $k_R = 2$. It can be observed from Figs. 6.7 and 6.8 that the maximum temperature for both fluid and solid phases are decreased with the increase in k_{sx}^*. These figures clearly show that the superheated vapor and the two-phase mixture regions are extended as k_{sx}^* is decreased from 0.8 to 0.2 [see Figs. 6.7 – 6.9]. This can be explained by considerably lower diffusive heat losses through the inlet for lower k_{sx}^*, which is responsible for the early initiation of phase change from sub-cooled liquid state to the two-phase mixture zone, as well as from the two-phase mixture zone to the superheated vapor state. As mentioned in chapter 5, an early initiation and termination of superheated vapor phase also depends on the amount of energy diffused in the upstream direction through the two-phase zone (from the boiling front to the condensation front), since the latter diffusive energy flux decreases with the decrease k_{sx}^*.This case leads to considerably increase in the temperature for both phases close to the heated surface at the bottom wall. On the contrary, the size of superheated vapor and two-phase mixture regions are reduced with increase in k_{sx}^{*}, while the sub-cooled liquid region is extended towards the downstream direction and the center of the channel [see Fig. 6.9].

Furthermore, it is also observed from Figs. 6.7 and 6.8 for $k_{sx}^{*}=0.2$, that the temperature field exhibits maximal gradient, indicating that the conduction is also still the dominant mechanism of energy transport. However, with the increasing k_{sx}^{*}, the temperature field is significantly changing due to the higher diffusive heat loss through the inlet, and to the diffusive energy flux in the upstream direction. It is also clear from the figures that the isotherms show a trend of moving towards the upstream direction with an increase in k_{sx}^{*}, and hence enhanced $k_{eff,sx}^{*}$, due to increased diffusive heat transfer from the superheated vapor phase to the two-phase mixture region. Due to relatively larger thermal conductivity in the axial direction (i.e., larger thermal conductivity in the transverse direction), the temperature gradients for the fluid and the solid phases for $k_{sx}^{*}=0.8$ are smaller than for $k_{sx}^{*}=0.5$ and 0.2 [see Figs. 6.7 and 6.8]. Most importantly, this study clearly shows that the effect of thermal conductivity of the solid phase plays an important role and hence, adequate care must be taken while designing such evaporator.

(a)

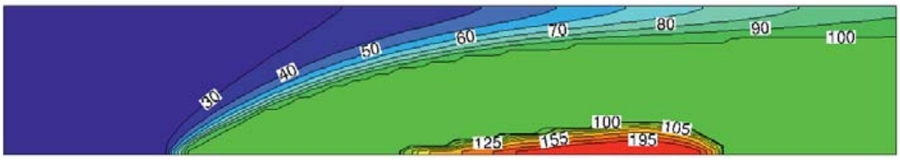

$k_{sx}^{*}=0.2$, $T_{f,\max}\approx 257^{\circ}\mathrm{C}$

(b)

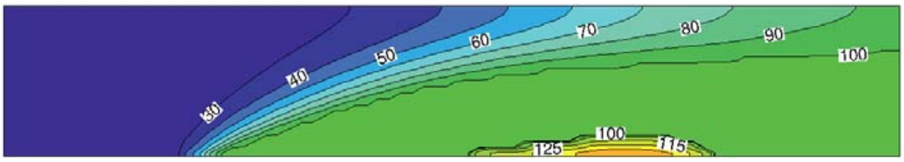

$k_{sx}^{*}=0.5$, $T_{f,\max}\approx 143^{\circ}\mathrm{C}$

(c)

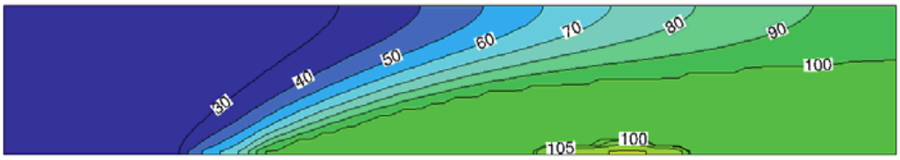

$k_{sx}^{*}=0.8$, $T_{f,\max}\approx 116^{\circ}\mathrm{C}$

Fig. 6.7: Fluid temperature distributions for different solid thermal conductivity for $K_R=1$, $k_R=2$, $Re_l=85$, $Q_w^{*}=32$, $\varepsilon=0.4$ and $K^{*}=5\times10^{-9}$

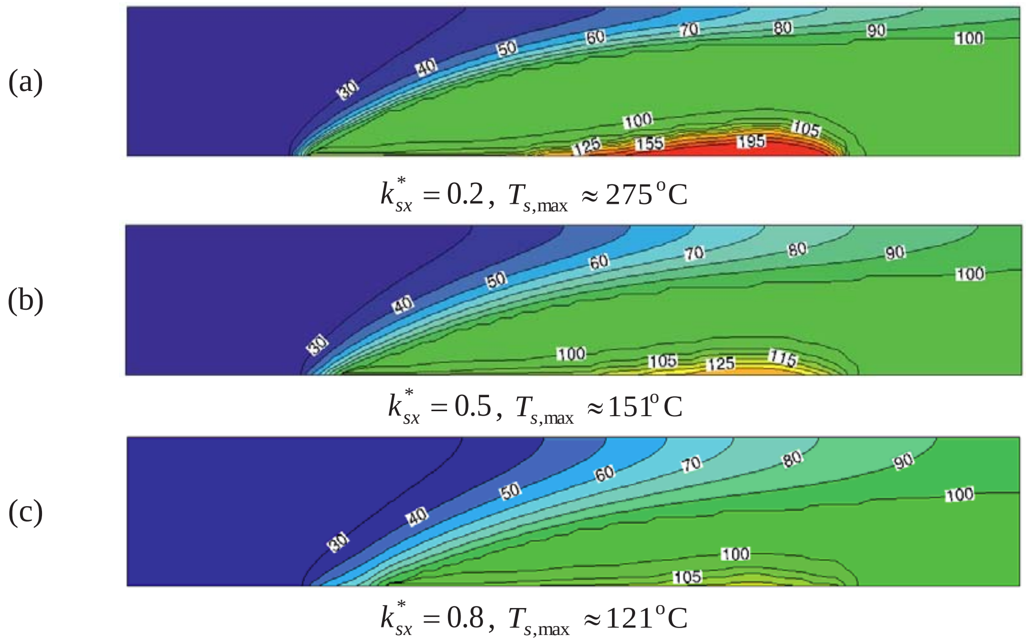

(a) $k_{sx}^{*} = 0.2$, $T_{s,\max} \approx 275^{\circ}\mathrm{C}$

(b) $k_{sx}^{*} = 0.5$, $T_{s,\max} \approx 151^{\circ}\mathrm{C}$

(c) $k_{sx}^{*} = 0.8$, $T_{s,\max} \approx 121^{\circ}\mathrm{C}$

Fig. 6.8: Solid temperature distributions for different solid thermal conductivity for $K_R = 1$, $k_R = 2$, $Re_l = 85$, $Q_w^{*} = 32$, $\varepsilon = 0.4$ and $K^{*} = 5\times10^{-9}$

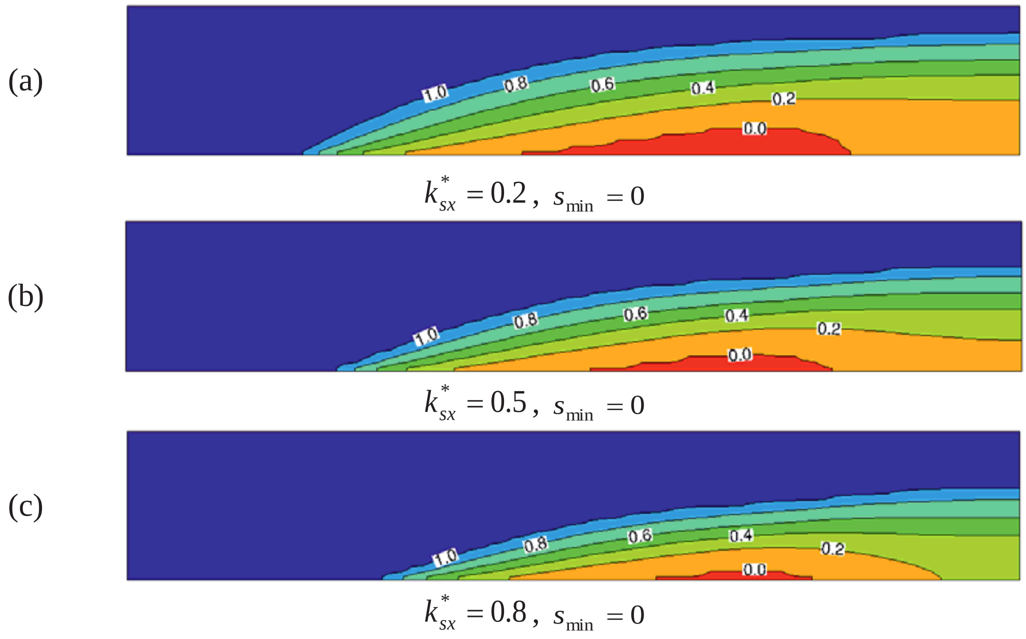

(a) $k_{sx}^{*} = 0.2$, $s_{\min} = 0$

(b) $k_{sx}^{*} = 0.5$, $s_{\min} = 0$

(c) $k_{sx}^{*} = 0.8$, $s_{\min} = 0$

Fig. 6.9: Liquid saturation distributions for different solid thermal conductivity for $K_R = 1$, $k_R = 2$, $Re_l = 85$, $Q_w^{*} = 32$, $\varepsilon = 0.4$ and $K^{*} = 5\times10^{-9}$

6.2.4. Effects of Darcy Number (K^{*})

A detail account of liquid-vapor phase change process for different Darcy number, while keeping the permeability ratio K_R fixed, is presented in this subsection. Figures 6.10 – 6.12 represent the variations of temperature for both fluid and solid phases and liquid saturation distributions, respectively, for various K^{*} (5×10^{-10} – 5×10^{-8}) at $K_R = 5$. As mentioned before, the Darcy number is defined based on the permeability K_x in the axial direction. As may be observed from Figs. 6.10 and 6.12, as the Darcy number increases, the superheated vapor region vanishes and the two-phase region is extended towards the upper wall due to increased diffusive energy flux in the transverse direction. For higher Darcy number, while keeping K_R fixed, the heat transport mechanism is dominated by both convection and conduction (by enhancement of the capillary diffusion affecting the effective diffusion coefficient in the two-phase region). For a given set of parameters, with increase in K^* the pressure drop is increased due to higher permeability of the porous medium in the axial direction. This leads to reduce the diffusive heat loss through the inlet, resulting in a reduction of the maximum temperature in both fluid and solid phases close to the heated section at the bottom wall [see Figs. 6.10(a) – (c) and 6.11(a) – (c)]. The reverse of the above discussed process happens when the Darcy number is decreased, as shown in Figs. 6.10(c) – 6.12(c). The size of superheated vapor region is significantly extended with the decrease in K^*. As Darcy number is decreased, the obstruction of the flow field increases, resulting in reduction of pressure drop. Therefore, the two-phase zone is more extended in the upstream direction for low K^* as compared to high K^* due to higher convective heat transfer as smaller pore diameter of the porous medium and higher diffusive heat loss are provided through the inlet [see Fig. 6.12]. Therefore, it can be concluded that the complete phase change process, keeping the permeability ratio constant, occurs for low as possible Darcy numbers.

(a)

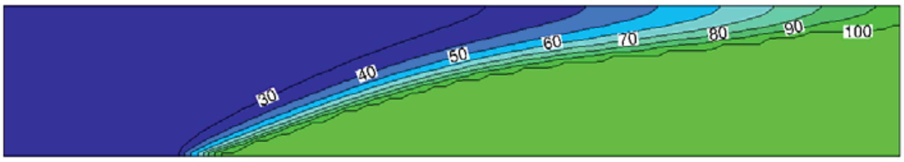

$K^* = 5\times10^{-8}$, $T_{f,\max} = 100\,^{\circ}\mathrm{C}$

(b)

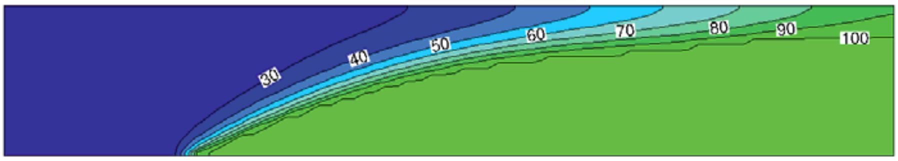

$K^* = 5\times10^{-9}$, $T_{f,\max} = 100\,^{\circ}\mathrm{C}$

(c)

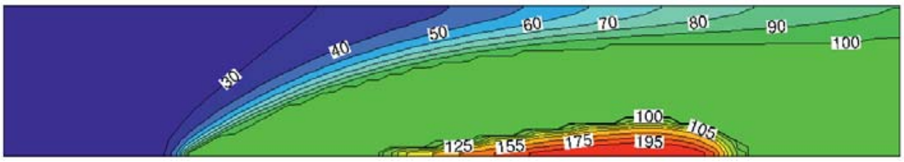

$K^* = 5\times10^{-10}$, $T_{f,\max} \approx 241\,^{\circ}\mathrm{C}$

Fig. 6.10: Fluid temperature distributions for different Darcy number for $K_R = 5$, $k_R = 1$, $Re_l = 85$, $Q_w^* = 32$, $\varepsilon = 0.4$ and $k_{sx}^* = 0.5$

(a)

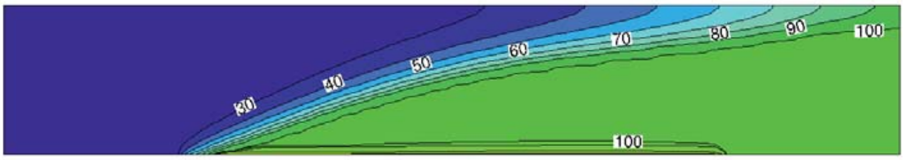

$K^* = 5\times10^{-8}$, $T_{s,\max} \approx 118^{\circ}\mathrm{C}$

(b)

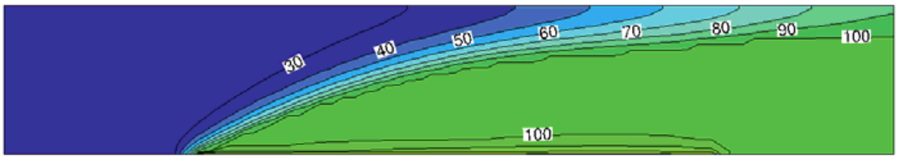

$K^* = 5\times10^{-9}$, $T_{s,\max} \approx 119^{\circ}\mathrm{C}$

(c)

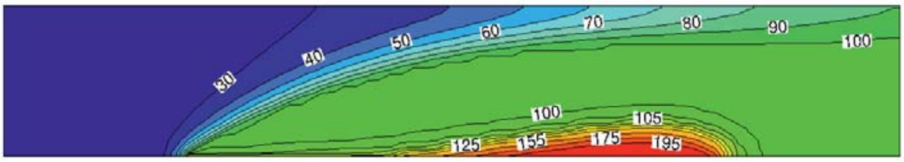

$K^* = 5\times10^{-10}$, $T_{s,\max} \approx 253^{\circ}\mathrm{C}$

Fig. 6.11: Solid temperature distributions for different Darcy number for $K_R = 5$, $k_R = 1$, $Re_l = 85$, $Q_w^* = 32$, $\varepsilon = 0.4$ and $k_{sx}^* = 0.5$

(a)

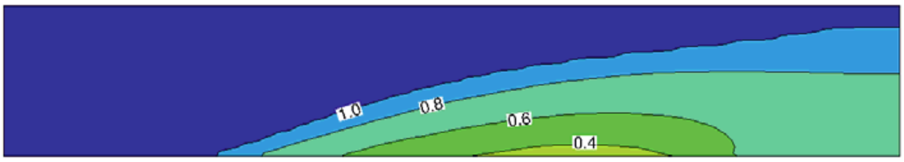

$K^* = 5\times10^{-8}$, $s_{\min} \approx 0.34$

(b)

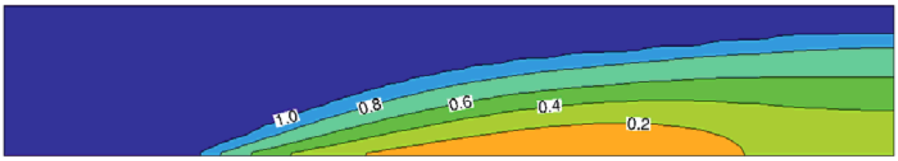

$K^* = 5\times10^{-9}$, $s_{\min} \approx 0.0004$

(c)

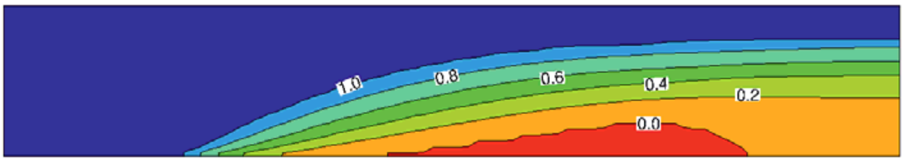

$K^* = 5\times10^{-10}$, $s_{\min} = 0$

Fig. 6.12: Liquid saturation distributions for different Darcy number for $K_R = 5$, $k_R = 1$, $Re_l = 85$, $Q_w^* = 32$, $\varepsilon = 0.4$ and $k_{sx}^* = 0.5$

6.3. Conclusions

This chapter involves the coupling of the anisotropy in both mechanical and thermal porous media properties in order to investigate the complete phase change process in channel flow. For all numerical simulations, formulations based on TPMM of Wang [33] have been used under steady state condition, along with the assumption of LTNE condition. The proposed smoothing algorithm for the effective diffusion coefficient has been extended and applied for the anisotropic model. The computed results show that the anisotropy of permeability and thermal conductivity of the solid phase have significant effect on the complete phase change process. The superheated vapor and the two-phase regions are extended as the thermal conductivity of the solid phase in the axial direction decreases due to considerably lower heat loss through the inlet. In this situation, the phase change process from sub-cooled liquid state to the two-phase mixture as well as from the two-phase mixture to the superheated vapor state initiates earlier. The decrease of maximum temperatures with increasing permeability ratio between the transverse and axial directions indicates that the diffusive energy flux in the transverse direction is enhanced, which is responsible for a delayed initiation of the superheated vapor region. Most importantly, the numerical results clearly show that the solid thermal conductivity, keeping thermal conductivity ratio of the solid phase between the transverse and axial directions fixed, plays an important role and hence, adequate care must be taken while designing such an evaporator based on an anisotropic porous medium.

CHAPTER 7. SIMULATION OF COMPLETE PHASE CHANGE PROCESS INSIDE DIVERGENT POROUS EVAPORATOR

An interesting aspect of evaporation inside porous media is the volume expansion of phase changing fluid due to huge difference in densities of liquid and vapor phases. During a liquid-vapor phase change process in a constant cross-sectional area duct the vapor-phase occupies significantly larger volume and therefore the velocity increases considerably. In this situation, it would be worthwhile to explore the possibility of using a duct with increasing cross-sectional area in the axial direction. Therefore, this chapter presents the numerical results of one-dimensional, steady-state condition of complete phase change process within divergent porous evaporator, based on the modified volumetric enthalpy formulation of Two-Phase Mixture Model (TPMM) [33] along with the Local Thermal Equilibrium (LTE) assumption. The simulations have been carried out using the proposed smoothing algorithm for the effective diffusion coefficient in order to avoid “jump” in the predicted temperature distribution. The consequences from smoothing of the diffusion coefficient and the effects of different parameters such as operating conditions, porous media properties and evaporator geometry on the temperature fields have been thoroughly investigated.

7.1. Problem Description and Basic Assumptions

A schematic representation of the divergent porous evaporator considered for the simulation of complete phase change process is shown in Fig. 7.1 along with its dimensions. The pipe has increasing cross-sectional area in the axial direction and has been filled with a porous medium of known properties. An external pressure gradient drives the sub-cooled liquid water, entering at a temperature T_{in} and a velocity u_{in}, to flow through the pipe. It is then heated to the superheated vapor state by applying uniform heat flux on the external surface of the evaporator at the diffuser section. The porous medium has been considered homogenous as well as isotropic and the LTE condition has been assumed. The flow has been considered steady as well as one dimensional. With these assumptions, the non-dimensional conservation of mass in Eq. (2.130) and energy in Eq. (2.134), where the variations remain only in the axial direction, are obtained as:

$$\frac{d}{dx^*}\left(\rho^* u_x^* A_c^*\right) = 0 \tag{7.1}$$

$$\frac{d}{dx^*}\left(A_c^* \gamma_H u_x^* H^*\right) = \frac{d}{dx^*}\left(A_c^* \Gamma_H^* \frac{dH^*}{dx^*}\right) + \frac{d}{dx^*}\left(A_c^* f \frac{K^* \Delta\rho^* h_{fg}^*}{\nu_v^*} b_x^*\right) + P^* \dot{q}_w''^{*} \tag{7.2}$$

where all the parameters and variables appearing in Eqs. (7.1) and (7.2) are provided in chapters 2 and 3. In Eq. (7.2), $\dot{q}_w''^{*} = Q_w^* / Re_l$ with $Q_w^* = \dot{q}_w'' R / \mu h_{fg}$ is the dimensionless heat flux. The solution of Eqs. (7.1) and (7.2) requires appropriate boundary conditions. At the inlet, i.e., at $x^* = 0$, $\rho_{in}^* = 1$, $u_{in}^* = 1$ and $H_{in}^* = \rho_{in}^*\left[h_{l,sat}^* - \rho_{in}^* C_{pl}^*\left(T_{sat}^* - T_{in}^*\right) - 2h_{v,sat}^*\right]$ have been specified. On the other hand, at the outlet, i.e., at $x^* = L/R_i$, the second derivatives of all variables have been set to zero (exit with zero diffusion). Under steady-state condition, owing to the conservation of mass in Eq. (7.1), the mass flow rates at all the cell faces can be set equal to that at the inlet and hence they have been obtained by using Eq. (3.11). The cell face velocity can be directly obtained as: $u_{xe}^* = A_{c,in}^* / \left(\rho_e^* A_{ce}^*\right)$, where ρ_e^* is the mixture density at the cell face and has to be calculated iteratively from the known liquid saturation as shown in Table 2.3.

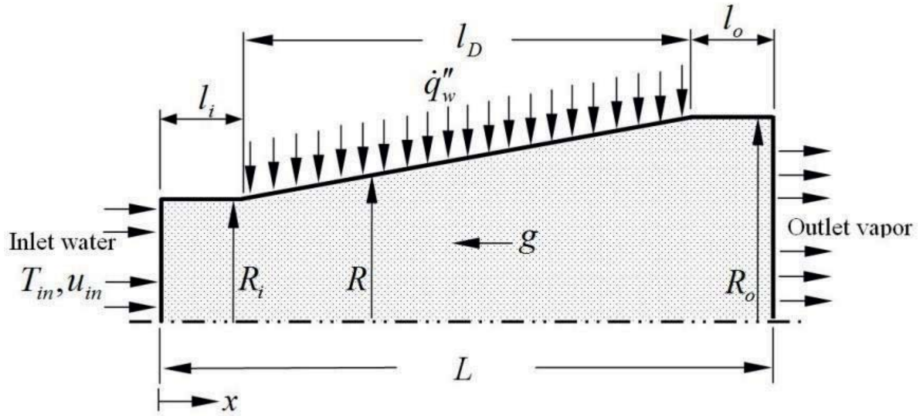

Fig. 7.1: Schematic representation of the porous evaporator

7.2. Ranges of Parameters and Numerical Results

For all the cases presented in this study, R_i has been taken as 25mm, R_o has been varied between 28mm and 35mm and L has been varied from 400mm to 450mm. The length of the divergent section l_D depends on l_i and l_o. In the present work, l_i has been varied between $0.1L$ and $0.2L$, whereas l_o has been always kept fixed at $0.1L$. The entire duct has been filled with a porous medium for which, the thermal conductivity of the solid matrix is $k_s = 20\text{W/mK}$. The porosity and the permeability have been varied from 0.2 to 0.4 and $6.25\times10^{-11}\text{m}^2$ to $6.25\times10^{-13}\text{m}^2$, respectively. Liquid water at $T_{in} = 20^\circ\text{C}$ enters the duct which is then heated to the superheated vapor state by adding constant heat flux, ranging from 15kW/m^2 to 24.5kW/m^2, at the periphery of divergent section of the duct. In a typical application involving phase change inside porous media, the mass flow rate of water is generally quite low and hence it has been varied between 1.25g/h and 2g/h, allowing the inlet velocity to vary from 0.2mm/s to 0.25mm/s. Consequently, the ranges of dimensionless parameters that have been considered for this study are summarized in Table 7.1:

Table 7.1: Ranges of dimensionless parameters used for one-dimensional problem along with LTE model inside a divergent porous evaporator

Parameters	Ranges of dimensionless values
Porosity, ε	$0.2-0.4$
Darcy number, K^*	$10^{-9}-10^{-7}$
Inlet Reynolds, number Re_l	$17.5-22.5$
Inlet radius, R_i^*	1
Outlet radius, R_o^*	$1.12-1.4$
Total length, L^*	$16-18$
Inlet length, l_i	$0.1L-0.2L$
Outlet length, l_o	$0.1L$
Length of divergent section, l_D	$0.7L-0.8L$
Heat Flux, Q_w^*	$6\times10^{-1}-9.5\times10^{-1}$

where, the reference case has been taken for $\tilde{b}_x = -1$, $\varepsilon = 0.3$, $K^* = 10^{-8}$, $Re_l = 20$, $R_o^* = 1.26$, $L^* = 16$, $l_i = 0.1L$, $l_o = 0.1L$, $l_D = 0.8L$, and $Q_w^* = 8.5\times10^{-1}$ and hence these parameters have been kept fixed for all the cases, unless otherwise mentioned. They have been varied only when their effects on the phase change have been studied. For all the cases presented in this chapter, the convergence criterion has been set to 10^{-5}, which ensures the overall energy conservation in the system to be satisfied within 0.01%.

7.2.1. Consequence of Smoothing of Diffusion Coefficient

Prior to obtaining results for the present investigation, a detailed grid independence study has been carried out and it has been observed that 1000 uniform control volumes are required for obtaining grid independent results. As far as the smoothing of the effective diffusion coefficient is concerned, the employed parameters are chosen identical to those specified in subsection 4.1.2. With these parameters, the consequence of smoothing is demonstrated in Fig. 7.2. In order to establish the usefulness of the proposed smoothing algorithm for the effective diffusion coefficient, results obtained in terms of the predicted axial temperature with and without its application are first presented in Fig. 7.2, where (a) shows the variation of incomplete phase change process for different porosities with a low heat flux $Q_w^* = 6\times10^{-1}$ condition, while in (b) the effect of variable exit radius (divergence angle) for complete phase change process is presented for the base heat flux of $Q_w^* = 8.5\times10^{-1}$. It is also evident from the figure that when phase change takes place only from the sub-cooled liquid to the two-phase mixture, no “jump” in the predicted temperature, close to the saturated liquid condition, is observed and solutions, obtained with and without the smoothing algorithm, are identical. On the other hand, for higher heat flux condition, when phase change also takes place from the two-phase mixture to the superheated vapor region, discontinuous temperature profiles are predicted if the proposed smoothing algorithm is not applied. Nevertheless, even for this case, the comparison also clearly shows that both solutions match each other close to the evaporator exit, indicating that the global energy balance is satisfied by both methods.

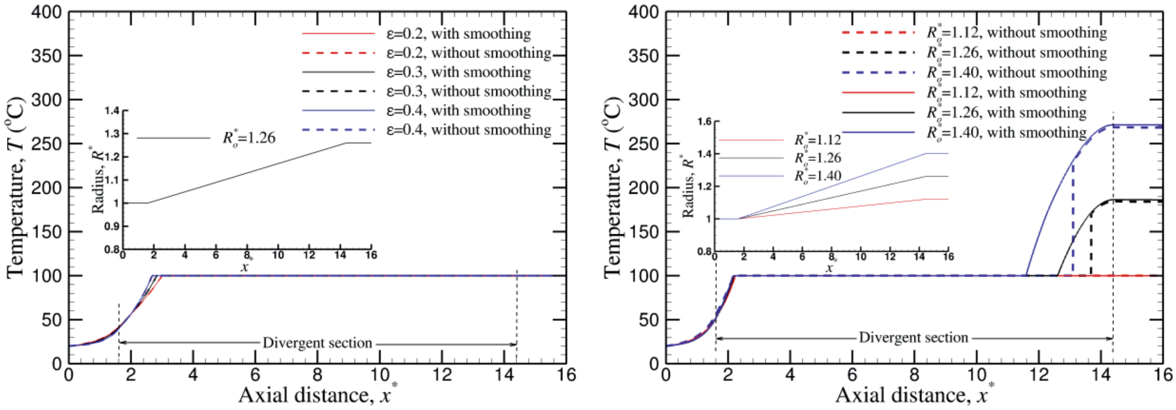

(a) (b)

Fig. 7.2: Comparison of predicted temperature profiles with and without applying smoothing algorithm: (a) partial phase change for different porosities with $Q_w^* = 6\times10^{-1}$, (b) complete phase change for different divergence angles with $Q_w^* = 8.5\times10^{-1}$

It may be noted here that the energy conservation equation is strongly nonlinear in nature. During discretization, the nonlinearity has been addressed in a semi-implicit manner, i.e., by pretending the coefficients, those depend on H^*, to be known from the previous iteration. As a result, the rate of convergence as well as converged solutions for certain cases depend on the guessed values. In a manner similar, it has been observed that if the converged solution obtained with smoothing is used as a guess solution to the solver that works without smoothing, the latter code not only converges very fast (since guessed values are too close to the true solution), but also to the nearly identical solution without any “jump” in predicted temperature field. Since these new solutions cannot be separately distinguished from those obtained using the smoothing algorithm, they could not be shown in Fig. 7.2. It can, therefore, also be safely concluded that the proposed smoothing algorithm provides a successful remedy for the occurrence of “jump” in predicted temperature fields without modifying the expected solution and hence can also be recommended for the simulation of complete phase change process within porous media.

7.2.2. Effects of Operating Conditions

Effects of heat addition and inlet Reynolds number on predicted temperature distributions are shown in Fig. 7.3. As a general observation, it may be recognized that for the present problem, heat has been added only in the diffuser section (marked as the “divergent section” in all similar figures) while the pipe surface at inlet and exit has been kept insulated. One may, therefore, expect the temperature at inlet and exit sections to remain unchanged, with their values being equal to those at inlet and exit of the evaporator, respectively. Although this is somewhat true for the exit section, the figure (for that matter all similar figures) clearly shows an increase in fluid temperature at the inlet section. This observation, however, is expected since the phase change problem inside porous media being elliptic in nature, axial diffusion plays a significant role which heats up the upstream section.

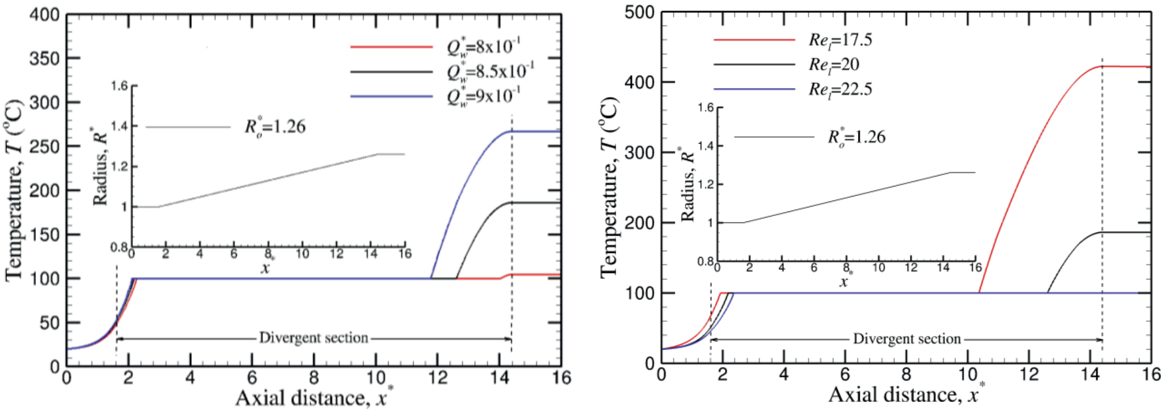

(a) (b)

Fig. 7.3: Effects of (a) applied heat flux and (b) inlet Reynolds number on the axial temperature distributions

Most importantly, owing to features of present formulation, axial diffusion remains present even in the two-phase region as there exists a finite gradient of H^*, although the temperature remains unchanged at saturation condition. Since heat is added in the backward direction due to axial diffusion, no back-heating effect is felt at the exit section, whereas it is quite prominent at the inlet section which is followed by the heating section. Other than this general observation, the effect of heat flux is more evident in the vapor phase and is less prominent for the liquid phase, as may be seen from Fig. 7.3(a). On the other hand, Fig. 7.3(b) clearly shows that reduction of inlet Reynolds number (i.e., decrease in mass flow rate and hence increase in residence time) leads to higher exit temperature. Although both these observations are quite expected, Fig. 7.3 clearly indicates that a marginal change in the operating condition can lead to a substantial change in the exit temperature. Therefore, operating conditions are required to be properly designed in order to achieve the desired objective.

7.2.3. Effects of Porous Media Properties

Figure 7.4 illustrates the effects of porous media properties (in the form of porosity and permeability) on temperature distribution within the porous evaporator. In order to study these effects, the porosity is changed by two-folds (from 0.2 to 0.4), whereas the Darcy number is changed by two orders of magnitude (from 10^{-9} to 10^{-7}). Perhaps this explains more pronounced effect of permeability [see Fig. 7.4(b)], as compared to porosity [see Fig. 7.4(a)], on the temperature distribution. As far as the energy transport during phase change process is concerned, porous media properties affect the temperature distribution by modifying the effective diffusion coefficient, which changes the amount of energy transport in the upstream direction due to axial diffusion. As evident from Table 2.3, an increase in porosity reduces Γ_H in the single phase region, by reducing the contribution of solid-phase conductivity in k_{eff}, whereas it enhances Γ_H by increasing D in the two-phase region. As a result, phase change initiates early with the increase in porosity and the process is prolonged to a larger axial distance. On the other hand, an increase in permeability increases Γ_H only in the two-phase region by enhancing the value of D. This causes early initiation of the phase change process and exit solutions remain nearly unaffected.

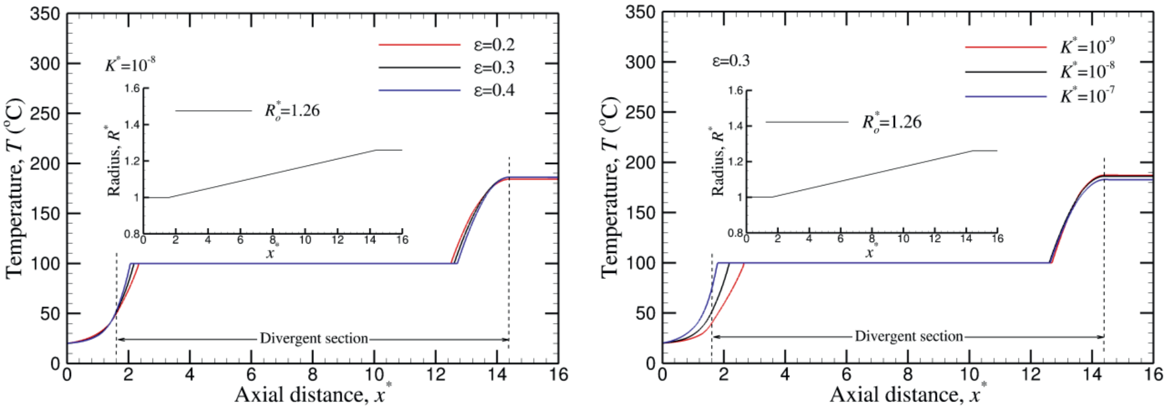

(a) (b)

Fig. 7.4: Effects of (a) porosity and (b) Darcy number on the axial temperature distributions

7.2.4. Effects of Evaporator Geometry

Effects of diffuser geometry, in terms of inlet length, radius ratio and length of the evaporator, on the temperature distribution are summarized in Fig. 7.5. It may be recognized here that the decrease in inlet length, the increase in diffuser angle (i.e., outlet diameter) and the increase in total length of the diffuser effectively enhance the surface area where heat flux is actually added. With the increase in heated surface area by keeping the same heat flux, the total heat input to the working fluid increases, which in turn, enhances the exit temperature of fluid from the evaporator. It is also evident from Fig. 7.5 that the quality of steam at the exit is extremely sensitive to the geometry of the divergent porous evaporator and hence adequate care must be taken while designing such evaporators in order to meet the process requirement.

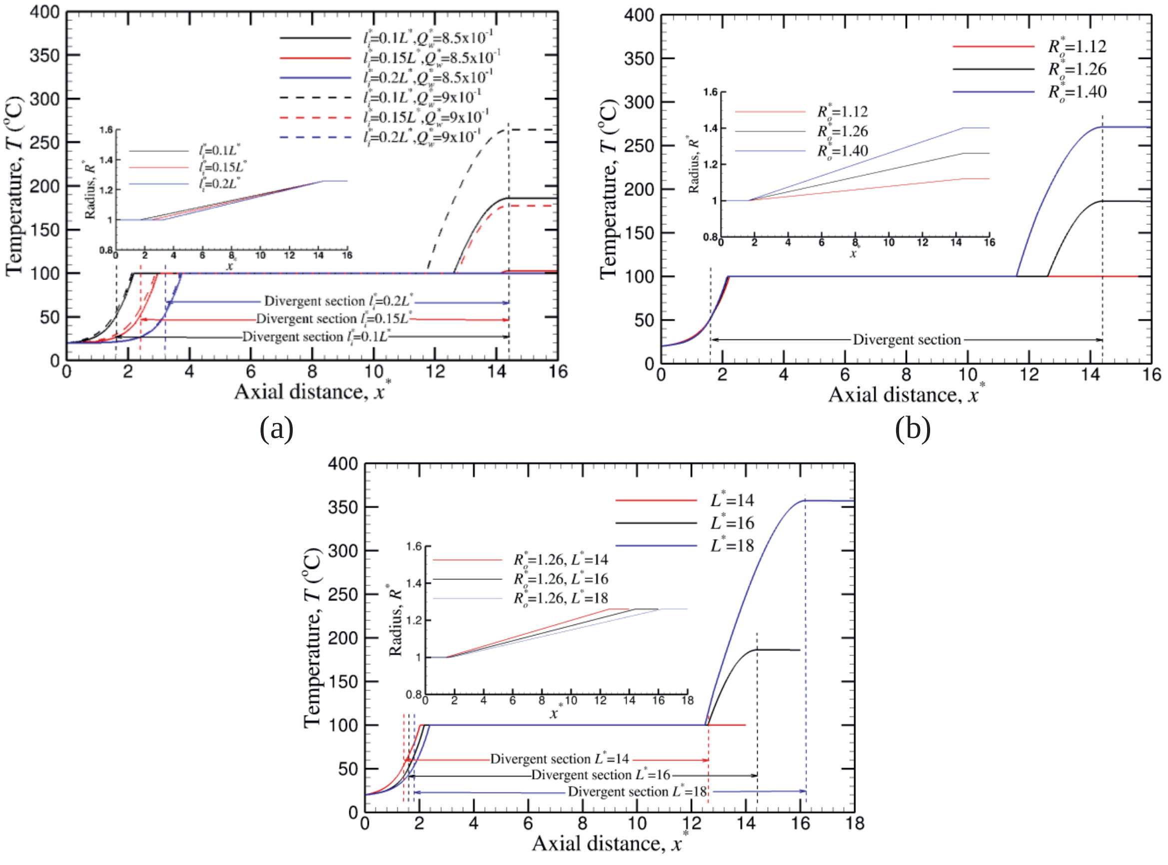

(a) (b)

(c)

Fig. 7.5: Effects of (a) inlet length (b) diffuser angle and (c) evaporator length on the axial temperature distributions

7.3. Conclusions

In this chapter, a thorough numerical simulation has been performed for the complete phase change process inside a divergent porous evaporator. The flow has been considered steady as well as one-dimensional. For numerical simulations, formulations based on TPMM of Wang [33] have been used, along with the assumption of LTE condition. A smoothing algorithm has been used in order to deal with the discontinuity in the effective diffusion coefficient, which proves to be essential for successfully avoiding the occurrence jump in the predicted temperature distribution. Effects of various parameters on the temperature distribution have been carefully investigated. The results clearly indicate that the operating conditions and the geometry of the diffuser strongly influence the outlet conditions of steam, whereas porous medium properties have only a minor impact. Most importantly, the analysis represents a useful tool for designing a divergent porous evaporator in order to achieve complete phase change.

CHAPTER 8. CONCLUSION AND RECOMMENDATION

This chapter concludes the thesis with a brief summary of the research work as well as with the main conclusions extracted from it. Furthermore, the suggestions for future work related with the thesis subject are outlined.

8.1. Summary and Conclusions

This thesis documents a comprehensive study of transport phenomena in porous media, including fluid flow and heat transfer associated with phase change process. This work also proposes a new method for dealing with sharp discontinuities in the modeled effective diffusion coefficient for numerical simulations of complete phase change process inside porous media.

Chapter 2 provides an overview on the Two-Phase Mixture Model (TPMM) [29] concept, which finally leads up to closed mathematical two-phase flow model. In order to be familiar with the *H*-formulation [33], the governing equations, along with constitutive relations, have been derived and presented once again from the basic assumptions and the fundamental conservation principles. This chapter also presents modified mathematical enthalpy formulation (i.e., modified *h*-formulation), which eliminates drawbacks in the original formulation of TPMM, for efficient simulation of complete phase change process inside porous media. These models consider phase change within isotropic porous medium and also assume that the solid and fluid phases are in Local Thermal Equilibrium (LTE) with each other. All governing equations have been non-dimensionalized and they, along with constitutive relations, appear in the same form as their dimensional counterparts. A special treatment method (i.e., smoothing function) for dealing with sharp discontinuities in the effective diffusion coefficient has been presented for both *H*- and *h*-formulations. The *H*-formulation has been extended in order to accommodate the Local Thermal Non-Equilibrium (LTNE) effect for the simulation of complete phase change process for both isotropic and anisotropic porous media.

Chapter 3 provides a brief description of the numerical method that has been applied. A fixed-grid numerical method, based on the TPMM using both LTE and LTNE models, has been adopted for this purpose. The governing equations have been discretized using the Finite Volume Method (FVM), where convective and diffusive terms have been represented by the upwind and the central differencing schemes, respectively. The method has been also presented for both staggered and non-staggered grid layouts. The two-dimensional CFD code was verified comparing results with those obtained from Najjari and Nasrallah [47].

In order to demonstrate the effectiveness of the suggested remedy for dealing with the sharp discontinuities in the effective diffusion coefficient at the phase change interfaces, the complete phase change process of water has been examined for one-dimensional pipe flow (for both constant and increasing cross-sectional area in the axial direction) and for two-dimensional channel and pipe flow problems. Chapter 4 presents the numerical results of one-dimensional pipe flow and two-dimensional channel and pipe flow models for incomplete and complete phase change process inside isotropic porous media, based on the H - and h-formulations using LTE model. In the case of two-dimensional problems, for both circular pipe and channel flow models, results have been obtained based on H -formulation. Moreover, this chapter presents the comparison between results obtained using non-staggered and staggered grid layouts for incomplete phase change process of water in channel flow. The main part of the simulations has been carried out with applying the strategy of the proposed smoothing algorithm in order to avoid the occurrence of non-physical jump in the predicted temperature distributions at the phase change interfaces.

The results show that the conventional treatment of effective diffusion coefficient leads to non-physical “jump” in the predicted temperature distribution, particularly close to the interface between the two-phase and the superheated vapor regions. The major achievement of this work is the development of a new smoothing algorithm for the effective diffusivity, which successfully eliminates non-physical “jump” in the temperature distribution for all tested cases. Most importantly, the results clearly indicate that the proposed relaxation of effective diffusion coefficient does not alter the overall energy and momentum balance. All results, obtained with parametric variations, can be physically explained and interpreted. Therefore, the methodology, suggested in this work, is strongly recommended for the simulation of complete phase change process.

Another interesting feature is the effect of the power index n for the relative permeability. Since the inertial and diffusion effects are neglected, Wang and Beckermann [29] used a phase relative permeability weighted pressure gradient to avoid the requirement of negligible slip velocity for a two phase flow. It was observed experimentally that the relative permeability of the liquid phase increases in a nonlinear fashion from 0 to 1 as the liquid saturation increases from 0 to 1. The relative permeability were obtained using the data of both drainage and imbibition steam-water capillary pressure. In the literature, the simplest correlations used for the relative permeabilities are the power functions of the phase saturations. It was reported that the power index for the relative permeabilities of the liquid and vapor phases may vary between 1 and 3. Both these values were empirically determined. In view of this discussion the effect of the power index for the relative permeability has been studied in this work. The results indicated that the effect of decreasing the exponent n in the expression for the relative permeability from 3 to 1 leads to substantial change in the predicted temperature distribution due to considerable enhancement in the effective diffusion coefficient Γ_H^* and hindrance coefficient f in the two-phase region. This means that when the phase change takes place at lower value of exponent n, the area of the two-phase zone is extended towards the upstream and downstream directions, and the temperature at the exit is extremely reduced due to increased heat losses in the upstream direction driven by enhanced axial diffusion. Therefore, adequate care must be taken while designing such evaporators in order to meet the process requirement and it is necessary to verify this phenomenon by experiments in the future. The results also show that the complete phase change process could never be achieved in a transient simulation due to the presence of sharp discontinuity in the modeled effective heat capacity ratio, especially at the saturated vapor, which could not be eliminated using conventional treatments.

The existing h-formulation [29] is restrictive since it is applicable only when ρ_l and ρ_v are assumed to be constants. Further, the formulation relies upon an implicit relation between s and h in the two-phase region and it contains an additional diffusion-like term, which has to be treated as a source in the energy conservation equation (2.138). Since its evaluation would lag the current calculation by one iteration, additional computation time would be required. The modified h-formulation eliminates the problems associated with the existing h-formulation [29]. It can be applied even in the presence of substantial density variations in ρ_l and ρ_v, without requiring any major modification, other than replacing them by their respective saturations values in the expressions for two-phase mixture properties. The theoretical analyses in chapter 2 clearly demonstrates that the existing H-formulation of Wang [33] cannot be applied in its present form if ρ_l and ρ_v are strong functions of the local temperature, particularly when the temperature difference in the vapor phase is substantial. The required modifications have been also presented that indicate the necessity for iterative solution of temperature from the computed H. For steady one-dimensional problems with prescribed mass flow rate, the assumption of either constant or variable ρ_l and ρ_v does not affect the solution of h and hence $T(x)$, although it would strongly affect the velocity solution and the resulting pressure drop in the evaporator. Such a simple conclusion, which is evident from the modified h-formulation, is not apparent from the H-formulation. For LTNE model, however, the solutions obtained for constant and variable ρ_l and ρ_v are expected to differ from each other, even for one-dimensional idealization. For multi-dimensional problems with large temperature variations, however, the constant density assumption or even the Boussinesq approximation would be invalid, although it has been invoked by several researchers [33, 65, 68]. For such cases, the modified h-formulation should be used. Nearly identical solutions predicted by both h- and H-formulations for all tested cases demonstrate the consistency and the accuracy of the proposed modification. It has been also observed that the present formulation requires considerably less computation time as compared to that required for the existing H-formulation. For multi-dimensional problems, the present formulation is expected to be even more beneficial with respect to the required computation time.

On the other hand, it has been observed that the LTE model, even after employing the smoothing algorithm, has been found to be unrealistic for the prediction of multi-dimensional complete phase change problems either in channel or pipe flow model since the superheated vapor zone has been observed to be restricted extremely close to the heated wall and the predicted maximum temperature of the combined medium at the wall has been recorded to be unrealistically high. These observations could be attributed to the extremely lower values of the effective diffusion coefficient in the two-phase mixture zone, close to the superheated vapor region, that restricts any recognizable diffusive energy transport across the interface in between. Therefore, the use of the LTE model should be avoided as far as possible. A comparison of the numerical results for the incomplete phase change process obtained using either non-staggered or staggered grid layout shows that the results are identical.

In chapter 5, the steady-state one-dimensional pipe flow as well as two-dimensional problems under both steady-state and transient flow conditions, based on H-formulation along with the assumption of LTNE, have been used to numerically study the complete phase change process inside porous evaporator. The latter problems include both channel and circular pipe flow models through porous media, applying constant heat flux at different locations and using both staggered and non-staggered grid layouts. Results are presented in terms of temperature for both fluid and solid phases and liquid saturation as well as velocity fields to understand the phase change physics. For one-dimensional problems, the results indicated that without applying the smoothing algorithm for the effective diffusion coefficient, even the LTNE model results in “jump” in the predicted temperature field, which demonstrates the necessity of a remedy. Since the LTNE model captures the true physical condition better than the commonly used LTE model, the difference in the predicted fluid temperature and combined medium temperature at the evaporator outlet using LTNE and LTE models suggests that the former should be applied wherever applicable, although the temperature of the fluid and the solid phases attain nearly the same temperature when LTNE model is used. The effect of employing different models for the partitioning of wall heat flux using the LTNE model has been found negligible owing to the extremely high convective heat transfer coefficient between the solid and the fluid phases that results from smaller characteristic pore diameter. However, these model could be important for other porous media with large characteristics pore diameter and higher porosity. The diffusive energy transport in the upstream direction through the porous evaporator is one of the key factors responsible for the initiation and the termination of the phase change process. For the same mass flow rate (Reynolds number) and wall heat flux, the outlet temperature of the working fluid (steam) is dictated by the heat loss through the inlet due to axial diffusion.

On the other hand, the use of a smoothing algorithm for the effective diffusion coefficient has been found to be essential in order to avoid “jump” in the predicted temperature distribution, even for numerical predictions of multi-dimensional complete phase change problems inside porous media (for both channel and pipe flow models) employing LTNE model using both staggered and non-staggered grid layouts, which could not be removed using LTE model while simulating the complete phase change process inside porous media. With LTNE model, the difference in T_s and T_f has been observed close to the heated wall and the boiling front, while everywhere else, $T_s \approx T_f$ is obtained. The additional mechanisms available for LTNE model in the form of conduction heat transfer through the solid phase and internal heat exchange between the solid and the fluid phases are considered to be responsible for the expansion of superheated vapor region in the transverse direction and the prediction of reasonable maximum temperatures for both solid and fluid phases. Different models for the partitioning of wall heat flux have negligible influence on the overall predictions, except in the vicinity of the wall. These models consider that the total heat flux imposed at the wall is partitioned into two parts which are added separately to the fluid and solid phases. A closer inspection of the results reveals that the model which assumes the total heat flux imposed at the wall to be distributed to the fluid and solid phases according to the ratio of effective thermal conductivities of the respective phases appears to be the most realistic, whereas the model considers that the entire amount of heat is added to the solid phase has been found to be the most stable. On the other hand, the models assume that the entire amount of heat to be added to the fluid and solid phases according to the ratio of thermal conductivities of the phases as well as according to the ratio of volume fractions should be avoided since they produce negative values of ($T_s - T_f$) at the wall owing mainly to the higher fraction of heat addition to the fluid phase at the evaporator wall.

The heterogeneous energy equations as well as the proposed smoothing algorithm are indeed successful in dealing with the rapid change in the modeled effective heat capacity ratio and effective diffusion coefficient in transient simulations of the complete phase change process, which may otherwise promote an undesirable jump in the temperature distribution. When the heater, supplying identical heat flux, is moved from the bottom to the upper plate, keeping all other parameters fixed, a marginal difference in the temperature distribution could be observed due to the buoyancy force. It is, however, interesting to note that when the same heat input is divided and supplied through two identical heaters located at the same axial distance on top and bottom walls, nearly symmetric temperature profile is obtained, indicating that the buoyancy force has only a minor influence. In a circular pipe flow model, the LTNE model predicts early initiation of the phase change process as compared to the results obtained using LTE model for identical conditions. The results also show that the accuracy and the efficiency of the non-staggered and staggered grid layouts are similar for both incomplete and complete phase change process.

Chapter 6 presents the numerical results of the complete phase change process in a two-dimensional flow inside an asymmetrically heated parallel plate channel, filled with anisotropic porous medium, under steady-state condition and based on the H-formulation along with LTNE model. The proposed smoothing algorithm for the effective diffusion coefficient has been extended and applied also for the anisotropic model. Numerical results have been presented for the incomplete and complete phase change process to conclude about the effect of different permeability ratio and thermal conductivity of the solid phase ratio on the temperature and liquid saturation distributions. The results demonstrate that the anisotropy in thermal and hydrodynamic properties of the porous medium have significant influence on the complete phase change process. The superheated vapor and the two-phase regions are extended as the thermal conductivity of the solid phase in the axial direction decreases due to considerably lower heat loss through the inlet. In this situation, the phase change process from sub-cooled liquid state to the two-phase mixture as well as from the two-phase mixture to the superheated vapor state initiates earlier. The decrease of maximum temperatures with increasing permeability ratio between the transverse and axial directions indicates that the diffusive energy flux in the transverse direction is enhanced, which is responsible for a delayed initiation of the superheated vapor region. As Darcy number is decreased, keeping K_R fixed, the phase change process initiates earlier due to decreased diffusive energy flux in the transvers direction, which occurs for reduced effective diffusion coefficient in the transverse direction. Most importantly, the numerical results clearly show that the solid thermal conductivity, keeping k_R fixed, plays an important role and hence, adequate care must be taken while designing such an evaporator based on an anisotropic porous medium.

Finally, chapter 7 describes the numerical results of complete phase change process inside a divergent porous evaporator regarding the one-dimensional problem, under steady-state condition, based on H-formulation along with LTE model. Numerical results indicated that the employment of the proposed smoothing algorithm for the effective diffusion coefficient has been found to be essential in order to avoid the occurrence of non-physical jump in the predicted temperature distribution. The results also clearly indicate that the operating conditions and the geometry of diffuser strongly affect the outlet condition of steam, whereas porous media properties have only minor influence. Most importantly, the analysis demonstrates a useful tool for designing a divergent porous evaporator in order to achieve complete phase change.

8.2. Recommendations for Future Work

This research work has addressed various distinct subjects, which are relevant to complete liquid-vapor phase change process inside porous media. Furthermore, working areas have been identified for obtaining an improved understanding. The methodology suggested in this work is strongly recommended for the simulation of complete phase change process within porous media and it is sufficiently flexible for application in other areas. Therefore, the proposed smoothing algorithm could also be tested for some subjects that need further attention such as the following:

8.2.1. Inclusion of Variable Densities in the Single Phase Regions

In view of the advantages and the proposed modified enthalpy formulation (modified *h*-formulation) does not rely upon the definition of any synthetic variable like *H* [33], it is strongly recommended for the future use of simulation of the complete evaporation process inside porous media. Nevertheless, it is also apparent that the method should be further employed in order to simulate the multi-dimensional phase change problems inside porous media without invoking any simplifying assumption with respect to the single phase densities. It is also important to note that the modified *h*-formulation relies upon the validity of LTE assumption, according to which, artificial insulation layers are formed across the interfaces separating the single and the two-phase regions, primarily owing to the extremely low effective diffusion coefficients in the two-phase region for $s \approx 0$ and $s \approx 1$.Since it has been already pointed out in chapters 4 and 5 that any realistic prediction of the multi-dimensional complete phase change process within porous media requires the employment of LTNE assumption, the present formulation (i.e., modified *h*-formulation) should be extended in order to accommodate such issues. It may, however, be expected that the proposed *h*-formulation, along with LTNE assumption, should also perform better than the existing *H*-formulation and should be beneficial particularly for variable ρ_l and ρ_v, since other than the additional volumetric heat exchange term, the main features of the energy conservation equation for the fluid phase remain nearly the same. As a final remark, it may be mentioned that when the existing *H*-formulation has been used along with the variable density assumption for the single phase regions after adopting the required modifications, no converged solution could be obtained since severe numerical oscillations in the residues for the energy conservation equation could only be detected. Therefore, no meaningful comparison in this respect could be reported in the thesis. Nevertheless, instead of identifying this observation as a real drawback of the existing *H*-formulation with variable ρ_l and ρ_v and reporting it in the thesis, this issue has been left out for the future debate, particularly for the researchers who would still prefer to use the existing *H*-formulation, instead of the proposed modification.

8.2.2. Modeling on Non-Orthogonal Coordinates

The comprehensive literature review on the present topic reveals that all simulations were performed only on orthogonal coordinates. However, it could be extremely useful to provide a varying cross-sectional area of the duct in order to accommodate higher volume flow rates of the vapor-phase. Such simulations would definitely require an extension of the present numerical method on non-orthogonal (i.e., curvilinear) coordinates using the non-staggered variable arrangements. This is definitely a complex as well as time consuming task. However, for the sake of completeness of the present research effort, it is suggested as an extension of the present work for two-dimensional coordinates and it should also be taken up in the future, along with solutions using the LTNE model.

8.2.3. Inclusion of Higher Order Effects

The presently available TPMM formulation is valid only for Darcy flow inside an isotropic porous medium and all simulations were performed only for very low velocity. At higher flow velocities, non-Darcian effects could be important for appropriate modeling. In this regard, the existing two-phase mixture model should be extended in order to include the non-Darcian effects along with LTNE model, by introducing the Forchheimer term, viscous and inertia effects. For this purpose, all mathematical formulation along with the constitutive relations must be derived once again form the basic assumptions and the fundamental conservation principles.

8.2.4. Experimental Study

Prospective work should include an experimental study on the complete phase change process inside porous evaporator. The experimental data are required to validate the numerical results obtained for the complete phase change process inside isotropic and anisotropic porous media using either LTE or LTNE model.

Bibliography

1. R.J. Lipinski, A model for boiling and dryout in particle beds, NUREG/CR-2646 (1982).
2. H.S. Lee and I. Catton, Two-phase flow in stratified porous media. In Proc. Of the 6th Information Exchange Meeting on Debris Coolability, EPRI-NP-4455 (1986).
3. V.X. Tung and V.K. Dhir, A hydrodynamic model for two-phase flow through porous media, Int. J. Multiphase Flow 14 (1988) 47 – 65.
4. M. Chung and I. Catton, Multi-dimensional two-phase flow in porous media with phase change, AIChE. Symp. Series No. 263, 84 (1988)177 – 185.
5. V.X. Tung and V.K. Dhir, Finite element solution of multi-dimensional two-phase flow through porous media with arbitrary heating conditions, Int. J. Multiphase Flow 16 (1990) 985 – 1002.
6. V.K. Dhir, Boiling and two-phase flow in porous media, Ann. Rev. Heat Transfer, 5 (1994) 303 – 350.
7. C. Doughty and K. Pruess, A semi-analytical solution for heat-pipe effects near high-level nuclear waste packages buried in partially saturated geological media, Int. J. Heat Mass Transfer 31 (1988) 79 – 90.
8. P. A. Witherspoon and K. Pruess, Environmental heat transfer in porous media, In *Collected Papers in Heat Transfer,* ASME HTD-Vol. 104, Part 3, ASME, New York (1988)17 – 23.
9. Y.T. Shah, Gas-Liquid Solid Reactor Design. McGraw- Hill, New York (1979).
10. A. Shekarriz and O.A. Plumb, A theoretical study of film condensation using porous fins, ASME Paper No. 86-HT-31 (1986).
11. O.A. Plumb, D.B. Burnett and A. Shekarriz, Film condensation on a vertical flat plate in a packed bed, ASME. J. Heat Transfer 112 (1) (1990) 234 – 239.
12. M. Sözen and K. Vafai, Analysis of the non-thermal equilibrium condensing flow of a gas through a packed bed, Int. J. Heat Mass Transfer 33 (1990) 1247 – 1261.
13. Y. Ogniewicz and C.L. Tien, Porous heat pipe. In Heat Transfer, Thermal Control, and Heat Pipes, Progress in Astronautics and Aeronautics (Edited by W. B. Olstad), 70 (1979) 329 – 345.
14. A. Faghri, Heat Pipe Science and Technology, Taylor & Francis, Washington, DC, (1995).
15. S. Whitaker, Simultaneous heat, mass, and momentum transfer in porous media: a theory of drying. In Advances in Heat Transfer (Edited by J.P. Hartnett and J.F. Irvine, Jr.), Academic Press, New York 13 (1977) 119 – 203.
16. K. Vafai and S. Whitaker, Simultaneous heat and mass transfer accompanied by phase change in porous insulations, ASME J. Heat Transfer, 108 (1986) 132 – 140.
17. J. Bear, Dynamics of Fluids in Porous Media. Elsevier, New York (1972).
18. A.E. Scheidegger, The Physics of Flow Through Porous Media (3rd Ed.). University of Toronto Press. Toronto (1974).
19. G. Chavent, A new formulation of diphasic incompressible flows in porous media, In Lecture Notes in Mathematics, Springer, New York 503 (1976).
20. J. Douglas, Jr., Finite difference methods for two-phase incompressible flow in porous media, SIAM J. Numer. Analysis 20 (1983) 681 – 696.

21. C.H. Sondergeld and D.L. Turcotte, An experimental study for two-phase convection in a porous medium with applications to geological problems, J. Geophys. Res. 82 (1977) 2045 – 2053.
22. P. Cheng, Heat transfer in geothermal systems, In Advances in Heat Transfer (Edited by J.P. Hartnett and J.F. Irvine, Jr.), Academic Press, New York 14 (1979) 1 – 105.
23. C.M. Marle, Multiphase Flow in Porous Media. Gulf, Houston (1981).
24. P.M. Adler and H. Brenner, Multiphase flow in porous media, Annu. Rev., Fluid Mech., 20 (1988) 35 – 59.
25. C.Y. Wang and P. Cheng, Multiphase Flow and Heat Transfer in Porous Media. In Advances in Heat Transfer, Academic Press, New York 30 (1997) 93 – 196.
26. P.S. Ramesh and K.E. Torrance, Stability of boiling in porous media, Int. J. Heat Mass Transfer 33(1990a) 1895 – 1908.
27. P.S. Ramesh and K.E. Torrance, Numerical algorithm for problems involving boiling and natural convection in porous materials, Numer. Heat Transfer B 17 (1990b) 1 – 24.
28. P.S. Ramesh and K.E. Torrance, Boiling in a porous layer heated from below: effects of natural convection and a moving liquid two-phase interface. J. Fluid Mech. 257 (1993) 289 – 309.
29. C.Y. Wang and C. Beckermann, A two-phase mixture model of liquid-gas flow and heat transfer in capillary porous media, I. Formulation, Int. J. Heat Mass Transfer 36 (11) (1993) 2747 – 2758.
30. C.Y. Wang, C. Beckermann and C. Fan, Numerical study of boiling and natural convection in capillary porous media using the two-phase mixture model. Numer. Heat Transfer, Part A 26 (1994) 375 – 398.
31. C.Y. Wang, C. Beckermann and C. Fan, Transient natural convection and boiling in porous layer heated from below, *10th Int. Heat Transfer Conf.*, Brighton, UK, 1994b.
32. C.Y. Wang and C. Beckermann, Boundary layer analysis of buoyancy-driven two-phase flow in capillary porous media, ASME J. Heat Transfer 117 (4) (1995) 1082 – 1087.
33. C.Y. Wang, A fixed-grid numerical algorithm for two-phase flow and heat transfer in porous media, Numer. Heat Transfer, Part B 32 (1997) 85 – 105.
34. K.S. Udell, Heat transfer in porous media considering phase change and capillarity-the heat pipe effect, Int. J. Heat Mass Transfer 28 (2) (1985) 485 – 495.
35. O.T. Easterday, C.Y. Wang and P. Cheng, A numerical and experimental study of two-phase and heat transfer in a porous formation with localized heating from below. Proc. ASME Heat Transf. Fluid Eng. Divisions 321 (1995) 723 – 732.
36. G. P. Peterson and C.S. Chang, Two-phase heat dissipation utilizing porous-channels of high-conductivity material, J. heat transfer 120 (1) (1998) 243 – 252.
37. T.S. Zhao, Q. Liao and P. Cheng, Variations of buoyancy-induced mass flux from single-phase to two-phase flow in a vertical porous tube with constant heat flux, ASME J. Heat Transfer 121 (3) (1999) 646 – 652.
38. Z.Q. Chen, P. Cheng and T.S. Zhao, An experimental study of two-phase flow and boiling heat transfer in bi-dispersed porous channels, Int. Comm. Heat Mass Transfer 22 (2000) 293 – 302.

39. T.S. Zhao and Q. Liao, On capillary-driven flow and phase-change heat transfer in a porous structure heated by a finned surface: measurements and modeling, Int. J. Heat Mass Transfer 43 (2000) 1141 – 1155.
40. K. Yuki, J. Abei, H. Hashizume and S. Toda, Super-high heat flux removal using sintered metal porous media, Int. J. Therm. Sci. 14 (3) (2005) 272 – 280.
41. K. Yuki, H. Hashizume and S. Toda, Key issues to enable high heat flux removal exceeding 10MW/M^2 by use of metal porous media as latent heat –transfer device, Special Topics & Reviews in Porous Media-An International Journal 1 (1) (2010) 1 – 13.
42. H.Y. Li and K.C. Leong, Experimental and numerical study of single and two-phase flow and heat transfer in aluminum foams, Int. J. Heat Mass Transfer 54(2011) 4904 – 4912.
43. M.W. Waite and M.R. Amin, Numerical investigation of two-phase fluid flow and heat transfer in porous media heated from the side, Numer. Heat Transf. A 35 (1999) 271 – 290.
44. T.S. Zhao and Q. Liao, Mixed convective boiling heat transfer in a vertical capillary structure heated asymmetrically, J. Thermophys. Heat Transfer 13 (3) (1999) 302 – 307.
45. T.S. Zhao, P. Cheng and C.Y. Wang, Buoyancy-induced flows and phase-change heat transfer in a vertical capillary structure with symmetric heating, Chem. Eng. Sci. 55 (2000) 2653 – 2661.
46. M. Najjari and S.B. Nasrallah, Numerical study of boiling with mixed convection in a vertical porous layer, Int. J. Therm. Sci. 41 (2002) 913 – 925.
47. M. Najjari and S.B. Nasrallah, Numerical study of boiling in inclined porous layer, J. Porous Media 6 (1) (2003) 71 – 81.
48. M. Najjari and S.B. Nasrallah, Numerical study of the effects of geometric dimensions on liquid-vapor phase change and free convection in a rectangular porous cavity, J. Porous Media 8 (1) (2005) 1 – 12.
49. M. Najjari and S.B. Nasrallah, Liquid-vapor phase-change and mixed convection in a porous layer discretely heated, J. Porous Media 9 (7) (2006) 671 – 681.
50. M. Najjari and S.B. Nasrallah, Effects of latent heat storage on heat transfer in a forced flow in a porous layer, Int. J. Therm. Sci. 47 (2008) 825 – 833.
51. M. Najjari and S.B. Nasrallah, Heat transfer between a porous layer and a forced flow: influence of layer thickness, Drying Technol. 27 (2009) 336 – 343.
52. H.Y. Li, K.C. Leong, L.W. Jin and J.C. Chai, Transient two-phase flow and heat transfer with localized heating in graphite foams, Int. J. Therm. Sci. 49 (2010) 1115 – 1127.
53. V.R. Voller and C.R. Swaminathan, Treatment of discontinuous thermal conductivity in control-volume solutions of phase change problems. Numer. Heat Transf., Part B 24 (1993) 161 – 180.
54. S.V. Patankar, Numerical Heat Transfer and Fluid Flow, Hemisphere, New York, (1980).
55. H.Y. Li, K.C. Leong, L.W. Jin and J.C. Chai, Transient behavior of fluid flow and transfer with phase change in vertical porous media, Int. J. Heat Mass Transfer 53 (2010) 5209 – 5222.
56. H.Y. Li, K.C. Leong, L.W. Jin and J.C. Chai, Three-dimensional numerical simulation of fluid flow with phase change heat transfer in an asymmetrically heated porous channel, Int. J. Therm. Sci. 49 (2010) 2363 – 2375.
57. F. He, J. Wang, L. Xu and X. Wang, Modeling and simulation of transpiration cooling with phase change, Applied Thermal Eng. 58 (2013) 173 – 180.

58. J.H. Wang and H. N. Wang, A discussion of transpiration cooling problems through an analytical solution of local thermal non-equilibrium model, ASME J. Heat Transfer. 128 (2006) 1093 – 1098.
59. M.A.A. Mendes, J.M.C. Pereira and J.C.F. Pereira, On the stability of ultra-lean H2/CO combustion in inert porous burners, Int. J. Hydrogen Energy 33 (2008) 3416-3425.
60. M.A.A. Mendes, J.M.C. Pereira and J.C.F. Pereira, Calculation of premixed combustion within inert porous media with model parametric uncertainty quantification, Combustion and Flame 158 (2011) 466-476.
61. S. Voss, M.A.A. Mendes, J.M.C. Pereira, S. Ray, J.C.F. Pereira and D. Trimis, Investigation on the thermal flame thickness for lean premixed combustion of low calorific H2/CO mixtures within porous inert media, Proceedings of the Combustion Institute, 34 (2013) 3335-3342.
62. Pei-Xue Jiang and Ze-Pei Ren, Numerical investigation of forced convection heat transfer in porous media using a thermal non-equilibrium model, International Journal of Heat and Fluid Flow 22 (1) (2001) 102 – 110.
63. G.P. Peterson and C.S. Chang, Numerical heat analysis and evaluation for two-phase flow in porous-channel heat sinks, Numer. Heat Transfer, Part A 31 (2) (1997) 113 – 130.
64. K. Yuki, J. Abei, H. Hashizume and S. Toda, Numerical investigation of thermofluid flow characteristics with phase change against high heat flux in porous media, ASME J. Heat Transfer. 130 (2008) 012602-1 – 012602-12.
65. J.X. Shi and J.H. Wang, Numerical investigation of transpiration cooling with liquid coolant phase change, Transp. Porous Media. 87 (2011) 703 – 716.
66. C. Xin, J. Wang, J. Xie and Y. Song, Modeling and numerical simulations of vapor-liquid flow and heat transfer within microchannel heat sinks, *ASME 2012 Third International Conference on Micro/Nanoscale Heat and Mass Transfer*. American Society of Mechanical Engineers, (2012) 377 -383.
67. K. Wei, J. Wang, M. Mao, Model discussion of transpiration cooling with boiling, Transp. Porous Media. 94 (2012) 303 – 318.
68. F. Lindner, C. Mundt and M. Pfitzner, Fluid flow and heat transfer with phase change and local thermal non-equilibrium in vertical porous channels, Transp. Porous Media., 106 (1) (2014) 201 – 220.
69. C. Xin, Z. Rao, X. You, Z. Song and D. Han, Numerical investigation of vapor–liquid heat and mass transfer in porous media, Energy Conversion and Management 78 (2014) 1 – 7.
70. D.A. Nield and A. Bejan, Convection in Porous Media, third ed. Springer, New York, (2006).
71. M. Kaviany, Principles of Heat Transfer in Porous Media, second ed. Springer-Verlag, New York, (1995).
72. K. Vafai, Handbook of Porous Media, second ed. Taylor & Francis, New York, 2005.
73. D.B. Ingham, I. Pop (Eds.), Transport Phenomena in Porous Media III, Elsevier, Oxford, (2005).
74. P. Vadasz, Emerging Topics in Heat and Mass Transfer in Porous Media. Springer, New York, (2008).
75. F. He and J. Wang, Numerical investigation on critical heat flux and coolant volume required for transpiration cooling with phase change, Energy Conversion and Management 80 (2014) 591 – 597.

76. J.P. Sheu, K.E. Torrance and D.L. Turcotte, On the structure of two-phase hydrothermal flows in porous media, J. Geophys. Res. 84, (1979) 7524 – 7532.
77. G. Schubert and J.M. Straus, Two-phase convection in a porous medium, J. Geophys. Res. 82, (1977) 3411 – 3421.
78. I. Fatt and W.A. Klikoff, Effect of fractional wettability on multiphase flow through porous media, ASME Trans. 216, 2462.51 (1959).
79. M.R.J. Wyllie, Relative Permeability. In Petroleum Production Handbook (Edited by T. C. Frick), Chap. 25. McGraw-Hill, New York (1962).
80. R.W. Lewis, E.A. Vemer and O.C. Zienkieicz, A finite approach to two-phase flow in porous media, Znt. Symp. on Finite Element Methods in Flow Problems, Swansea (1974).
81. M. C. Leverett, Capillary behavior in porous solids, ASME Trans. 142, (1941) 152 – 169.
82. R. H. Davis and A. Acrivos, Sedimentation of non-colloidal particles at low Reynolds numbers, Ann. Reu. Fluid Mech. 17, (1983) 91 – 118.
83. W.H. Somerton, J.A. Keese and S. L. Chu, Thermal behavior of unconsolidated oil sands, Sot. Pet. Gig. J.14, (1974) 5 – 12.
84. M.A.A. Mendes, S. Ray and D. Trimis, A simple and efficient method for the evaluation of effective thermal conductivity of open-cell foam-like structures. International Journal of Heat and Mass Transfer, 66 (2013) 412 – 422.
85. M.A.A. Mendes, S. Ray and D. Trimis, Evaluation of Effective Thermal Conductivity of Porous Foams in Presence of Arbitrary Working Fluid, Int. J. Therm. Sci. 79 (2014) 260 – 265.
86. M.A.A. Mendes, S. Ray and D. Trimis, An Improved Model for the Effective Thermal Conductivity of Open-cell Porous Foams, Int. J. Heat Mass Transfer 75 (2014) 224 – 230.
87. M.A.A. Mendes, S. Ray and D. Trimis, Determination of Effective Thermal Conductivity of Open-cell Porous Foams for Arbitrary Working Fluid using Single Point Measurement, *Proc. 22nd National & 11th ISHMT-ASME Heat and Mass Transfer Conf.*, Indian Institute of Technology, Kharagpur, India, December, (2013) 28 – 31.
88. C. Borgnakke and R.E. Sonntag, Fundamentals of Thermodynamics, John Wiley & Sons, 2009.
89. F.P. Incropera, D.P. Dewitt, T.L. Bergman and A.S. Lavine, Fundamentals of Heat and Mass Transfer, John Wiley & Sons, 2007.
90. S.W. Churchill and R. Usagi, A general expression for the correlation of rates of transfer and other phenomena. AIChE. J., 18 (1972) 1121 – 1128.
91. N. Wakao, effect of fluid dispersion coefficient on particle-to-fluid heat transfer coefficient in packed beds, Chem. Eng. Sci., 34 (1979) 325 – 336.
92. J.H. Wang and j. X. Shi, A discussion of boundary conditions of transpiration cooling problems using analytical solution of LTNE model, ASME J. Heat Transfer. 130 (2008) 014504-01 – 014504-5.
93. J. Ni and C. Beckermann, Natural convection in a vertical enclosure filled with anisotropic porous media. Trans. ASME J. Heat Transf. 113 (1991) 1033 – 1035.
94. L. Storesletten, Effect of anisotropy on convection in horizontal and inclined porous layers, Emerging Technologies and Techniques in Porous Media. Kluwer Academic Publishers, The Netherlands (2004) 285 – 306.

95. D.A.S. Rees, L. Storesletten and A. Postelnicu, The onset of convection in an inclined anisotropic porous layer with oblique principle axes. Transp. Porous Media 62 (2006) 139 – 156.
96. D. Jaya Krishna, Tanmay Basak and Sarit K. Das, Natural convection in a heat generating hydrodynamically and thermally anisotropic non-Darcy porous medium, International Journal of Heat and Mass Transfer 51 (2008) 4691 – 4703.
97. S.M. Muasavi and M.R. Shahnazari, Investigation of natural convection in a vertical cavity filled with a anisotropic porous media. Iran. J. Chem. Chem. Eng. 27(2), (2008) 39 – 45.
98. I.S. Shivakumara, Jinho Lee, A.L. Mamatha and M. Ravisha, Boundary and thermal non-equilibrium effects on convective instability in an anisotropic porous layer, Journal of Mechanical Science and Technology 25 (4) (2011) 911 – 921.
99. Prakash Chandra and M. Ravisha, Non-Darcian and anisotropic effects on free convection in a porous enclosure, Transp. Porous Media 90 (2011) 301 – 320.
100. C.M. Rhie and W.L. Chow. A numerical study of the turbulent flow past an isolated airfoil with trailing edge separation, AIAA Journal, 21 (1983) 1525–1532.
101. M. Peric, R. Kessler and G. Scheuerer, Comparison of finite-volume Numerical Methods with Staggered and Collocated Grids, Comput. Fluids, 16 (1988) 389 – 403.
102. H.F. Meier, J.J.N. Alves and M. Mori, Comparison between staggered and collocated grids in the finite-volume method performance for single and multi-phase flows, Computers and Chemical Engineering, 23 (1999) 247 – 262.
103. C.R. Maliska, Heat Transfer and Computational Fluid Mechanics two: Fundamentals, Generalized coordinates, LTC Editora, Brazil.
104. A.W. Date, Solution of Navier-Stokes equations on non-staggered grid, Int. J. Heat Mass Transfer, 36, (1993) 1913 – 1992.